Numerical modelling of an acoustically-driven bubble: the growth and collapse near a wall

Thesis by

Bradley Boyd

A thesis submitted in partial fulfilment of the requirements

for the Degree of Doctor of Philosophy in Mechanical Engineering

University of Canterbury

2018

Acknowledgements

First and foremost, many thanks to my supervisor, Dr Sid Becker. His guidance throughout my PhD has had a tremendous influence on my development. I was very fortunate to have a supervisor that dedicated so much time and attention to me and our Research.

Additional thanks to my co-supervisors, Dr Mathieu Sellier and Dr Paul Docherty, for advising me throughout my PhD.

Thanks to my research colleague, Jeremy Robertson.

Thanks to Alice McSweeney and my Parents, Kim and Bill Boyd for your ongoing support.

And of course, praise to Odin, the All-Father, see you in Valhalla.

This work was supported by the Royal Society of New Zealand's Marsden Fund.

Abstract

The acoustically-driven collapse of a bubble results from the oscillating position of an ultrasound transducer face in a liquid medium. Existing fully-compressible models of bubble collapse have been applied to represent the Rayleigh collapse and the shock-induced collapse. These applications may not adequately represent the conditions associated with the acoustically-driven collapse. The current work presents a fully-compressible model that is the first to capture the collapse of a bubble set in a liquid medium subjected to an ultrasound transducer. The oscillating transducer face is represented by an immersed moving reflective boundary. The flow is simulated using a conservative interface capturing method, which includes the use of a high-order WENO reconstruction, a maximum-principle-satisfying and positivity-preserving limiter, and the HLLC approximate Riemann flux. The numerical method is verified by quantitative comparison to the benchmark shock-bubble problem.

The bubble growth, before the bubble collapse, is considered using a Rayleigh-Plesset (RP) approximation. The RP growth initialised collapse (RPGI) model is used to investigate the collapse of a near-wall cavitation bubble. The RPGI model is also used to investigate the influence of common growth assumptions, like neglecting surface tension, on the subsequent collapse of the bubble.

The direct simulation of both the growth and collapse, which we refer to as the acoustically-driven growth and collapse (ADGC) model, is used to investigate the dynamics of the bubble growth and the subsequent collapse with varying standoff distance from the near-wall. The ADGC model is also modified to capture the influence of nearby bubbles on the growth and collapse of the single bubble, providing insight into bubble cloud dynamics.

Contents

List of Figures

List of Tables

List of Publications

Journal articles

[1] Boyd, B. and Becker, S, *Numerical modelling of an acoustically-driven bubble collapse near a solid boundary*. Fluid Dynamics Research, 2018

[2] Argus, F. Boyd, B., and Becker, S., *Electroporation of tissue and cells: A three-equation model of drug delivery*, Computers in Biology and Medicine, 2017, 84: p. 226-234.

[3] Boyd, B. and Becker, S., *Macroscopic Modeling of In Vivo Drug Transport in Electroporated Tissue*, Journal of Biomechanical Engineering, 2016, 138(3): p. 031008-031008-11.

Conference proceedings

Boyd, B. and Becker, S., *Simulation of the acoustically-driven growth and collapse of a cavitation bubble near a wall*, Gallery of Fluid Motion, 71st Annual Meeting of the APS Division of Fluid Dynamics, Atlanta, Georgia, USA, 2018.

Conference Contribution – Video

Boyd, B. and Becker, S., *Simulation of the ultrasound-induced growth and collapse of a near-wall bubble*, Recent Advances in Moving Boundary Problems in Mechanics, IUTAM, Christchurch, New Zealand, 2017.

Conference Contribution – Conference Paper and Oral Presentation

Boyd, B. and Becker, S., *Simulation of the ultrasound-induced growth and collapse of a near-wall bubble*, 70th Annual Meeting of the APS Division of Fluid Dynamics, Denver, Colorado, USA, 2017.

Conference Contribution - Conference Abstract and Oral Presentation

Boyd, B. and Becker, S., *Simulation of the ultrasound-induced growth and collapse of a near-wall bubble*, Gallery of Fluid Motion, 70th Annual Meeting of the APS Division of Fluid

Dynamics, Denver, Colorado, 2017.

Conference Contribution – Video

Boyd, B. and Becker, S., *Simulation of the ultrasound-induced bubble collapse near a rigid boundary*, Fluids in New Zealand (FiNZ), Christchurch, New Zealand, 2017.

Conference Contribution - Conference Paper and Oral Presentation

Boyd, B. and Becker, S., *Modeling of In Vivo Tissue Electroporation and Cellular Uptake Enhancement*, 1st World Congress on Electroporation (WC2015), Portoroz, Slovenia, 2015.

Conference Contribution - Conference Paper and Oral Presentation

Boyd, B. and Becker, S., *Modeling of In Vivo Tissue Electroporation and Cellular Uptake Enhancement*, 9th IFAC Symposium on Biological and Medical Systems (BMS), Berlin, Germany, 2015.

Conference Contribution - Conference Paper and Oral Presentation

Boyd, B. and Becker, S., *Modeling of In Vivo Tissue Electroporation and Cellular Uptake Enhancement*, OMICS World Drug Delivery Summit, Houston, USA, 2015.

Conference Contribution - ePoster Presentation

Boyd, B. and Becker, S., *Modeling of In Vivo Tissue Electroporation and Cellular Uptake Enhancement*, Health Research Society of Canterbury 2015 Poster Expo, Christchurch, New Zealand, 2015.

Conference Contribution - Poster Presentation

Boyd, B. and Becker, S., *Theoretical modelling of in vivo skin electroporation: degree of electroporation and mass transfer enhancement*, Fluids in New Zealand (FiNZ), Christchurch, New Zealand, 2015.

Conference Contribution - Conference Paper and Oral Presentation

Boyd, B. and Becker, S., *Theoretical modelling of in vivo skin electroporation: degree of electroporation and mass transfer enhancement*, D4: Devices for Diagnostics and Drug Delivery, Dunedin, New Zealand, 2014.

Conference Contribution - Poster Presentation

Nomenclature

a	Transducer face displacement amplitude (m)
A	Area (m^2)
A	Jacobian in the *x*-direction
B	Jacobian in the *y*-direction
B	the left Cauchy-Green strain tensor (Chapter 8)
B	Gilmore equation parameter (Pa)
c	The speed of sound (m/s)
CFL	Courant–Friedrichs–Lewy number
d	Bubble centroid displacement
e	Internal energy (J/kg)
E	Total energy (J)
f	Frequency (1/s)
F	Force (N)
F	Flux in the *x*-direction
F	The deformation gradient tensor (Chapter 8)
f	Force vector (Chapter 8 - N)
$\mathbf{f}^p$	the corner forces acting on the node (Chapter 8 - N)
$\mathbf{f}^z$	the corner forces acting on the zone (Chapter 8 - N)
g	mesh growth rate
G	Flux in the *x*-direction
H	depth dimension in the *z*-direction (m)
H	Enthalpy difference in the Gilmore equation (Chapter 5 - J/kg)
I	Integration interval
I	Identity matrix
k	Computational Schlieren shading function parameter
l_1	Tensorial invariant (Chapter 8)
l_2	Tensorial invariant (Chapter 8)
m	Minimum limit
M	Maximum limit
m	Element subzone mass (Chapter 8 – kg)

M Element zone mass (Chapter 8 – kg)

n Gilmore equation parameter

N Number of finite volume cells

n unit normal vector (Chapter 8)

p Pressure (Pa)

P Polynomial

P Perimeter (Chapter 6 - m)

r, z Axisymmetric cylindrical coordinates (m)

R Bubble radius or radial dimension (m)

s Wave speed (m/s)

S Bubble standoff distance (the shortest distance from the bubble centre to the wall - m)

S Entropy (Chapter 8 – J/K)

S Source terms

t Time (s)

T Temperate (K)

T_U Ultrasound wave period (s)

u Velocity (m/s)

u_a Speed of the refracted shock (m/s)

u_r Velocity in the *r*-direction (m/s)

u_s Speed of the incident shock (m/s)

u_t Speed of the transmitted shock (m/s)

u_z Velocity in the *z*-direction (m/s)

u Velocity vector (m/s)

U State variables

V Volume (m^3)

V Primitive variables

W Characteristic Variables

x_T Transducer face displacement position (m)

x, y Cartesian coordinates (m)

Greek Symbols

α Volume fraction

β	Interface smoothness parameter
γ	Stiffened equation of state parameter
Γ	Stiffened equation of state parameter
Δr	Cell width in *r*-direction
Δt	Time step size (s)
Δt	Time duration (s)
ΔV	Cell volume
Δx	Cell width in *x*-direction
Δy	Cell width in *y*-direction
Δz	Cell width in z-direction
ε	Small numerical constant
ε	The strain tensor (Chapter 8)
η	Polytropic index
θ	Positivity-preserving and maximum-principle-satisfying limiter variable
κ_1	Positivity-preserving and maximum-principle-satisfying limiter variable
κ_2	Positivity-preserving and maximum-principle-satisfying limiter variable
λ	Lamé parameter (Chapter 8)
Λ	Diagonal matrix of eigenvalues
μ	Dynamic viscosity ($\text{Pa} \cdot \text{s}$)
μ	Lamé parameter (Chapter 8 - Pa)
π_∞	Stiffened equation of state parameter (Pa)
Π	Stiffened equation of state parameter (Pa)
ρ	Density (kg/m^3)
σ	Interface surface tension (N/m)
σ	Cauchy stress tensor (Chapter 8 - Pa)
ϕ	Sphericity of the bubble shape
ϕ	Signed distance (Chapter 8 - m)
ψ	Computational Schlieren shading function

Subscripts

Q_0	Initial value

Q_1 Fluid 1 - Bubble fluid (air)

Q_2 Fluid 2 - Surrounding fluid (water)

Q_3 Fluid 3 (Chapter 8)

Q_A Amplitude

Q_{atm} Atmospheric value

Q_B Bubble property

Q_d Domain

Q_D Additional duration for developing the ultrasound field

Q_{ext} Extrapolated value (Chapter 8)

Q_f Refined region

Q_I Value at the interface (Chapter 8)

$Q_{i,j}$ Value at coordinate $\left[r_i, z_j\right]$

Q_L Blake threshold or lower transient threshold

Q_M Minnaert resonant bubble

$Q_{\max}$ Maximum value

$Q_{\min}$ Minimum value

Q_p Corresponding corner node (Chapter 8)

Q_R Ultrasound ramping duration

Q_{RP} A value from the RP equation at pre-collapse bubble state

Q_U Fully developed ultrasound field

Q_∞ Infinite boundary condition

Superscripts

$\overline{Q}$ Nondimensionalized variable

$\overline{Q}$ Finite volume cell average value (Chapter 3 and Appendices)

$\dot{Q}$ First-time derivative

$\ddot{Q}$ Second-time derivate

Q^* Effective value

Q^{-1}	The inverse of a matrix
Q^{L}	Reconstructed value at the left of the cell edge
Q^{n}	Value at time level, n
Q^{pk1}	first Piola-Kirchoff (Chapter 8)
Q^{R}	Reconstructed value at the right of the cell edge
Q^{T}	The transpose of a matrix

Abbreviations

1D	One-dimensional
2D	Two-dimensional
3D	Three-dimensional
ADGC	Acoustically-driven growth and collapse model
CFL	Courant–Friedrichs–Lewy
EOS	Equation of State
HLLC	Harten-Lax-van Leer-Contact (HLLC) approximate Riemann flux
RC	Rayleigh collapse
RGC	Rayleigh growth and collapse
RK3	Third-order Runge-Kutta
RP	Rayleigh-Plesset
RPGI	RP growth initialised collapse model
TVD	Total Variation Diminishing
WENO	Weighted essentially non-oscillatory

Chapter 1 Introduction

1.1 Acoustic Cavitation

Acoustic cavitation is employed in applications such as ultrasonic surface cleaning [4], water filtration [5], and food processing [6]. The medical field employs acoustic cavitation in ultrasound lithotripsy [7], the antitumor effect [8], hemostasis [9], phacoemulsification [10], drug and gene delivery [11], sonoporation [12], and cancer immunotherapy [13]. These medical applications use the violent collapse of cavities (bubbles) to disrupt the barrier properties of biological microstructures.

Physically, an ultrasound (acoustic) field is introduced into a fluid medium through the oscillating position of an ultrasound transducer face. With a sufficient drop in the fluid pressure, resulting from the applied acoustic field, the fluid may undergo a phase change in localised regions: this is described as cavitation [14, 15]. Following the appearance of a gas and vapour filled cavity (or bubble), the bubble will expand and compress in harmony with its pressure oscillations resulting from the acoustic field. In time, as it continues to expand and compress, the bubble's mass may continue to increase as gas and vapour from the surrounding liquid medium diffuse into the bubble in a process termed rectified diffusion [14-16].

If this bubble reaches a sufficient size and if the pressure amplitude of the acoustic field is sufficient (Blake threshold), the bubble may experience a very violent collapse [14, 15]. The bubble size naturally increases when the acoustic field is in a period of decreasing pressure. As the acoustic pressure begins to increase, the bubble's rate of growth starts to decrease until the bubble radius reaches its maximum size. As the acoustic pressure continues to increase, the bubble begins a compression stage that ultimately ends in a violent collapse. When this collapse occurs near a solid boundary, a fluid jet develops through the centre of the bubble towards this boundary, see the representative depiction in Figure 1.1. The development of the jet is also seen in the images of a laser-induced bubble collapse near

a solid wall from the experimental study [17] depicted in Figure 1.2. The impact of the jet on such a solid boundary results in large pressures at the solid boundary [4, 18-21].

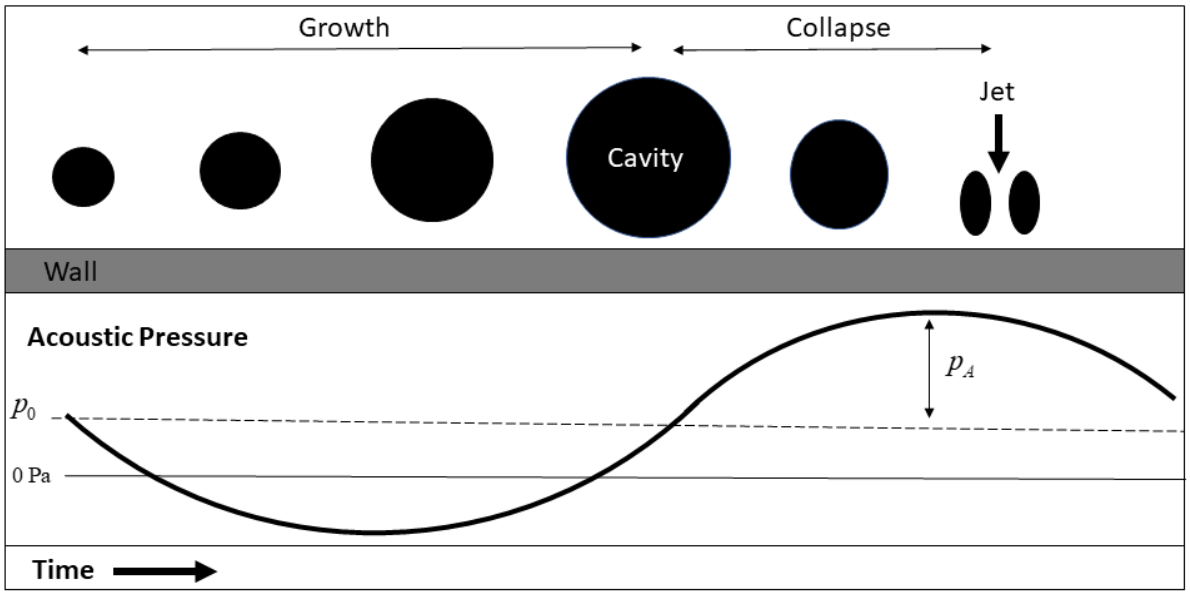

Figure 1.1. A representative depiction of the acoustically-driven growth and collapse of a bubble near a wall.

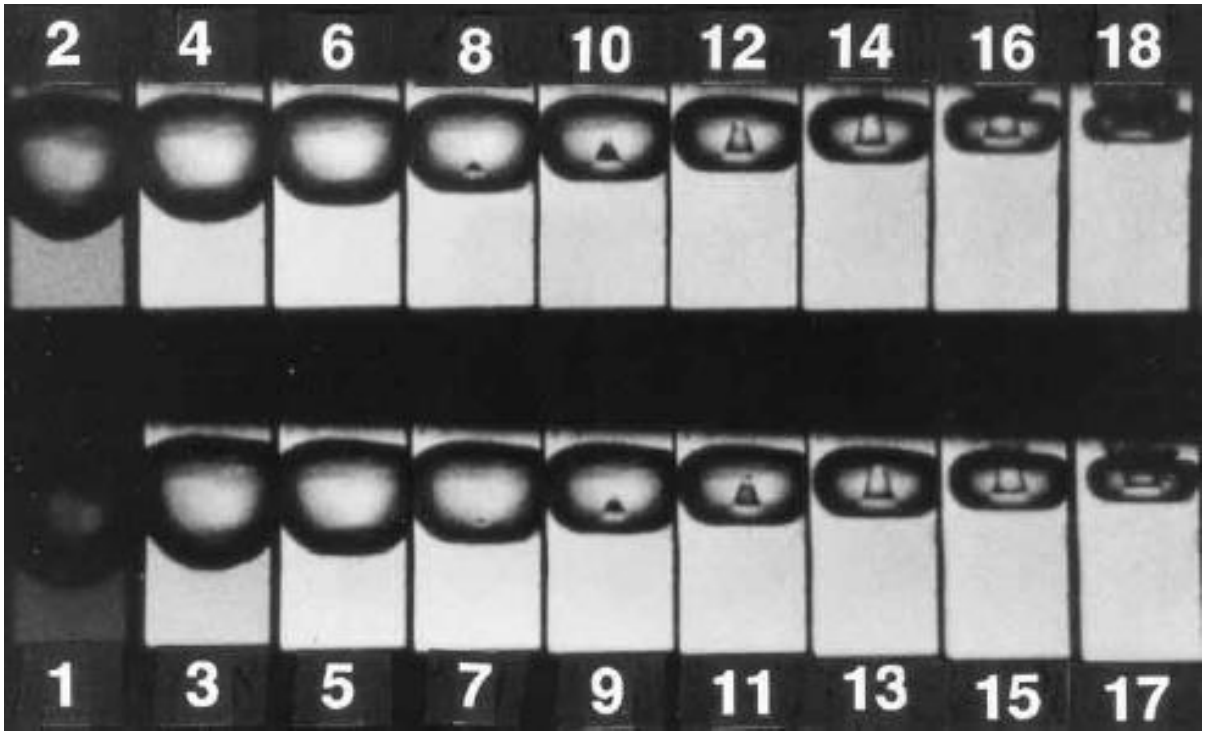

Figure 1.2. Photographs of the laser-induced bubble collapse near a solid wall (at the top of the frame), where the interval between the frames 10 μs. The figure is from [17], reproduced with the permission of the author.

The sudden localised high pressure on a boundary that is near an acoustically-driven bubble collapse has been associated with permeability increases in biological tissues [12, 22-25]. It is of importance for researchers to model the collapse of a bubble resulting from an acoustic field.

The most common method for describing the dynamics of a bubble is the Rayleigh-Plesset (RP) equation [14, 15]. The RP equation makes assumptions to consider a spherical bubble and is not applicable in cases like the near-wall bubble collapse. However, it is still a very useful tool for considering the fundamental dynamics of a bubble in a liquid. Before introducing the motivation of the acoustically-driven bubble, we first describe the RP equation that is referred to on numerous occasions in this thesis.

1.1.1 Rayleigh-Plesset (RP) Analysis

The Rayleigh-Plesset (RP) equation is used to describe the dynamics of a spherical bubble in an infinite body of incompressible liquid. The Rayleigh-Plesset (RP) equation is derived from the Navier-Stokes equations. It describes the dynamics of a spherical bubble in spherical coordinates

$$\frac{p_B(t)-p_\infty(t)}{\rho_L}=R\ddot{R}+\frac{3}{2}\dot{R}^2+\frac{4\mu}{\rho_L R}\dot{R}+\frac{2\sigma}{\rho_L R} \tag{1.1}$$

where R is the bubble radius, $\dot{R}$ and $\ddot{R}$ are the first and second-time derivatives, p_B is the bubble pressure, p_∞ is the pressure infinitely far from the bubble, σ is the interface surface tension, ρ_L is the density of the surrounding liquid, and μ is the dynamic viscosity of the surrounding liquid. For an acoustic field, the far-field pressure p_∞ is approximated by

$$p_\infty = p_0 - p_A \sin(2\pi ft) \tag{1.2}$$

where p_A is the pressure amplitude of the acoustic field, f is the frequency of the acoustic wave, and p_0 is the steady pressure in the absence of the sound field, which is typically equal to the atmospheric pressure: $p_0 = p_{atm}$.

For a spherical air bubble, the bubble pressure changes as a function of the bubble radius [14, 15]:

$$p_B = p_{0,B}\left(\frac{R_0}{R}\right)^{3\eta} \tag{1.3}$$

where $p_{0,B}$ is the pre-growth bubble pressure and R_0 is the pre-growth bubble radius. The behaviour of the gas in the bubble is polytropic with a constant value of η [14]. Typically, the bubble growth is considered to be either isothermal (constant bubble temperature) with $\eta=1$ or adiabatic with $\eta=1.4$ [14, 15]. The initial pressure of the bubble to give a bubble in equilibrium with the surrounding liquid is

$$p_{0,B} = p_{atm} + \frac{2\sigma}{R_0}. \tag{1.4}$$

The ideal gas law is used to determine the density of the air in the pre-growth bubble $\left(\rho_{0,B}\right)$, given $p_{0,B}$, the specific gas constant of air is 287 J/(kg·K), and assuming the air temperature is 293.15 K.

1.2 Motivation

1.2.1 Acoustically-driven bubble collapse (Chapter 2-4)

This work focuses on the modelling of a cavitation bubble driven by an acoustic field, with a focus on the growth and collapse of a near-wall bubble. Acoustic cavitation is a complex process making it difficult to model. It is difficult to model because it involves multiple fluids (air, water, and vapour), a transient acoustic field, and high velocities where the effects of compressibility become important (e.g. shock waves). A model able to capture the growth and collapse of an acoustic bubble near a wall is a significant development in the field as it would provide a tool to investigate the physics of an acoustically-driven bubble. The model would also provide a tool for insight into specific acoustic-cavitation applications, like ultrasonic surface cleaning [4] or sonoporation [12].

Published models of bubble collapse have not yet represented the bubble collapse that results from a low-frequency ultrasound (acoustic) field associated with the oscillating position of the ultrasound transducer face. Some researchers have initiated the bubble collapse by a specified initial pressure difference between the bubble and the surrounding liquid for which the pressure distribution in each of the two domains is uniform [4, 26-38]. Such an initial pressure difference drives the violent collapse of the bubble: this type of collapse is termed a Rayleigh collapse. Other researchers have initiated the bubble collapse by modelling a shockwave that travels through the surrounding liquid towards the bubble [18, 19, 38-40]. During the bubble-shock interaction, the bubble collapses violently. The published methods of modelling the collapse of a bubble may be categorised as incompressible, weakly compressible, or fully compressible. We briefly summarise these methods and note on their limitations in representing the acoustically-driven collapse next.

The earliest models of near-wall bubble collapse represent the liquid medium surrounding the bubble as incompressible [26-29]. The assumption of an incompressible surrounding liquid allows the problem to be reduced to the Laplace equation of the velocity potential within the surrounding liquid. The representation of the surrounding medium as incompressible also simplifies the application of the far-field boundary condition. The far-field pressure is treated as constant and the velocity potential there is typically taken to be zero. While the numerical method is greatly simplified, this method for modelling the bubble collapse is unable to capture the effects of compressibility, which are important at the later stages of the collapse [14]. Furthermore, these studies all represent the far-field pressure to be constant for the duration of the collapse. However, in an acoustically-driven collapse, the far-field pressure is anticipated to vary sinusoidally in time.

Later models modify the incompressible model by representing the surrounding fluid as weakly compressible and simulate an acoustic input from the far-field [41, 42]. The studies by Wang and Blake [41, 42] show the influence of acoustic waves on the bubble dynamics, but do not capture the violent collapse of a bubble near a wall (which is of importance to the current work). Because significant Mach numbers are anticipated near the bubble during a violent collapse, the assumption of infinite propagation rates of the weakly compressible model becomes less valid. The weakly compressible model is unable to capture the formation of shocks, which are anticipated in a violent bubble collapse case [14, 15, 43].

Alternately, fully compressible models, which are capable of capturing shocks, have also been published in which both the fluid of the bubble and the surrounding liquid are represented as compressible. In some of these studies, the collapse is induced by a shock wave travelling through the domain [18, 19, 38-40]. Other fully compressible studies induce the collapse in a manner more consistent with the acoustically-driven collapse by using an initial condition in which there is a pressure difference between the bubble and the surrounding medium [4, 37, 38]. In the studies by Chahine [4, 37], they initialised the bubble at a higher pressure than the surrounding liquid, resulting in the growth and collapse of the bubble. In the study by Johnsen [38], they study the Rayleigh collapse near a wall. When applying these models to an acoustically-driven collapse, it is unclear what choice of initial

pressure difference would correctly represent the conditions of the bubble in the acoustic field. Because the collapse is highly dependent on the magnitude of this pressure difference, the choice is not arbitrary.

Instead of considering an assumed bubble collapse case, we wish to simulate the growth and collapse of a bubble in an ultrasound field where the growth and initial conditions are given by the details of the system. An example case would be a bubble initially in equilibrium with the surrounding fluid with a radius of 50 μm (pre-growth bubbles); the bubble would then grow and collapse due to an acoustic field with a frequency of 30 kHz and a pressure amplitude of 200 kPa.

In the studies [44, 45], they do a comprehensive job of capturing a bubble in a megasonic acoustic field. The key difference between their model and our model is the application is different: we wish to consider low frequency (LF) (e.g. 30 kHz) ultrasound-induced cavitation which is typically more violent (and more unstable) than high frequency (1 MHz) megasonic-induced cavitation. Additionally, the numerical method used in [44, 45] has computational issues as described in [46]. They also use a lower order reconstruction (third-order) which results in more numerical diffusion of the material (fluid-fluid) interface, reducing the sharpness of the interface. Numerical diffusion of the material interface is the main disadvantage of the interface capturing method.

The published collapse models may not be directly applied to represent the physics of the acoustically-driven collapse correctly. The velocity, pressure, and density distributions associated with the acoustic field experience dynamic changes during the growth and collapse of the bubble and these changes are not captured in the Rayleigh collapse case or the shock-induced collapse case. To the authors knowledge, none of the existing fully compressible models can initiate bubble collapse in a manner that is consistent with the physics of a low-frequency ultrasound-induced collapse. The lack of a model that captures the physics of this acoustically-driven bubble collapse is the primary motivation of the work presented in this thesis.

1.2.2 Investigating the bubble growth assumptions (Chapter 5)

In numerical models of bubble growth and collapse, assumptions are commonly made for the bubble growth phase: for example, an incompressible surrounding fluid. These growth assumptions are not

quantitatively verified. The acoustically-driven bubble collapse model we develop could be used to analyse the effect of many assumptions commonly associated with the growth phase of the bubble (e.g. surface tension) and how these effects change the subsequent collapse of the bubble. Determining which effects significantly influence the growth and collapse would provide valuable information for future numerical models. Additionally, this new information may lead to modifying the effects in applications; for example, adding a surfactant to reduce the surface tension.

1.2.3 Acoustically-driven bubble *growth* and collapse (Chapter 6)

To further investigate the growth phase, we modify the model to directly simulate both the growth and collapse phase of the bubble, instead of using the RP equation to approximate the growth. The direct simulation of the bubble growth is important because the near-wall bubble does not grow spherically, which is implied by the RP growth. The RP equation assumes no influence of any near-wall, so the near-wall bubble growth also results in restricted growth (reduced volume) and centroid displacement. The consideration of the near-wall bubble growth is also expected to influence the subsequent collapse of the bubble.

To the author's knowledge, the studies [4, 37, 44, 45] and are the only fully-compressible studies that directly simulate the growth and collapse of a bubble near a wall. In the studies [4, 37], they initialised the bubble at a higher pressure than the surrounding liquid, resulting in the growth and collapse of the bubble. However, this model is *not* able to represent an acoustically-driven bubble because a transient pressure field drives an acoustically-driven bubble: in the absence of this transient pressure field, no initial pressure difference between the bubble and the surrounding medium would correctly represent the conditions of the bubble in a transient acoustic field.

In the studies [44, 45], they consider the growth of bubbles in a high frequency megasonic field. As previously discussed (section 1.2.1), their application is significantly different from low-frequency ultrasound applications and results in a less violent bubble collapse. It is unclear if their model with be stable for this more violent collapse case.

Additionally, there has been no numerical investigation into the effect the acoustic field has on the near-wall bubble growth and collapse. The acoustic field in ultrasound applications depends on the frequency and displacement of the ultrasound transducer face, but it is also dependent on the influence of near boundaries (e.g. the solid boundary). The inclusion of near boundaries, like the wall, can dramatically change the magnitude acoustic field because of the acoustic interface. The standing waves in the fluid is an important consideration for the acoustically-driven bubble. With the model developed, the acoustic field is directly simulated using an immersed moving boundary. The influence of the subsequent acoustic standing wave on the bubble growth can be investigated.

1.2.4 Acoustically-driven bubble in a cloud (Chapter 7)

Considering the dynamics of a single cavitation bubble provides valuable insight into acoustic cavitation applications; however, in practice, multiple bubbles or even bubble clouds are always observed in acoustic cavitation applications [15]. The conjugation or a cluster of bubbles is referred to as a cloud of bubbles. The presence of nearby bubbles, in a bubble cloud, influences the growth and collapse of the single bubble. Numerical studies of bubble cloud dynamics have been conducted previously [47-53]. These previous studies consider the small cluster of bubbles in a large domain of liquid so that the acoustic far-field pressure is uninfluenced by the bubble cloud distribution. What we wish to model is a case where the bubbles are distributed through the entire domain where the near bubbles may reduce the magnitude of the acoustic pressure wave and suppress the transient/inertial cavitation behaviour.

1.2.5 Growth and collapse of a bubble near a tissue (Chapter 8 – Future Work)

Finally, in some acoustic cavitation applications, the near-wall is not rigid. The influence of a deformable boundary on the growth and collapse of the acoustic bubble is, therefore, of interest. One important application which involves the acoustically-driven collapse of a cavitation bubble near a deformable boundary is skin tissue sonoporation [12, 22, 23, 54-57]. Skin sonoporation involves the violent collapse of a cavitation bubble near skin tissue, introducing porous pathways in the skin allowing

mass transport (e.g. drug delivery) [22]. However, the field is still unclear on what causes the introduction of the porous pathways. Thus, the development of a model able to capture the growth and collapse of an acoustically-driven bubble near a deformable solid, where the deformable solid represents the skin tissue, would be a valuable contribution to the field. The most developed model of the ultrasound-induced growth and collapse of a bubble near tissue is in [58]; however, it does not capture the compressibility of the surrounding fluid and the tissue which is important when the bubble collapses violently.

1.3 Contributions and Outline

In the present work, we develop a high-order fully-compressible model to capture an acoustically-driven bubble: the growth and collapse of a near-wall bubble in an acoustic field. The idealised physical problem of an acoustically-driven cavitation bubble is presented (Chapter 2). The main contributions of the thesis are:

- (Chapter 3) Development and verification of the numerical methods used in the numerical models. The numerical model uses a conservative interface capturing method, which includes the use of a high-order WENO reconstruction, a maximum-principle-satisfying and positivity-preserving limiter, and the HLLC approximate Riemann flux. The acoustic input is generated using an oscillating of an immersed moving reflective boundary, which represents the ultrasound transducer face.
- (Chapter 4) Development of the model to represent the acoustically-driven collapse of a near-wall bubble. The collapse problem is initialised using the Rayleigh-Plesset (RP) equation to approximate the growth phase of the bubble. The RP bubble is superimposed onto the developed acoustic field to give the initial condition of the acoustically-driven bubble collapse. The model is compared to the previously develop Rayleigh collapse model. This model is termed the RP growth initialised collapse (RPGI) model.
- (Chapter 5) Investigation of the significance of various effects on the growth phase and their influence on the subsequent collapse of the acoustically-driven bubble.

- (Chapter 6) Further development of the acoustically-driven bubble model to directly simulate the growth before the collapse. We investigated the influence of the near-wall on the growth of the bubble and the influence of the spatial variation in pressure amplitude of the acoustic field. The subsequent wall pressure of the growth and collapse model of the near-wall bubble is considered at various standoff distances. The model is compared to the RP growth initialised collapse (RPGI) model and the previously developed Rayleigh growth and collapse (RGC) model.
- (Chapter 7) In acoustic cavitation applications, multiple cavitation bubbles typically appear forming a cloud of bubbles. In this Chapter, we investigate the influence of nearby bubbles on the growth and collapse of the acoustically-driven bubble.
- (Chapter 8) In an attempt to investigate the growth and collapse of an acoustically-driven bubble near soft tissue, we began developing a compressible solid model to capture the tissue and to couple this to the compressible-multiphase flow model. In its current state, the model is not complete, but it is in the numerical verification stages.

Concluding remarks are presented in Chapter 9 followed by the Appendices. Note that the main contributions of this thesis are presented in Chapter 4 and Chapter 6.

Chapter 2 Physical Model

2.1 Idealised problem

The ultrasound-induced collapse of a bubble is a result of acoustic cavitation. With a sufficient drop in the fluid pressure, caused by the acoustic field, the fluid undergoes a phase change in localised regions where nucleation is possible, described as cavitation [14, 15]. The newly formed cavity, composed of vapour and air, appears as a bubble in the solution, where it can continue to grow in time as air from the solution diffuse into the bubble: this is termed rectified diffusion [14, 15]. If the initial stable cavitation bubble is large enough and the amplitude of the acoustic field is sufficient in magnitude the bubble will respond transiently: often described as the lower transient threshold or Blake threshold [15]. This cavity will then grow rapidly with decreasing fluid pressure to at least twice its initial size [15]. As the fluid pressure begins to increase, the bubbles rate of growth starts to decelerate until the bubble radius reaches its maximum and the transient collapse begins. The violent collapse of a cavitation bubble near a wall results in a high pressure experienced by the wall and in cases a re-entrant jet threads the bubble and violently impacts the surface of the wall [18, 19].

The primary force driving the growth and collapse of a bubble is the difference in the pressure between the bubble and the surrounding liquid. The pressure in the surrounding liquid varies due to the acoustic input. The change in the acoustic pressure field in the liquid results in the pressure difference between the bubble and the liquid, driving the bubble growth or collapse; hence, we refer to the bubble as being acoustically-driven. For more details on the fundamental physics of acoustic cavitation we refer the reader to the text by Young [15].

The current study uses a few simplifications that previous works have also implemented. The nucleation and formation of the cavity are not considered, as they are difficult to model and provide no additional insight into the collapse of a cavity [38]. Instead, we assume a cavity (the bubble) is already present in the solution. Surface tension, viscous effects, gravity, and heat conduction are considered to be of secondary importance during the collapse [19, 27, 29, 34, 59, 60]; thus they are neglected. However, if

the wall erosion due to the collapsing bubble is of interest, the inclusion of heat conduction may become important [61]. We also assume that no mass transport occurs across the interface during the collapse and that the cavitation bubble is entirely composed of air. This can be justified as follows: while the vapour present in the bubble will add additional cushioning to the collapse, in practice the cushioning of the vapour is likely to be insignificant [14, 62]. Considering the condensation and evaporation of the vapour across the interface and rectified diffusion of air across the interface during the collapse would greatly increase the complexity of the model, with minimal additional insight into the collapse. Additional chemical forces, like intermolecular forces, are neglected as they are expected to be relatively insignificant when compared to the large pressures driving the bubble. These assumptions result in the idealised model of an ultrasound-induced bubble collapse of an air bubble, using a compressible multiphase model to capture the different fluids and any shock waves that develop.

The transducer face oscillates in the fluid medium producing the ultrasound (acoustic) field. Thus, the acoustic field in the fluid depends on the displacement amplitude (a) and frequency (f) of the transducer face. A representation of an experimental acoustic cavitation setup (e.g. ultrasonic cleaning [63] or sonoporation [54]) including the transducer, cavitation bubble, surrounding fluid, and the solid boundary is depicted in Figure 2.1. The dashed line in this figure represents the physical domain that is modelled in the present study. Note that the width of the domain is smaller than the width of the transducer face: this allows the outer boundary to be treated as a reflective boundary, capturing the symmetry at that boundary, see section 3.8.1. This study only considers the region in the vicinity of a single bubble. No bubble-bubble interactions are considered, until Chapter 7.

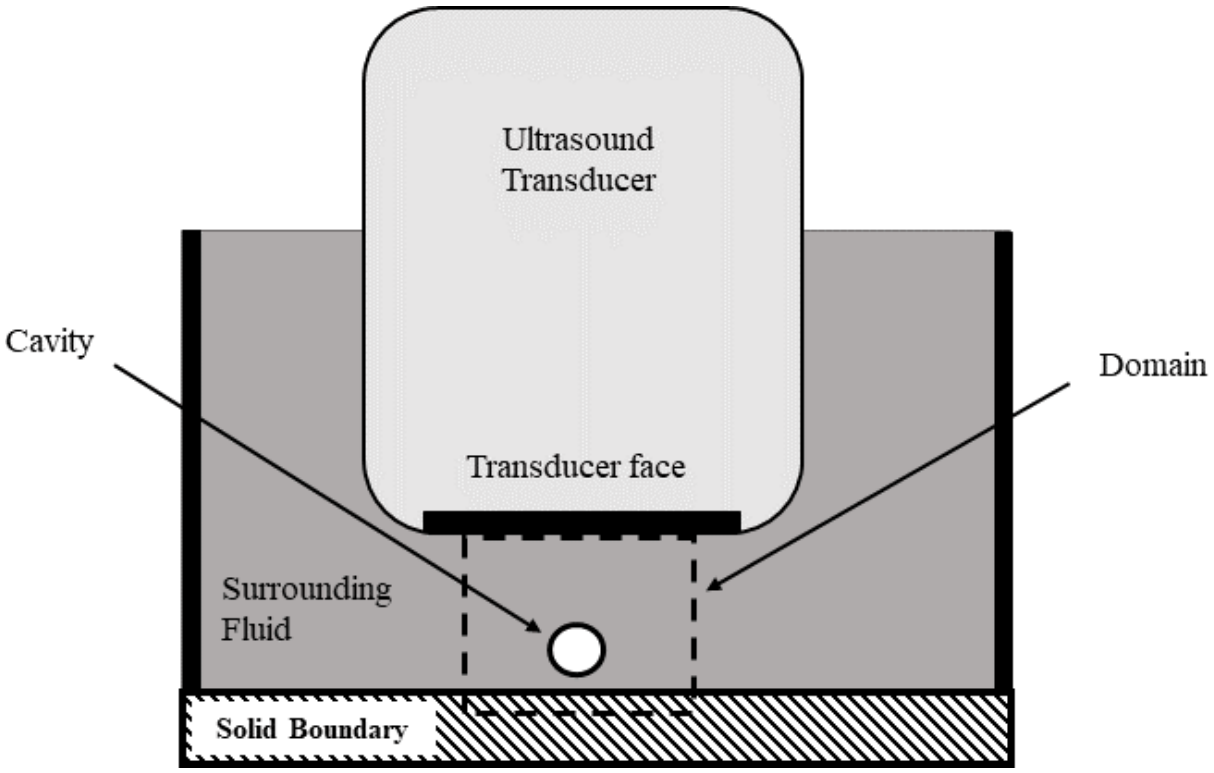

Figure 2.1. A representative depiction of an ultrasound transducer setup with water as the surrounding fluid (not drawn to scale).

2.2 The Governing Equations

The multiphase flow that is composed of the two fluids (the gas-filled bubble and the surrounding liquid) is considered to be compressible and inviscid. This two-fluid system is described using the five-equation model of [64] consisting of two continuity equations (one for each fluid), one momentum equation, one energy equation, and one advection equation of the volume fraction of the gas:

$$\frac{\partial(\alpha_1\rho_1)}{\partial t} + \nabla\cdot(\alpha_1\rho_1\mathbf{u}) = 0 \tag{2.1}$$

$$\frac{\partial(\alpha_2\rho_2)}{\partial t} + \nabla\cdot(\alpha_2\rho_2\mathbf{u}) = 0 \tag{2.2}$$

$$\frac{\partial(\rho\mathbf{u})}{\partial t} + \nabla\cdot(\rho\mathbf{u}\otimes\mathbf{u} + p\mathbf{I}) = \mathbf{0} \tag{2.3}$$

$$\frac{\partial E}{\partial t}+\nabla\cdot\left(\mathbf{u}\left(E+p\right)\right)=0 \tag{2.4}$$

$$\frac{\partial \alpha_1}{\partial t}+\mathbf{u}\cdot\nabla\alpha_1=0 \tag{2.5}$$

where α_1 is the volume fraction of bubble fluid, α_2 is the volume fraction of the surrounding fluid, ρ is the density, $\mathbf{u}$ is the velocity vector, p is the pressure, E is the total energy $E=\rho\left(e+\left|\mathbf{u}\right|^2/2\right)$, e is the internal energy, and $\mathbf{I}$ is the identity matrix. The subscript 1 denotes the bubble fluid (gas) and the subscript 2 denotes the surrounding fluid (liquid). These equations combined with an equation of state (EOS) and a set of mixture rules completely define the compressible-multiphase system.

The advection of the bubble fluid volume fraction $\left(\alpha_1\right)$ captures the advection of the interface between the bubble fluid and the surrounding fluid. Later in the results, we visualize the interface location by depicting a contour of the bubble fluid volume fraction $\left(\alpha_1\right)$, typically at $\alpha_1=0.95$ (for an example, see Figure 4.4).

2.3 The Equation of State (EOS)

The system of Eqs. (2.1)-(2.5) requires an EOS to close the system. In this model, the stiffened equation of state is used [18, 38, 39, 46, 60, 64-67]:

$$\Gamma p+\Pi=E-\frac{1}{2}\rho\left|\mathbf{u}\right|^2. \tag{2.6}$$

$\Gamma=\frac{1}{\gamma-1}$, $\Pi=\frac{\gamma\pi_\infty}{\gamma-1}$, γ, and π_∞ are properties of the fluid (typically determined using shockwave Hugoniot data) [65, 68, 69]. For an ideal gas, $\pi_\infty=0$, simplifying the stiffened EOS to the ideal gas law where γ becomes the ratio of specific heats. The speed of sound is $c=\sqrt{\gamma\left(p+\pi_\infty\right)/\rho}$ [65].

2.4 Mixture Rules

The interface-capturing scheme requires a set of mixture rules for the fluid properties that must be thermodynamically consistent with the governing equations to suppress spurious oscillations at the interface [39]. When the interface surface tension is neglected, the pressure across the interface should not vary: this is the isobaric assumption [64]. The mixture rules for a two-fluid system, which were derived in [64] and stated explicitly in [64, 65], are

$$\alpha_1 + \alpha_2 = 1 \tag{2.7}$$

$$\rho = \alpha_1\rho_1 + \alpha_2\rho_2 \tag{2.8}$$

$$E = \alpha_1 E_1 + \alpha_2 E_2 \tag{2.9}$$

$$\Gamma = \alpha_1\Gamma_1 + \alpha_2\Gamma_2 \tag{2.10}$$

$$\Pi = \alpha_1\Pi_1 + \alpha_2\Pi_2 . \tag{2.11}$$

where, as previously stated, the subscript 1 denotes the bubble fluid (gas) and the subscript 2 denotes the surrounding fluid (liquid); thus, $\Gamma_i = \dfrac{1}{\gamma_i - 1}$, $\Pi_i = \dfrac{\gamma_i \pi_{\infty,i}}{\gamma_i - 1}$ $\quad i = 1, 2$. The mixture rules provide the properties of the multi-fluid mixture. For example, the speed of sound (c) of a numerical cell containing a fluid mixture is determined using the properties of the mixture, γ and π_∞, which are derived from the properties evaluated by the mixture rules, Γ (Eq. (2.10)) and Π (Eq. (2.11)). Note that the mixture rule for energy, Eq. (2.9), is only explicitly used in the initiation of the energy Eq. (2.4) .

The multiphase system, used to capture the acoustically-driven bubble, is then fully defined by the governing equations, stiffened EOS, and the set of mixture rules. In the next Chapter, we describe the numerical methods used for solving the governing equations, including the treatment of an immersed boundary condition to simulate the acoustic input. The numerical method is then verified and validated.

Chapter 3 Numerical Method

The methods of modelling multiphase flow are categorised as either interface-tracking or interface-capturing. Interface-tracking is achieved by modelling the interface as a sharp discontinuity, providing the exact location of the interface. Interface capturing schemes treat the material interface as a mixture, allowing the material interface to diffuse numerically over a small region. A comprehensive review of interface capturing and interface tracking methods is provided in the introduction of [65]. In the present study, the interface capturing approach was chosen as it is generally more efficient, the complexity does not increase with the number of dimensions or fluids, and it is fully conservative [65].

Studies that focus on the shock-induced collapse of a cavity and its application in shockwave lithotripsy have been conducted using a compressible-multiphase flow model [18, 19, 38-40]. These studies use the interface-capturing method, combined with the Weighted Essentially Non-Oscillatory (WENO) reconstruction [60, 70] and the Harten-Lax-van Leer-Contact (HLLC) approximate Riemann flux [60, 71]. These methods do not ensure numerical stability as they are not Total-Variation-Diminishing (TVD), and unphysical properties may develop (e.g. negative density). The recent study [65] addressed this stability concern by using monotonicity preserving bounds for the WENO reconstruction (initially developed in [72]) in combination with a smearing of the material interface in the initial condition.

To further increase the stability of the high-order models previously discussed, we consider the positivity-preserving and maximum-principle-satisfying non-linear stability conditions [73]. Zhang and Shu [74] developed a maximum-principle-satisfying and positivity-preserving method for high-order schemes. This method was then successfully implemented to solve the compressible Euler equations using a finite-volume WENO scheme [75]. The authors are not aware of any instance in the literature that has implemented this method in compressible-multiphase flows. We investigate the possibility of preserving positivity for the fluid density and limiting the volume fraction of the fluids by satisfying the maximum principle.

The numerical method used in this study was amended from the work of Johnsen and Colonius in [60] and Coralic and Colonius in [65] where they also model compressible multifluid problems (shock-

induced bubble collapse). The finite-volume method is used in conjunction with the conservative Godunov flux to ensure any discontinuities (shocks and material interfaces) are handled conservatively. To determine the Godunov flux, the Riemann problem at the cell interfaces is approximated using the HLLC approximate Riemann flux, which has been successfully implemented in multifluid problems [18, 38, 60, 65]. The differences from our numerical method and the numerical method presented in [65] are that

(1) we use an inviscid version of the fully-conservative five-equation model from [65] (we do *not* consider the influence of viscosity) in axisymmetric cylindrical coordinates
(2) we use a single point Gaussian quadrature to determine the flux (as opposed to using the two-point Gaussian quadrature), and
(3) we add a positivity-preserving and maximum-principle-satisfying limiter to the WENO reconstruction.

We also develop the numerical method to simulate the oscillatory movement of the transducer face by using an immersed moving boundary condition; this is unique to our work.

3.1 Spatial Discretisation

3.1.1 Advection Equation

It was found in [60] that it is necessary to change the form of the advection equation (Eq. (2.5)) to use the HLLC Riemann flux approximation (section 3.5) [39]

$$\frac{\partial \alpha_1}{\partial t} + \nabla \cdot \left(\alpha_1 \mathbf{u} \right) = \alpha_1 \nabla \cdot \mathbf{u} \,. \tag{3.1}$$

The advection equation in this form can be included in the system of conservation equations, with the source term $\alpha_1 \nabla \cdot \mathbf{u}$ [39].

3.1.2 Conservation Equations

To approximate the solution of multidimensional conservation laws using the WENO reconstruction method, we must first describe the finite volume formulation [76]. A two-dimensional (2D) conservation law is

$$\frac{\partial \mathbf{U}(x,y,t)}{\partial t}+\frac{\partial \mathbf{F}\left(\mathbf{U}(x,y,t)\right)}{\partial x}+\frac{\partial \mathbf{G}\left(\mathbf{U}(x,y,t)\right)}{\partial y}=\mathbf{S}\left(\mathbf{U}(x,y,t)\right) \tag{3.2}$$

where

$$\mathbf{U}=\left[\alpha_1\rho_1,\ \alpha_2\rho_2,\ \rho u_x\ \rho u_y,\ E,\ \alpha_1\right]^T \tag{3.3}$$

are the state variables,

$$\mathbf{F}=\left[\alpha_1\rho_1 u_x,\ \alpha_2\rho_2 u_x,\ \rho u_x u_x+p,\ \rho u_x u_y,\ u_x\left(E+p\right),\ u_y\alpha_1\right]^T \tag{3.4}$$

is the flux in the *x*-direction,

$$\mathbf{G}=\left[\alpha_1\rho_1 u_y,\ \alpha_2\rho_2 u_y,\ \rho u_x u_y,\ \rho u_y u_y+p,\ u_y\left(E+p\right),\ u_y\alpha_1\right]^T \tag{3.5}$$

is the flux in the *y*-direction

$$\mathbf{S}=\left[0,\ 0,\ 0,\ 0,\ 0,\ \alpha_1\nabla\cdot\mathbf{u}\right]^T \tag{3.6}$$

are the source terms, see Eqs. (2.1)-(2.5) and Eq. (3.1). Note that the advection equation is not a conservation equation and, therefore, has a non-zero source term: $\alpha_1\nabla\cdot\mathbf{u}$.

Integration over an interval $I_{i,j}=\left[x_{i-1/2},x_{i+1/2}\right]\times\left[y_{j-1/2},y_{j+1/2}\right]$ gives

$$\frac{d\bar{\mathbf{U}}_{i,j}(t)}{dt}=\frac{1}{\Delta x_i\Delta y_j}\left(\begin{array}{l}\int_{y_{i-1/2}}^{y_{i+1/2}}\mathbf{F}\left(\mathbf{U}\left(x_{i-1/2},y_j,t\right)\right)\,dy-\int_{y_{i-1/2}}^{y_{i+1/2}}\mathbf{F}\left(\mathbf{U}\left(x_{i+1/2},y_j,t\right)\right)dy\\ +\int_{x_{i-1/2}}^{x_{i+1/2}}\mathbf{G}\left(u\left(x_i,y_{i-1/2},t\right)\right)\,dx+\int_{x_{i-1/2}}^{x_{i+1/2}}\mathbf{G}\left(u\left(x_i,y_{i+1/2},t\right)\right)dx\end{array}\right)+\frac{d\bar{\mathbf{S}}_{i,j}(t)}{dt} \tag{3.7}$$

where,

$$\frac{d\bar{\mathbf{U}}_{i,j}(t)}{dt} \equiv \frac{1}{\Delta x_i \Delta y_j} \int_{y_{i-\frac{1}{2}}}^{y_{i+\frac{1}{2}}} \int_{x_{i-\frac{1}{2}}}^{x_{i+\frac{1}{2}}} \mathbf{U}(x,y,t)\, dx\, dy \qquad \text{and} \qquad \frac{d\bar{\mathbf{S}}_{i,j}(t)}{dt} = \frac{1}{\Delta x_i \Delta y_j} \int_{y_{i-1/2}}^{y_{i+1/2}} \mathbf{S}_{i,j}\left(\mathbf{U}(x,y_j,t)\right) dxdy$$

(3.8)

Eq. (3.7) is approximated using the following scheme,

$$\frac{d\bar{\mathbf{U}}_{i,j}(t)}{dt} = \frac{1}{\Delta x_i}\left(\hat{\mathbf{F}}_{i-\frac{1}{2}} - \hat{\mathbf{F}}_{i+\frac{1}{2}}\right) + \frac{1}{\Delta y_j}\left(\hat{\mathbf{G}}_{j-\frac{1}{2}} - \hat{\mathbf{G}}_{j+\frac{1}{2}}\right) + \frac{d\bar{\mathbf{S}}_{i,j}(t)}{dt} \tag{3.9}$$

where the numerical flux $\hat{\mathbf{F}}_{i-\frac{1}{2}}$ is defined as,

$$\hat{\mathbf{F}}_{i-\frac{1}{2}} = \mathbf{H}\left(\mathbf{U}^L_{i-\frac{1}{2},\, y_j+0.5\Delta y_j}, \mathbf{U}^R_{i-\frac{1}{2},\, y_j+0.5\Delta y_j}\right) \tag{3.10}$$

and, similarly, for the flux $\hat{\mathbf{G}}_{i-\frac{1}{2}}$

$$\hat{\mathbf{G}}_{i-\frac{1}{2}} = \mathbf{H}\left(\mathbf{U}^L_{x_i+0.5\Delta x_i,\, j-\frac{1}{2}}, \mathbf{U}^R_{x_i+0.5\Delta x_i,\, j-\frac{1}{2}}\right) \tag{3.11}$$

where $\mathbf{H}\left(\mathbf{U}^L, \mathbf{U}^R\right)$ is the Riemann flux, given by the Riemann solution and a monotone Godunov flux [71]. We approximate the Riemann flux, $\mathbf{H}\left(\mathbf{U}^L, \mathbf{U}^R\right)$, using the HLLC Riemann solver, see section 3.5. It is also important to note that Eq. (3.10) is evaluated at Gaussian quadrature points to approximate the integration in Eq. (3.7). The conserved variables $\mathbf{U}^L$ and $\mathbf{U}^R$ at the quadrature points are found using the WENO reconstruction procedure. Note that $\frac{d\bar{\mathbf{S}}_{i,j}(t)}{dt}$ term is zero for all of the equations except for the advection equation: the source term for the advection equation is accounted for in the adapted numerical HLLC flux, see section 3.5.1. We show the discretisation for the single-point Gaussian quadrature. For details of the discretisation using the two-point or more Gaussian quadrature see [39, 70].

3.2 Temporal Discretisation

The semi-discretised Eq. (3.9), which may be expressed as $\frac{d\bar{\mathbf{U}}(t)}{dt} = \zeta\left(\bar{\mathbf{U}}\right)$, requires temporal discretisation. The use of the explicit third-order Runge-Kutta (RK3) total-variation-diminishing (RK3TVD) scheme is easy to implement, avoids the introduction of spurious oscillations, and is high-order accurate. The Runge-Kutta total-variation-diminishing (RK3TVD) scheme is

$$\bar{\mathbf{U}}_1 = \bar{\mathbf{U}}^n + \Delta t\ \zeta\left(\bar{\mathbf{U}}^n\right) \tag{3.12}$$

$$\bar{\mathbf{U}}_2 = \left(\frac{3}{4}\right)\bar{\mathbf{U}}^n + \left(\frac{1}{4}\right)\bar{\mathbf{U}}_1 + \left(\frac{1}{4}\right)\Delta t\ \zeta\left(\bar{\mathbf{U}}_1\right) \tag{3.13}$$

$$\bar{\mathbf{U}}^{n+1} = \left(\frac{1}{3}\right)\bar{\mathbf{U}}^n + \left(\frac{2}{3}\right)\bar{\mathbf{U}}_2 + \left(\frac{2}{3}\right)\Delta t\ \zeta\left(\bar{\mathbf{U}}_2\right). \tag{3.14}$$

where $\bar{\mathbf{U}}^n$ is the solution at the previous time step and $\bar{\mathbf{U}}^{n+1}$ is the solution at the current time step.

The time-step size (Δt) is governed by the Courant–Friedrichs–Lewy (CFL) condition. Note that the CFL condition in 2D axisymmetric cylindrical coordinates (r, z) is

$$\Delta t = \frac{\mathrm{CFL}}{\max\left(\dfrac{|u_r| + c}{\Delta r} + \dfrac{|u_z| + c}{\Delta z}\right)} \tag{3.15}$$

where CFL is the CFL number, u_r is the velocity in the *r*-direction, u_z is the velocity in the *z*-direction, c is the speed of sound, Δr is the cell-width in the *r*-direction, and Δz is the cell-width in the *z*-direction.

3.3 WENO reconstruction

The reconstruction of the state variables $(\mathbf{U})$ is often implemented to give a high-order accurate scheme for smooth solutions. Care is required when reconstructing solutions containing discontinuities as it can

result in unphysical interpolation. The WENO procedure provides high-order reconstruction in smooth regions as well as handling discontinuities using smoothness indicators. We use the fifth-order WENO reconstruction method (WENO5) [76]. The details on the WENO5 scheme are shown explicitly in the Appendix of [77].

The main drawback in using the finite volume method with WENO reconstruction compared to the finite difference method is that it becomes more computationally expensive when the number of spatial dimensions increases [76]. The reason the finite volume method using WENO reconstruction is more computationally expensive is that another reconstruction step is required to reconstruct at the Gaussian quadrature points. For example, to determine the flux in Eq. (3.10) we first need to reconstruct in the *x*-direction to determine $\mathbf{U}^L_{i-\frac{1}{2}}$ and $\mathbf{U}^R_{i-\frac{1}{2}}$, followed by a reconstruction step in the *y*-direction (using a single-point gaussian quadrature) to determine $\mathbf{U}^L_{i-\frac{1}{2},\, y_j+\frac{\Delta y_j}{2}}$ and $\mathbf{U}^R_{i-\frac{1}{2},\, y_j+\frac{\Delta y_j}{2}}$.

The choice of the reconstructed variables is not arbitrary. Spurious oscillations of the variables may be introduced in numerical experiments if the conserved variables are reconstructed near discontinuities (e.g. shocks and the material interface) where different characteristic fields interact [78]. The reconstruction of the primitive variables is common but may cause spurious oscillations at a material interface [60]. The safest approach is to reconstruct the primitive variables in characteristic space; thus, reconstructing the characteristic variables. Reconstructing the characteristic variables isolates the characteristic fields, ensuring they do not interact. To reconstruct the characteristic variables, a local characteristic decomposition is first performed [65, 76, 78].

Here we show the local characteristic decomposition of the primitive variables. The governing system of Eqs. (2.1)-(2.5) expressed as a function of the primitive variables in the two-dimensional system is

$$\mathbf{V}_t + \mathbf{A}(\mathbf{V})\mathbf{V}_x + \mathbf{B}(\mathbf{V})\mathbf{V}_y = \mathbf{0} \ . \tag{3.16}$$

When considering the reconstruction in the *x*-direction, we need the Jacobian matrix in the *x*-direction, $\mathbf{A}$, and the vector of primitive variables, $\mathbf{V}$. Note that the decomposition in the other directions follows

the same process with the corresponding Jacobian matrix (e.g. $\mathbf{B}$ in the *y*-direction). Firstly, we decompose $\mathbf{A}$:

$$\mathbf{A} = \mathbf{Q}\boldsymbol{\Lambda}\mathbf{Q}^{-1} \tag{3.17}$$

where the columns of $\mathbf{Q}$ are the eigenvectors and $\boldsymbol{\Lambda}$ is a diagonal matrix of the eigenvalues [39, 77, 79]. The characteristic variables, $\mathbf{W}$, are obtained using the projection of the primitive variable onto the characteristic fields in the *x*-direction,

$$\mathbf{W} = \mathbf{Q}^{-1}\mathbf{V}. \tag{3.18}$$

Given the characteristic variables, the WENO construction is performed. After, the characteristic variables are projected back to physical space,

$$\mathbf{V} = \mathbf{Q}\mathbf{W}. \tag{3.19}$$

The decomposition matrices are included in the Appendix C. Note that the process used for the WENO reconstruction in two-dimensional Cartesian coordinates (x, y) is the same as for the axisymmetric cylindrical coordinates (r, z).

3.4 Finite Volume Method in Axisymmetric Cylindrical Coordinates

The process used for the WENO reconstruction in two-dimensional Cartesian coordinates (x, y) is the same as for the axisymmetric cylindrical coordinates (r, z) (section 3.3). The differences between the use of two-dimensional Cartesian coordinates (x, y) and the axisymmetric cylindrical coordinates (r, z) arise in the discretisation using the finite volume method (discretisation is provided in Appendix A) and in the HLLC Riemann solver. The semi-discrete form of the governing equations in axisymmetric coordinates (r, z) are presented here.

3.4.1 Cartesian Coordinates (*z*-direction)

The governing equations, Eqs. (2.1)-(2.5), are discretised in the *z*-direction $\left(I_i = \left[z_{j-1/2}, z_{j+1/2} \right]\right)$ in Appendix A.1 to give the following semi-discrete equations

$$\left(\frac{\partial \overline{\alpha_1 \rho_1}}{\partial t} \right) = - \frac{\left(\alpha_1 \rho_1 u_z \right)_{j+1/2} - \left(\alpha_1 \rho_1 u_z \right)_{j-1/2}}{\Delta z} \tag{3.20}$$

$$\left(\frac{\partial \overline{\alpha_2 \rho_2}}{\partial t} \right) = - \frac{\left(\alpha_2 \rho_2 u_z \right)_{j+1/2} - \left(\alpha_2 \rho_2 u_z \right)_{j-1/2}}{\Delta z} \tag{3.21}$$

$$\left(\frac{\partial \overline{\rho u_r}}{\partial t} \right) = - \frac{\left[\left(\rho u_r u_z \right)_{j+1/2} - \left(\rho u_r u_z \right)_{j-1/2} \right]}{\Delta z} \tag{3.22}$$

$$\left(\frac{\partial \overline{\rho u_z}}{\partial t} \right) = - \frac{\left[\left(\rho u_z^2 + p \right)_{j+1/2} - \left(\rho u_z^2 + p \right)_{j-1/2} \right]}{\Delta z} \tag{3.23}$$

$$\left(\frac{\partial \overline{E}}{\partial t} \right) = - \frac{\left(\left(E + p \right) u_z \right)_{j+1/2} - \left(\left(E + p \right) u_z \right)_{j-1/2}}{\Delta z} \tag{3.24}$$

$$\left(\frac{\partial \overline{\alpha_1}}{\partial t} \right) = - \frac{\left(\left(\alpha_1 u_z \right)_{j+1/2} - \overline{\alpha}_1 \left(u_z \right)_{j+1/2} \right) - \left(\left(\alpha_1 u_z \right)_{j-1/2} - \overline{\alpha}_1 \left(u_z \right)_{j-1/2} \right)}{\Delta z} \tag{3.25}$$

3.4.2 Radial Coordinates (*r*-direction)

The governing equations, Eqs. (2.1)-(2.5), are discretised in the *r*-direction in Appendix A.2 to give the semi-discrete equations. The discretisation procedure differs for a finite volume element at the axis of symmetry (*z*-axis), thus, we discrete for a typical element (no boundary - section 3.4.2.1) and an element on the axis of symmetry (section 3.4.2.2).

3.4.2.1 No boundary

The semi-discrete equations in the *r*-direction for the interval $I_i = \left[r_{i-1/2}, r_{i+1/2} \right]$ are

$$\left(\frac{\partial\overline{\alpha_1\rho_1}}{\partial t}\right)=-\frac{\left(\alpha_1\rho_1u_r\right)_{i+1/2}-\left(\alpha_1\rho_1u_r\right)_{i-1/2}}{\Delta r}-\frac{\left(\alpha_1\rho_1u_r\right)_{i+1/2}+\left(\alpha_1\rho_1u_r\right)_{i-1/2}}{2r_i} \tag{3.26}$$

$$\left(\frac{\partial\overline{\rho u_r}}{\partial t}\right)=-\frac{\left[\left(\rho u_r^2+p\right)_{i+1/2}-\left(\rho u_r^2+p\right)_{i-1/2}\right]}{\Delta r}-\frac{\left[\left(\rho u_r^2\right)_{i+1/2}+\left(\rho u_r^2\right)_{i-1/2}\right]}{2r_i} \tag{3.27}$$

$$\left(\frac{\partial\overline{\rho u_z}}{\partial t}\right)=-\frac{\left[\left(\rho u_ru_z\right)_{i+1/2}-\left(\rho u_ru_z\right)_{i-1/2}\right]}{\Delta r}-\frac{\left[\left(\rho u_ru_z\right)_{i+1/2}+\left(\rho u_ru_z\right)_{i-1/2}\right]}{2r_i} \tag{3.28}$$

$$\left(\frac{\partial\overline{E}}{\partial t}\right)=-\frac{\left((E+p)u_r\right)_{i+1/2}-\left((E+p)u_r\right)_{i-1/2}}{\Delta r}-\frac{\left((E+p)u_r\right)_{i+1/2}+\left((E+p)u_r\right)_{i-1/2}}{2r_i} \tag{3.29}$$

$$\begin{aligned}\left(\frac{\partial\overline{\alpha_1}}{\partial t}\right)=&-\frac{\left(\left(\alpha_1u_r\right)_{i+1/2}-\bar{\alpha}_1\left(u_r\right)_{i+1/2}\right)-\left(\left(\alpha_1u_r\right)_{i-1/2}-\bar{\alpha}_1\left(u_r\right)_{i-1/2}\right)}{\Delta r}\\&-\frac{\left(\left(\alpha_1u_r\right)_{i+1/2}-\bar{\alpha}_1\left(u_r\right)_{i+1/2}\right)+\left(\left(\alpha_1u_r\right)_{i-1/2}-\bar{\alpha}_1\left(u_r\right)_{i-1/2}\right)}{2r_i}\end{aligned} \tag{3.30}$$

3.4.2.2 At the axis of symmetry (z-axis)

The semi-discrete equations in the *r*-direction at the *z*-axis for the interval $I_i=\left[0,r_{i+1/2}\right]$ are

$$\left(\frac{\partial\overline{\alpha_1\rho_1}}{\partial t}\right)=-\frac{4\left(\alpha_1\rho_1u_r\right)_{i+1/2}}{\Delta r} \tag{3.31}$$

$$\left(\frac{\partial\overline{\rho u_r}}{\partial t}\right)=-\frac{4\left(\left(\rho u_r^2+p\right)_{i+1/2}-\bar{p}\right)}{\Delta r} \tag{3.32}$$

$$\left(\frac{\partial\overline{\rho u_z}}{\partial t}\right)=-\frac{4\left(\rho u_ru_z\right)_{i+1/2}}{\Delta r} \tag{3.33}$$

$$\left(\frac{\partial\overline{E}}{\partial t}\right)=-\frac{4\left((E+p)u_r\right)_{i+1/2}}{\Delta r} \tag{3.34}$$

$$\left(\frac{\partial\overline{\alpha_1}}{\partial t}\right)=-\frac{4\left(\left(\alpha_1u_r\right)_{i+1/2}-\bar{\alpha}_1\left(u_r\right)_{i+1/2}\right)}{\Delta r} \tag{3.35}$$

3.4.3 Axisymmetric Cylindrical Coordinates (*r*,*z*)

The combination of the semi-discrete equations considered in the *r*-direction and the *z*-direction gives the semi-discrete equation of a finite volume cell in asymmetrical cylindrical coordinates with an interval $I_{i,j} = \left[r_{i-1/2}, r_{i+1/2}\right] \times \left[z_{j-1/2}, z_{j+1/2}\right]$. For example, the semi-discrete equation for the momentum in the *r*-direction for a cell (that is not at the *z*-axis) is

$$\left(\frac{\partial \overline{\rho u_r}}{\partial t}\right) = -\frac{\left[\left(\rho u_r u_z\right)_{j+1/2} - \left(\rho u_r u_z\right)_{j-1/2}\right]}{\Delta z} - \frac{\left[\left(\rho u_r^2 + p\right)_{i+1/2} - \left(\rho u_r^2 + p\right)_{i-1/2}\right]}{\Delta r} - \frac{\left[\left(\rho u_r^2\right)_{i+1/2} + \left(\rho u_r^2\right)_{i-1/2}\right]}{2r_i} \tag{3.36}$$

As discussed previously, these semi-discrete equations are solved temporally using the RK3TVD scheme, see section 3.2. To determine the flux terms, (e.g. $\left(\rho u_r^2 + p\right)_{i+1/2}$), the HLLC approximate Riemann flux is used.

3.5 The HLLC approximate Riemann solver

A Godunov-type scheme requires the Riemann problem to be solved to approximate the flux conservatively [71]. The use of the exact Riemann solver makes the numerical scheme very computationally expensive and is often replaced by an approximate Riemann solver. In Ref. [60] the HLLC approximate Riemann solver is implemented effectively in multicomponent flow problems. The choice of the HLLC solver is justified by the fact that it is less computationally expensive than Roe solvers and improves on the HLL scheme by restoring the contact discontinuity [71, 77]. The numerical advection flux for a two-dimensional Cartesian case $\left(x, y\right)$ with the left $\mathbf{U}^L$ and right $\mathbf{U}^R$ states of the Riemann problem in the *x*-direction (Eq. (3.10)), is given by the HLLC flux

$$\mathbf{H}_x^{HLLC} = \frac{1-\mathrm{sgn}\left(s^*\right)}{2}\left[\mathbf{F}^L + s^-\left(\mathbf{U}^{*L} - \mathbf{U}^L\right)\right] + \frac{1-\mathrm{sgn}\left(s^*\right)}{2}\left[\mathbf{F}^R + s^+\left(\mathbf{U}^{*R} - \mathbf{U}^R\right)\right] \tag{3.37}$$

where $\mathbf{F}$ is shown in section 3.1.2, and

$$\mathbf{U}^{*K} = \left(\frac{s^K - {u_x}^K}{s^K - s^*} \right) \begin{pmatrix} \left(\alpha_1 \rho_1\right)^K \\ \left(\alpha_2 \rho_2\right)^K \\ \rho^K s^* \\ \left(\rho u_y\right)^K \\ E^K + \left(s_* - {u_x}^K\right)\left(\rho^K s^* + \dfrac{p^K}{s^K - {u_x}^K}\right) \\ \alpha_1 \end{pmatrix} \tag{3.38}$$

for $K = L, R$. The wave speeds are approximated by

$$s^- = \min\left(0, s^L\right),\ s^+ = \max\left(0, s^R\right) \tag{3.39}$$

where

$$s^L = \min\left(\bar{u}_x - \bar{c},\ {u_x}^L - c^L\right),\ s^R = \max\left(\bar{u}_x + \bar{c},\ {u_x}^R + c^R\right) \tag{3.40}$$

$\bar{u}_x$ and $\bar{c}$ are the averages computed using either the Roe average or an arithmetic average of the left and right states. With the two averaging method providing nearly identical results [65], we use an arithmetic average as it is less computationally expensive.

The contact or intermediate wave speed is given by

$$s^* = \frac{p^R - p^L + \rho^L {u_x}^L \left(s^L - {u_x}^L\right) - \rho^R {u_x}^R \left(s^R - {u_x}^R\right)}{{\rho^L}_L \left(s^L - {u_x}^L\right) - {\rho^R}_R \left(s^R - {u_x}^R\right)} \tag{3.41}$$

3.5.1 HLLC adapted for the advection equation

The advection equation also has a source term, see section 3.1.1. In [77], the source term is considered in the numerical flux. As seen previously, the discretised advection equation considered in one-dimension is

$$\left(\frac{\partial \overline{\alpha_1}}{\partial t} \right) = -\frac{\left(\left(\alpha_1 u\right)_{i+1/2} - \bar{\alpha}_1 \left(u\right)_{i+1/2} \right) - \left(\left(\alpha_1 u\right)_{i-1/2} - \bar{\alpha}_1 \left(u\right)_{i-1/2} \right)}{\Delta z}\ . \tag{3.42}$$

The HLLC flux gives the terms $(\alpha_1 u)_{i+1/2}$ and $(\alpha_1 u)_{i-1/2}$ but $\bar{\alpha}_1(u)_{i+1/2}$ and $\bar{\alpha}_1(u)_{i-1/2}$ are yet to be determined. The $\bar{\alpha}_1(u)_{i+1/2}$ and $\bar{\alpha}_1(u)_{i-1/2}$ terms are given by the average cell volume fraction $\bar{\alpha}_1$, and the velocity is given by the HLLC approximation

$$u_x^{HLLC} = \frac{1-\mathrm{sgn}(s^*)}{2}\left[u_x{}^L + s^-\left(\left(\frac{s^L-u^L}{s^L-s^*}\right)-1\right)\right] + \frac{1-\mathrm{sgn}(s^*)}{2}\left[u_x{}^R + s^+\left(\left(\frac{s^R-u^R}{s^R-s^*}\right)-1\right)\right]. \quad (3.43)$$

3.5.2 HLLC adapted in the Radial direction (*r*-direction)

As previously shown, the semi-discrete equation for momentum in the radial direction (Eq. (3.27)) is

$$\left(\frac{\partial\overline{\rho u_r}}{\partial t}\right) = -\frac{\left[\left(\rho u_r^2 + p\right)_{i+1/2} - \left(\rho u_r^2 + p\right)_{i-1/2}\right]}{\Delta r} - \frac{\left[\left(\rho u_r^2\right)_{i+1/2} + \left(\rho u_r^2\right)_{i-1/2}\right]}{2r_i}. \quad (3.44)$$

The equation includes the typical momentum term, $\rho u_r^2 + p$, but it also includes a different flux term ρu_r^2 due to the source pressure which appears in the differential form of the momentum equation in cylindrical coordinates (see Appendix A). Thus, the HLLC solver is also required to determine ρu_r^2

$$\begin{aligned}\left(\rho u_r^2\right)_r{}^{HLLC} = {} & \frac{1-\mathrm{sgn}(s^*)}{2}\left[\left(\rho u_r^2\right)^L + s^-\left(\left(\frac{s^L-u^L}{s^L-s^*}\right)\rho^L s^* - \left(\rho u_r\right)^L\right)\right] \\ & + \frac{1-\mathrm{sgn}(s^*)}{2}\left[\left(\rho u_r^2\right)^R + s^+\left(\left(\frac{s^R-u^R}{s^R-s^*}\right)\rho^R s^* - \left(\rho u_r\right)^R\right)\right]\end{aligned} \quad (3.45)$$

3.6 Maximum principle Satisfying and Positivity Preserving Limiter

Unphysical results may arise because the numerical scheme is not strictly TVD, allowing negative values of density, negative volume fractions, volume fractions greater than one, and negative values of $p+\pi_\infty$ to develop. These unphysical results are realised in the numerical simulations when a complex speed of sound is computed. To resolve this issue without using a lower-order scheme, we implement

the maximum-principle-satisfying and positivity-preserving method for high-order schemes that was developed in [74]. This method has previously been successfully implemented for WENO finite-volume schemes for the Euler equations [74, 75], but, to the authors' knowledge, this is the first time this has been implemented in a compressible multifluid flow model.

The limiter is applied to the WENO reconstructed variables. For the finite volume model, each finite volume cell has an average state value of $\bar{\mathbf{U}}_{i,j}^{n}$. $\bar{\mathbf{U}}_{i,j}^{n} \in [m, M]$, where m and M are the minimum and maximum limits, respectively. The WENO reconstructed variables using the single-point Gaussian quadrature (see section 3.1) are $\mathbf{U}_{i,j-\frac{1}{2}}^{L}$, $\mathbf{U}_{i,j+\frac{1}{2}}^{R}$, $\mathbf{U}_{i-\frac{1}{2},j}^{L}$, and $\mathbf{U}_{i+\frac{1}{2},j}^{R}$. The limiter is describing in a two-step procedure [74]:

1. Compute $\theta_{i,j} = \min\left\{\left|\frac{M-\bar{\mathbf{U}}_{i,j}^{n}}{M_{i,j}-\bar{\mathbf{U}}_{i,j}^{n}}\right|, \left|\frac{m-\bar{\mathbf{U}}_{i,j}^{n}}{m_{i,j}-\bar{\mathbf{U}}_{i,j}^{n}}\right|, 1\right\}$, where

$$M_{i,j} = \max\left\{P_{ij}\left(x_i^*, y_j^*\right), \mathbf{U}_{i,j-\frac{1}{2}}^{L}, \mathbf{U}_{i,j+\frac{1}{2}}^{R}, \mathbf{U}_{i-\frac{1}{2},j}^{L}, \mathbf{U}_{i+\frac{1}{2},j}^{R}\right\},$$

$$m_{i,j} = \min\left\{P_{ij}\left(x_i^*, y_j^*\right), \mathbf{U}_{i,j-\frac{1}{2}}^{L}, \mathbf{U}_{i,j+\frac{1}{2}}^{R}, \mathbf{U}_{i-\frac{1}{2},j}^{L}, \mathbf{U}_{i+\frac{1}{2},j}^{R}\right\}, \text{ the polynomial value, } P_{i,j}\left(x_i^*, y_j^*\right), \text{ is}$$

$$P_{i,j}\left(x_i^*, y_j^*\right) = \frac{3}{2}\left(\bar{\mathbf{U}}_{i,j}^{n} - \frac{1}{6}\left[\kappa_1\left(\mathbf{U}_{i-\frac{1}{2},j}^{L}, \mathbf{U}_{i+\frac{1}{2},j}^{R}\right) + \kappa_2\left(\mathbf{U}_{i,j-\frac{1}{2}}^{L} + \mathbf{U}_{i,j+\frac{1}{2}}^{R}\right)\right]\right),$$

$$\kappa_1 = \frac{\max\left(\frac{|u_r|+c}{\Delta r}\right)}{\max\left(\frac{|u_r|+c}{\Delta r}\right) + \max\left(\frac{|u_z|+c}{\Delta z}\right)}, \text{ and } \kappa_2 = 1-\kappa_1.$$

2. Determine the limited reconstructed variables $\tilde{\mathbf{U}}_{i,j-\frac{1}{2}}^{L} = \theta_{i,j}\left(\mathbf{U}_{i,j-\frac{1}{2}}^{L} - \bar{\mathbf{U}}_{i,j}^{n}\right) + \bar{\mathbf{U}}_{i,j}^{n}$,

$\tilde{\mathbf{U}}_{i,j+\frac{1}{2}}^{R} = \theta_{i,j}\left(\mathbf{U}_{i,j+\frac{1}{2}}^{R} - \bar{\mathbf{U}}_{i,j}^{n}\right) + \bar{\mathbf{U}}_{i,j}^{n}$, $\tilde{\mathbf{U}}_{i-\frac{1}{2},j}^{L} = \theta_{i,j}\left(\mathbf{U}_{j-\frac{1}{2},i}^{L} - \bar{\mathbf{U}}_{i,j}^{n}\right) + \bar{\mathbf{U}}_{i,j}^{n}$, and

$\tilde{\mathbf{U}}_{i+\frac{1}{2},j}^{R} = \theta_{i,j}\left(\mathbf{U}_{j+\frac{1}{2},i}^{R} - \bar{\mathbf{U}}_{i,j}^{n}\right) + \bar{\mathbf{U}}_{i,j}^{n}$.

The limited reconstructed variables are then using in the HLLC flux calculation (see section 3.5).

We implement the simplified maximum-principle-satisfying and positivity-preserving limiter (developed in [74]) to the multifluid system by considering the limits of volume fraction, density, and pressure:

$$0 \le \alpha_1 \le 1 \tag{3.46}$$

$$0 < \alpha_1 \rho_1 \tag{3.47}$$

$$0 < \alpha_2 \rho_2 \tag{3.48}$$

$$0 \le \left(p + \pi_\infty \right) \tag{3.49}$$

These limits ensure that $\gamma\left(p + \pi_\infty \right)/\rho \ge 0$; thus, avoiding an unphysical speed of sound.

3.7 Domain

The geometric representation of the physical domain, shown in Figure 3.1, was chosen to represent the physical system while being computationally efficient and simple. An axisymmetric cylindrical coordinate system was used to reduce the spatial dimensions of the model to two: r and z. Note that to increase computational efficiency, a growing mesh with increased refinement in the region encompassing the bubble was used (see Figure 3.1).

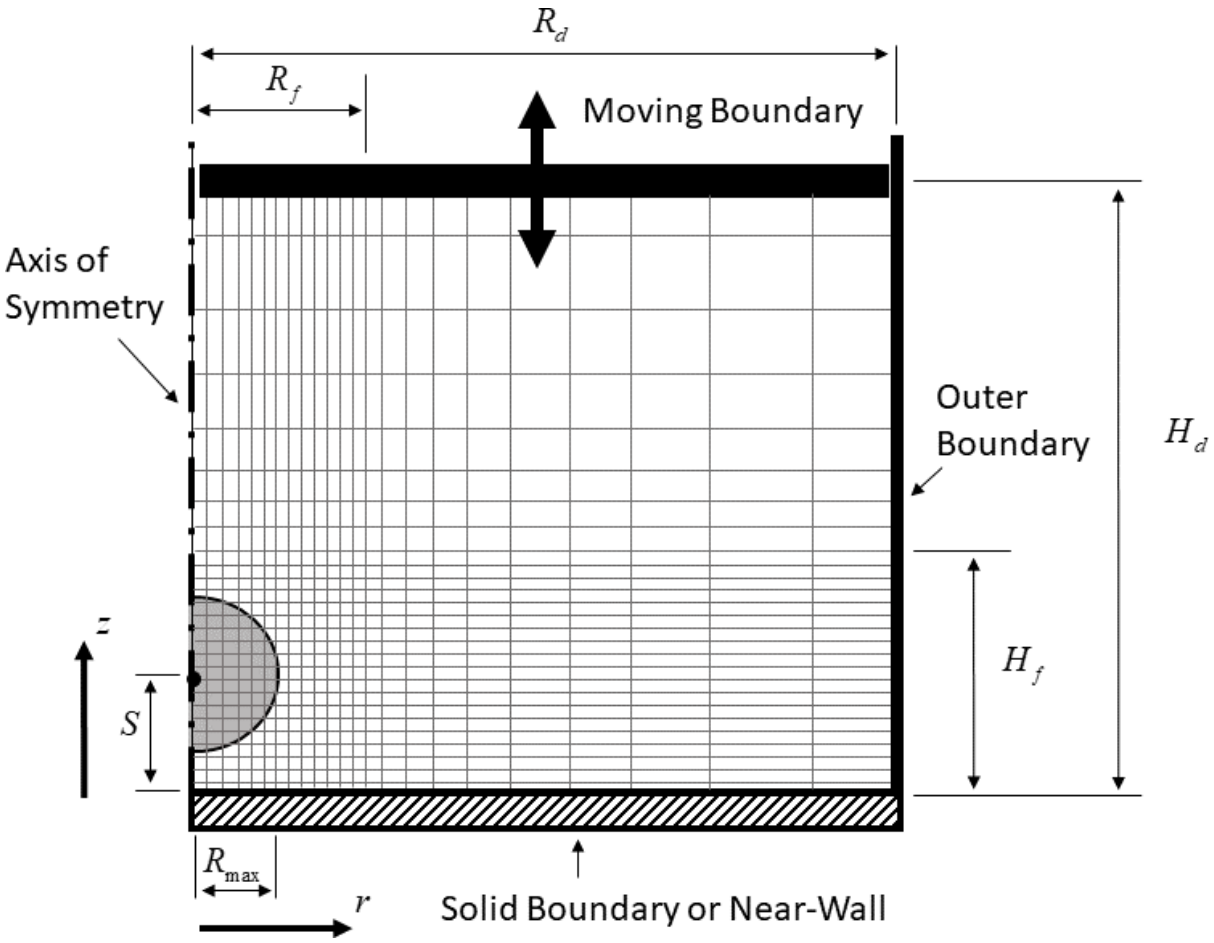

Figure 3.1. A representative depiction of the computational domain for the acoustically-driven bubble in cylindrical coordinates with symmetry about the axis (not drawn to scale). At the top, the acoustic (ultrasound) input is simulated using a moving boundary condition.

Figure 3.1 shows the domain, where R_d and H_r are the radius and height of the domain, respectively. The dimensions of the refined region are H_f and R_f, were a uniform mesh is used. The mesh cells grow at a constant rate (g) in the *r* and *z* directions, from the refined region to the boundaries. The mesh parameter values used in the current study are provided in Table 4.1. The standoff distance of the bubble from the wall, denoted S, is the *initial* distance from the centre of the bubble to the near-wall along the *z*-axis.

3.8 Boundary Conditions

A symmetric boundary condition is used at the axis of symmetry. The acoustic input is modelled using an immersed moving reflective boundary. The solid boundary and the outer boundary are modelled using the reflective boundary condition, see Figure 3.1.

A reflective boundary condition is applied at the outer boundary, and this results in symmetry about that boundary. This simulates an acoustic field that does not vary in the radial direction at locations far from the bubble. The outer boundary was positioned sufficiently far away from the bubble to ensure that over the duration of the collapse simulation, any shocks emitted by the bubble collapse would not be reflected from that boundary into the region of interest surrounding the bubble (the refined region – see Figure 3.1).

3.8.1 Reflective and symmetrical boundary conditions

A no-through-flow condition is enforced at reflective and symmetric boundaries. The no-through-flow condition is enforced using ghost cells to mirror all of the variables across the boundary, except for the normal velocity, which is reflected across the boundary (see Eq. (3.50)-(3.52)) [77]. Defining the ghost cells in this manner results in the physically correct Riemann problem at the boundary [71]. The number of ghost cells is dependent on the order of the WENO reconstruction method being used [70]: the fifth-order WENO reconstruction, which is used in this study, requires three layers of ghost cells. The application of a boundary on a line of symmetry is practically the same as the reflective boundary as it also implies no flow across the boundary.

Consider a 2D model that uses the fifth-order WENO reconstruction with a reflective or symmetry boundary on the east end of the domain, see Figure 3.2. The boundary condition is applied to the domain by setting the three ghost cells

$$\left(\rho \quad u_r \quad u_z \quad p \quad \alpha_1\right)_{n+1} = \left(\rho \quad -u_r \quad u_z \quad p \quad \alpha_1\right)_n \tag{3.50}$$

$$\left(\rho \quad u_r \quad u_z \quad p \quad \alpha_1\right)_{n+2} = \left(\rho \quad -u_r \quad u_z \quad p \quad \alpha_1\right)_{n-1} \tag{3.51}$$

$$\left(\rho \quad u_r \quad u_z \quad p \quad \alpha_1\right)_{n+3} = \left(\rho \quad -u_r \quad u_z \quad p \quad \alpha_1\right)_{n-2} \tag{3.52}$$

where n is the last cell inside of the domain of interest and the WENO5 scheme requires three ghost cells ($n+1,\ n+2,$ and $n+3$) to complete the reconstruction stencil.

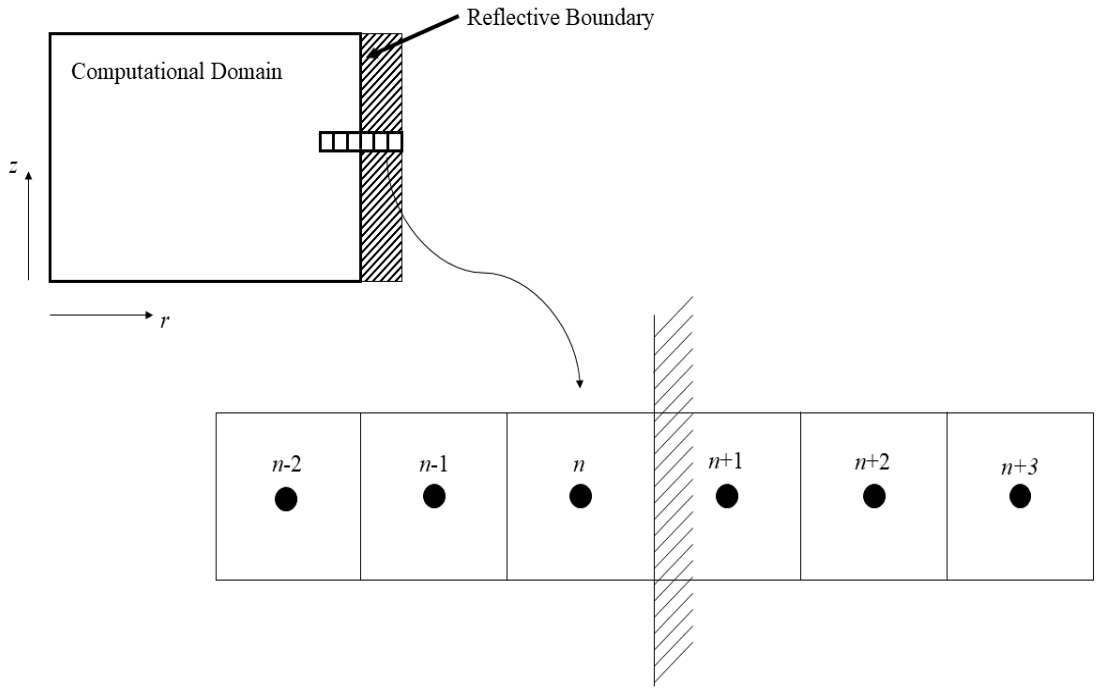

Figure 3.2. Ghost cells used for the reflective and symmetry boundaries when using the fifth-order WENO reconstruction.

The maximum-principle-satisfying and positivity-preserving limiter requires the reconstructed variables of the nearby cell. For example, if the limiter is applied to the cell denoted n in Figure 3.2 it, therefore, requires the reconstructed variables from $n+1$ at the interface. Thus, the numerical method using the fifth-order WENO reconstruction with the maximum-principle-satisfying and positivity-preserving limiter requires four layers of ghost nodes (only three layers of ghost nodes are depicted in Figure 3.2).

3.8.2 Immersed Moving Reflective Boundary Condition (Acoustic Input)

An immersed moving reflective boundary is used to simulate the ultrasound transducer face, producing the acoustic input into the compressible flow field. The transducer face position, x_T, is approximated by the sinusoidal function:

$$x_T(t) = a\sin(2\pi ft) \tag{3.53}$$

where a is the displacement amplitude of the transducer face and f is the frequency of the applied ultrasound. The period of the ultrasound is $T_U = f^{-1}$.

The moving boundary is implemented conservatively using an approach similar to the interface method developed in [80]. The interaction between the moving boundary and the fluid is evaluated using the one-sided Riemann problem, where the interface velocity is determined using the time derivative of the displacement:

$$\dot{x}_T(t) = 2\pi fa\cos(2\pi ft)\ . \tag{3.54}$$

The interaction between the moving boundary and the fluid results in a change in momentum due to the boundary acting on the fluid as well as a change in the energy from the work done on the fluid by the boundary. The one-sided Riemann flux at the moving boundary is determined using the HLLC approximate Riemann flux.

When the moving boundary is set in a Eulerian grid, the boundary will bisect the grid cells, resulting in cut cells. If a cut cell is sufficiently small, it may violate the CFL stability condition of the rest of the domain. Instead of lowering the time-step size to satisfy the CFL condition of the cut cell (increasing in the computational time), the cut cell is conservatively combined with its neighbouring uncut cell as is suggested in [80]. The volume of the combined cells changes over the duration of a time-step due to the change in displacement of the moving boundary. The change in the volume of the combined cells is explicitly accounted for in the numerical scheme following the methodology outlined in [80]; thus,

ensuring conservation of the conserved variables. The discretisation of combined finite volume cells is provided in Appendix A.

3.9 Flow Visualisation

Computational Schlieren images are used to visualise flow features involving density gradients: shocks and material interfaces [40]. Computational Schlieren images are generated using the shading function

$$\psi = \exp\left(-k \frac{|\nabla \rho|}{|\nabla \rho|_{\max}} \right) \tag{3.55}$$

where k is a constant that is assigned a value to accentuate the compressible flow features. The shading function is used to generate an RGB triplet: $(255\psi, 255\psi, 255\psi)$ for outside the bubble and $(230\psi, 230\psi, 230\psi)$ inside the bubble. Thus, the bubble is initially light grey, the surrounding fluid is initially white, and the darker regions of the image have larger density gradients. For the validation case in section 3.10, $k = 600$ for the bubble composed of the helium-air mixture and $k = 120$ for the surrounding medium of air [40]. In the case study of section 4.4, $k = 40$ for the bubble composed of air and $k = 4000$ for the surrounding medium of water. For this case, the density gradients in the surrounding fluid are sensitive to the diffusion of the interface (small volume fractions of air in the water); thus, the computational Schlieren images do not show any interesting flow features in the diffuse interface region. Therefore, the density gradients are not shown in the diffuse interface region, between $\alpha_1 = 1.0 \times 10^{-7}$ and $\alpha_1 = 0.95$.

3.10 Verification and Validation

The numerical model is verified using a 1D gas-liquid Riemann problem test case in section 3.10.1 and a Shock-Bubble interaction test case in section 3.10.2. The Shock-Bubble interaction test case which is in axisymmetric cylindrical coordinates is an especially important validation and verification case because the axisymmetric cylindrical coordinates are used throughout this thesis. Ideally, we would

have experimental results to an acoustically-driven growth and collapse of a single cavitation bubble in water; however, to the authors knowledge, an experiment of this description has not been conducted. Experiments involving acoustic cavitation are notoriously difficult. To maintain the presence of only a single bubble and control its position and size while exposed to an ultrasound field is an extremely difficult task. If this experiment was conducted, it would be of interest to compare the simulation of the acoustically-driven bubble to the experimental results by considering the growth and collapse durations, the evolution of the bubble shape, and the subsequent wall pressure to further validate the model.

3.10.1 1D gas-liquid Riemann test case

We use the gas-liquid Riemann test case taken from [60, 66] to numerically verify the model in one dimension. Initially, a stationary diaphragm between two fluids is located at $x = 0.5$, with a liquid on the left and a gas on the right. The initial properties of the liquid are

$$\left(\rho,\, u,\, P,\, \gamma,\, \pi_\infty,\, \alpha_1\right)_L = \left(0.991,\, 0,\, 3.059\times10^{-4},\, 5.5,\, 1.505,\, 0\right). \tag{3.56}$$

The initial properties of the gas are

$$\left(\rho,\, u,\, P,\, \gamma,\, \pi_\infty,\, \alpha_1\right)_R = \left(1.241,\, 0,\, 2.753,\, 1.4,\, 0,\, 1\right) \tag{3.57}$$

where α_1 is the volume fraction of the gas. Note that the key difference that differentiates the properties of the liquid from the gas is the EOS parameters, not the density. The liquid is stiff with $\pi_\infty = 1.505$; whereas, the gas is not stiffened $\left(\pi_\infty = 0\right)$, simplifying the stiffened EOS to the ideal gas law.

Figure 3.3 shows the subsequent volume fraction, density, pressure, velocity, and energy after 0.1 seconds. The results from the 1D multiphase model using WENO reconstruction with the maximum-principle-satisfying and positivity-preserving limiter (WENO-PP) are compared to the exact solution to the Riemann problem [71]. In this case, WENO-PP used a mesh of 100 cells and a CFL=0.4. The comparison between the numerical solution, WENO-PP, and the exact solution shows very close agreement. As anticipated from a high-order non-oscillatory scheme, the numerical solution matches

closely without oscillations. The limits applied to the model using maximum-principle-satisfying and positivity-preserving limiter (section 3.6) were monitored over the duration of the simulation and were never violated.

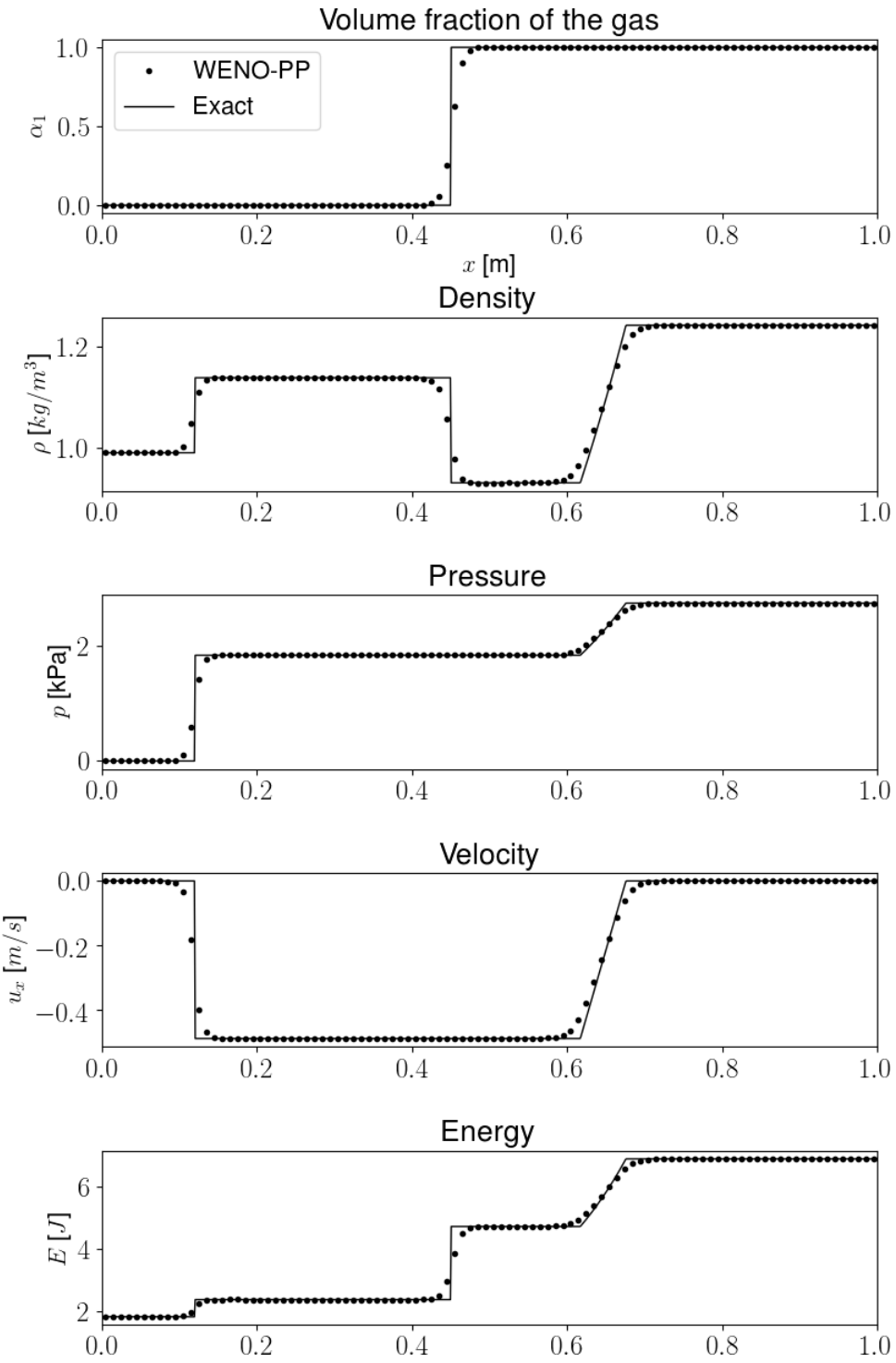

Figure 3.3. The results of the 1D gas-liquid Riemann problem at time t=0.1. The solid line is the exact solution, and the points are the solution from the presented numerical scheme for a mesh of 100 cells and a CFL = 0.4.

3.10.2 Shock-Bubble interaction test case

The shock-bubble test case presented in multiple studies [40, 60, 81-89] was used to qualitatively and quantitatively validate the model, ensuring the numerical model developed represents the flow physics correctly. The shock-bubble test case considers a shock wave that is travelling through a tube which contains a bubble composed of a helium-air mixture in a surrounding fluid composed of air [40, 90], see Figure 3.4. The qualitative validation is achieved by comparing the computational Schlieren images of the shock-bubble interaction, like the ones shown in Figure 3.4, to the experimental images published in [90].

The speed of the incident shock (u_s), the speed of the refracted shock (u_a), and the speed of the transmitted shock (u_t) are calculated and compared to the experimental results of [90] and the numerical results in [39] to validate the model quantitatively. Table 3.1 contains the quantitative validation results. The flow features of interest are annotated in Figure 3.4. The shock speed measurements from the simulation are all within the experimental range determined in [90], showing a good quantitative agreement. The qualitative images also agree with the experimental [90] and published numerical results [39], displaying all of the important flow features of the shock-bubble interaction. Over the duration of the validation simulation (310 μs), the mass of the bubble changed by approximately 1.5×10^{-4} % due to the numerical truncation error; thus, the mass was accurately conserved.

Table 3.1. The quantitative validation of the shock speeds: the incident shock speed (u_s), the refracted shock speed (u_a), and the transmitted shock speed (u_t). The shock speed was determined by averaging the shock velocity over the specified time interval.

	u_s (m/s)	u_a (m/s)	u_t (m/s)
Time interval	-60 to 0 μs	0 to 53 μs	53 to 240 μs
Simulation results from the present study	420	933	362
Benchmark [39]	420	945	379
Experiment [90]	410±41	900±90	393±39

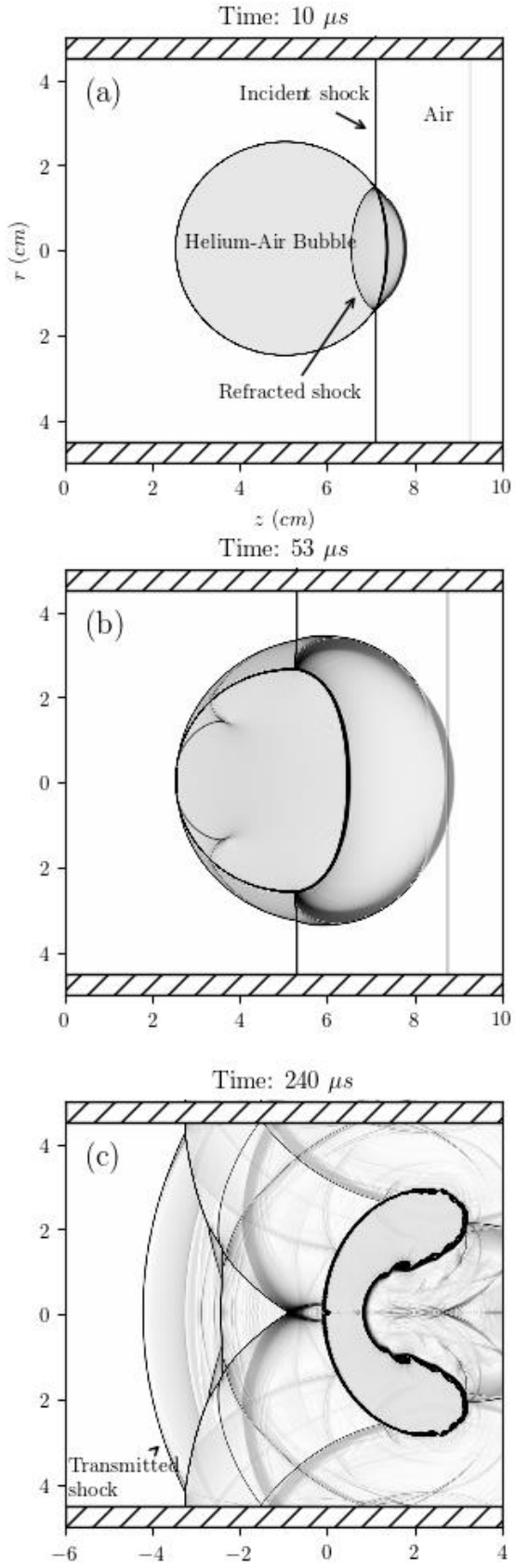

Figure 3.4. The shock-bubble interaction visualised using the computational Schlieren images (a function of density gradient – see section 3.9)

Chapter 4 Rayleigh-Plesset Growth Initialised (RPGI) Bubble Collapse Model

4.1 Introduction: Numerical Modelling the Acoustically-Driven Bubble Collapse

Published models of bubble collapse have not yet represented the bubble collapse that results from an acoustic field associated with the oscillating position of the transducer face. Some researchers have initiated the bubble collapse by a specified initial pressure difference between the bubble and the surrounding liquid for which the pressure distribution in each of the two domains is uniform [4, 26-38]. Such an initial pressure difference drives the violent collapse of the bubble: this type of collapse is termed a Rayleigh collapse. Other researchers have initiated the bubble collapse by modelling a shockwave that travels through the surrounding liquid towards the bubble [18, 19, 38-40]. During the bubble-shock interaction, the bubble collapses violently. The published methods of modelling the collapse of a bubble may be categorised as incompressible, weakly compressible, or fully compressible. We briefly summarise these methods and note on their limitations in representing the acoustically-driven collapse next.

The earliest models of near-wall bubble collapse represent the liquid medium surrounding the bubble as incompressible [26-29]. This allows the problem to be reduced to the Laplace equation of the velocity potential within the surrounding liquid. The representation of the surrounding medium as incompressible also simplifies the application of the far-field boundary condition. The far-field pressure is treated as constant and the velocity potential there is typically taken to be zero. While the numerical method is greatly simplified, this method for modelling the bubble collapse is unable to capture the effects of compressibility, which are important at the later stages of the collapse [14]. Furthermore, these studies all represent the far-field pressure to be constant for the duration of the collapse. However, in an acoustically-driven collapse, the far-field pressure is anticipated to vary sinusoidally in time.

Later models modify the incompressible model by representing the surrounding fluid as weakly compressible and simulate an acoustic input from the far-field [41, 42]. The studies by Wang and Blake [41, 42] show the influence of acoustic waves on the bubble dynamics, but do not capture the violent collapse of a bubble near a wall (which is of importance to the current work). Because significant Mach numbers are anticipated near the bubble during a violent collapse; the assumption of infinite propagation rates of the weakly compressible model becomes less valid. The weakly compressible model is unable to capture the formation of shocks, which are anticipated in a violent bubble collapse case [14, 15, 43].

Alternately, fully compressible models, which are capable of capturing shocks, have also been published that represent both the fluid of the bubble and the surrounding medium as compressible. In some of these studies, the collapse is induced by a shock wave travelling through the domain [18, 19, 38-40]. Other fully compressible studies induce the collapse in a manner more consistent with the acoustically-driven collapse by using an initial condition in which there is a pressure difference between the bubble and the surrounding medium [4, 37, 38]. In the studies by Chahine [4, 37], they initialised the bubble at a higher pressure than the surrounding liquid, resulting in the growth and collapse of the bubble. In the study by Johnsen [38], they study the Rayleigh collapse near a wall. When applying these models to an acoustically-driven collapse, it is unclear what choice of initial pressure difference would correctly represent the conditions of the bubble in the acoustic field. Because the collapse is highly dependent on the magnitude of this pressure difference, the choice is not arbitrary.

The published collapse models may not be directly applied to represent the physics of the acoustically-driven collapse correctly. The velocity, pressure, and density distributions associated with the acoustic field experience dynamic changes during the growth and collapse of the bubble and these changes are not captured in the Rayleigh collapse case or the shock-induced collapse case. None of the existing studies can initiate bubble collapse in a manner that is consistent with the physics of an acoustically-driven collapse. The lack of a model that captures the physics of an acoustically-driven bubble collapse is the primary motivation of the work presented in this thesis.

In the following sections, we introduce a fully compressible model of a bubble collapse near a solid surface that is the first to initiate the bubble collapse from the acoustic field resulting from an oscillating

transducer face. The numerical methods are described in detail in Chapter 3. This Chapter includes the method for initialising the bubble collapse model by superimposing the RP solution onto the solution of the 1D acoustic field. We call this model the RP Growth Initialized (RPGI) model of the acoustically-driven collapse of a near-wall bubble. A case study of this collapse is presented, and a comparison between the acoustically-driven collapse and the Rayleigh collapse near a solid boundary is presented.

4.2 Bubble collapse model

This Chapter focuses on modelling the collapse phase of the bubble in an acoustic field. We estimate the conditions of the bubble just as the bubble begins its collapse. The issue is determining the state of the bubble and the surrounding liquid just at the instant the bubble reaches its maximum volume and begins its collapse phase. Later in Chapter 6, we directly model the growth of the near-wall bubble and the subsequent bubble collapse.

The bubble's pre-collapse shape is represented as initially spherical, which implies that the bubble growth is uninfluenced by the solid boundary. This assumption becomes more valid the further the bubble is from the solid boundary. For the case where $S \leq 1R_{\max}$, the spherical bubble joins the wall; this does not occur for the near-wall bubble growth in experimental studies [91] and numerical simulations [4]. Therefore, we assume for cases where $S > 1R_{\max}$; however, a more comprehensive investigation into the validity of the assumption is a topic for future work. The initial conditions of the model are detailed in section 4.3.

4.3 Initialising the System

In seeking to represent the collapse of a bubble in a manner more consistent with acoustically-driven collapse, and additional complication has been introduced: how to initialise the system. The simulation is initialised at the instant when the bubble is at its maximum size (just at the beginning of the collapse phase). Solving Eqs. (2.1)-(2.5) requires knowledge of all of the conserved variables at this instant, and knowledge of the conserved variables at this instant is complicated by the influences of the applied

acoustic field leading up to that instant. Thus, we have developed a method of approximating the state of the system at the beginning of the bubble collapse: this is discussed in detail in this section.

The collapse begins when the bubble has reached its maximum radius, $R_{\max}$. To determine the properties of the bubble at this instant, the growth of the bubble from R_0 to $R_{\max}$ (growth phase) is approximated using the Rayleigh-Plesset (RP) equation. The duration of the growth phase, Δt_{RP}, is used to determine the initial state of the acoustic field, ensuring the pressure of the acoustic field is in phase with the far-field pressure of the RP analysis. In this way, the method for the initiation of the bubble collapse simulation is split into three steps: (1) use the RP equation to compute the bubble growth (from R_0 to $R_{\max}$) to determine the state of the bubble at $R_{\max}$ and the growth duration Δt_{RP}, (2) determine the acoustic field in the absence of a bubble, and (3) superimpose the RP bubble onto the acoustic field to give the initial condition for the collapse simulation. The details of these three steps, which are depicted in Figure 4.1, are outlined in the next three sections.

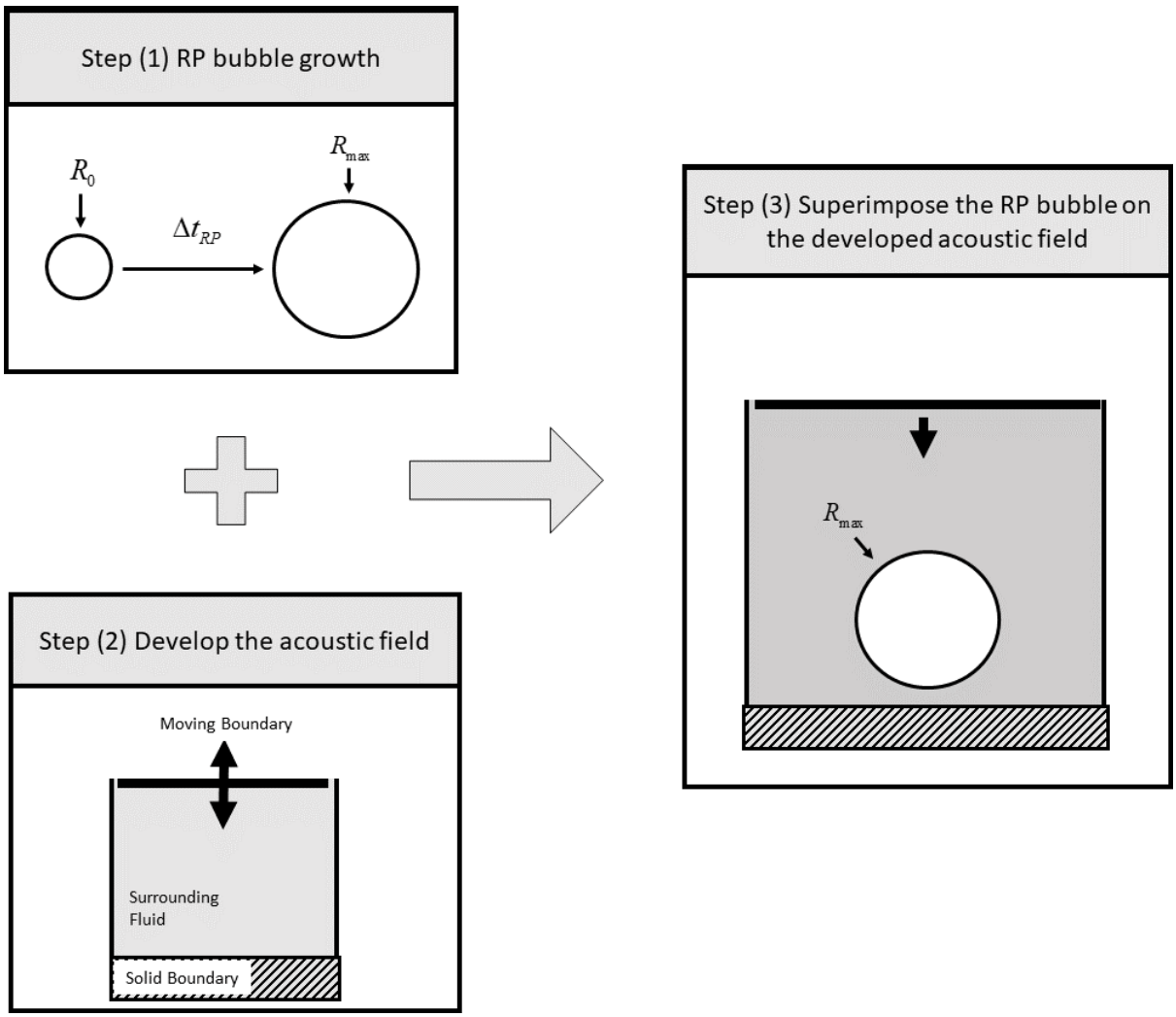

Figure 4.1. A representation of the process for initialising the acoustically-driven bubble collapse (not drawn to scale).

An additional benefit of representing the growth phase using the RP equation is that it is simple to include the influence of surface tension and viscosity during the growth phase. The influence of surface tension and other effects on the growth and the subsequent collapse are investigated later in Chapter 5.

4.3.1 Rayleigh-Plesset (RP) Analysis

The growth of the bubble is approximated using the RP equation. The RP equation is used to simulate the bubble growth to the instant before collapse when the bubble is at its maximum size $\left(R_{\max}\right)$: termed the pre-collapse bubble state. The properties of the pre-collapse bubble are later used to initialise the

bubble collapse simulation, and the growth duration $\left(\Delta t_{RP}\right)$ is used to initialise the acoustic field at the instant before the collapse. Here we discuss the RP equation briefly.

The RP equation is derived from the Navier-Stokes equations by assuming the bubble is in an infinite body of incompressible liquid (the surrounding fluid). It describes the dynamics of a spherical bubble in spherical coordinates

$$\frac{p_B(t)-p_\infty(t)}{\rho_L}=R\ddot{R}+\frac{3}{2}\dot{R}^2+\frac{4\mu}{\rho_L R}\dot{R}+\frac{2\sigma}{\rho_L R} \tag{4.1}$$

where R is the bubble radius, $\dot{R}$ and $\ddot{R}$ are the first and second-time derivatives, p_B is the bubble pressure, p_∞ is the pressure infinitely far from the bubble, σ is the interface surface tension, ρ_L is the density of the surrounding liquid, and μ is the dynamic viscosity of the surrounding liquid. Note that the influences of viscosity and surface tension are considered during the growth phase (RP analysis) but are neglected in the collapse phase (compressible-multiphase-flow model). In the appendix of the current paper, we investigate the influence of the surface tension during the growth phase on the subsequent bubble collapse. The RP growth also considers the surrounding fluid to be incompressible, whereas the effects of compressibility of the surrounding fluid are considered in the collapse simulation. For an acoustic field, the far-field pressure p_∞ is approximated by

$$p_\infty = p_0 - p_A \sin\left(2\pi ft\right) \tag{4.2}$$

where p_A is the pressure amplitude of the acoustic field found from the analysis of the developed acoustic field using a transducer amplitude of $a_{\max}$ (section 4.3.2). p_0 is the steady pressure in the absence of the sound field, which is equal to the atmospheric pressure in this study: $p_0 = p_{atm}$.

For a spherical air bubble, the bubble pressure changes as a function of the bubble radius [14, 15]:

$$p_B = p_{0,B}\left(\frac{R_0}{R}\right)^{3\eta} \tag{4.3}$$

where $p_{0,B}$ is the pre-growth bubble pressure and R_0 is the pre-growth bubble radius (not to be confused with the bubbles initial radius before collapse: $R_{\max}$). The behaviour of the gas in the bubble is polytropic with a constant value of η [14]. For the present study, we assume that the bubble growth is isothermal, thus, $\eta = 1$ [14, 15]. Note that the five-equation model, Eqs. (2.1)-(2.5), does not consider heat transfer; therefore, the bubble is adiabatic during the collapse. For the case considered in this Chapter, we assume the bubble is isothermal during the growth phase and adiabatic during the collapse phase. These assumptions are appropriate because the duration of the growth phase is typically longer than the collapse phase, meaning there is more time for significant heat conduction to occur during the growth. The significance of changing the heat transfer assumption during the growth phase is studied later in section 5.5. The initial pressure of the bubble used in this study is

$$p_{0,B} = p_{atm} + 2\sigma / R_0 \,. \tag{4.4}$$

The density of the pre-growth bubble air $\left(\rho_{0,B}\right)$ is determined by the ideal gas law, given $p_{0,B}$, the specific gas constant of air is 287 J/(kg·K), and assuming the air temperature is 293.15 K (20 ºC).

The RP equation was solved using the forward Euler method, with a 1 ns time step, following the methodology used in [92]. The RP bubble growth from the case study (section 4.4) is depicted in Figure 4.2. When the RP bubble reaches its maximum radius $\left(R_{\max}\right)$ the value of the variables ρ_B, p_B, and p_∞, are recorded as $\rho_{RP,B}$, $p_{RP,B}$, and $p_{RP,\infty}$, respectively. Note that the density of the bubble fluid (air), ρ_B, is determined using the ideal gas law. These values: ρ_B, p_B, and p_∞, along with $R_{\max}$ and Δt_{RP}, are later used to determine the initial condition of the collapse simulation. Note that at $R_{\max}$ the radial velocity of the bubble interface $\left(\dot{R}\right)$ is zero and that the velocity within the bubble is also zero because the RP analysis neglects the momentum of the bubble fluid.

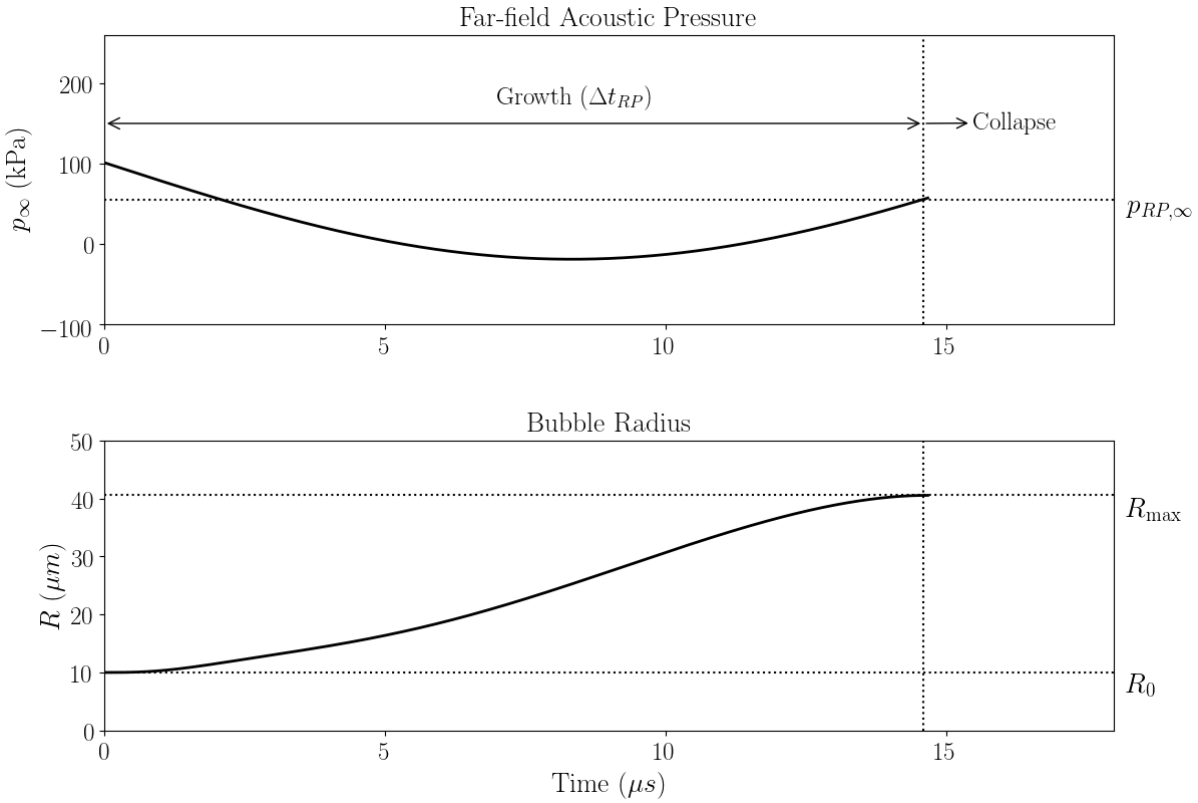

Figure 4.2. The RP response of an air bubble surrounded by water in the presence of an acoustic (ultrasound) field. The bubble grows until it reaches its maximum radius $(R_{\max})$, followed by the collapse phase. The parameters used are described later (section 4.4.1) and are provided in Table 4.1.

4.3.2 Acoustic Field

In this step, we develop the solution to the problem of the surrounding fluid (in the absence of a bubble) that is exposed to a moving boundary. Without the bubble, the governing Eqs. (2.1)-(2.5) simplify to a single fluid problem: $\alpha_1 = 0$ and $\alpha_2 = 1$. After the consideration of the symmetric boundary condition at the *z*-axis and the reflective boundary condition at the outer boundary (Figure 3.1), the single fluid problem further simplifies to a one-dimensional transient problem in the *z*-direction:

$$\frac{\partial(\rho_2)}{\partial t} + \frac{\partial(\rho_2 u_z)}{\partial z} = 0 \tag{4.5}$$

$$\frac{\partial(\rho_2 u_z)}{\partial t} + \frac{\partial(\rho_2 u_z^2 + p)}{\partial z} = 0 \tag{4.6}$$

$$\frac{\partial E}{\partial t}+\frac{\partial\left(u_z\left(E+p\right)\right)}{\partial z}=0 \tag{4.7}$$

where u_z is the velocity in the *z*-direction.

To determine the acoustic field at the beginning of the collapse phase, the one-dimensional transient problem is solved for an initially stationary fluid, $u_z\left(z,t=0\right)=0$, $p\left(z,t=0\right)=p_{atm}$, $\rho\left(z,t=0\right)=\rho_0$, to the fully developed acoustic field, $u_U=u_z\left(z,t_U\right)$, $p_U=p\left(z,t_U\right)$, $\rho_U=\rho_2\left(z,t_U\right)$, where t_U is the solver duration. The development of the acoustic field from the stationary state is achieved by ramping the amplitude of the moving boundary to simulate the starting process of the transducer face. The ramping function used to develop the acoustic field is

$$a\left(t\right)=\begin{cases}a_{\max}\dfrac{t}{\Delta t_R} & \text{if} \quad t<\Delta t_R\\ a_{\max} & \text{if} \quad t\geq\Delta t_R\end{cases} \tag{4.8}$$

where a is the displacement amplitude of the moving boundary and Δt_R is the ramping duration.

The 1D acoustic simulation is run for an additional duration of Δt_D to capture any further transient development of the acoustic flow field after the ramping duration $\left(\Delta t_R\right)$, see Figure 4.3. Note that the duration t_D ends when the wall pressure drops to the equilibrium pressure $\left(p_0\right)$; this ensures that the pressure near the solid boundary is in phase with the far-field acoustic pressure that is used in the RP analysis (p_∞ - see section 4.3.1). The acoustic field is further evolved to the initial time of collapse using the RP growth duration to generate the acoustic field required to initialise the collapse simulation, Δt_{RP}. Thus, the total duration of the acoustic development simulation is $t_U=\Delta t_R+\Delta t_D+\Delta t_{RP}$.

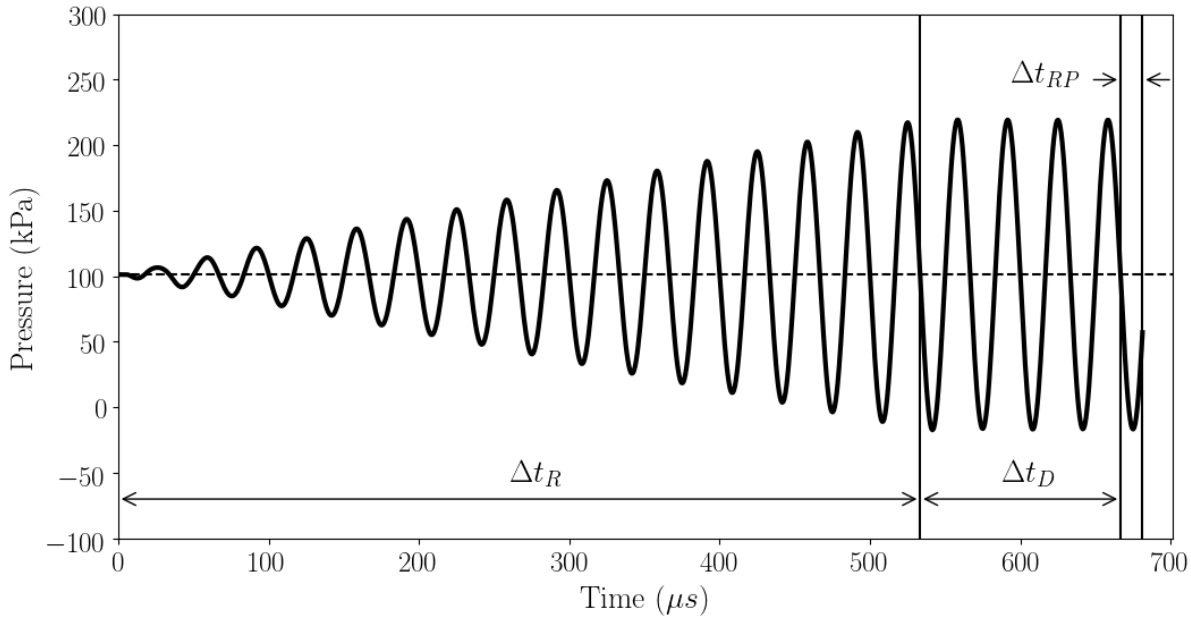

Figure 4.3. The development of the acoustic pressure at the solid boundary $(z = 0)$. Δt_R is the period where the moving boundary amplitude is linearly ramped $(\Delta t_R \approx 16T_U)$, Δt_D is the extra development period $(\Delta t_D \approx 4T_U)$ where the moving boundary amplitude is at its maximum $(a_{\max})$ and Δt_{RP} is the duration required to grow the bubble from R_0 to $R_{\max}$, given by the RP analysis.

A grid refinement study of the 1D acoustic field was used to determine if the grid was sufficiently refined near the moving boundary. The grid was considered to be sufficiently refined when the successive refinement of the grid resulted in a negligible change (less than 1%) to the fully developed pressure amplitude (p_A) at the solid boundary $(z = 0)$. The grid near the moving boundary was refined by reducing the grid cell growth rate (g). The resulting grid parameters used in the case study (section 4.4) are provided in Table 4.1.

A study was conducted to determine if the ramping duration (Δt_R) and the extra development duration (Δt_D) used were sufficiently large. The durations, Δt_R and Δt_D, were investigated separately by doubling the durations until the successive increase in the duration resulted in a negligible change in the pressure amplitude (the same convergence criteria that were used in the grid refinement study - $\Delta p_A / p_A < 1\%$). This results in the durations $\Delta t_R = 16T_U$ and $\Delta t_D \approx 4T_U$, where T_U is the period of the acoustic wave.

4.3.3 Superimposing the RP Bubble on the Acoustic Field

To initialise the acoustically-driven bubble collapse, the RP bubble is superimposed onto the developed acoustic field. The acoustically-driven collapse simulation, referred to as the RGPI model, begins at t_0, where the RP bubble is at $R_{\max}$, and the developed acoustic field is taken at t_U. The RP bubble fluid at $R_{\max}$ has a uniform pressure $\left(p_{RP,B}\right)$, density $\left(\rho_{RP,B}\right)$, and zero velocity, determined from Eq. (4.1) at the instant when the bubble is at its maximum size (pre-collapse state – see section 4.3.1). Thus, the primitive variables inside the bubble in axisymmetric cylindrical coordinates are

$$\rho_1\left(r,z,t_0\right)=\rho_{RP,B},\ p\left(r,z,t_0\right)=p_{RP,B},\ \mathbf{u}\left(r,z,t_0\right)=\mathbf{0}\quad \text{for}\quad \sqrt{r^2+\left(z-S\right)^2}<R_{\max}\ . \tag{4.9}$$

where S is the *initial* distance from the centre of the bubble to the near-wall along the *z*-axis referred to as the standoff distance. From the RP analysis, the pressure distribution of the liquid surrounding the RP bubble $\left(p_L\right)$ at $R_{\max}$ is inversely related to the radial distance from the bubble centre [14, 93] and is described in axisymmetric cylindrical coordinates as

$$p_L\left(r,z,t_0\right)=p_{RP,B}+\left(1-\frac{R_{\max}}{\sqrt{r^2+\left(z-S\right)^2}}\right)p_{RP,\infty}\quad \text{for}\quad \sqrt{r^2+\left(z-S\right)^2}\geq R_{\max} \tag{4.10}$$

where $p_{RP,\infty}$ is the far-field pressure when the RP bubble is at $R_{\max}$. Additional complexity arises when the RP solution of the bubble is superimposed onto the fully developed 1D acoustic field. The pressure distribution of the 1D acoustic field is not uniform, but it must be reconciled with the RP solution (which assumes a uniform far field pressure: $p_{RP,\infty}$). To superimpose the bubble onto the acoustic field, the pressure distribution of the surrounding fluid is defined as

$$p\left(r,z,t_0\right)=p_{RP,B}+\left(1-\frac{R_{\max}}{\sqrt{r^2+\left(z-S\right)^2}}\right)p_U\left(z,t_U\right)\quad \text{for}\quad \sqrt{r^2+\left(z-S\right)^2}\geq R_{\max} \tag{4.11}$$

where p_U is the pressure distribution of the developed acoustic field that is estimated in section 4.3.2. Once the fluid pressure is defined, the adiabatic stiffened EOS is used to define the surrounding fluid density (ρ_2) [94]

$$\rho_2(r,z,t_0)=\rho_{0,2}\left(\frac{\gamma_2 p_2(r,z,t_0)+\pi_{\infty,2}}{\gamma_2 p_{0,2}+\pi_{\infty,2}}\right)^{\frac{1}{\gamma_2}} \quad \text{for} \quad \sqrt{r^2+(z-S)^2}\geq R_{\max} \tag{4.12}$$

where $\rho_{0,2}$ is a reference density of the surrounding fluid at the reference pressure $p_{0,2}$ - in this study, the reference pressure is atmospheric pressure $(p_{0,2}=p_{atm})$.

Finally, the velocity distribution of the bubble needs to be superimposed onto the velocity distribution of the acoustic field. The interface velocity of the RP bubble and velocity distribution of the bubble fluid is zero at $R_{\max}$. Because the RP analysis assumes the surrounding fluid is incompressible, the velocity distribution of the RP surrounding fluid is also zero. However, in the acoustically-driven collapse model the surrounding fluid is compressible, and, therefore, its velocity distribution is not uniformly zero.

The pressure amplitude and the velocity amplitude of an acoustic wave are proportionally related [95]. Assuming the proportionality between velocity and pressure exists in the acoustic field surrounding the bubble, we superimpose the velocity distributions using a relation similar to the pressure distribution (Eq. (4.10)). Thus, to superimpose the bubble velocity in the acoustic velocity field we assume that the same inverse relation used for the pressure can be applied for the velocity distribution in the surrounding fluid $(\mathbf{u})$

$$\mathbf{u}(r,z,t_0)=\begin{bmatrix}u_r(r,z,t_0)\\ u_z(r,z,t_0)\end{bmatrix}=\begin{bmatrix}0\\ \left(1-\frac{R_{\max}}{\sqrt{r^2+(z-S)^2}}\right)u_U(z,t_U)\end{bmatrix} \quad \text{for} \quad \sqrt{r^2+(z-S)^2}\geq R_{\max} \tag{4.13}$$

where u_U is the velocity distribution in the developed acoustic field that is estimated in section 4.3.2. Note that the radial velocity (u_r) is initially zero throughout the domain.

The volume fraction is initialised with a smoothing of the initial material interface over a few grid cells to increase the numerical stability. The Cartesian smoothing function presented in [77] was adopted and applied to the cylindrical coordinate system. The volume fraction of the bubble, α_1, is initialised in cylindrical coordinates using

$$\alpha_1\left(r,z,t_0\right)=\left(\frac{|z|}{|z|+|r|}\right)\left(\frac{1-\tanh\left(\frac{\beta}{\Delta z_{\min}}\left(\sqrt{r^2+\left(z-S\right)^2}-R_{\max}\right)\right)}{2}\right)+\left(\frac{|r|}{|z|+|r|}\right)\left(\frac{1-\tanh\left(\frac{\beta}{\Delta r_{\min}}\left(\sqrt{r^2+\left(z-S\right)^2}-R_{\max}\right)\right)}{2}\right)^2 \tag{4.14}$$

where $\Delta r_{\min}$ and $\Delta z_{\min}$ are the dimensions of the cells in the refined region of the domain (Figure 3.1). β is a coefficient which governs the amount of interface smoothing, which is typically taken between 1 and 10 [77]: the present study uses $\beta=2$.

4.3.4 Summary of the RPGI method

The RPGI method consists of first initialising the bubble at the beginning of the collapse by superimposing the RP grown bubble onto the developed acoustic field (section 4.3). The bubble collapse is then simulated by solving the governing Eqs. (2.1)-(2.5) using the numerical method described in Chapter 3.

4.4 Case Study using the RPGI model

4.4.1 Case Study Parameters

A representative case study of an acoustically-driven bubble collapse near a solid boundary, as depicted in Figure 3.1, using the RPGI model that is developed in this Chapter is presented here. The parameters used are listed in Table 4.1. The ultrasound frequency of 30 kHz is used in low-frequency ultrasound-

induced cavitation applications; however, the model can capture any frequency (e.g. 2 MHz - high-frequency ultrasound applications). A bubble standoff distance of $S = 1.1R_{max}$ was chosen as it gives a bubble close to the solid boundary, but not so close that it joins to the wall in an unrealistic manner, see section 4.2. The water (properties are given in Table 4.1) has a speed of sound of 1449 m/s; thus, the wavelength of the 30 kHz ultrasound is 4.83 cm. The domain depth of 1 cm is approximately a quarter of the ultrasound wavelength and these conditions result in a standing wave between the moving boundary and the solid boundary. The displacement amplitude of the transducer $a = 0.4174$ μm was chosen to give a pressure amplitude of the acoustic field at the solid boundary of $p_A \approx 120$ kPa , which is a sufficient pressure amplitude to cause the transient growth and collapse of a $R_0 = 10$ μm bubble.

The pre-growth bubble radius of $R_0 = 10$ μm was arbitrarily chosen to represent a small transient cavitation bubble that is above the Blake (lower transient) threshold bubble radius (R_L) and below the Minnaert resonant bubble radius (R_M) [15]. The Blake threshold bubble radius for the case described is about $R_L = 2$ μm and the Minnaert resonant bubble radius is about $R_M = 154$ μm ; thus, $(R_L = 2\ \mu\text{m}) < (R_0 = 10\ \mu\text{m}) < (R_M = 154\ \mu\text{m})$. It is also interesting to note that the Minnaert resonant frequency for a $R_0 = 10$ μm bubble would be approximately 461.3 kHz.

Recall that in Figure 3.1 the refined region that encompasses the bubble has a very fine grid where the cell dimensions are Δr_{min} and Δz_{min} (Table 4.1). The cell dimensions in the refined region are chosen to generate a sufficiently refined grid to accurately capture the collapse of the bubble. In the case study results shown in this section, the minimum cell dimensions were chosen to be within the limits of our computational resources: $\Delta r_{min} \approx \Delta z_{min} \approx 0.13\mu m$. The simulations took 10 hours using 100 compute nodes. In a comparison with a much less refined grid (double the cell dimensions - $\Delta r_{min} \approx \Delta z_{min} \approx 0.26\mu m$) we found that the coarser grid resulted in a 25 % decrease in peak pressure experienced at the wall and a change in the simulation duration to the peak wall pressure: 4.67 μs (refined grid) to 4.62 μs (coarse grid). This change in the results is due to the sharpness of the bubble interface: more numerical diffusion of the air-water interface results in cushioning of the collapse. The

grid used in this study, however, is sufficiently refined for the qualitative analysis of the results. The grid is also sufficient for the quantitative comparison of the model to previously developed models because the same grid resolution is used for all of the studies and, therefore, the sharpness of the bubble interface is very similar over the duration of the collapse.

Table 4.1. Model parameters and fluid properties

Symbol	Description	Value
f	Ultrasound frequency	30.0 kHz
a	The amplitude of the transducer face	0.4174 μm
p_A	Subsequent acoustic pressure amplitude	120 kPa
R_0	Initial bubble radius (pre-growth)	10.0 μm
H_d	Domain depth	1.0 cm
R_d	Domain radius	1.0 cm
H_f	Refined region depth	100.0 μm
R_f	Refined region radius	50.0 μm
S	Standoff distance	1.1 $R_{\max}$
$\Delta r_{\min}$	Refined cell radial width	0.13 μm
$\Delta z_{\min}$	Refined cell depth	0.13 μm
N	Cells	134400
g	Cell growth rate	1.1
CFL	CFL condition (to compute Δt)	0.4
p_{atm}	Atmospheric pressure	1 atm
$\rho_{0,2}$	The density of water (surrounding fluid) at p_{atm}	10^3 kg/m^3
γ_1	EOS parameter for air [39]	1.4
γ_2	EOS parameter for water [39]	6.12
$\pi_{\infty,1}$	EOS parameter for air [39]	0.0 Pa
$\pi_{\infty,2}$	EOS parameter for water [39]	3.43×10^8 Pa
μ	Dynamic viscosity of water (RP only)	1.002×10^{-3} Pa.s
σ	Air-water interface surface tension (RP only)	0.07286 N/m

4.4.2 RP Growth Results

The RP analysis (Eq. (4.1)) used for the initialisation of the case study, resulted in a bubble that grew to approximately four times its initial size ($R_{\max}/R_0 \approx 4$ - see Table 4.2). This growth results in a pressure inside the bubble $\left(p_{RP,B}\right)$ of 1.737 kPa, compared to the far-field pressure $\left(p_{RP,\infty}\right)$ of

57.39 kPa. During the collapse, the far-field acoustic pressure will continue to increase to the peak acoustic pressure, driving the violent collapse of the bubble. Note that Figure 4.2 shows the RP bubble growth for this case study.

Table 4.2. The results from the RP growth simulation, where the results are used to initialise the collapse simulation.

Symbol	Description	Value
Δt_{RP}	Growth duration	14.68 µs
$R_{\max}$	Maximum bubble radius	40.56 µm
$p_{RP,B}$	Bubble pressure at $R_{\max}$	1.737 kPa
$p_{RP,\infty}$	The far-field acoustic pressure at $R_{\max}$	57.39 kPa
$\rho_{RP,B}$	Bubble density at $R_{\max}$	0.02064 kg/m^3

4.4.3 RPGI Bubble Collapse Results

The RPGI bubble collapse was simulated from t_0 for a duration of 4.9 µs. The transient behaviour of the air-water interface is presented in Figure 4.4 by incrementing the interface location in time. A volume fraction contour line of $\alpha_1 = 0.95$ indicates the interface location.

Initially, the bubble is spherical (Figure 4.4). During the collapse, the upward flow is restricted near the solid boundary (no-through-flow boundary), resulting in a small change in the interface location at the lower portion of the bubble (Figure 4.4). This causes the bubble to elongate in the direction normal to the solid boundary and the centroid of the bubble to move toward the solid boundary (Figure 4.4). The upper portion of the bubble, which is unhindered by the solid boundary, gains kinetic energy and momentum. Because the movement of the lower portion of the bubble is restricted, the net momentum is directed toward the solid boundary. The upper portion begins to flatten and a jet forms. The jet accelerates through the centre of the bubble toward the solid boundary.

The pressure inside the bubble increases as the bubble is compressed. When the pressure within the bubble becomes sufficiently high $\left(p_B > p_\infty\right)$, the bubble begins to decelerate the surrounding fluid, opposing the large momentum developed in the surrounding fluid. The momentum of the surrounding fluid causes further compression of the bubble resulting in very large pressures. The pressure reaches its maximum when the bulk compression is complete, signifying the end of the collapse. The large

pressure developed during the collapse results in the rebounding of the bubble: the rebound phase begins immediately after the collapse phase.

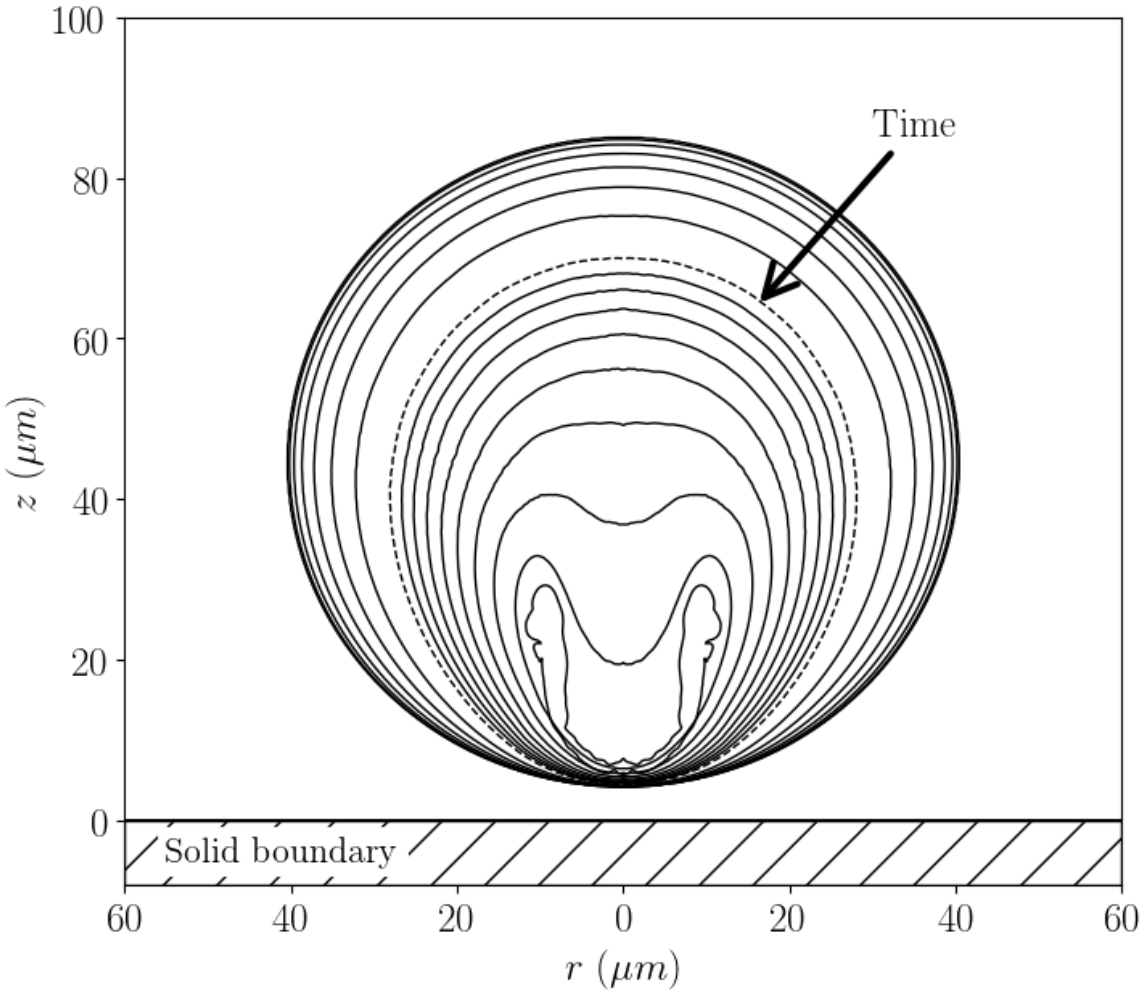

Figure 4.4. A depiction of the interface location contour $(\alpha_1 = 0.95)$ at representative times from t_0 to $t_0 + 4.7$ μs after 273,500 time steps. The interface contour lines are shown at every 27,350 time steps $(\approx 0.5$ μs$)$ until the dashed interface line where the spacing between the interface contour lines reduces to every 6,837 time steps $(\approx 0.13$ μs$)$.

The computational Schlieren images taken at representative times from the simulation are presented in Figure 4.5, showing the compressible flow features of the collapse. Figure 4.5 also includes the interface location contour as a solid contour line. Figure 4.5a shows the initial state of the system prior to the collapse, where the initial bubble shape is perfectly spherical. After 4.3 μs of the bubble collapsing, the bubble elongates, compresses, and the upper region of the bubble interface flattens (Figure 4.5b). After

another 0.4 μs $(t_0 + 4.7\ \mu s)$ the collapse phase is complete (Figure 4.5c). In this short duration, the bubble drastically reduces in size with the formation of a jet which penetrates the bubble, see Figure 4.5c. At the end of the collapse, large density gradients are present within the bubble which influence the collapse physics and the rebounding (Figure 4.5c). These density gradients within the bubble become more apparent in the rebound phase (after $t_0 + 4.7\ \mu s$), see Figure 4.5d. At the end of the collapse and the beginning of the rebound phase, the jet reaches the surrounding fluid on the other side of the bubble forming a toroidal bubble with a distorted interface location (Figure 4.5d).

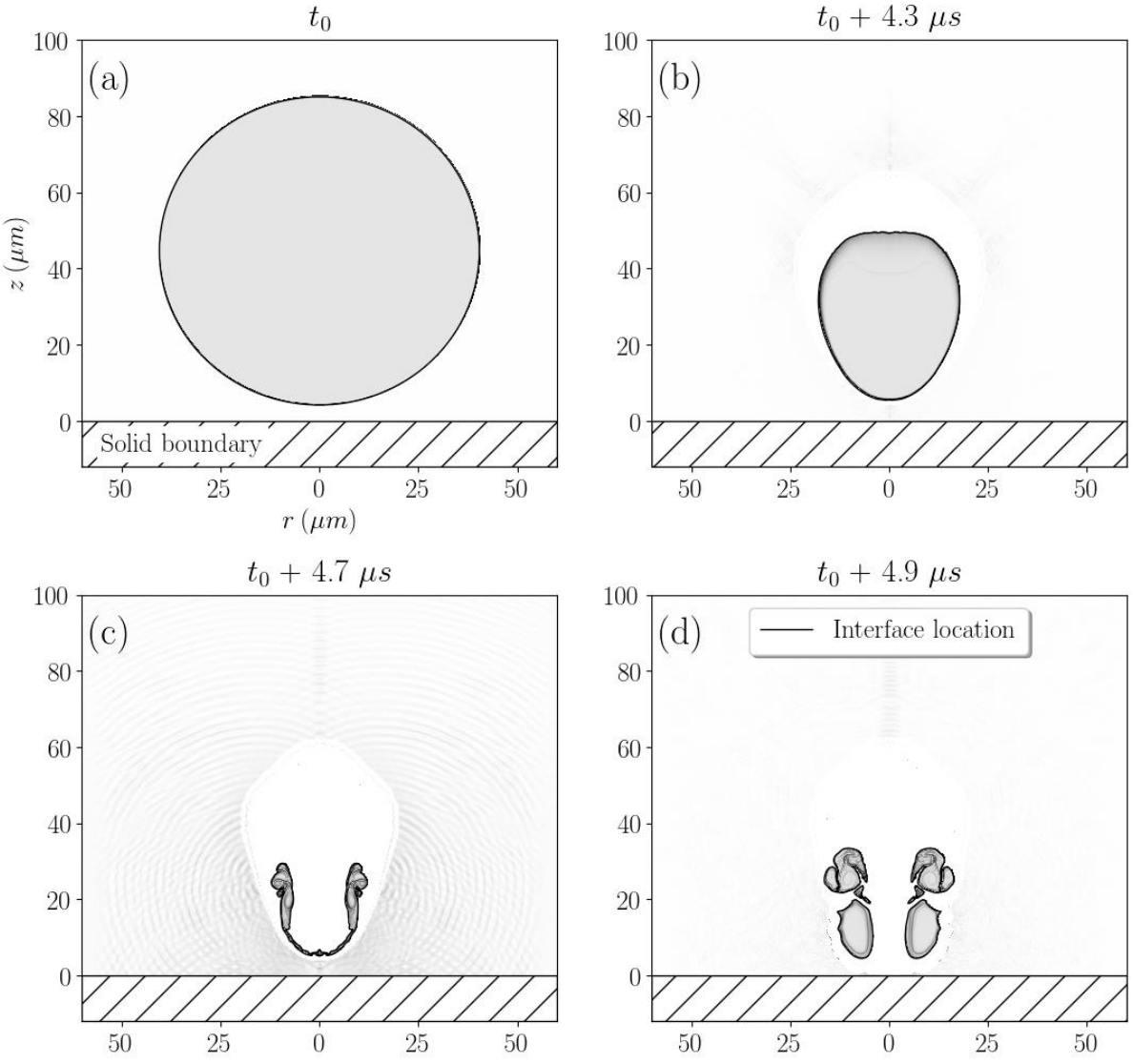

Figure 4.5. Visualisation of the bubble collapse using computational Schlieren images (a function of density gradient – see section 3.9) at representative times after t_0. The black contour line overlaid on the images corresponds to the interface location $(\alpha_1 = 0.95)$.

The bubble shape for the majority of the collapse phase is qualitatively consistent with the collapse shape found in multiple studies [4, 26, 28, 29, 96]. The key consistent features of the collapse shape include the bubble elongation and the jet formation (Figure 4.4). In the later stages of the collapse, large density gradients within the bubble become apparent (Figure 4.5c). This shows that the assumption of a uniform bubble pressure and density that has been used in other studies [27, 28] becomes less valid at the later stages of the collapse and in the rebound phase.

The compressibility of the surrounding fluid becomes important at the later stages of the collapse as the velocities approach the speed of sound. The pressure and velocity distributions during the collapse are depicted in Figure 4.6. A high pressure develops above the bubble at 4.3 μs (Figure 4.6a), causing the jet to develop through the centre of the bubble towards the wall. As the jet penetrates the bubble at 4.7 μs (Figure 4.6b), a large water-hammer pressure develops at the lower region of the bubble, near the solid boundary. This high-pressure region corresponds to the source of the acoustic emission in the surrounding fluid, seen in Figure 4.5c. At the later stages of the collapse, interface instabilities develop; these instabilities continue to grow during the rebounding phase. As the jet penetrates the bubble, a Kelvin-Helmholtz instability begins to develop at the interface as a result of the velocity difference between the two fluids (Figure 4.5c). The velocity difference causing the Kelvin-Helmholtz instability is depicted in Figure 4.6. The Kelvin-Helmholtz instability appears as the deformation of the interface location in Figure 4.5c. The Kelvin-Helmholtz instability is particularly apparent after a short duration of the rebounding (Figure 4.5d). The rebounding is a particularly unstable process because it involves the large accelerations of a heavy fluid (surrounding water) forced by a lighter fluid (bubble air). The high pressure within the bubble that causes the light bubble fluid to accelerate the heavy surrounding liquid is depicted in Figure 4.6b. In this case, the Rayleigh-Taylor interface instability begins to occur at the final stages of the collapse and becomes apparent in the rebounding (see Figure 4.5d) where there are large perturbations in the interface location.

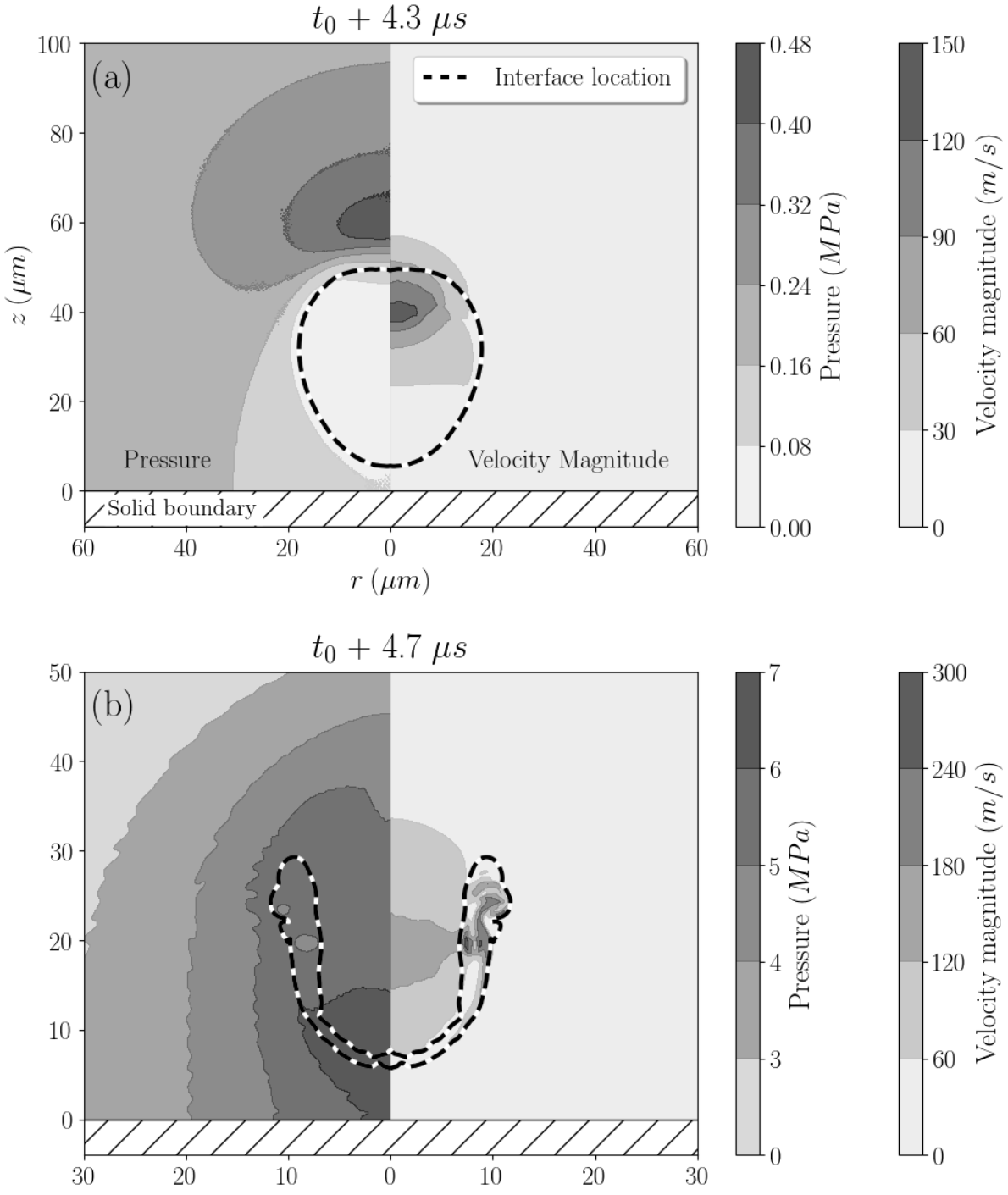

Figure 4.6. A depiction of the pressure and velocity distribution at two stages of the RPGI bubble collapse: (a) 4.3 µs and (b) 4.7 µs after t_0. The left-hand side panel depicts the pressure contour, and the right-hand side panels depict the velocity contours.

4.4.4 Solid boundary pressure

The pressure experienced by the nearby solid boundary is a key measure of the potential for a bubble collapse to cause damage. The pressure experienced by the nearby solid boundary during the collapse is presented in Figure 4.7a and Figure 4.8, where Figure 4.7a shows the pressure at $(r = 0,\ z = 0)$ and Figure 4.8 shows the pressure along the radial coordinate (r) at $z = 0$. The pressure rises rapidly at the later stages of the collapse and results in a maximum pressure at the solid boundary of approximately 6.7 MPa at $r = 0$ after approximately 4.7 μs, see Figure 4.7a. As expected, the pressure at the solid boundary is localised below the bubble (Figure 4.8). Depending on the solid boundary material, this pressure could result in damage (e.g. pitting). A more violent collapse would result in a higher pressure experienced by the solid boundary, increasing the likelihood of material damage. For example, if the wall was made of 6061 aluminium alloy with a yield strength of 55 MPa, pitting would occur if the wall pressure exceeded the yield strength.

4.4.5 Far-field pressure

As anticipated, the acoustic pressure at the outer boundary (far-field pressure) was uninfluenced by the collapse as it was sufficiently far away from the bubble (Figure 4.7b). The transient far-field pressure of the simulation is plotted alongside the far-field pressure used for the RP analysis (p_∞ - Eq. (4.2)) in Figure 4.7b. This agreement confirms that the method of superimposing the RP bubble into the 1D acoustic field produces a far-field pressure that is consistent and in phase with the far-field pressure of the RP analysis. The results presented in Fig. 10b also indicate that during the 4.9 μs of the collapse, the far-field experiences a pressure increase of approximately 100 kPa. In contrast, previous models of collapse assume that during the collapse the far-field pressure remains constant. This further supports the importance of the contribution of the current model.

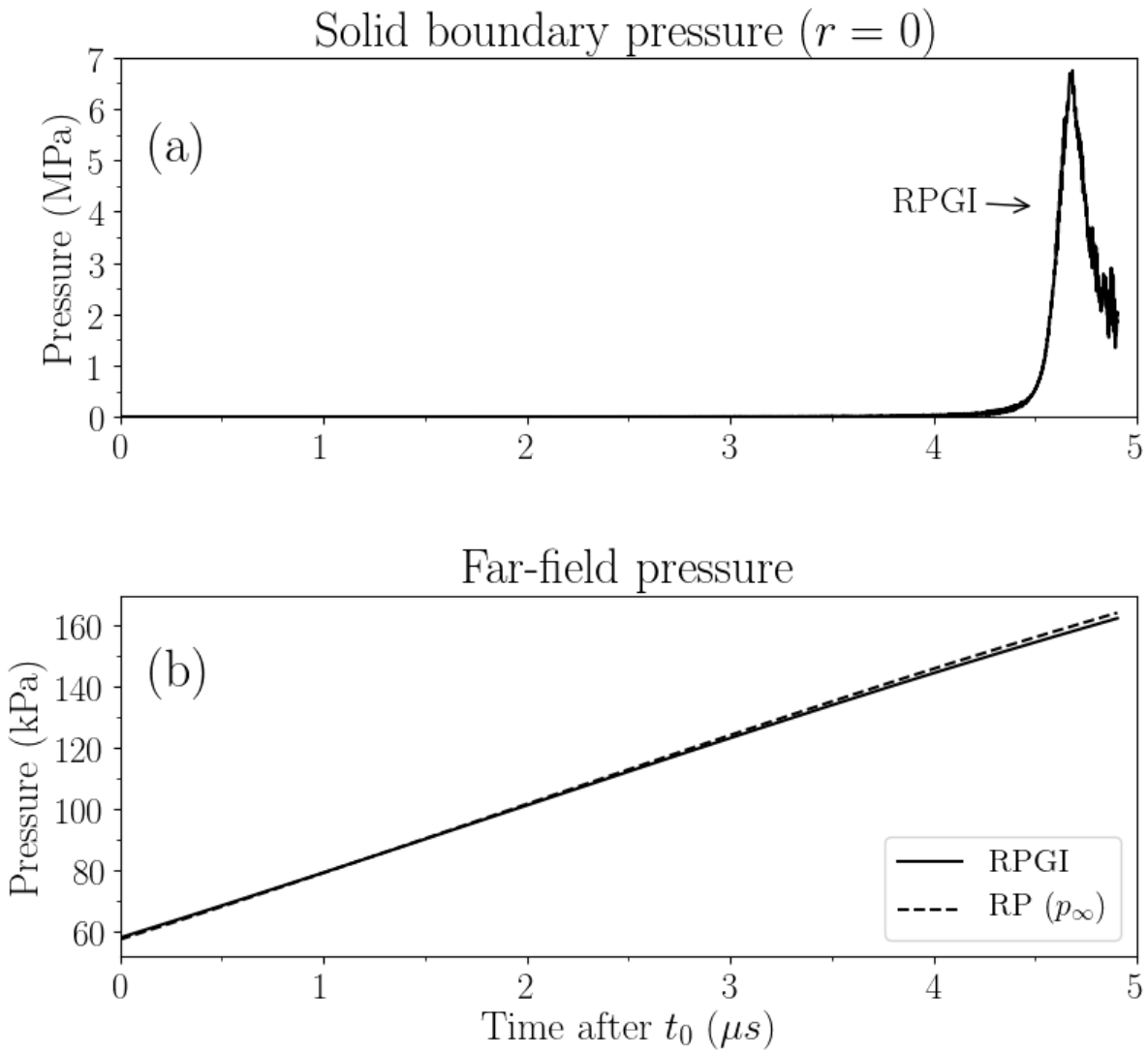

Figure 4.7. (a) The pressure at the solid boundary at $r = 0$ and (b) the far-field pressure of the ultrasound field during the RPGI collapse simulation (RPGI) compared to the estimated far-field pressure function (Eq. (4.2)) used in the RP analysis for initialisation of the bubble (p_∞).

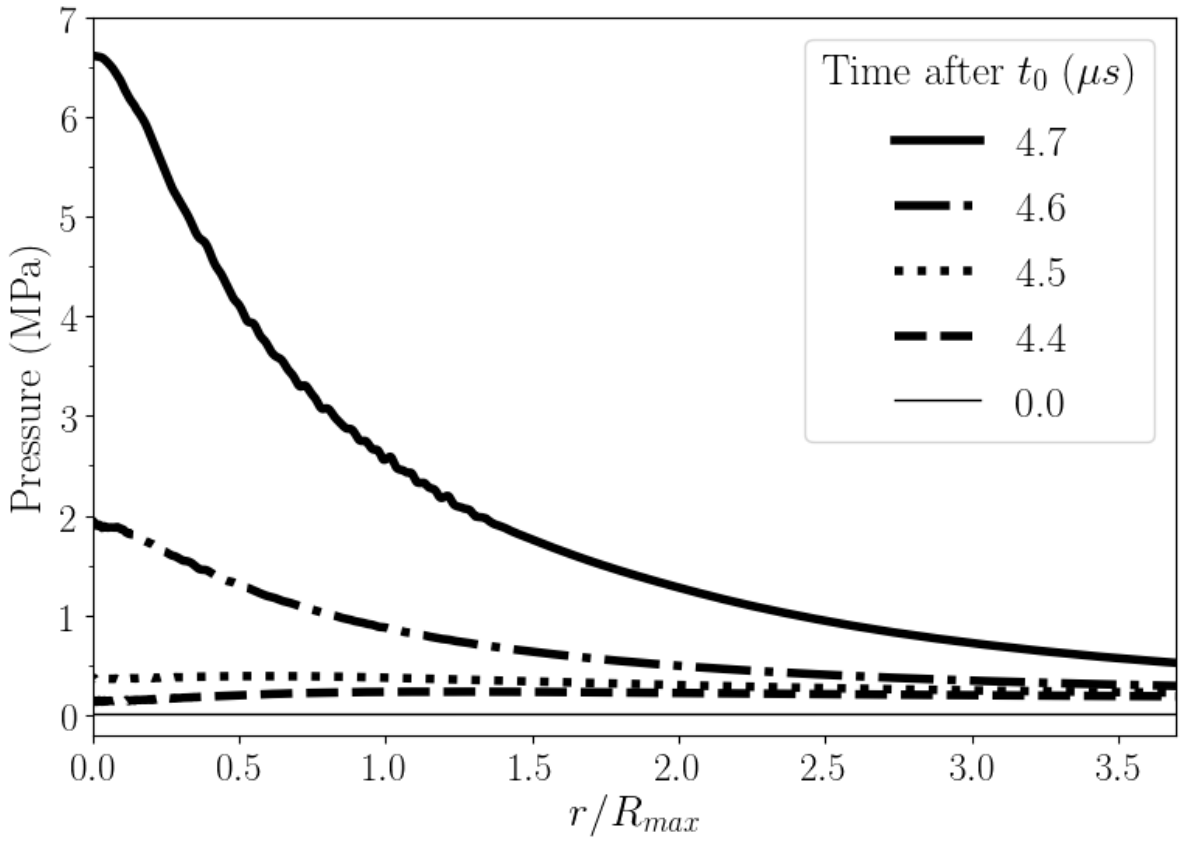

Figure 4.8. The pressure at the solid boundary $(z = 0)$ during the RPGI bubble collapse shown in non-dimensionalized radial coordinates $(r / R_{\max})$ at representative times after t_0.

4.4.6 Comparison of the RPGI Collapse to the Rayleigh Collapse

In this section, a comparison between the RPGI model and the fully compressible representation of the Rayleigh collapse of a near-wall bubble is made. The Rayleigh collapse is achieved by specifying uniform initial pressures of the bubble and of the surrounding medium such that the surrounding fluid is at a higher pressure than the bubble: this results in the Riemann problem across the interface. A similar comparison is made in the work by [38] that investigates the shock-induced collapse.

Given the very short timescales associated with the collapse, it seems reasonable to consider that the Rayleigh collapse may be a good candidate for representing the acoustically-driven collapse. However, when the results of Figure 4.7b are considered, it is clear that the far-field pressure experiences a large change in pressure during the collapse. Perhaps more importantly, this figure raises questions of the

best choice in initial pressure difference that would allow the Rayleigh collapse to closely represent the acoustically-driven collapse; clearly, the choice in initial pressure difference should not be arbitrary.

To compare the current model to a Rayleigh-type collapse and to quantify the influence of the initial pressure difference, three simulations representative of a Rayleigh collapse (RC) are conducted. To estimate the initial conditions, the RC cases use some of the results of the RP analysis at the instant that the collapse begins (Table 4.2). The initial bubble radius is $R_{\max} = 40.56\ \mu\text{m}$, and the uniform initial bubble pressure is $p_{RP,B} = 1.737\ \text{kPa}$. In the following analysis, three different values of the initial pressure of the surrounding liquid are considered: a minimum, a maximum, and an intermediate pressure.

The minimum estimate of the initial surrounding liquid pressure is represented by the magnitude of the far-field pressure of the RP simulation at the instant that the collapse begins, $p_{RP,\infty} = 57.39\ \text{kPa}$. The Rayleigh collapse that uses this minimum initial fluid pressure shall be denoted RC1. As a maximum estimate of the fluid pressure, we consider the maximum far-field pressure that can result from the RP analysis represented by Eq. (4.2) : $p_A + p_{atm} = 221.3\ \text{kPa}$. The Rayleigh collapse that uses this maximum initial fluid pressure shall be denoted RC2. For the third Rayleigh collapse case (RC3), we consider a case where the constant far-field pressure results in the same collapse duration as the RPGI case. Note that the collapse duration is measured from the start of the simulation until the bubble reaches its minimum volume. The constant far-field pressure that results in the same collapse duration as RPGI case cannot be found analytically and, therefore, is determined by iteratively changing the far-field pressure for the RC collapse simulation until the correct collapse duration is achieved. The far-field pressure for RC3 was found to be $89.9\ \text{kPa}$ after four iterations of the Bisection method, where the RC3 collapse duration was negligibly different $(<1\ \%)$ from the RPGI collapse duration. The comparison between RC3 and RPGI will highlight the effect the transient acoustic field has on the collapse.

From these initial conditions, the Rayleigh collapse is simulated in the same manner as that of the collapse phase of the acoustically-driven case - using Eqs. (2.1)-(2.5) and using the domain and property

values described in Table 4.1 of the case study with the single exception that a reflective boundary condition is used in place of the moving boundary.

As a simple measure of comparison, the local pressures at $r = 0$ on the near solid boundary are calculated and presented in Figure 4.9a. Note that the line indicated as RPGI is the case study depicted in Figure 4.7. To further illustrate the differences in pressures of these simulations, consider the far-field pressure distributions depicted in Figure 4.9b. The constant far-field pressures for RC1 and RC2 are representative of the limits of the transient far-field pressure of the acoustically-driven case. The RC1 case underestimates the peak pressure at the solid boundary where the peak pressure is 60 % lower than the RPGI case and takes 1.3 μs longer to collapse (Figure 4.7a). Whereas, the RC2 case over-approximates the peak pressure at the solid boundary with a peak pressure which is approximately two times higher than the RPGI case. While the Rayleigh model does simplify the initialisation of the system, the collapse is very sensitive to the choice in initial pressure difference. and it is not clear what that choice should be without the solution to the acoustically-driven collapse.

As previously stated, the initial pressure of the surrounding fluid for the RC3 case is determine by iteratively changing the pressure to give a collapse duration that is the same as the acoustically-driven collapse case (RPGI), as shown in Figure 4.9c where the minimum bubble volume occurs at the same instant in time for RC3 and RPGI. The far-field pressure of RC3 is depicted in Figure 4.9b. The acoustically-driven collapse (RPGI) results in a more violent collapse than RC3, where RC3 results in a 4.7 MPa peak pressure on the solid boundary (Figure 4.9a). The RPGI case results in a more violent collapse than RC3 due to the larger driving pressure at the final stages of the collapse, see Figure 4.9b. Although the collapse duration is the same for RC3 and RPGI, the evolution of the bubble volume is different (Figure 4.9c). The bubble in the RPGI case collapses at a reduced rate at the beginning of the collapse and then collapses at a faster rate in the later stages of the collapse compared to the RC3 case, see Figure 4.9c. The increased rate of collapse at the later stages of the collapse for the RPGI case is consistent with the increased pressure experienced by the nearby solid boundary.

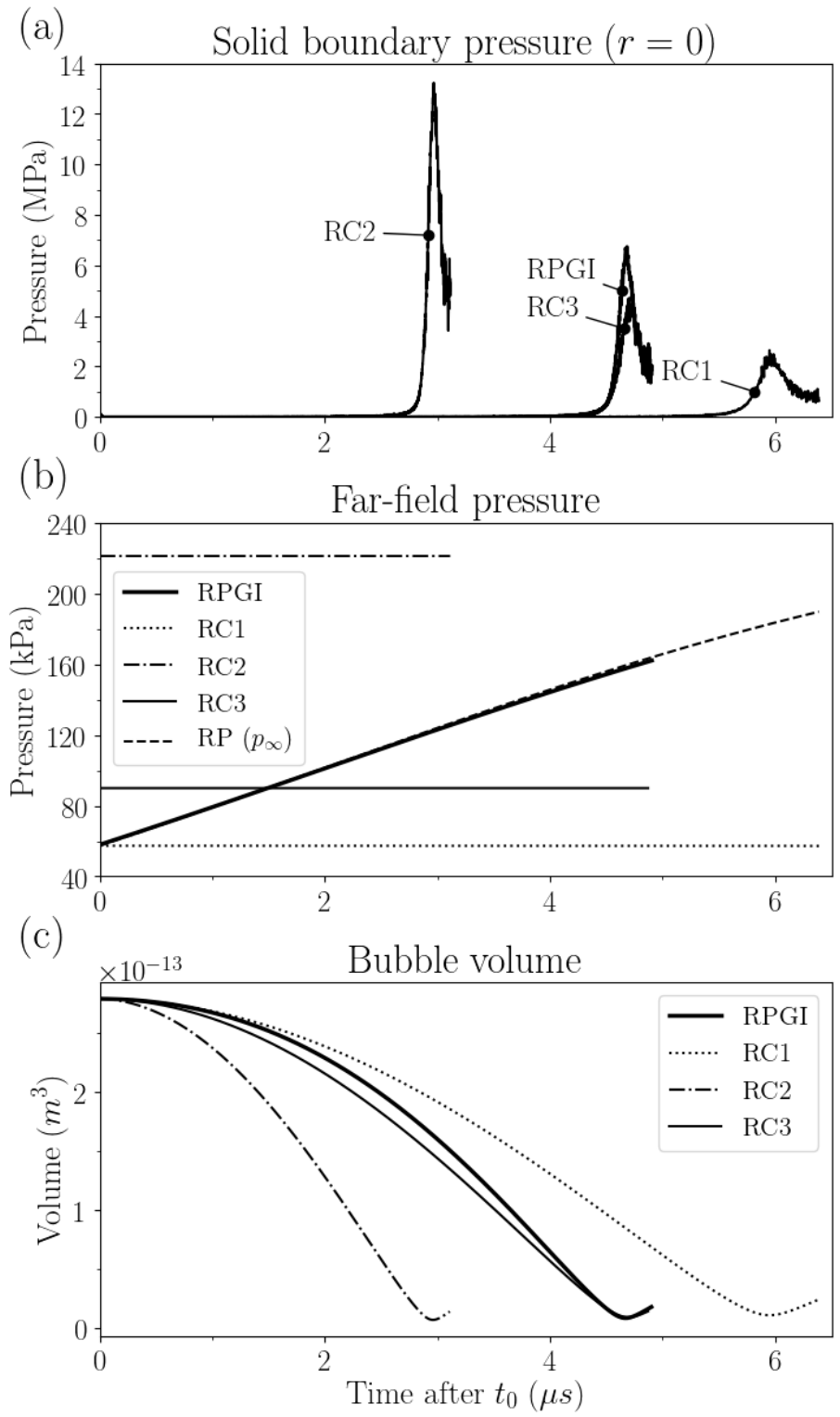

Figure 4.9. Comparison of the results of the acoustically-driven collapse model (RPGI) with the Rayleigh collapse cases (RC1, RC2, and RC3). (a) The pressure at the solid boundary at $r = 0$, (b) the far-field pressure of the acoustic field, and (c) the bubble volume during the collapse simulation. The estimated far-field pressure function (Eq. (4.2)) used in the RP analysis for the initialisation of the bubble (p_∞) is also included in (b).

The Rayleigh collapse case is also unable to capture the spatial variations in the acoustic pressure field near the bubble; however, these variations are not critical for the case presented as the wavelength of the ultrasound field is much greater than the dimensions of the bubble: $R_{\max}/\lambda = 0.00084 \ll 1$. For high-frequency ultrasound studies, the spatial variations in the acoustic pressure field near the bubble would become more significant, and model developed in this paper would be able to capture the subsequence changes to the bubble collapse dynamics.

4.4.7 Model limitations and motivation for further development

The numerical scheme does not guarantee stability and becomes troublesome when simulating more violent collapse cases. This is because a violent collapse involves the interaction between shockwaves and material interfaces with large density and pressure gradients. In practice, we found that the positivity-preserving and maximum-principle-satisfying limiter significantly increased the stability of the numerical scheme (compared to the numerical scheme without the limiter), allowing more violent collapse cases to be simulated. However, even with the limiter, the numerical scheme may be unstable depending on the collapse case. Up to this point, the most violent acoustically-driven collapse we have successfully simulated used a pressure amplitude $\left(p_A\right)$ of 300 kPa for an initial bubble of $R_0 = 10$ μm which results in the growth ratio $R_{\max}/R_0 \approx 16$. To further increase the numerical stability of the scheme, a reduction of the order of reconstruction or the implementation of flux limiters may be necessary [65]. Alternatively, the inclusion of the regularising effects of viscosity (implemented in [65]) and surface tension may increase the stability of the numerical scheme.

In this Chapter, we assume the growth phase is uninfluenced by the near solid boundary: spherical growth. The closer the bubble is to the solid boundary, the more the solid boundary will influence the bubble growth. For spherical growth, if the stand-off distance is less than unity, the bubble will grow onto the solid boundary. In this case, we expect the non-spherical growth to be of critical importance with other studies observing a flattening of the bubble near the solid boundary, avoiding any contact between the bubble and solid boundary [4]. A study of interest is to investigate the assumption of

spherical growth and determine at what standoff distance (S) does non-spherical growth significantly influence the dynamics of the bubble collapse, see Chapter 6.

4.4.8 Summary of the RPGI bubble collapse model

In the present study, a model that captures the acoustically-driven collapse of a cavitation bubble was presented. The acoustic input was modelled using an immersed moving reflective boundary. A method was developed to approximate the initial condition at the beginning of the collapse simulation using the RP equation to compute the bubble and a 1D compressible model to develop the acoustic field. A positivity-preserving and maximum-principle-satisfying limiter was successfully implemented in order to increase the stability of the numerical scheme and to ensure that no unphysical properties arise. This numerical scheme was verified and validated using a shock-bubble test case, showing qualitative and quantitative agreement with published experimental and numerical results.

The model is applied in a simulation of an initially spherical bubble with a pre-collapse radius of $R_{\max} = 40.56$ μm that experiences collapse resulting from the acoustic field produced by a transducer face oscillating with a frequency of $f = 30$ kHz and a displacement amplitude of $a = 0.4174$ μm. The collapse shape is found to be qualitatively consistent with previous work, and a jet is observed after 4.7 μs. The resulting pressure experienced by the nearby solid boundary is presented and following the collapse, a maximum pressure at the solid boundary of 6.7 MPa is calculated.

The maximum wall pressure resulting from the acoustically-driven collapse is compared to that of three Rayleigh collapse simulations. The results show the sensitivity of the Rayleigh collapse to the choice in initial pressure difference which further enforces the importance of the need to represent the acoustic field in acoustically-induced bubble collapse cases.

Chapter 5 Bubble Growth Influences and the effect on the Subsequent Collapse

It is common for numerical studies of bubble collapse to neglect the influence of fluid effects like viscosity and surface tension. This is because the presence of vapour during the collapse and the influence of surface tension and viscosity are found to be of secondary importance during the collapse phase [19, 27, 29, 34, 59, 60].

However, consideration of growth influences, like surface tension, on the subsequent collapse have not been investigated previously. An example of a question we ask in this Chapter is how does the influence of the surface tension during the growth phase change the dynamics of the subsequent bubble collapse?

In the previous Chapter, we developed the Rayleigh-Plesset growth initialised model (RPGI model) that uses the RP equation to determine the pre-collapse state of the bubble (at the instant when the bubble is at its maximum size). Its radius $\left(R_{\max}\right)$, density $\left(\rho_{B,RP}\right)$, and pressure $\left(p_B\right)$ define the state of the pre-collapse bubble. Additionally, from the RP growth calculation, we determine the growth duration $\left(\Delta t_{RP}\right)$ and the acoustic far-field pressure at the beginning of the collapse $\left(p_{RP,\infty}\right)$. The pre-collapse bubble is then superimposed onto the surrounding liquid whose properties (velocity, pressure, and density) are approximated using the 1D solution of the fluid exposed to the moving boundary (see section 4.3). The near-wall bubble collapse is then simulated from the pre-collapse state (RPGI model).

The RP equation, which is used to approximate the bubble growth, assumes that

1. the bubble is in an infinite body of fluid (no nearby boundaries),
2. the surrounding fluid is incompressible,
3. and the bubble is polytropic.

The numerical model assumptions that are used to simulate the collapse phase are different than those that are used in the RP equation to model the growth. The numerical model for the collapse neglects

1. surface tension,

2. viscous effects,
3. the presence of vapour in the bubble,
4. and heat conduction.

The RP equation, however, does capture these effects: surface tension, viscosity, and heat conduction. These effects are of secondary importance during the collapse phase (thus, they are neglected in the numerical collapse model), but may be of importance during the growth phase (in the RP equation to model the growth). This initiated the question of whether the effects (surface tension, etc.) considered in the growth phase would strongly influence the pre-collapse state of the bubble and the subsequent collapse of the RPGI model.

In this Chapter, we investigate the effects that influence the growth of the bubble and the subsequent collapse. The growth effects are considered by changing the assumptions in the RP equation used to initialise the collapse simulation for the RPGI model. Note that the numerical method for the collapse simulation is unchanged (it always neglects surface tension, viscous effects, and heat conduction); only the parameters in the RP equation are changed. The case that is considered is described in the previous Chapter, see section 4.4.1. The RP equation (Eq. (4.1)) used is described in section 4.3.1. To simulate the collapse, the Eqs. (2.1)-(2.5) are solved in the manner described in Chapter 3 and initialised using the pre-collapse bubble as described in section 4.3 using the same parameters and fluid properties listed in Table 4.1, unless stated otherwise.

The key growth influences we study are

1. surface tension (section 5.1),
2. viscosity (section 5.2),
3. bubble vapour (section 5.3),
4. the compressibility of the surrounding fluid (section 5.4),
5. and the isothermal vs adiabatic growth assumption (section 5.5).

Changing the parameters or assumptions in the RP equation results in the change in the pre-collapse state of the bubble and, therefore, results in a change in the subsequent collapse of the bubble. In this

Chapter, we study how significantly the growth influences (surface tension, viscosity, etc) affect the pre-collapse state of the bubble which is described by

- the growth duration - Δt_{RP} ,
- the maximum size of the bubble - $R_{\max}$,
- the bubble pressure and density at the maximum size - $p_{RP,B}$, $\rho_{RP,B}$,
- and the acoustic far-field pressure at the beginning of the collapse - $p_{RP,\infty}$).

We also investigate how the subsequent collapse is influenced by the change in the pre-collapse state of the bubble by quantifying the change in the pressure experienced by the near-wall. In the following sections, all of the near-wall collapse simulations use a standoff distance of $S = 1.1R_{\max}$, where $R_{\max}$ is the size of the pre-collapse bubble, which depends on the RP growth calculation. For example, if, considering the influence of surface tension, the bubble growths to a pre-collapse bubble size $\left(R_{\max}\right)$ of 40 μm then the standoff distance $\left(S = 1.1R_{\max}\right)$ with be 44 μm, but if the growth neglects surface tension and the bubble grows to a pre-collapse size of 55 μm then the bubble standoff distance $\left(S = 1.1R_{\max}\right)$, in that case, is 55 μm .

5.1 Surface Tension

During the collapse phase, the pressure and inertial terms are shown to be dominant over the surface tension force [29, 97] and, therefore, surface tension is typically neglected in collapse calculations [27-29, 34, 60, 77]. Thus, surface tension is not considered in the numerical model of the near-wall collapse presented in Chapter 3. It is, however, unclear whether the surface tension is negligible in the RP model of growth used in the RPGI model to determine the state of the pre-collapse bubble. This section presents a brief investigation of the influence that the existence of surface tension in the RP growth has on the state of the pre-collapse bubble and the severity of the subsequent collapse in the RPGI model.

In order to highlight the influence of the presence of surface tension in the RP growth phase, the nonzero surface tension case (RPGI - $\sigma = 0.07286$ N/m) is compared with a zero surface tension case (RPGI initialised without surface tension - $\sigma = 0$). The surface tension term is only present in Eq. (4.1) and Eq. (4.4); these equations are reproduced here

$$\overbrace{R\ddot{R} + \frac{3}{2}\dot{R}^2}^{\text{Inertial terms}} + \overbrace{\frac{4\mu}{\rho_L R}\dot{R}}^{\text{Viscous term}} + \overbrace{\frac{2\sigma}{\rho_L R}}^{\textbf{Surface tension term}} + \overbrace{\frac{p_\infty(t) - p_B(t)}{\rho_L}}^{\text{Driving pressure term}} = 0 \tag{5.1}$$

$$p_{0,B} = p_{atm} + \frac{2\sigma}{R_0}. \tag{5.2}$$

From Eq. (5.2), the inclusion and exclusion of surface tension results in two different initial bubble pressures for the RP growth calculation: $p_{0,B} = 115.897$ kPa with surface tension and $p_{0,B} = 101.325$ kPa without surface tension.

The influence of the surface tension in the growth phase results in significantly different results from the RP growth analysis, shown in Table 5.1 and Figure 5.1, where the state of pre-collapse bubble is significantly different. From Table 5.1, it is apparent that the exclusion of surface tension in the RP equation results in a 3.3% longer growth duration (Δt_{RP}) and a 11.2% larger maximum bubble radius $(R_{\max})$. This is because the surface tension force acts against the bubble growth; therefore, without the surface tension force restricting the growth the bubble growths larger for a longer duration. The bubble pressure at the maximum size is 36.4% lower because the maximum bubble radius is larger (see Eq. (4.3)). The bubble density is 36.4% less because the volume of the bubble is larger. The far-field acoustic pressure gets 17.8% higher because of the increased growth duration (Δt_{RP}), see Eq. (4.2). The driving pressure $(\Delta p = p_\infty - p_b)$ of the collapse is larger when surface tension is neglected in the growth phase because the far-field pressure (p_∞) is higher and the bubble pressure (p_b) is lower. Note that the longer growth duration does not always result in a higher far-field pressure; for example, if the

growth duration exceeded three-quarters of the ultrasound wave period $\left(\frac{3}{4}(T_U)=\frac{3}{4}\left(\frac{1}{f}\right)\approx 25\mu s\right)$ the far-field pressure would be decreasing, see Eq. (4.2).

Here we compare the surface tension term in the RP equation to the driving pressure term (Eq. (5.1)) Considering the significance of the surface tension term $\left(\frac{2\sigma}{\rho_L R}\right)$, we approximate the average quantity of the term for the duration of the growth phase. We take the approximate average radius as the radius that is halfway between the maximum and minimum radius:

$$R=\frac{(R_{\max}+R_{\min})}{2}=\frac{(40.56+10)}{2}\times 10^{-6}\left[\mathrm{m}\right]=25.25\times 10^{-6}\left[\mathrm{m}\right]. \tag{5.3}$$

Thus, the approximate average surface tension term is

$$\frac{2\sigma}{\rho_L R}=\frac{2\times 0.07286\left[\mathrm{N/m}\right]}{1000\left[\mathrm{kg/m^3}\right]\times 25.25\times 10^{-6}\left[\mathrm{m}\right]}=5.771\left[\frac{m}{s}\right]^2 \tag{5.4}$$

Compared to the maximum driving pressure term taken when the acoustic pressure is $p_{\infty,\min}=\left(p_0-p_A\right)=\left(101.325\left[\mathrm{kPa}\right]-200\left[\mathrm{kPa}\right]\right)\approx 100{,}000$ Pa and the bubble pressure is approximately 0 Pa (see Figure 5.1).

$$\frac{p_\infty(t)-p_B(t)}{\rho_L}=\frac{100000\left[\mathrm{Pa}\right]-0\left[\mathrm{Pa}\right]}{1000\left[\mathrm{kg/m^3}\right]}=100\left[\frac{m}{s}\right]^2 \tag{5.5}$$

Thus, the maximum driving pressure term is approximately 17-fold greater than the average surface tension term over the duration of the growth, and, therefore the pressure term is dominant over the surface tension term. However, as previously stated, the surface tension term does significantly influence the growth phase for the case presented.

It is also important to note that the magnitude of the surface tension effect is dependent on the bubble radius, see Eq. (5.1) and Eq. (5.2). Thus, for smaller bubbles, the influence of surface tension is greater and for larger bubbles, the influence of surface tension becomes less.

Table 5.1. The results from the RP growth simulation, where the results are used to initialise the collapse simulation, for the cases with surface tension and without surface tension.

Symbol	Description	Surface tension	No surface tension
Δt_{RP}	Growth duration	14.68 μs	15.16 μs
$R_{\max}$	Maximum bubble radius	40.56 μm	45.11 μm
$p_{RP,B}$	Bubble pressure at $R_{\max}$	1.737 kPa	1.104 kPa
$p_{RP,\infty}$	The far-field acoustic pressure at $R_{\max}$	57.39 kPa	67.59 kPa
$\rho_{RP,B}$	Bubble density at $R_{\max}$	0.02064 kg/m^3	0.01311 kg/m^3
S	Standoff distance - $S = 1.1R_{\max}$	44.62 μm	49.62 μm

The standoff distance, $S = 1.1R_{\max}$, is dependent on the maximum radius $\left(R_{\max}\right)$ so that the distance of the bubble from the wall relative to the size of the pre-collapse bubble is consistent. Because the maximum radius is significantly different for the cases with surface tension $\left(R_{\max} = 40.56\ \mu\text{m}\right)$ and without surface tension $\left(R_{\max} = 45.11\ \mu\text{m}\right)$, the standoff distances also differ significantly: $S = 44.62\ \mu\text{m}$ with surface tension and $S = 49.62\ \mu\text{m}$ without surface tension (see Table 5.1). In a later Chapter (section 6.11), we investigate the influence of the standoff distance, showing that a minor difference in the standoff distance will have negligible influence on the collapse

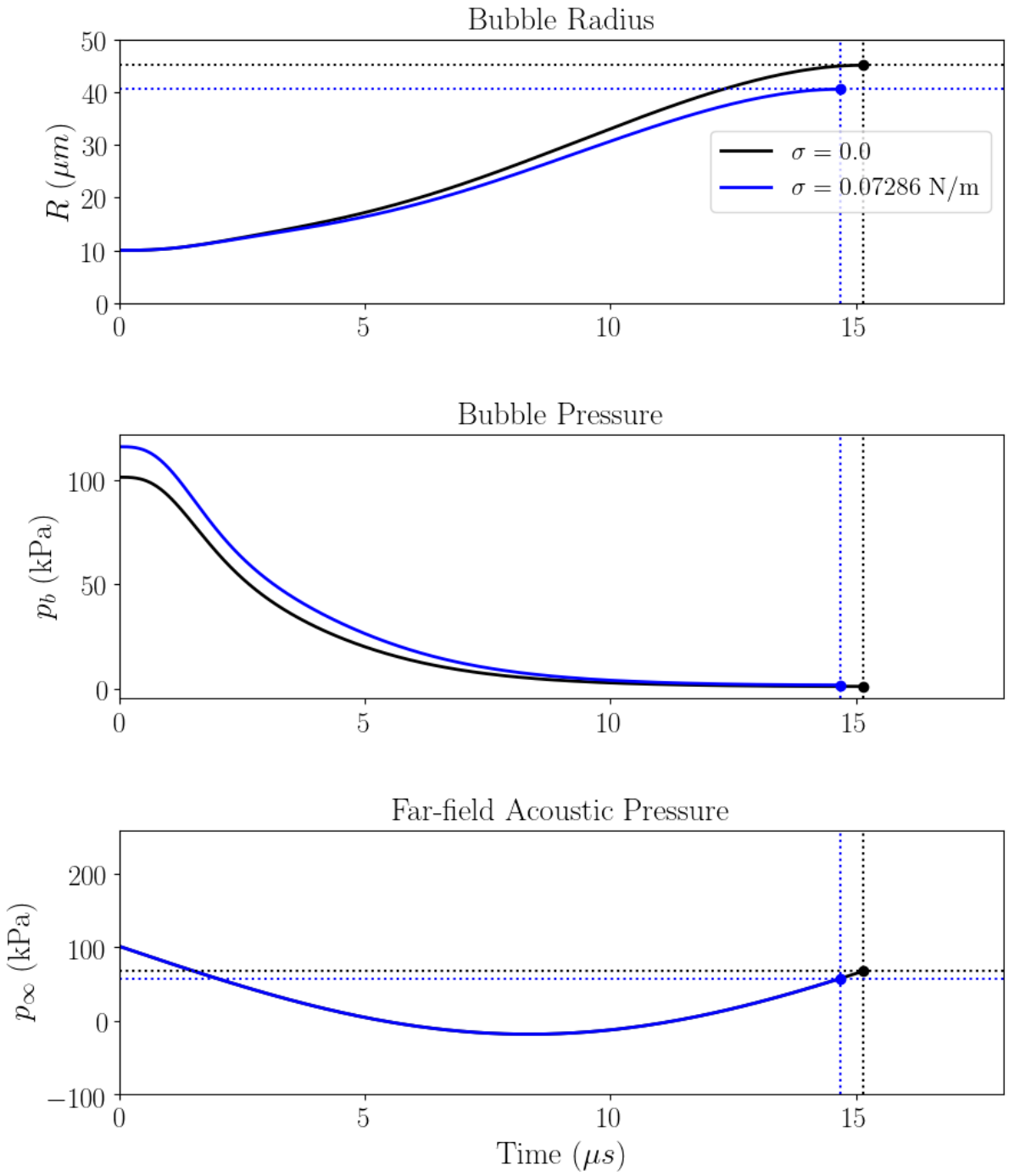

Figure 5.1. Comparison of the results of the RP growth calculation for the cases with and without surface tension. The depiction compares the bubble radius (R), the far-field acoustic pressure (p_∞), and the bubble pressure (p_b) for the duration of the growth phase until the pre-collapse bubble state is reached.

The results for the collapse cases initialised with and without surface tension are depicted in Figure 5.2. Note that these cases are solved in the same manner as the case study in section 4.4, and that the results for the case initialised with surface tension (RPGI) are the same as the results depicted in Figure 4.7.

Neglecting surface tension in the growth resulted in a subsequent collapse that takes longer (approximately 0.2 μs longer) and a wall pressure that is larger (approximately 2 MPa larger), see Figure 5.2a. The collapse duration is shorter for the case that considered surface tension in the growth calculation (RPGI) because of the smaller pre-collapse bubble size (Table 5.1).

The longer growth duration $\left(\Delta t_{RP}\right)$ when surface tension is neglected means that the pre-collapse bubble coincides with a far-field pressure which is approximately 10 kPa higher (Table 5.1), and, subsequently, the far-field pressure is approximately 10 kPa higher for the duration of the collapse, see Figure 5.2b. A higher far-field pressure for the duration of the collapse means a larger pressure is driving the collapse which results in a more violent collapse.

Another contributing factor that causes the collapse to be more violent is the larger growth ratio $\left(R_{\max} / R_0\right)$. The pre-collapse bubble pressure $\left(p_B\right)$ is lower if the bubble grows larger, which means the driving pressure is larger $\left(\Delta p = p_\infty - p_B\right)$, increasing the initial acceleration of the collapse. Additionally, if the bubble grows larger, the bubble also has further to collapse, from $R_{\max}$ to around R_0, where the bubble pressure will be high enough to deaccelerate the collapse. Thus, more momentum develops during the collapse because the bubble has further to collapse (from $R_{\max}$ to around R_0), hence, a more violent collapse.

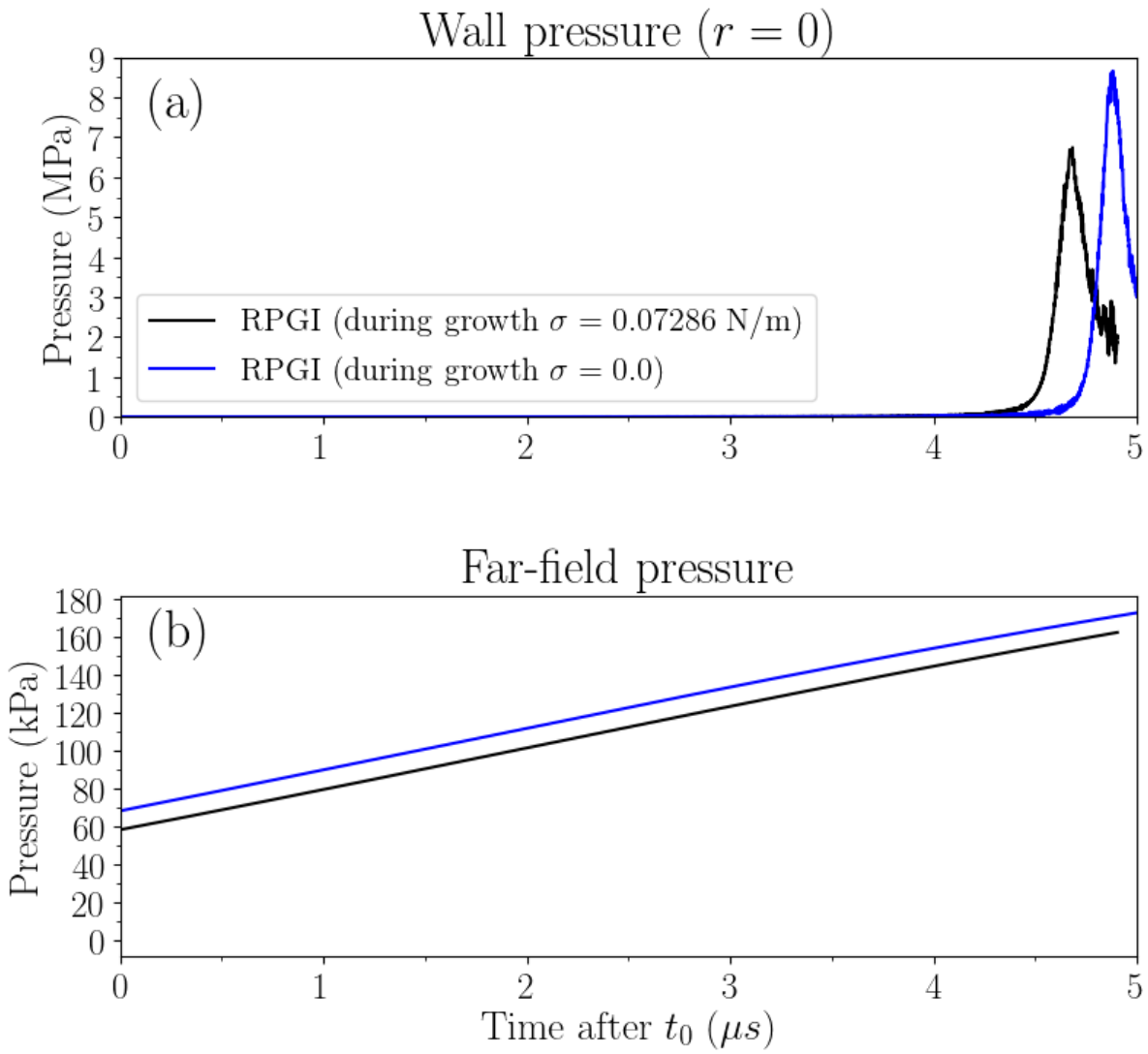

Figure 5.2. Comparison of the collapse results of an acoustically-driven collapse (RPGI) which is initialised with and without surface tension. (a) The pressure at the wall at $r = 0$ and (b) the far-field pressure of the ultrasound field during the collapse simulation.

It was found, for the case presented, that surface tension significantly changed the pre-collapse state. The change in the pre-collapse bubble resulted in a significant change to the subsequent collapse of the bubble, changing the duration of the collapse and the peak pressure experienced by the near-wall.

To determine whether the surface tension significantly influences the bubble growth for a general case it would be of value to compare the RP terms describing surface tension effects and the driving pressure.

If

$$\frac{2\sigma}{R(t)} \ll p_\infty(t) - p_B(t) \quad \text{for} \quad 0 < t < \Delta t_{RP} \tag{5.7}$$

then the influence of surface tension will be negligible. However, $R(t)$ and $p_B(t)$ are typically unknown for the duration of the growth phase. So, to quantify the influence of surface tension for other cases, it would be of greater value to consider the comparison between the pre-collapse bubble state by solving the RP equation with and without the surface tension term to quantify the influence (like we did in Table 5.1).

It is also unclear how sensitive the collapse simulation is to the change in the pre-collapse bubble state. In the next section on the influence of viscosity (section 5.2), we find that slight changes in the pre-collapse bubble state result in negligible changes to the subsequent collapse.

5.2 Viscosity

Here, in a similar fashion to the previous section, we investigate the influence that the existence of viscous effects in the RP growth has on the resulting pre-collapse bubble characteristics and the subsequent bubble collapse dynamics.

To highlight the influence of the presence of viscosity in the RP growth phase, the nonzero viscosity case (RPGI initialised with viscosity - $\mu = 1.002 \times 10^{-3}$ Pa.s) is compared with a zero viscosity case (RPGI initialised without viscosity - $\mu = 0$). The viscous term is only present in Eq. (4.1); this equation is reproduced here

$$\overbrace{R\ddot{R} + \frac{3}{2}\dot{R}^2}^{\text{Inertial terms}} + \overbrace{\frac{4\mu}{\rho_L R}\dot{R}}^{\textbf{Viscous term}} + \overbrace{\frac{2\sigma}{\rho_L R}}^{\text{Surface tension term}} + \overbrace{\frac{p_\infty(t) - p_B(t)}{\rho_L}}^{\text{Driving pressure term}} = 0 \tag{5.8}$$

The difference in the RP growth calculation is only slight when comparing the case with viscosity to the case without viscosity, see Table 5.2 and Figure 5.3. The viscosity increases the growth duration by

0.3 % and decreases the maximum radius of the bubble by 1 %. The reduction in growth is due to the viscous term (Eq. (5.8)) opposing the rate of growth. Considering the significance of the viscous term (see Eq. (5.8)), we approximate the average quantity of the term for the duration of the growth phase. We take the approximate average radius as the radius that is halfway between the maximum and minimum radius:

$$R = \frac{(R_{\max} + R_{\min})}{2} = \frac{(40.56 + 10)}{2} \times 10^{-6}\left[\mathrm{m}\right] = 25.25 \times 10^{-6}\left[\mathrm{m}\right]. \tag{5.9}$$

The average velocity is taken as

$$\dot{R} = \frac{(R_{\max} - R_{\min})}{\Delta t_{RP}} = \frac{(40.56 - 10) \times 10^{-6}\left[\mathrm{m}\right]}{14.68 \times 10^{-6}\left[s\right]} = 2.08\left[\mathrm{m/s}\right]. \tag{5.10}$$

Thus, the approximate average viscous term is

$$\frac{4\mu}{\rho_L R}\dot{R} = \frac{4 \times 1.002 \times 10^{-3}\left[\mathrm{Pa.s}\right]}{1000\left[\mathrm{kg/m^3}\right] \times 25.25 \times 10^{-6}\left[\mathrm{m}\right]} 2.08\left[\mathrm{m/s}\right] = 0.33\left[\frac{m}{s}\right]^2 \tag{5.11}$$

Compared to the maximum driving pressure term taken when the acoustic pressure is $p_{\infty,\min} = \left(p_0 - p_A\right) = \left(101.325\left[\mathrm{kPa}\right] - 200\left[\mathrm{kPa}\right]\right) \approx 100{,}000$ Pa , and the bubble pressure is approximately 0 Pa (see Figure 5.3)

$$\frac{p_\infty(t) - p_B(t)}{\rho_L} = \frac{100000\left[\mathrm{Pa}\right] - 0\left[\mathrm{Pa}\right]}{1000\left[\mathrm{kg/m^3}\right]} = 100\left[\frac{m}{s}\right]^2 \tag{5.12}$$

Thus, the maximum driving pressure term is approximately 300-fold greater than the average viscous term over the duration of the growth, and, therefore the viscous term does *not* significantly influence the growth phase in the case presented.

Table 5.2. The results from the RP growth simulation, where the results are used to initialise the collapse simulation, for the cases with viscosity and without viscosity.

Symbol	Description	Viscosity	No viscosity
Δt_{RP}	Growth duration	14.68 μs	14.72 μs
$R_{\max}$	Maximum bubble radius	40.56 μm	40.97 μm
$p_{RP,B}$	Bubble pressure at $R_{\max}$	1.737 kPa	1.685 kPa
$p_{RP,\infty}$	The far-field acoustic pressure at $R_{\max}$	57.39 kPa	58.23 kPa
$\rho_{RP,B}$	Bubble density at $R_{\max}$	0.02064 kg/m^3	0.02003 kg/m^3
S	Standoff distance - $S = 1.1R_{\max}$	44.62 μm	45.07 μm

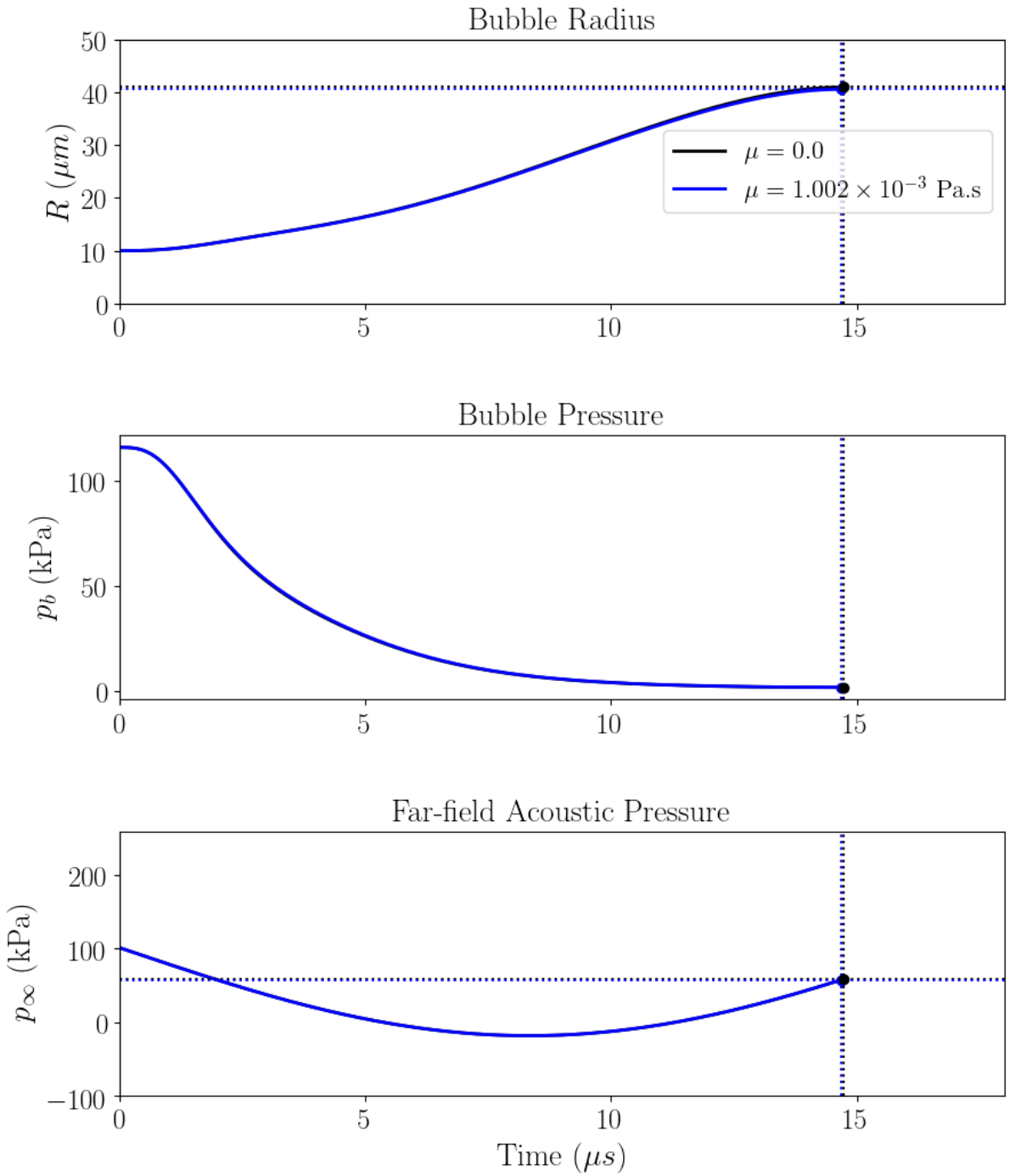

Figure 5.3. Comparison of the results of the RP growth calculation for the cases with and without viscosity. The depiction compares the bubble radius (R), the far-field acoustic pressure (p_∞), and the bubble pressure (p_b) for the duration of the growth phase until the pre-collapse bubble state is reached.

However, it is unclear how sensitive the collapse simulation is to the change in the state of the pre-collapse bubble. To quantify the influence of this small change, 0.3 % increase in growth duration and 1.0 % decrease in the maximum radius of the bubble, has on the collapse simulation, we simulate the

collapse from both pre-collapse bubble states and compare the subsequent pressure experience by the near-wall. Collapse simulation from the pre-collapse bubble determined *without* viscosity resulted in a 3.4 % larger peak wall pressure compared to the collapse from the pre-collapse bubble that considered the viscous effects. Thus, for the case considered, viscosity has negligible influence on the bubble growth and the subsequent collapse. It is also apparent that the collapse simulation is not super sensitive (3.4 % change in peak wall pressure) to slight changes in the initial condition (0.3 % increase in growth duration and 1.0 % decrease in the maximum radius of the bubble).

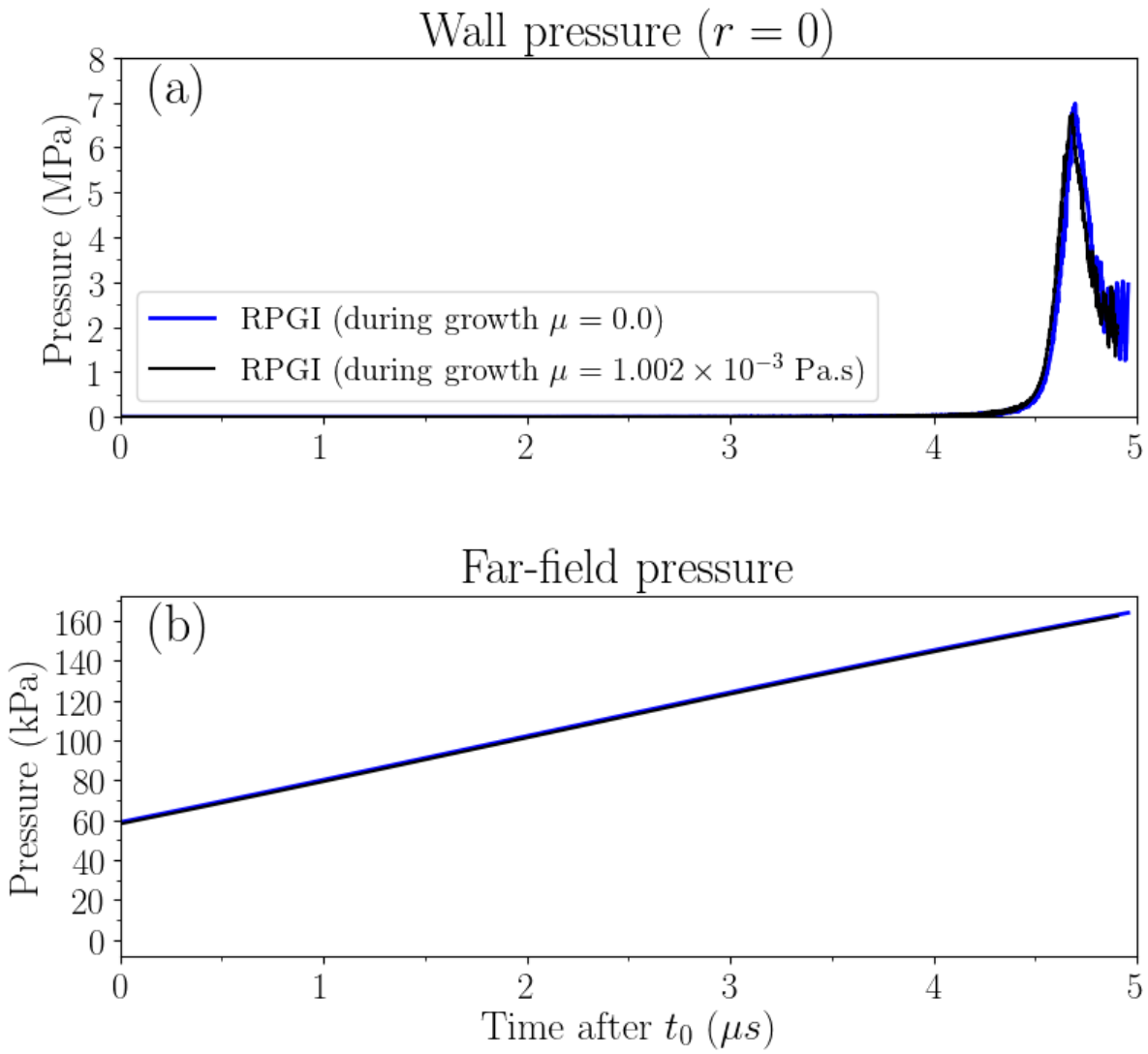

Figure 5.4. Comparison of the collapse results of an acoustically-driven collapse (RPGI) which is initialised with and without viscous effects. (a) The pressure at the wall at $r = 0$ and (b) the far-field pressure of the ultrasound field during the collapse simulation.

5.3 Vapour

In acoustic cavitation applications, the cavitation bubble is typically composed of both air and water vapour. For example, in ultrasonic surface cleaning, the cavities nucleate heterogeneously in the coupling fluid which is typically water, where that water is free to evaporate into the cavity, especially when the water pressure is very low. Air from the solution diffuses (rectified diffusion) from the water into the cavity as the bubble oscillates in a stable manner about an equilibrium bubble size. When the bubble at equilibrium reaches a sufficient size (Blake threshold) it grows to more than twice its initial

size and then collapses abruptly, referred to as transient cavitation, where the bubble no longer oscillates in a stable manner. See section 2.1 for more details.

In the numerical model (Chapter 3) and in the RP growth calculation (RPGI model) we neglect the presence of vapour (section 4.3.1), considering the bubble to be entirely composed of air. The vapour present in the bubble will add additional cushioning to the collapse, in practice the cushioning of the vapour is likely to be insignificant [14, 62]. However, it is not clear how the presence of vapour will influence the growth phase. Here, in a similar fashion to the previous sections, we investigate the influence that the presence of vapour in the bubble has on the RP growth to the pre-collapse bubble and the subsequent bubble collapse near a wall.

In the RP equation, the vapour pressure is included in the equations describing the bubble pressure (Eq. (4.3) and (4.4))

$$p_B = p_{0,a}\left(\frac{R_0}{R}\right)^{3\eta} + p_v \tag{5.14}$$

$$p_{0,a} = p_{atm} - p_v + \frac{2\sigma}{R_0}. \tag{5.15}$$

where p_v is the vapour pressure and $p_{0,a}$ is the initial pressure of the air (which is different from the initial pressure of the bubble $\left(p_{0,B}\right)$). Because the bubble is assumed to be isothermal (constant temperature - $\eta = 1$), the partial pressure of the vapour (vapour pressure) is constant. At 20 ºC, the vapour pressure is $p_v = 2.3388$ kPa [98] and since the bubble is considered to be isothermal (constant temperature) the vapour pressure remains constant. The initial pressure of the bubble $\left(p_{0,B}\right)$ is the sum of the partial pressures

$$p_{0,B} = p_{0,a} + p_v. \tag{5.16}$$

Note that the pressure of the bubble is initially $\left(p_{0,B}\right)$ the same for the case with vapour present and the case without vapour present:

$$p_{0,B} = p_{atm} + \frac{2\sigma}{R_0}. \tag{5.17}$$

The key difference between the two cases (with and without the vapour term included) arises in the later stages of collapse when the bubble is large $\left(R_{\max}\right)$ relative to its initial state $\left(R_0\right)$. This is because the air pressure term $p_{0,a}\left(\frac{R_0}{R}\right)^3$ gets very small and, thus, the bubble pressure $\left(p_B\right)$ gets very low (see Eq. (5.14)). However, when the pressure is included the bubble pressure approaches p_v as the bubble gets large; the vapour pressure acts as a pressure source term in Eq. (5.14).

The difference in the RP growth calculation to determine the pre-collapse bubble state is significant when comparing the case where the vapour is present in the bubble $\left(p_v = 2.3388 \text{ kPa}\right)$ to the case without vapour $\left(p_v = 0\right)$, see Table 5.3 and Figure 5.5. The vapour increases the growth duration by 1.8 % and increases the maximum size of the bubble by 5.0 %. This is due to the vapour pressure significantly increasing the bubble pressure $\left(p_B\right)$ as the bubble gets large during the growth, see Figure 5.5. The increase in the bubble pressure as the bubble grows results in an increase in the driving pressure term $\left(p_\infty - p_B\right)$. The increased driving pressure causes the bubble to grow for a longer duration $\left(\Delta t_{RP}\right)$ to a larger size $\left(R_{\max}\right)$.

Table 5.3. The results from the RP growth simulation, where the results are used to initialise the RPGI collapse simulation, for the cases with and without vapour present in the bubble.

Symbol	Description	Vapour	No vapour
Δt_{RP}	Growth duration	14.94 µs	14.68 µs
$R_{\max}$	Maximum bubble radius	42.59 µm	40.56 µm
$p_{RP,B}$	Bubble pressure at $R_{\max}$	1.470 kPa	1.737 kPa
$p_{RP,\infty}$	The far-field acoustic pressure at $R_{\max}$	63.04 kPa	57.39 kPa
$\rho_{RP,B}$	Bubble density at $R_{\max}$	0.01783 kg/m^3	0.02064 kg/m^3
S	Standoff distance - $S = 1.1R_{\max}$	46.84 µm	44.62 µm

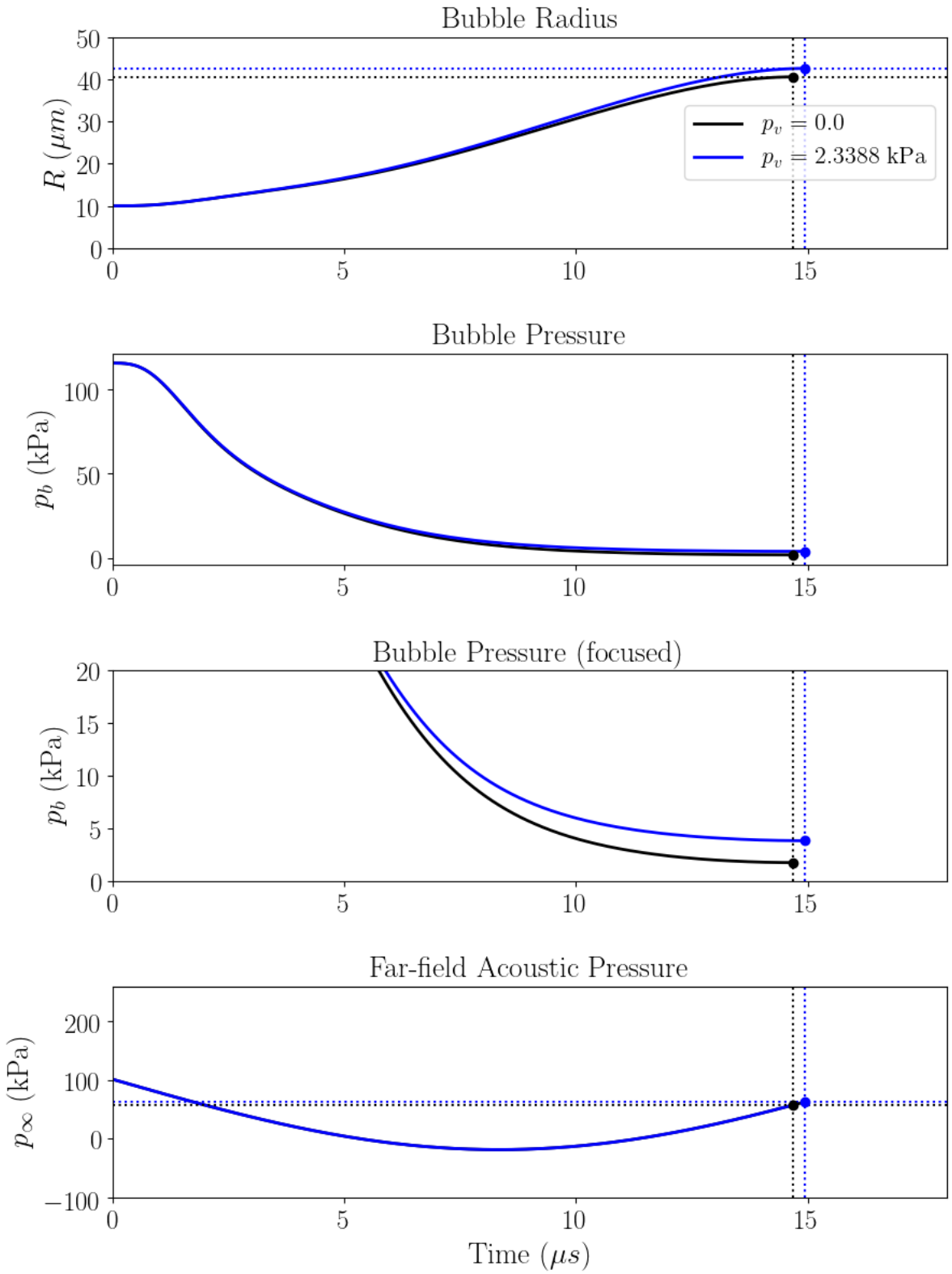

Figure 5.5. Comparison of the results from the RP growth calculation for the cases with and without vapour present in the bubble. The depiction compares the bubble radius (R), the far-field acoustic pressure (p_∞), and the bubble pressure (p_b) for the duration of the growth phase until the pre-collapse bubble state is reached.

It is important to note that the bubble pressure at pre-collapse state $\left(p_{RP,B}\right)$ in Table 5.3 does not include the vapour pressure; it is only the partial pressure of the air in the bubble $\left(p_{RP,B} = p_{0,a}\left(\frac{R_0}{R_{\max}}\right)^3\right)$. This is because the numerical collapse model is unable to capture the presence of vapour and would require modification of the governing equations (Eqs. (2.1)-(2.5)) to be able to consider the presence of vapour. So, we only present the partial pressure of the air in the bubble because this is what is required for the initialisation of the RPGI collapse model. The pressure of the bubble after the bubble growth using the RP equation is $\left(p_{RP,B} + p_v\right) = \left(1.470\ [\text{kPa}] + 2.3388\ [\text{kPa}]\right) \approx 3.809$ kPa .

It is of interest to compare the vapour pressure $\left(p_v\right)$ to the partial pressure of the air at the bubbles maximum size $\left(p_{RP,B}\right)$ to analyse the significance of the presence of vapour in the RP growth calculation. If we assume that the vapour pressure is much less than the initial pressure of the bubble $\left(p_v \ll p_{0,B}\right)$, the initial partial pressure of the air will be approximately

$$p_{0,a} = p_{atm} + \frac{2\sigma}{R_0} = 101.325[\text{kPa}] + \frac{2 \times 0.07286[\text{N/m}]}{10 \times 10^{-6}[\text{m}]} \approx 116 \text{ kPa} \tag{5.19}$$

If the maximum size of the bubble is $R_{\max} \approx 41\ \mu$m , then the partial pressure of the air in the bubble at the maximum size (pre-collapse state) is

$$p_{RP,B} = p_{0,a}\left(\frac{R_0}{R_{\max}}\right)^3 = 116[\text{kPa}]\left(\frac{10\ [\mu\text{m}]}{41\ [\mu\text{m}]}\right)^3 \approx 1.68 \text{ kPa} \tag{5.20}$$

With the estimated partial pressure of air becoming lower than the vapour pressure at the later stages of the growth, it is not surprising that the presence of vapour significantly influences the growth phase for the case presented. The influence of vapour would become more significant for larger growth ratios $\left(R_{\max}/R_0\right)$ because of the reduction in the partial pressure of air in the bubble (Eq. (5.20)). If the bubble is considered to be entirely composed of air the bubble pressure $\left(p_B\right)$ approaches 0 Pa as the growth ratio becomes very large $\left(R_{\max}/R_0\right)$; however, if the bubble vapour is considered (the bubble is

composed of both vapour and air) then as the growth ratio becomes very large $\left(R_{\max}/R_0\right)$ then the bubble pressure $\left(p_B\right)$ approaches p_v. With this in mind, the maximum influence of the vapour is limited by the amount it changes the driving pressure term in the growth calculation $\left(p_\infty(t)-p_B(t)\right)$. Comparing the maximum possible change to the driving pressure term during the growth for the air bubble case and the air-vapour bubble case occurs when the bubble ratio is very large; thus, the driving pressures differ from $p_\infty(t)$ to $p_\infty(t)-p_v$. The maximum magnitude in driving pressure during the growth phase is $p_\infty = p_0 - p_A$. For our case, the largest driving pressure is $p_\infty = p_0 - p_A = 101.325[\text{kPa}] - 200[\text{kPa}] \approx -100$ kPa, and, therefore the maximum possible change to the driving pressure term by considering the presence of vapour would be

$$\frac{\left|\left(p_\infty - p_B\right)-\left(p_\infty - p_B\right)\right|}{\left|\left(p_\infty - p_B\right)\right|} = \frac{\left|\left(p_\infty - 0\right)-\left(p_\infty - p_v\right)\right|}{\left|\left(p_\infty - 0\right)\right|} = \frac{|p_v|}{|p_\infty|} = \frac{2.3388[\text{kPa}]}{100[\text{kPa}]} = 2.3\% . \qquad (5.21)$$

Therefore, as the pressure amplitude increases $\left(p_A\right)$, the influence of the vapour pressure becomes less significant.

For the opposite case, when the pressure amplitude is $\left(p_A\right)$ low, the growth ratio $\left(R_{\max}/R_0\right)$ will be low because of the reduced pressure difference driving the growth. If the growth ratio $\left(R_{\max}/R_0\right)$ is low then the bubble pressure is less significantly influenced by the vapour pressure. For example, if the bubble pressure is expressed in terms of the atmospheric pressure $\left(p_{atm}\right)$, vapour pressure $\left(p_v\right)$, and the surface tension component

$$p_B = \left(p_{atm} + \frac{2\sigma}{R_0} - p_v\right)\left(\frac{R_0}{R}\right)^{3\eta} + p_v . \qquad (5.22)$$

Consider the case when the acoustic pressure amplitude is reduced to about 43.6 kPa, resulting in bubble growth from $R_0 = 10\ \mu$m to $R_{\max} = 12\ \mu$m; the bubble pressure at the maximum radius is then

$$p_B = \left(101.325[\text{kPa}] + \frac{2(0.07286)}{20\times10^{-6}}\times10^{-3}[\text{kPa}] - 2.3388[\text{kPa}]\right)\left(\frac{10}{12}\right)^{3\times1.4} + 2.3388[\text{kPa}] \approx 51.75 \text{ kPa} \tag{5.23}$$

with the vapour pressure term included. Without the vapour pressure term included, the bubble pressure at the maximum radius is

$$p_B = \left(101.325[\text{kPa}] + \frac{2(0.07286)}{20\times10^{-6}}\times10^{-3}[\text{kPa}]\right)\left(\frac{10}{12}\right)^{3\times1.4} \approx 50.5 \text{ kPa}\,. \tag{5.24}$$

Thus, for this low pressure amplitude (P_A) case, the exclusion of the vapour pressure term results in a maximum change in bubble pressure of approximately 2.4 %.

So, in general, the influence of the water vapour pressure on the bubble growth is limited: the influence of the vapour becomes less significant for low pressure amplitudes (p_A) and less significant for high pressure amplitudes (p_A). However, the influence of vapour may become more significant if the bubble is at a higher temperature during the growth phase because the vapour pressure of water approaches 1 atm at 100 ºC.

For the cases considered, the subsequent wall pressure experienced by the wall is 13.8 % larger for the case considering the presence of vapour during the growth, see Figure 5.6. This is due to the presence of vapour increasing in the size of the pre-collapse bubble and the increased far-field pressure at the beginning to collapse phase because of the longer growth duration, see Table 5.3. The presence of vapour is expected to cushion the collapse phase due to the vapour pressure in the bubble, but, as previously discussed, we are unable to capture the influence of the vapour present in the bubble in the collapse model.

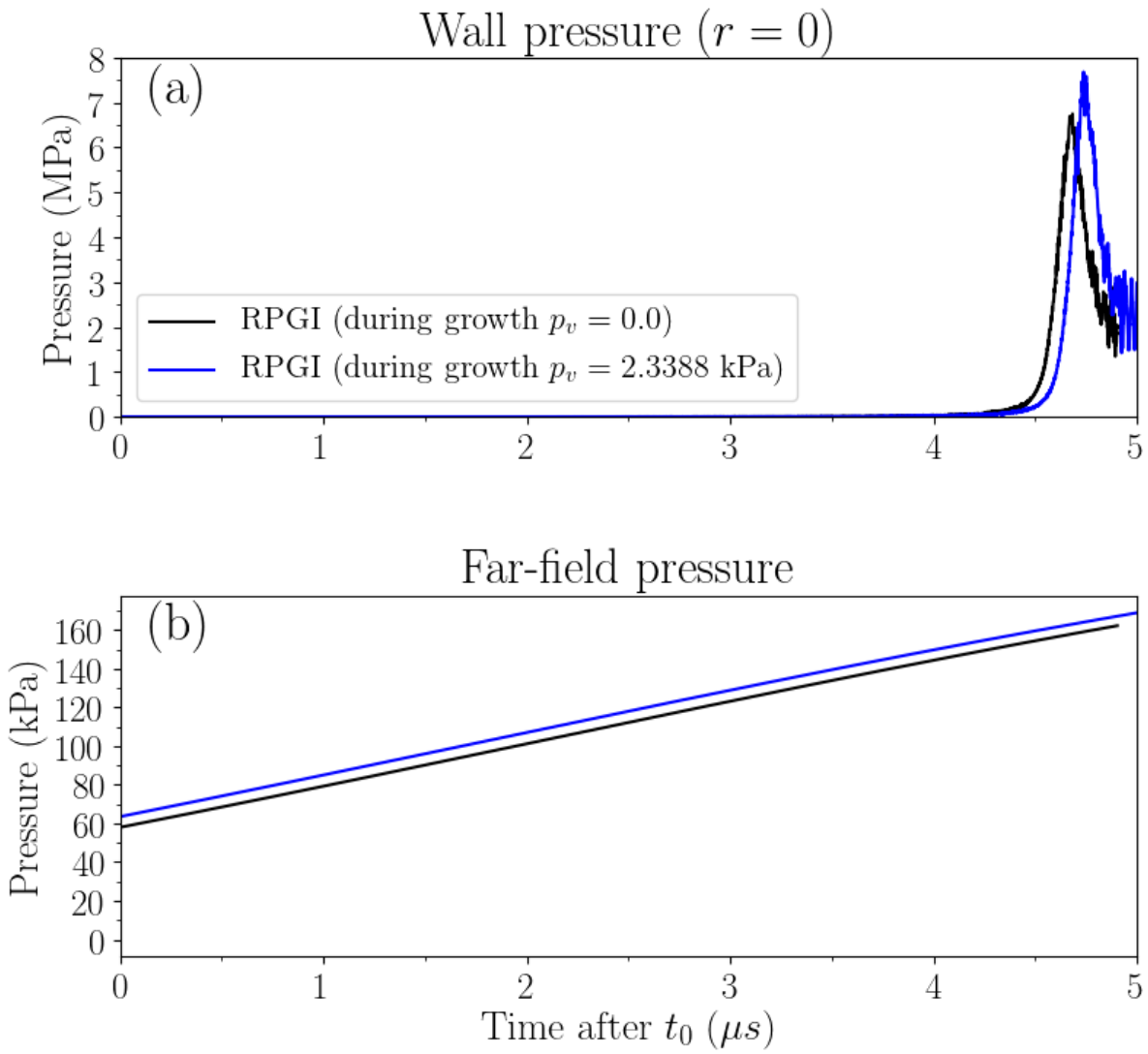

Figure 5.6. Comparison of the collapse results of an acoustically-driven collapse (RPGI) which is initialised with and without vapour present in the bubble for the RP growth calculation. (a) The pressure at the wall at $r = 0$ and (b) the far-field pressure of the ultrasound field during the collapse simulation.

5.4 The compressibility of the surrounding fluid

The RPGI model does *not* consider the effects of compressibility in the surrounding fluid in the growth calculation: the RP equation assumes the surrounding fluid is incompressible. However, the RPGI model does consider the surrounding fluid as compressible because at the later stages of the collapse high fluids velocities and large pressures occur, and shocks may be emitted. But, during the growth phase, the velocity of the fluid is not anticipated to be large enough (approaching the speed of sound) for compressibility effects to be significant. To confirm this prediction and assumption, we investigate

the compressibility effects of the surrounding fluid during the growth phase. This is done by comparing the RP growth calculation to the growth simulating using the Gilmore equation that captures the effects of compressibility in the surrounding liquid.

The Gilmore equation, which captures the effects of fluid compressibility, including shocks, is considered the most comprehensive compressible 1D spherical bubble model [15, 99-101]:

$$\left(1-\frac{\dot{R}}{c}\right)R\ddot{R}+\frac{3}{2}\left(1-\frac{\dot{R}}{3c}\right)\dot{R}^2=\left(1+\frac{\dot{R}}{c}\right)H+\frac{R}{c}\left(1-\frac{\dot{R}}{c}\right)\dot{H} \tag{5.25}$$

$$H=n\left(\frac{p_\infty+B}{(n-1)\rho}\right)\left[\left(\frac{p+B}{p_\infty+B}\right)^{\frac{n-1}{n}}-1\right] \tag{5.26}$$

$$c=c_\infty\left[\left(\frac{p+B}{p_\infty+B}\right)^{\frac{n-1}{2n}}\right] \tag{5.27}$$

$$p=p_0\left(\frac{R_0}{R}\right)^{3\eta}+p_v-\frac{2\sigma}{R}-4\mu\frac{\dot{R}}{R} \tag{5.28}$$

$$c_\infty=\left[n\left(\frac{p_\infty+B}{\rho}\right)\right]^{\frac{1}{2}} \tag{5.29}$$

where R is the bubble radius, ρ is the water density, p_∞ is the far-field acoustic pressure, p_0 is the initial pressure of the air in the bubble, p_v is the vapour pressure (we assume there is no vapour present in this study), R_0 is the initial radius of the bubble, η is the polytropic index (varies from 1 (isothermal) to 1.4 (adiabatic)), H is the enthalpy difference between the liquid at pressure p and p_∞, and c_∞ is the speed of sound in water infinitely far away from the bubble. The parameters $B=3000$ atm and $n=7$ are used to determine the local speed of sound (c) and the enthalpy [101].

The RP growth calculation was compared to the Gilmore bubble growth calculation, see Figure 5.7. The Gilmore equation resulted in insignificant differences in the pre-collapse bubble state, making the

growth duration $\left(\Delta t_{RP}\right)$ 0.2 % shorter and the pre-collapse bubble radius $\left(p_{RP,B}\right)$ 0.1 % smaller, see Table 5.4. With no significant change to the pre-collapse bubble, the subsequent collapse will not change significantly. Thus, the influence of the compressibility effects of the surrounding fluid for the growth phase is negligible as expected.

Table 5.4. The results from the RP growth simulation compared to the results from the Gilmore growth simulation, where the Gilmore equation considers the effects of compressibility in the surrounding liquid.

Symbol	Description	Gilmore Eq.	RP Eq.
Δt_{RP}	Growth duration	14.65 µs	14.68 µs
$R_{\max}$	Maximum bubble radius	40.53 µm	40.56 µm
$p_{RP,B}$	Bubble pressure at $R_{\max}$	1.74 kPa	1.737 kPa
$p_{RP,\infty}$	The far-field acoustic pressure at $R_{\max}$	56.78 kPa	57.39 kPa
$\rho_{RP,B}$	Bubble density at $R_{\max}$	0.02068 kg/m^3	0.02064 kg/m^3
S	Standoff distance - $S = 1.1R_{\max}$	44.58 µm	44.62 µm

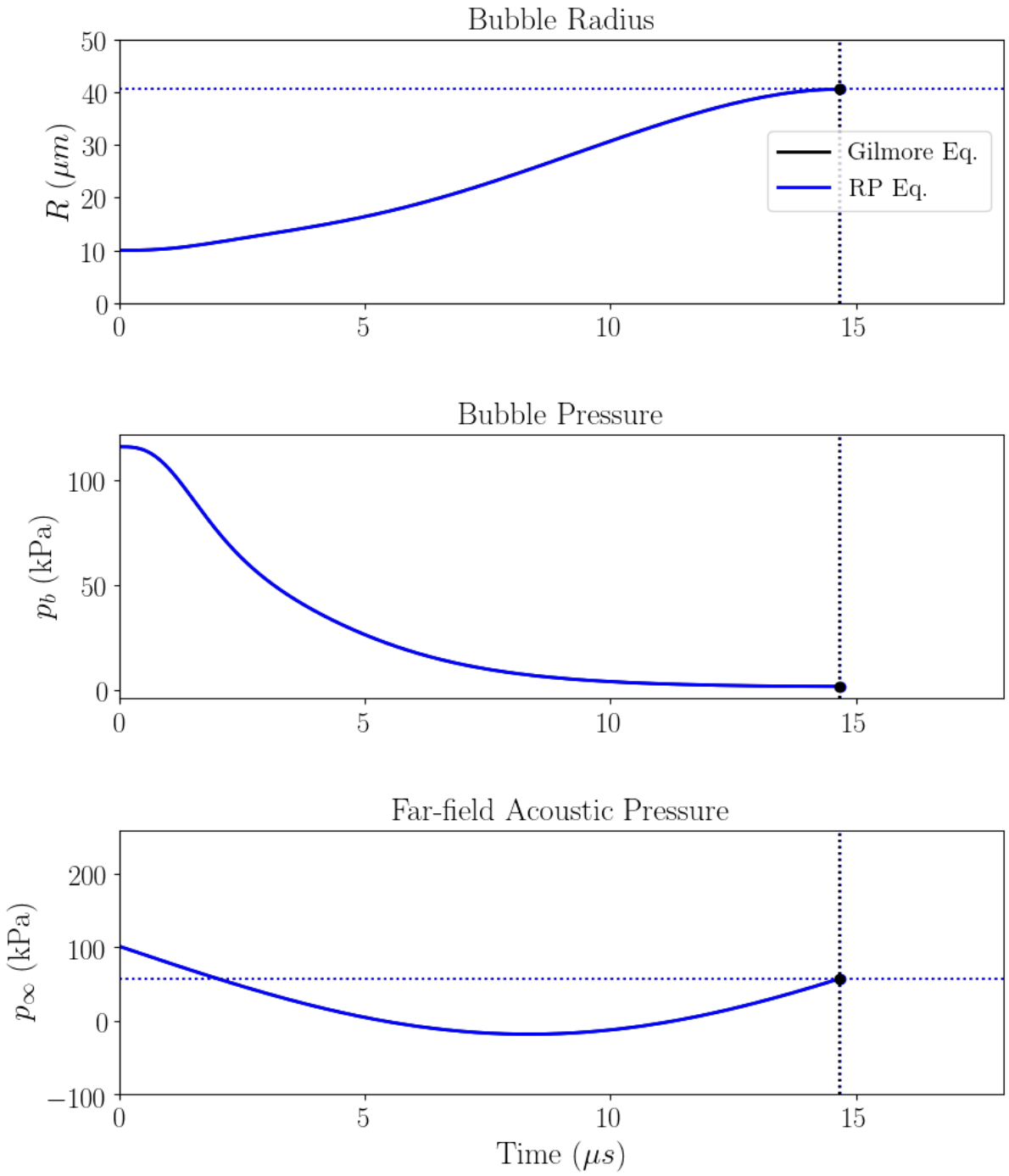

Figure 5.7. Comparison of the results of the RP growth calculation to the Gilmore growth calculation, where the Gilmore equation considers the effects of compressibility in the surrounding liquid. The depiction compares the bubble radius (R), the far-field acoustic pressure (p_∞), and the bubble pressure (p_b) for the duration of the growth phase until the pre-collapse bubble state is reached.

5.5 The polytropic growth assumption (isothermal vs adiabatic)

The importance of the use of the correct assumption, adiabatic or isothermal, on the bubble growth is investigated. The RP equation assumes that the behaviour of the gas in the bubble is polytropic [14], where the bubble pressure is described by Eq. (4.3) which is reproduced here

$$p_B = p_{0,B}\left(\frac{R_0}{R}\right)^{3\eta} \tag{5.31}$$

The limits of the polytropic air bubble growth parameter (η) are $\eta = 1$ (isothermal) and $\eta = 1.4$ (adiabatic) [14, 15]. The isothermal assumption implies that the bubble temperature remains constant during the growth. The adiabatic assumption implies that there is no heat conduction from the bubble to the surrounding liquid during the growth. Therefore, the choice of the assumption depends on the rate of heat conduction between the bubble and the surrounding fluid and the growth duration. However, we do not investigate which assumption (adiabatic or isothermal) is more applicable here.

We seek to determine if the change in heat conduction assumption, from adiabatic to isothermal, results in significant changes to the pre-collapse state of the bubble and the subsequent collapse. If the change is significant, then the choice of the heat conduction assumption during the growth phase becomes important.

The results from the two RP growth cases, adiabatic and isothermal, are provided in Table 5.5 and Figure 5.8, where the state of the pre-collapse bubble is significantly different. The isothermal growth results in a 3.7 % longer growth duration (Δt_{RP}) and a 18.2% larger maximum bubble radius $(R_{\max})$ than the adiabatic growth (Figure 5.8 and Table 5.5). This is because the adiabatic bubble pressure (p_B) reduces at an increased rate with increasing bubble size (R)

$$p_B = p_{0,B}\left(\frac{R_0}{R}\right)^{4.2} \tag{5.32}$$

compared to the isothermal bubble

$$p_B = p_{0,B}\left(\frac{R_0}{R}\right)^3. \tag{5.33}$$

Subsequently, the pressure is higher for most of the growth phase of the isothermal case even with the larger bubble size, see Figure 5.8. The pressure of the pre-collapse isothermal bubble is approximately 1.7 times higher than the adiabatic bubble, see Table 5.5. Because of the larger pre-collapse bubble size $\left(R_{\max}\right)$ in the isothermal, the density is 40 % lower (Table 5.5). The far-field pressure is 23 % higher for the isothermal case because the growth duration is longer and the pre-collapse bubble state coincides with a larger acoustic far-field pressure, see Figure 5.8 and Table 5.5.

Table 5.5. Comparison of the pre-collapse state determined using the RP growth simulation use the adiabatic bubble assumption and the isothermal bubble assumption. Note that these results are used to initialise the collapse simulations to compare the behaviour of the bubble collapse (Figure 5.9).

Symbol	Description	RP adiabatic	RP isothermal
Δt_{RP}	Growth duration	14.15 µs	14.68 µs
$R_{\max}$	Maximum bubble radius	34.32 µm	40.56 µm
$p_{RP,B}$	Bubble pressure at $R_{\max}$	0.653 kPa	1.737 kPa
$p_{RP,\infty}$	The far-field acoustic pressure at $R_{\max}$	46.53 kPa	57.39 kPa
$\rho_{RP,B}$	Bubble density at $R_{\max}$	0.03406 kg/m^3	0.02064 kg/m^3
S	Standoff distance - $S = 1.1R_{\max}$	37.75 µm	44.62 µm

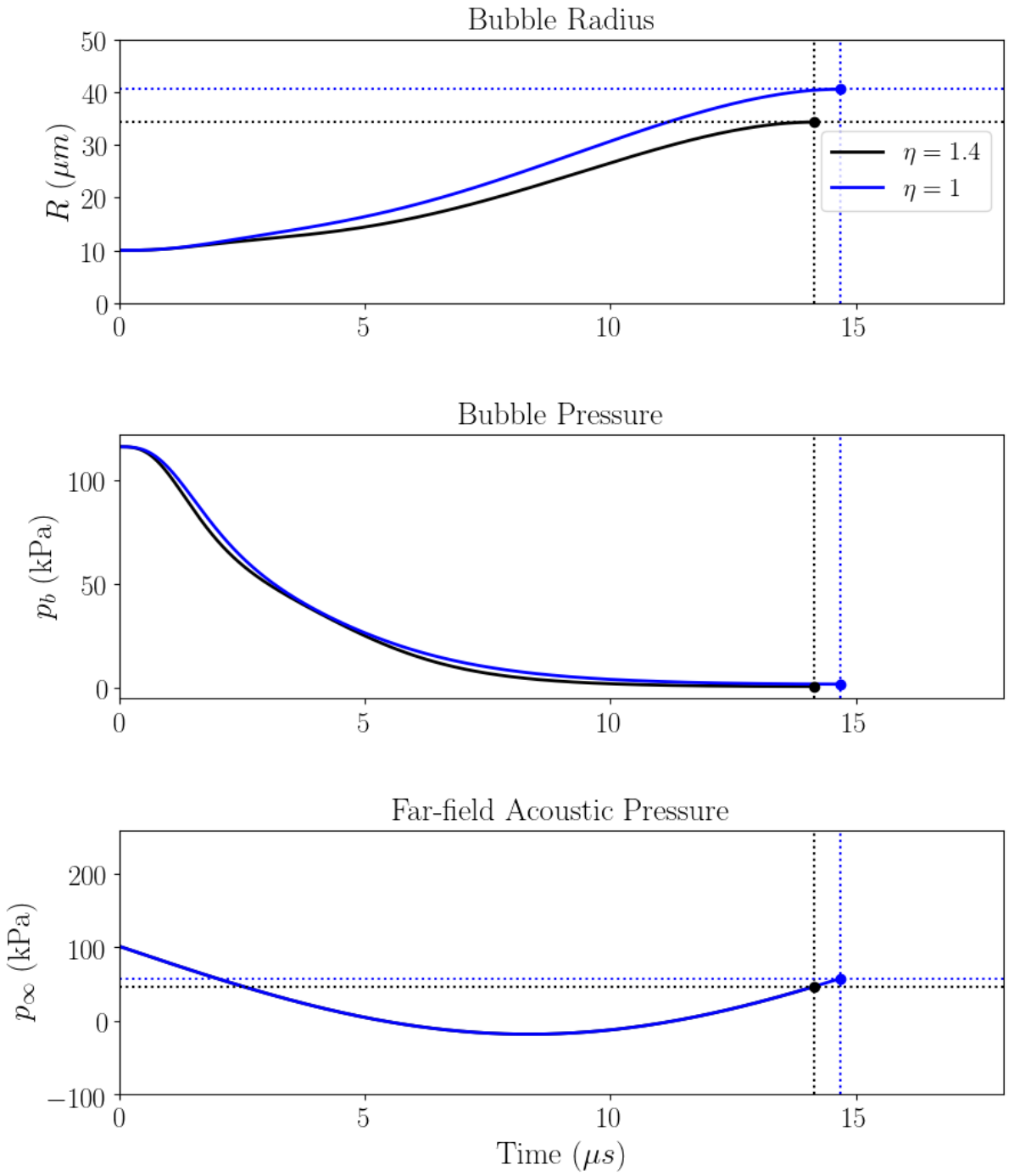

Figure 5.8. The results of the RP growth calculation using the adiabatic assumption $(\eta = 1.4)$ compared to the isothermal bubble assumption $(\eta = 1)$. The depiction compares the bubble radius (R), the far-field acoustic pressure (p_∞), and the bubble pressure (p_b) for the duration of the growth phase until the pre-collapse bubble state is reached.

The pressure experienced by the wall after RPGI collapse is presented comparing the result given by the adiabatic growth assumption and the isothermal growth assumption, see Figure 5.9. The duration of the collapse is much shorter (~0.5 μs) in the adiabatic growth case compared to the isothermal growth case due to the smaller pre-collapse bubble size $\left(R_{\max}\right)$, Figure 5.9b

The peak wall pressure is very similar, with the isothermal growth case resulting in a peak pressure that is 1.5 % larger in the adiabatic growth case (Figure 5.9). This is interesting because, given the larger initial bubble size $\left(R_{\max}\right)$ and the higher far-field pressure (~10 kPa) for the duration of the collapse (Figure 5.9b) in the isothermal growth case, it would be expected to result in a more violent collapse. The only factor contributing to reducing the rate of growth in the isothermal case is that the bubble pressure is initially higher (1.737 kPa compared to 0.653 kPa - Table 5.5), but this ~1 kPa change in pressure does not offset the ~10kPa higher far-field pressure when considering the driving pressure $\left(\Delta p = p_{\infty} - p_{B}\right)$. Thus, it does not explain why the peak pressure in the isothermal growth case is lower than expected: it is expected to result in a significantly larger peak pressure than the adiabatic growth case

One explanation for the reduced peak pressure for the isothermal case is due to a limitation in the numerical model. The numerical method uses a diffuse interface between the fluids (the bubble air and the surrounding water), and in time the interface diffused numerically reducing the sharpness of the bubble interface. The influence of the interface sharpness is investigated later in this thesis in section 6.12. The reduction in sharpness cushions the collapse, reducing the peak pressure experienced by the wall. In the isothermal growth case, the collapse duration is significantly longer than the adiabatic growth case resulting in more numerical diffusion of the interface. Therefore, this increased diffusion may account for the reduction in the peak wall pressure from the anticipated peak wall pressure.

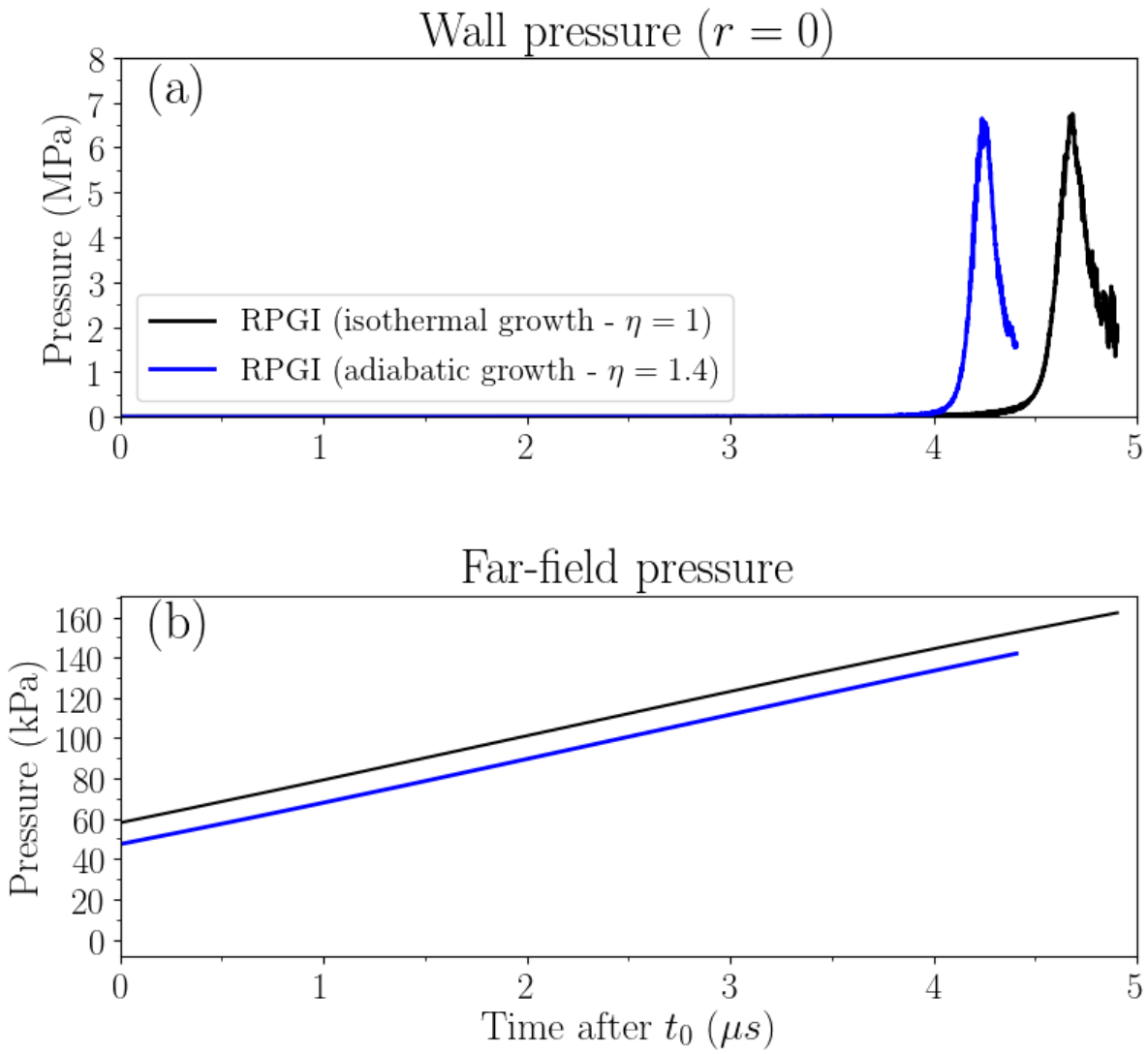

Figure 5.9. Comparing the collapse results of an acoustically-driven collapse (RPGI) cases where we consider the bubble growth to be isothermal and adiabatic. (a) The pressure at the wall at $r = 0$ and (b) the far-field pressure of the ultrasound field during the collapse simulation.

5.6 Summary

The RPGI model provided a valuable tool to investigate the effects on the growth phase and the subsequent collapse because of the simplicity of the RP growth calculation. Approximating the growth using the RP equation allowed the effects during growth like surface tension, the presence of vapour, viscous effects, surrounding fluid compressibility, and heat transfer (adiabatic vs isothermal growth) to be considered, investigating their significance on the growth and the subsequent collapse of the bubble.

The two key values determined from the growth calculation that changed the violence of the subsequent collapse are (1) the growth ratio $\left(R_{\max}/R_0\right)$ (2) growth duration $\left(\Delta t_{RP}\right)$. A larger growth ratio $\left(R_{\max}/R_0\right)$ typically results in a more violent collapse of the bubble because the pre-collapse bubble pressure $\left(p_B\right)$ is lower and because the collapse distance is greater, from $R_{\max}$ to R_0. The lower bubble pressure means the bubble pressure opposing the collapse is lower and, therefore, the pressure difference driving the collapse will be larger $\left(p_\infty - p_B\right)$. The greater collapse distance, from $R_{\max}$ to R_0, means more momentum develops in the surrounding fluid during the collapse, hence, a more violent collapse.

Another contributing factor to the violence of the collapse is the far-field pressure over the duration of the collapse. The far-field pressure over the duration of the collapse is not the same in all cases because the acoustic pressure changes in time (the pressure changes approximately sinusoidally). The far-field pressure over the duration of the collapse, therefore, depends on the bubble growth duration $\left(\Delta t_{RP}\right)$ and the parameters of the acoustic pressure: frequency $\left(f\right)$ and pressure amplitude $\left(p_A\right)$. In the cases considered, a longer growth duration resulted in a larger far-field pressure during the collapse phases, resulting in a more violent collapse. It is important to note that the larger growth duration $\left(\Delta t_{RP}\right)$ may result in a far-field pressure that is lower if it exceeds three-quarters of the ultrasound wave period $\left(3T_U/4\right)$ where the far-field pressure begins to decrees. This would result in a lower driving pressure and a less violent collapse.

For the cases considered, the influence of surface tension, vapour, and heat transfer during the growth phase were found to affect the growth and the subsequent collapse significantly. However, the influence of viscous effects and the compressibility effects of the surrounding fluid had an insignificant effect on the growth and the subsequent collapse.

Surface tension acts against the bubble growth resulting in a smaller pre-collapse bubble size $\left(R_{\max}\right)$ and a shorter growth duration $\left(\Delta t_{RP}\right)$. Thus, the surface tension in the growth phase resulted in a less

violent collapse because of the shorter collapse distance, from $R_{\max}$ to R_0, a high initial bubble pressure $\left(p_{RP,B}\right)$, and a lower far-field pressure for the duration of the collapse.

The influence of the presence of vapour in the bubble during the growth phase significantly changed the growth duration $\left(\Delta t_{RP}\right)$ and the growth ratio $\left(R_{\max}/R_0\right)$ by increasing the pressure difference driving the growth at the later stages of the growth phase. As a result, the presence of vapour significantly changed the subsequent bubble collapse.

The influence of the heat transfer of the bubble during the growth phase resulted in significant changes to the growth ratio $\left(R_{\max}/R_0\right)$ and the growth duration $\left(\Delta t_{RP}\right)$. The adiabatic case (no heat transfer from the bubble) resulted in a smaller growth ratio $\left(R_{\max}/R_0\right)$ and a shorter growth duration $\left(\Delta t_{RP}\right)$ than the isothermal case (constant bubble temperature). This is because the adiabatic bubble pressure reduces faster as the bubble grows and, therefore, the bubble pressure that drives the growth is less.

Despite these findings, the driving pressure and the inertial terms are still dominant (Eq. (5.1)) and the primary contributor to the driving pressure is the acoustic pressure (as opposed to the bubble pressure). So, the effects studied in the Chapter may significantly influence the bubble dynamics, but they are not the primary concern. Neglecting surface tension, the presence of vapour, and assuming an adiabatic bubble during the growth phase are still reasonable assumptions. However, these assumptions may impair the accuracy of the results.

Chapter 6

Simulation of the Acoustically-driven Bubble Growth and Collapse (ADGC model)

6.1 Abstract

With a single exception [4, 37], previous fully-compressible models of bubble collapse do *not* include the growth phase; they only model the collapse phase beginning with a perfectly spherical bubble at its maximum size. This Chapter introduces a model that models the near-wall growth of the bubble in axisymmetric cylindrical coordinates, before the collapse, so that when the bubble is at its maximum volume at the instant the collapse phase begins (pre-collapse state). The bubble is no longer constrained to being spherical prior to the collapse, and, therefore, better represents the physics of a near-wall bubble collapse.

A high-order accurate, fully compressible, multiphase model is used to simulate the acoustically-driven growth and collapse of a gas bubble in water. The model is used to investigate the growth of a near-wall bubble and the subsequent collapse when the bubble is positioned in an acoustic field. The growth phase of the near-wall bubble is studied: the influences of the wall and the acoustic field are investigated. The near-wall is found to significantly restrict the growth of the bubble, with decreasing influence as the bubble standoff distance from the wall is increased. The variation in the standing pressure wave of the acoustic field is also found to be an important consideration, as a reduction in the acoustic driving pressure results in less bubble growth and subsequently a less violent collapse.

The model is compared to the previously developed models that are able to capture the collapse of a near-wall bubble, (1) the Rayleigh growth and collapse and (2) the RPGI model, highlighting the limitations of the previously developed models. The newly developed acoustically-driven bubble model is a significant contribution to the field as it enables the direct simulation of the growth and collapse of

a near-wall bubble in an acoustic field. The model captures the compressibility of the fluids, subsequent shocks, and a physically correct representation of the acoustic input via the use of an immersed moving boundary that represents the active face of the ultrasound transducer face.

6.2 Introduction: Numerical Modelling Bubble Growth and Collapse of a near-wall bubble

The first fully compressible model to capture the collapse of a bubble in an acoustic field was recently developed, which we refer to as the RGPI model (see Chapter 3). The collapse of the bubble occurs in an acoustic field, where the acoustic field is produced by an immersed moving boundary that represents the oscillation of the ultrasound transducer face. The RPGI model uses the Rayleigh-Plesset (RP) equation to capture the growth phase of the bubble which provides the approximation of the initial state of the bubble at the beginning of the collapse. The RP equation assumes the bubble is an infinite body of water, so the main limitation of the RP initialisation (RPGI model) is that it assumes that the bubble growth is uninfluenced by the near-wall.

To the author's knowledge, the studies by Chahine [4, 37] are the only fully-compressible studies that directly simulate the growth and collapse of a bubble near a wall. All of the other studies of bubble collapse consider the bubble to be spherical at the moment that collapse begins. However, it is seen in experiments studies [17, 91] (see Figure 1.2) and in numerical studies [4, 37] that a near-wall bubble deviates from the spherical shape during the growth.

In the studies by Chahine [4, 37] that capture the near-wall bubble growth and collapse, they initialised the bubble at a higher pressure than the surrounding liquid, resulting in the growth and collapse of the bubble. However, this model is not able to represent an acoustically-driven bubble because an acoustically-driven bubble is driven by a transient pressure field: a simple initial pressure difference cannot correctly represent the conditions of the bubble in a transient acoustic field.

The field lacks a model that is able to capture both the growth and collapse of a bubble near a wall in an acoustic field. In previous works, the influence of the growth phase on the collapse is often overlooked: the previous studies consider the bubble collapse occurs from an assumed initial state of the bubble that is not derived from knowledge of the bubble growth prior to the collapse [18, 19, 38-40]. The RPGI model (Chapter 4) is able to capture the acoustically-driven collapse of a bubble; however, the growth phase, prior to the collapse, was assumed to grow in accordance with the RP equation. Yet, the RP growth is unable to capture the influence of the near-wall, resulting in the spherical growth of the bubble. However, as previously stated, the bubble growth has been observed to deviate from the spherical shape for bubbles close to a wall [4, 17, 37, 91]. This motivates the need to directly simulate the bubble growth near a wall to capture the influence of the near-wall on the bubble growth.

We have developed a model that captures the growth and collapse of a bubble in an acoustic field. The model is used to study the growth phase of the bubble and its subsequent collapse. In our investigation of the growth of a near-wall bubble, we look at the influence of the standoff distance of the bubble from the wall. The growth of a near-wall bubble in an acoustic field changes with an increase in standoff distance for two reasons: (1) because the wall boundary condition is further away from the bubble and (2) because the pressure wave of the acoustic wave varies spatially between the transducer face and the wall. The change in standoff distance influences the growth volume, sphericity, and centroid displacement. The collapse model developed is compared to two previously developed models of bubble growth and collapse: (1) Rayleigh growth and collapse (RGC) and (2) the RP growth initialised (RPGI) collapse.

6.3 Initialising the System

The distinction of this work is that it enables the simulation of the acoustically-driven growth and collapse of a cavitation bubble (the acoustic field is introduced to the system by a moving boundary). The bubble is initialised at the pre-growth bubble state just prior to its the growth and collapse cycle, where the bubble radius is R_0. The pre-collapse bubble is assumed to be initially stationary in the

surrounding fluid and subject to a developed acoustic field. The state of the pre-growth bubble and the developed acoustic field is required to initialise the growth-collapse simulation. The initial condition of the collapse simulation is given by superimposing the pre-*growth* bubble onto the acoustic field.

The initialization of the current study is slightly different from that described in section 4.3. In the current Chapter, the initial bubble radius $\left(R_0\right)$ represents the size of a spherical pre-growth bubble just prior to the growth phase. In Chapter 4, the initial bubble size corresponds to the pre-*collapse* bubble just before the collapse stage when the volume of the bubble is at its maximum value, where the radius of the bubble is $R_{\max}$.

In this section, we explicitly describe the initialisation procedure for the acoustically-driven growth and collapse model. The initialisation is described by two steps: step (1) develop the acoustic field (section 6.3.2), and step (2) superimpose the pre-growth bubble on the developed acoustic field (section 6.3.3), see Figure 6.1.

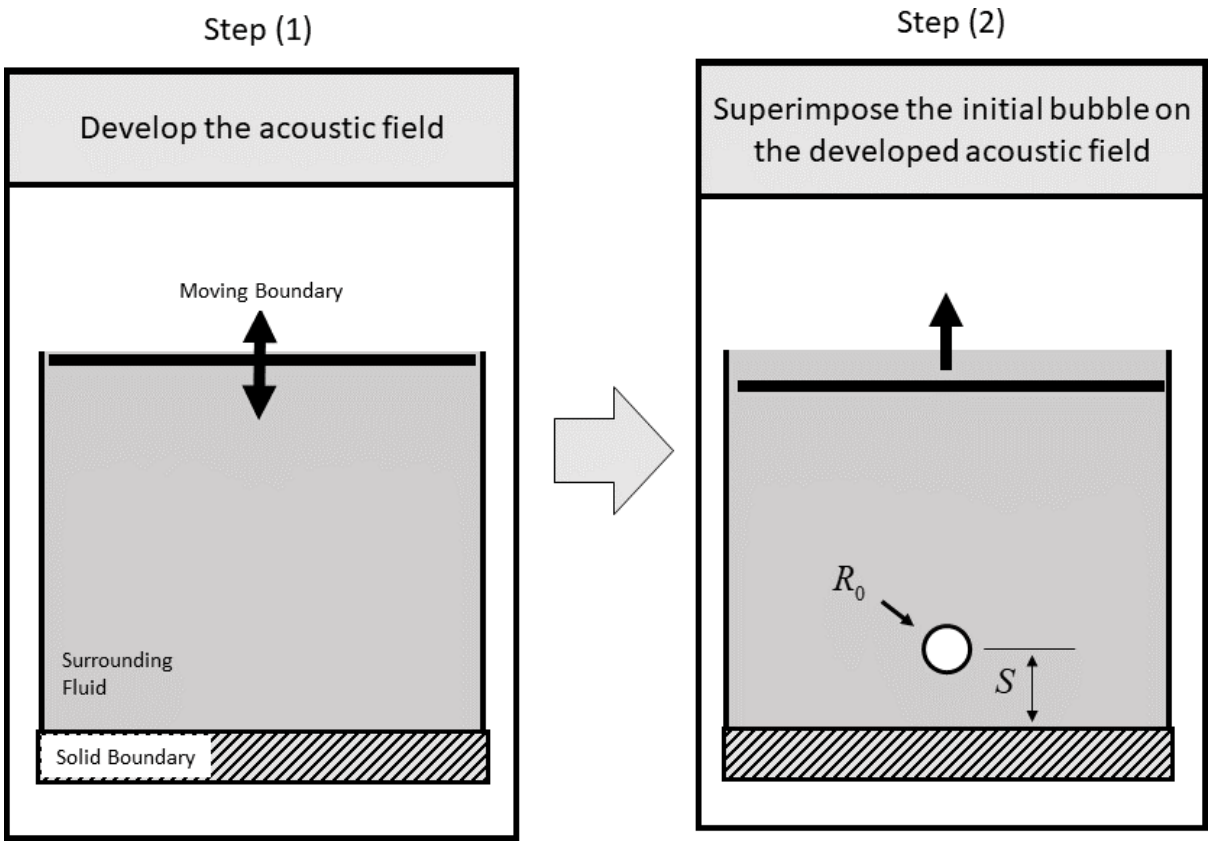

Figure 6.1. The initialisation steps of the bubble in the developed acoustic field to simulate the acoustically-driven growth and collapse of a near-wall bubble.

6.3.1 Initial Bubble

The state of the initial bubble is described by its density $\left(\rho_{0,B}\right)$ and pressure $\left(p_{0,B}\right)$ where R_0 is the radius of the initial bubble. Thus, the primitive variables inside the bubble in axisymmetric cylindrical coordinates are

$$\rho_1\left(r,z,t_0\right)=\rho_B,\ p\left(r,z,t_0\right)=p_B,\ \mathbf{u}\left(r,z,t_0\right)=\mathbf{0} \quad \text{for} \quad \sqrt{r^2+\left(z-S\right)^2}<R_0\ . \tag{6.1}$$

6.3.2 Acoustic Field

In this step, we develop the solution to the problem of the surrounding fluid (in the absence of a bubble) that is exposed to a moving boundary. Without the bubble, the governing Eqs. (2.1)-(2.5) simplify to a single fluid problem: $\alpha_1=0$ and $\alpha_2=1$. When the radial boundary conditions are applied (section 3.8.1), these Eqs. (2.1)-(2.5) reduce to the one-dimensional transient problem in the *z*-direction:

$$\frac{\partial(\rho_2)}{\partial t}+\frac{\partial(\rho_2 u_z)}{\partial z}=0 \tag{6.2}$$

$$\frac{\partial(\rho_2 u_z)}{\partial t}+\frac{\partial\left(\rho_2 u_z^2+p\right)}{\partial z}=0 \tag{6.3}$$

$$\frac{\partial E}{\partial t}+\frac{\partial\left(u_z(E+p)\right)}{\partial z}=0 \tag{6.4}$$

where u_z is the velocity in the *z*-direction.

To determine the ultrasound field at the beginning of the collapse phase, the one-dimensional transient problem is solved from the initially stationary fluid, $u_z(z,t=0)=0$, $p(z,t=0)=p_{atm}$, $\rho(z,t=0)=\rho_0$, to the fully developed ultrasound field, $u_U=u_z(z,t_U)$, $p_U=p(z,t_U)$, $\rho_U=\rho_2(z,t_U)$, where t_U is the solver duration. The development of the ultrasound field from the stationary state is achieved by ramping the amplitude of the moving boundary to simulate the starting process of the transducer face. The ramping function used to develop the ultrasound field is

$$a(t)=\begin{cases} a_{\max}\dfrac{t}{\Delta t_R} & \text{if} \quad t<\Delta t_R \\ a_{\max} & \text{if} \quad t\geq\Delta t_R \end{cases} \tag{6.5}$$

where a is the displacement amplitude of the moving boundary and Δt_R is the ramping duration.

To capture any further transient development of the ultrasound flow field after the ramping duration (Δt_R), the ultrasound simulation is run for an additional duration of Δt_D, see Figure 4.3. Note that the duration t_D ends when the wall pressure drops to the equilibrium pressure (p_0); this ensures that the pressure near the wall is in phase with the initial bubble pressure. The total duration of the ultrasound development simulation is $t_U=\Delta t_R+\Delta t_D$.

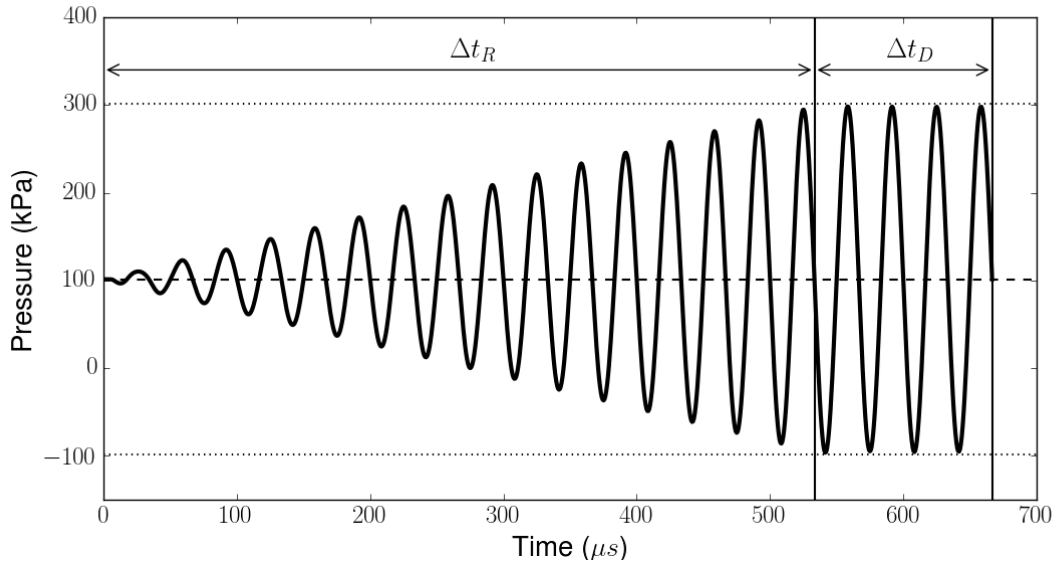

Figure 6.2. The development of the ultrasound pressure at the solid boundary $(z = 0)$. Δt_R is the period where the moving boundary amplitude is linearly ramped $(\Delta t_R \approx 16T_U)$ and Δt_D is the extra development period $(\Delta t_D \approx 4T_U)$ where the moving boundary amplitude is at its maximum $(a_{\max})$.

6.3.3 Superimposing the Initial Bubble on the Acoustic Field

To initialise the acoustically-driven bubble collapse, the pre-growth bubble is superimposed onto the developed ultrasound field. The acoustically-driven collapse simulation begins at $t_0 = 0$ μs , where the pre-growth bubble size is R_0 and the developed ultrasound field is taken at t_U . The pre-growth bubble fluid at R_0 has a uniform pressure $\left(p_B\right)$, density $\left(\rho_B\right)$, and zero velocity. Thus, the primitive variables inside the bubble in axisymmetric cylindrical coordinates are

$$\rho_1\left(r,z,t_0\right)=\rho_B,\ p\left(r,z,t_0\right)=p_B,\ \mathbf{u}\left(r,z,t_0\right)=\mathbf{0} \quad \text{for} \quad \sqrt{r^2+\left(z-S\right)^2}<R_0\ . \tag{6.6}$$

To superimpose the bubble onto the acoustic field, the surrounding fluid pressure distribution $\left(p\right)$ is defined as

$$p\left(r,z,t_0\right)=p_B\left(R_{\max}\right)+\left(1-\frac{R_{\max}}{\sqrt{r^2+\left(z-S\right)^2}}\right)p_U\left(z,t_U\right) \quad \text{for} \quad \sqrt{r^2+\left(z-S\right)^2}\geq R_0 \tag{6.7}$$

where p_U is the pressure distribution of the developed ultrasound field that is estimated in section 4.3.2. Once the fluid pressure is defined, the adiabatic stiffened EOS is used to define the surrounding fluid density $\left(\rho_2\right)$ [94]

$$\rho_2\left(r,z,t_0\right)=\rho_{0,2}\left(\frac{\gamma_2 p_2\left(r,z,t_0\right)+\pi_{\infty,2}}{\gamma_2 p_{0,2}+\pi_{\infty,2}}\right)^{\frac{1}{\gamma_2}} \quad \text{for} \quad \sqrt{r^2+\left(z-S\right)^2}\geq R_0 \tag{6.8}$$

where $\rho_{0,2}$ is a reference density of the surrounding fluid at the reference pressure $p_{0,2}$ - in this study, the reference pressure is atmospheric pressure $\left(p_{0,2}=p_{atm}\right)$.

Finally, the velocity distribution of the bubble needs to be superimposed onto the velocity distribution of the ultrasound field. The interface velocity of the bubble and the velocity distribution of the bubble fluid is assumed to be zero when the bubble is at the pre-growth state $\left(R_0\right)$. In the acoustically-driven

growth and collapse (AGDC) model, the surrounding fluid is compressible and subject to an acoustic field so its velocity distribution is non-zero.

The pressure amplitude and velocity amplitude of an acoustic wave are proportionally related [95]. Assuming the proportionality between velocity and pressure exists in the acoustic field surrounding the bubble, we superimpose the velocity distributions using a relation similar to the pressure distribution (Eq. (6.7)). Thus, to superimpose the bubble velocity in the ultrasound velocity field we assume that the same inverse relation used for the pressure can be applied for the velocity distribution in the surrounding fluid $(\mathbf{u})$

$$\mathbf{u}(r,z,t_0)=\left[0,\ \left(1-\frac{R_0}{\sqrt{r^2+(z-S)^2}}\right)u_U(z,t_U)\right] \quad \text{for} \quad \sqrt{r^2+(z-S)^2}\geq R_0 \tag{6.9}$$

where u_U is the velocity distribution in the developed ultrasound field that is estimated in section 4.3.2. Note that the radial velocity (u_r) is initially zero throughout the domain.

The volume fraction is initialised with a smoothing of the initial material interface over a few grid cells to increase the numerical stability. The Cartesian smoothing function presented in [77] was adopted and applied to the cylindrical coordinate system. The volume fraction of the bubble α_1 is initialised in cylindrical coordinates using

$$\begin{aligned}\alpha_1(r,z,t_0)=&\left(\frac{|z|}{|z|+|r|}\right)\left(\frac{1-\tanh\left(\frac{\beta}{\Delta z_{\min}}\left(\sqrt{r^2+(z-S)^2}-R_0\right)\right)}{2}\right)\\&+\left(\frac{|r|}{|z|+|r|}\right)\left(\frac{1-\tanh\left(\frac{\beta}{\Delta r_{\min}}\left(\sqrt{r^2+(z-S)^2}-R_0\right)\right)}{2}\right)^2\end{aligned} \tag{6.10}$$

where Δr_{min} and Δz_{min} are the dimensions of the cells in the refined region of the domain (Figure 2.1b). β is a coefficient which governs the amount of interface smoothing, which is typically taken between 1 and 10 [77]: the present study uses $\beta = 2$ which results in minimal interface smoothing.

6.4 Summary of the Acoustically-Driven Growth and Collapse (ADGC) method

The ADGC method consists of first initialising the pre-growth bubble (R_0) onto the developed acoustic field (in a similar manner to the initialisation of the RPGI model in section 4.3). The growth and collapse of the bubble are then simulated by solving the governing Eqs. (2.1)-(2.5) using the numerical method described in Chapter 3. The computational domain and the boundary conditions, which include the immersed moving boundary (the transducer face input) and the near-wall, are depicted in Figure 3.1.

6.5 Case Studies Parameters

In the following sections, we consider various cases of the acoustically-driven growth and collapse of a bubble. Before we present the cases, we discuss the model parameters and fluid properties that are consistent to all of the cases, unless stated otherwise.

The ultrasound frequency of 30 kHz is used in low-frequency ultrasound-induced cavitation applications; however, the model is able to capture any frequency (e.g. 2 MHz – high-frequency ultrasound applications). The pre-growth bubble radius of $R_0 = 50$ μm was arbitrarily chosen to represent a small transient cavitation bubble that is below the resonant bubble radius and above the Blake (lower transient) threshold [15]. The initial pressure of the air bubble $(p_{0,B})$ is 1 atm and the initial density of the bubble air $(\rho_{0,B})$ is 1.204 kg/m^3. The model parameters and fluid properties used are provided in Table 6.1.

Recall that in Figure 3.1 the refined region that encompasses the bubble has a very fine grid where the cell dimensions are $\Delta r_{\min}$ and $\Delta z_{\min}$. The cell dimensions in the refined region are chosen to generate a sufficiently refined grid to accurately capture the collapse of the bubble. In the case study results shown in this section, the minimum cell dimensions were chosen to be within the limits of our computational resources: $\Delta r_{\min} \approx \Delta z_{\min} \approx 1\ \mu m$. The simulations took 34 hours using 4 compute nodes. The grid used in this study is sufficiently refined for the qualitative analysis of the results. The grid is also sufficient for the quantitative comparison of the model to previously developed models because the same grid resolution is used for all of the studies and, therefore, the sharpness of the bubble interface is very similar throughout the growth and collapse.

Table 6.1. Model parameters and fluid properties

Symbol	Description	Values
f	Ultrasound frequency	30.0 kHz
R_0	Initial bubble radius	50.0 µm
$p_{0,B}$	The initial pressure of the air bubble	1 atm
$\rho_{0,B}$	The initial density of the bubble air	1.204 kg/m^3
H_f	Refined region depth	$4\,R_0$
R_f	Refined region radius	$2\,R_0$
$\Delta r_{\min}$	Refined cell radius	1 µm
$\Delta z_{\min}$	Refined cell depth	1 µm
g	Cell growth rate	1.1
CFL	CFL condition (to compute Δt)	0.4
p_{atm}	Atmospheric pressure	101.325 kPa
$\rho_{0,2}$	The density of water (surrounding fluid) at p_{atm}	10^3 kg/m^3
γ_1	EOS parameter for air [39]	1.4
γ_2	EOS parameter for water [39]	6.12
$\pi_{\infty,1}$	EOS parameter for air [39]	0.0 Pa
$\pi_{\infty,2}$	EOS parameter for water [39]	3.43×10^8 Pa

6.6 Bubble Volume Approximation

In the following case studies, the evolution of the bubble volume is often considered to show the rate of bubble growth and collapse. To approximate the volume occupied by the air bubble, we integrate the volume fraction of the air

$$V_B = \sum_{i=1}^{N} \left(\alpha_{1,i} \pi \Delta z_i \left(r^2_{i+\frac{1}{2}} - r^2_{i-\frac{1}{2}} \right) \right) . \tag{6.11}$$

where i is the index of the finite volume cells and N is the number of finite volume cells.

Due to the numerical diffusion of the material interface, the numerical volume integration of the volume fraction of air over-approximates the bubble volume significantly at the end of the collapse where the bubble is at its minimum size.

6.7 Verification

Parts of the model used in this Chapter were verified previously using the shock-bubble interaction test case (section 3.10). In this section, we will verify that the ADGC model that is developed in this Chapter does capture the anticipated bubble dynamics. To do this, the ADGC model is used to capture the bubble dynamics of the growth and collapse of a small bubble far away from a solid boundary. These results are compared to the solution provided by the 1D RP equation.

6.7.1 Comparison of the ADGC bubble to the RP bubble

The 1D (spherical) RP equation does not capture the influence of the wall for the near-wall bubble collapse. To enable a realistic comparison of the 1D RP bubble to the simulated growth using the ADGC model developed in this Chapter, we use a large domain to consider the growth of a bubble far away from the boundaries so that there is no significant influence from the wall or the outer boundary (Figure 2.1b). The model parameters and fluid properties used are provided in Table 6.1. The model parameters specific to the large domain are given in Table 6.2.

Table 6.2. Domain-specific model parameters for the comparison to the RP bubble (large domain)

Symbol	Description	Values
a	The amplitude of the transducer face	0.5253 μm
$p_A(z = 4.815 \text{ cm})$	Acoustic pressure amplitude at the bubble location	200 kPa
H_d	Domain depth	10 cm
R_d	Domain radius	10 cm

The acoustic-field is developed in 1D between the immersed moving boundary (transducer face) and the wall (see section 6.3.2). The subsequent fully developed acoustic field results in a standing pressure wave between the immersed moving boundary (transducer face ~ $z \approx 9$ cm) and the wall $(z = 0)$, as shown in Figure 6.3. This large domain (Table 6.2) results in a case were the standing ultrasound pressure wave gives a pressure antinode near $z = 5$ cm, shown in Figure 6.3. The displacement amplitude of the transducer $a = 0.5253$ μm was chosen to give a pressure amplitude of the acoustic field at the pressure antinode at $z = 4.815$ cm of $p_A \approx 200$ kPa, which is a sufficient pressure amplitude to cause the transient growth and collapse of a $R_0 = 50$ μm bubble.

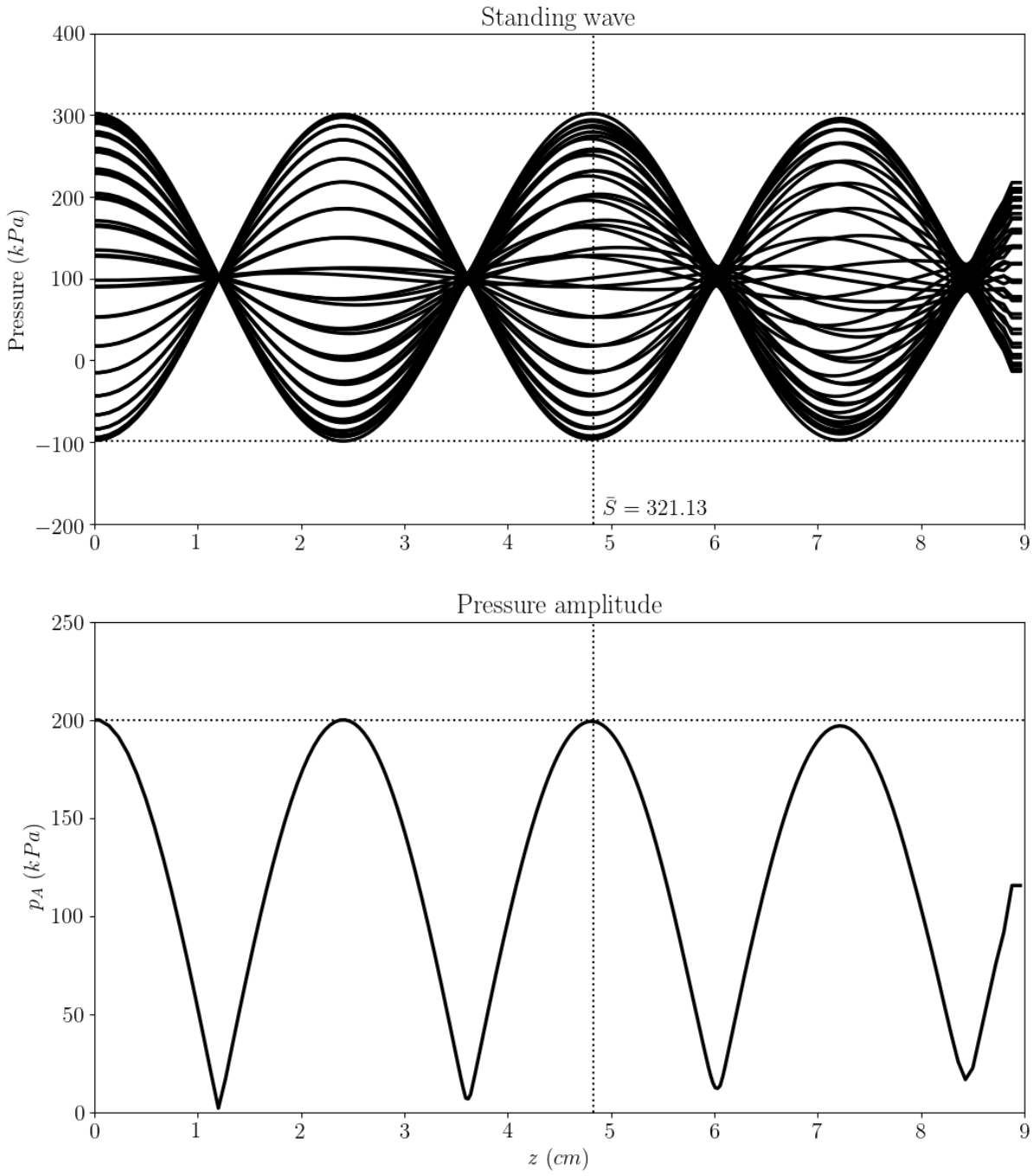

Figure 6.3. The ultrasound standing pressure wave (two waves) between the transducer face $(z \approx 9 \text{ cm})$ **and the wall** $(z = 0 \text{ cm})$ **for the larger domain case (see section 6.3.2). The standing pressure wave is presented by showing the acoustic pressure wave at multiple different instances during the acoustic wave cycle after the acoustic field has been fully developed. The local pressure amplitude varies in the** z **direction:** $p_A(z) = \left(p_{\max}(z) - p_{\min}(z)\right)/2$

In Figure 6.4, the temporal evolution of the bubble volume from RP equation is compared to the ADGC simulation (section 6.4) of the bubble in the centre of the big domain $S = 4.815\ \text{cm}$. Two RP cases are shown in Figure 6.4, (1) an adiabatic bubble $(\eta = 1.4)$ and (2) an isothermal bubble $(\eta = 1)$. The ADGC bubble results in a volume distribution that is closer to the adiabatic RP case than the isothermal case. This is an expected result as the simulated growth does not consider heat conduction; thus, the bubble is adiabatic.

Note that we do *not* consider the influence of viscosity $(\mu = 0)$ and surface tension $(\sigma = 0)$ because the compressible-multiphase-flow model (Chapter 3) does not capture these effects. The RP growth also considers the surrounding fluid to be incompressible, whereas the effects of compressibility of the surrounding fluid are considered in the collapse simulation. However, the effects of compressibility in the water during the growth phase are expected to be negligible (see section 5.4).

The comparison between the adiabatic RP bubble and the ADGC bubble shows a similar evolution in the volume of the bubble. ADGC results in maximum bubble volume that is 9.0 % less, a growth duration that is 2.4 % less and the collapse duration that is 4.6 % less. The slight difference in the results verifies the ADGC captures the dynamics of the acoustically-driven bubble as expected. The slight difference in the results are likely due to the numerical diffusion of the bubble interface (changing the bubble volume calculation – section 6.6), the limitations on the mesh refinement, and the difference in the acoustic field - the p_∞ of the RP model only approximates the far-field pressure experience by the bubble, whereas, the simulated acoustic field from the immersed moving boundary results in spatial variations in the pressure field (see Figure 6.3).

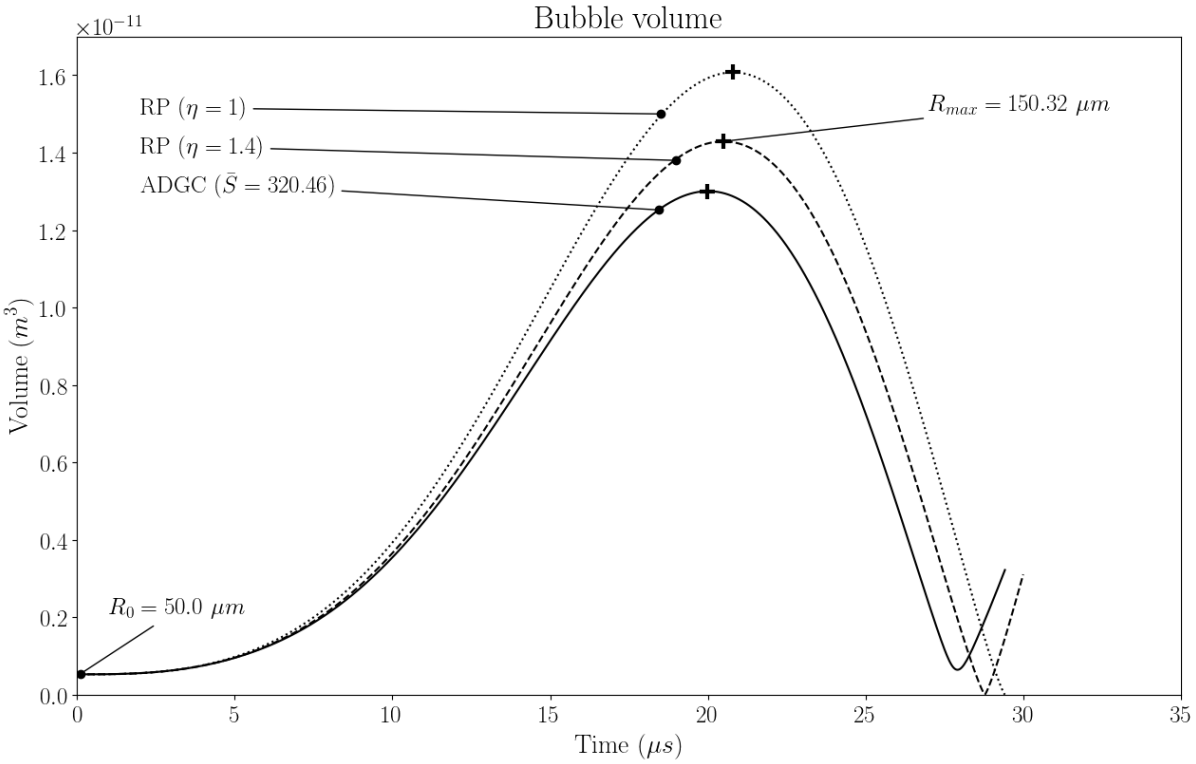

Figure 6.4. The bubble volume determining using RP equation assuming an isothermal bubble and an adiabatic bubble, and the ADGC simulated case where $\bar{S} = 320.46$ in the large domain. $R_{\max}$ is the maximum radius of the RP adiabatic bubble.

6.8 Nondimensionalized Standoff Distance

In this Chapter, we investigate the growth and collapse of an acoustically-driven bubble near-wall at various standoff distances. Here, the standoff distance (S) represents the distance from the bubble's centre to the wall when the bubble is at its pre-*growth* (initial) state, where the bubble radius is R_0. This is different from the standoff distance in Chapter 4 where it is taken as the distance from the centre of the pre-*collapse* bubble to the wall. The nondimensionalized standoff distance is

$$\bar{S} = \frac{S}{R_{\max}} \ . \tag{6.12}$$

It is of interest to present the standoff distance in terms of a dimension of the bubble when it is at its maximum size as it gives insight into how close the fully-grown bubble is to the wall before it collapses. However, the bubble growth near a wall is restricted and non-spherical, so the bubble size and shape

after growth varies with standoff distance. Thus, we nondimensionalize the standoff distance with a consistent dimension being the maximum radius after the spherical growth of the bubble in the absence of the nearby boundaries, which are computed using the RP equation to give $R_{\max}$. Presenting the standoff distance in terms of $R_{\max}$ has previously been done in [37]. As seen previously (section 6.7.1), the growth is represented as adiabatic, and, therefore $R_{\max} = 150.32$ μm for all of the cases presented in this Chapter.

6.9 Simulated Growth and Collapse

Two representative case studies of the acoustically-driven growth and collapse (ADGC) of a near-wall bubble were conducted using the ADGC model that is summarised in section 6.4. Table 6.1 contains the parameters describing the case study and the fluid properties used, and Table 6.3 provides the domain-specific parameters (these differ from the parameters used in the large domain case given in Table 6.2). The displacement amplitude of the transducer $a = 0.6956$ μm was chosen to give a pressure amplitude of the acoustic field at the pressure antinode at the wall $z = 0$ cm of $p_A \approx 200$ kPa. The two representative cases differ in the initial standoff distance of the bubble: Case 1 - $\bar{S} = 0.78$ and Case 2 - $\bar{S} = 1.14$. We look at these two example cases, $\bar{S} = 0.78$ and $\bar{S} = 1.14$, because they highlight the main characteristics of the near-wall bubble dynamics (growth and collapse). Later in this Chapter, we show more analysis of different standoff distances.

Table 6.3. Domain-specific model parameters for the ADGC case studies

Symbol	Description	Values
a	The amplitude of the transducer face	0.6956 μm
$p_A(z=0)$	Acoustic pressure amplitude at the wall	200 kPa
H_d	Domain depth	1 cm
R_d	Domain radius	1 cm

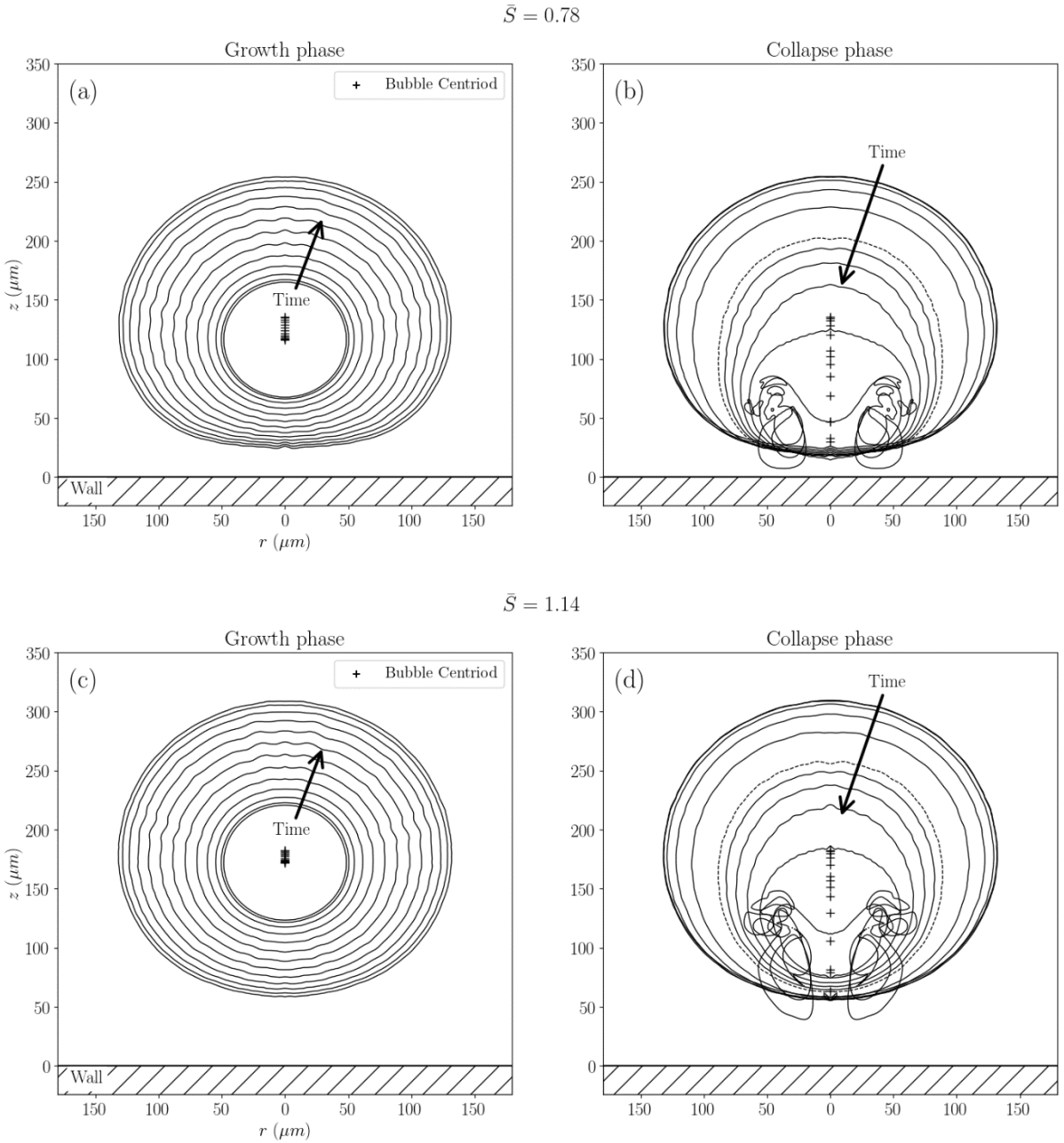

Figure 6.5. Case 1 - the (a) growth and (b) collapse of a bubble near a wall $\left(\bar{S} = 0.78\right)$. Case 2 - the (c) growth and (d) collapse of a bubble near a wall $\left(\bar{S} = 1.14\right)$. The bubble interface contour lines $\left(\alpha_1 = 0.95\right)$ are stepped in time in increments of 1.463 µs until the dashed contour line where the interface is stepped in time in increments of 0.3658 µs. The markers (+) show the centroid of the bubble are each time increment.

The closer the initial bubble is to the wall, the more the geometry of the fully-grown bubble deviates from a spherical shape (Figure 6.5a and Figure 6.5c). The outward growth of the lower region of the bubble interface is hindered by the wall due to the flow restriction imposed by the wall boundary

condition. The hindered flow results in the flattening of the bubble interface near the wall as the bubble grows (Figure 6.5a). This leaves a layer of water between the fully grown bubble and the wall, which is observed in experiments [91] and other numerical studies [4].

The collapse phase begins once the bubble reaches its maximum size. The simulation captures the formation of a jet which penetrates the bubble towards the wall at the later stages of the collapse (Figure 6.5b and Figure 6.5d). The final three contours of Figure 6.5b and Figure 6.5d show the formation of a toroidal bubble as the jet fully penetrates the bubble and the rebounding of the bubble (the growth of the toroidal bubble after the collapse). The bubble shape for the majority of the collapse phase is qualitatively consistent with the collapse shape found in multiple numerical and experimental studies [4, 26, 28, 29, 96], showing a similar interface contours with the formation of the jet through the centre of the bubble. For the case where the bubble is closer to the wall (Figure 6.5d), however, the collapse shape begins to differ significantly from the bubble shape presented in previous studies that consider the bubble as initially spherical at the beginning of the collapse phase [4, 26, 28, 29, 96] including the results presented in Chapter 4. The main difference between the bubble collapse shape in this study (Figure 6.5d) and the bubble shape of previous studies is the initially non-spherical shape of the bubble. This initially non-spherical results in changes to the subsequent shape of the collapsing bubble.

During the growth of the near-wall bubble, the bubble centroid moves away from the wall, see Figure 6.5a. During the collapse phase, the centroid of the bubble moves toward the wall, see Figure 6.5b. The displacement of the bubble centroid during the growth and collapse is due to the influence of the near-wall boundary. If the bubble is in an infinite body of liquid (far from a wall), the centroid of a bubble does not move due to the symmetry of the system. The movement of the bubble centroid away from the wall during the growth is due to the flow restriction introduced by the wall boundary. With the flow restriction on the wall side of the bubble, more growth occurs on the far and unrestricted side of the bubble. More growth on the side of the bubble that is far from the wall results in the centre of volume (centroid) to move away from the wall.

The restriction of the wall has the opposite effect of the displacement of the bubble centroid during the collapse. As the bubble collapses, the flow on the wall side of the bubble is again restricted, reducing

the collapse rate of that side of the bubble. The far side of the bubble is not redistricted and, thus, the centre of bubble volume moves towards the wall. Increasing the standoff distance of the bubble from the wall reduces the effect the wall has on the dynamics of the collapse (e.g. less centroid displacement).

6.10 Bubble Growth Analysis

The growth of the bubble, prior to collapse, is often overlooked. Instead of considering the growth prior to the collapse, the collapse is produced using an assumed or arbitrary initial state of the bubble; thus, no explicit attempt has been made to determine the condition at the start of the collapse using knowledge of the growth [18, 19, 38-40]. The consideration of the growth is important for a more realistic simulation of a bubble collapse. The collapse is fully dependant on the growth phase; thus, an investigation into the bubble growth is necessary/important to adding insight/understanding/knowledge of the collapse dynamics.

The growth phase of the bubble is important to consider because it provides information about the state of the bubble at the beginning of the collapse. A larger bubble growth – the change in bubble volume from the pre-growth bubble to the pre-collapse bubble - typically results in a more violent bubble collapse [4, 15]. In this section, the influence of the wall and the acoustic field on the bubble growth are investigated. To analyse the dynamics of the growth, we consider the bubble volume, the shape of the bubble, and the displacement of the bubble at various standoff distances.

The ADGC model is used in this section, where Table 6.1 contains the parameters describing the case study and the fluid properties used unless the results state the large domain case was used, where the domain-specific parameters are provided in Table 6.2. Any changes of parameters, like the standoff distance, will be explicitly stated.

6.10.1 Influence of the Wall

To investigate the influence of the wall on the bubble growth, we simulate the bubble for various standoff distances: $\bar{S} = 0.52$, $\bar{S} = 0.78$, $\bar{S} = 0.94$, $\bar{S} = 1.14$, $\bar{S} = 2.08$, $\bar{S} = 5.2$, and $\bar{S} = 7.8$. For the

various standoff distances, we present the temporal evolution of the bubble shape during the growth phase in Figure 6.6 and the temporal evolution of the bubble volume in Figure 6.7. These standoff distances result in a bubble that is relatively close to the wall.

The evolution of the bubble shapes during the growth phase (Figure 6.6) show that the closer the bubble is to the wall the more the bubble shape deviates from the spherical shape: this will be discussed in more detail in section 6.10.3. Also, the closer the bubble is to the wall the further the bubble centroid moves away from the wall during the growth phase (Figure 6.6) which is investigated in section 6.10.4.

In Figure 6.7, it is shown that as the standoff distance increases, the rate of bubble growth and the maximum volume of the bubble after growth increases. In other words, the closer the bubble is to the wall the less the bubble grows. This is because the wall (no-through-flow boundary) restricts the flow, reducing the rate of growth. The closer the bubble is to the wall the more the wall hinders the bubble growth.

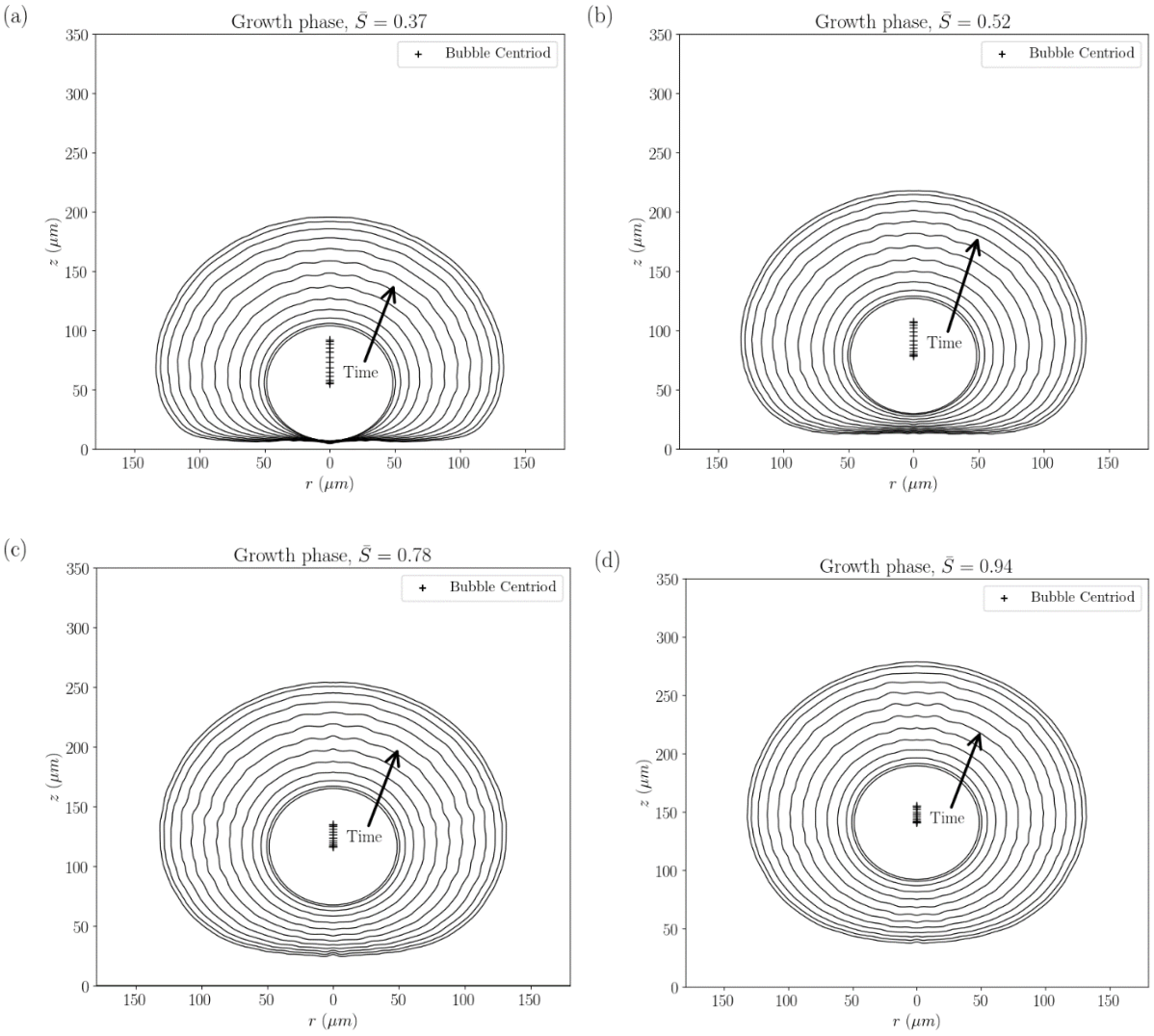
(a)
Growth phase, $\bar{S} = 0.37$
Bubble Centriod
Time
(b)
Growth phase, $\bar{S} = 0.52$
Bubble Centriod
Time
(c)
Growth phase, $\bar{S} = 0.78$
Bubble Centriod
Time
(d)
Growth phase, $\bar{S} = 0.94$
Bubble Centriod
Time
$z\ (\mu m)$
$r\ (\mu m)$

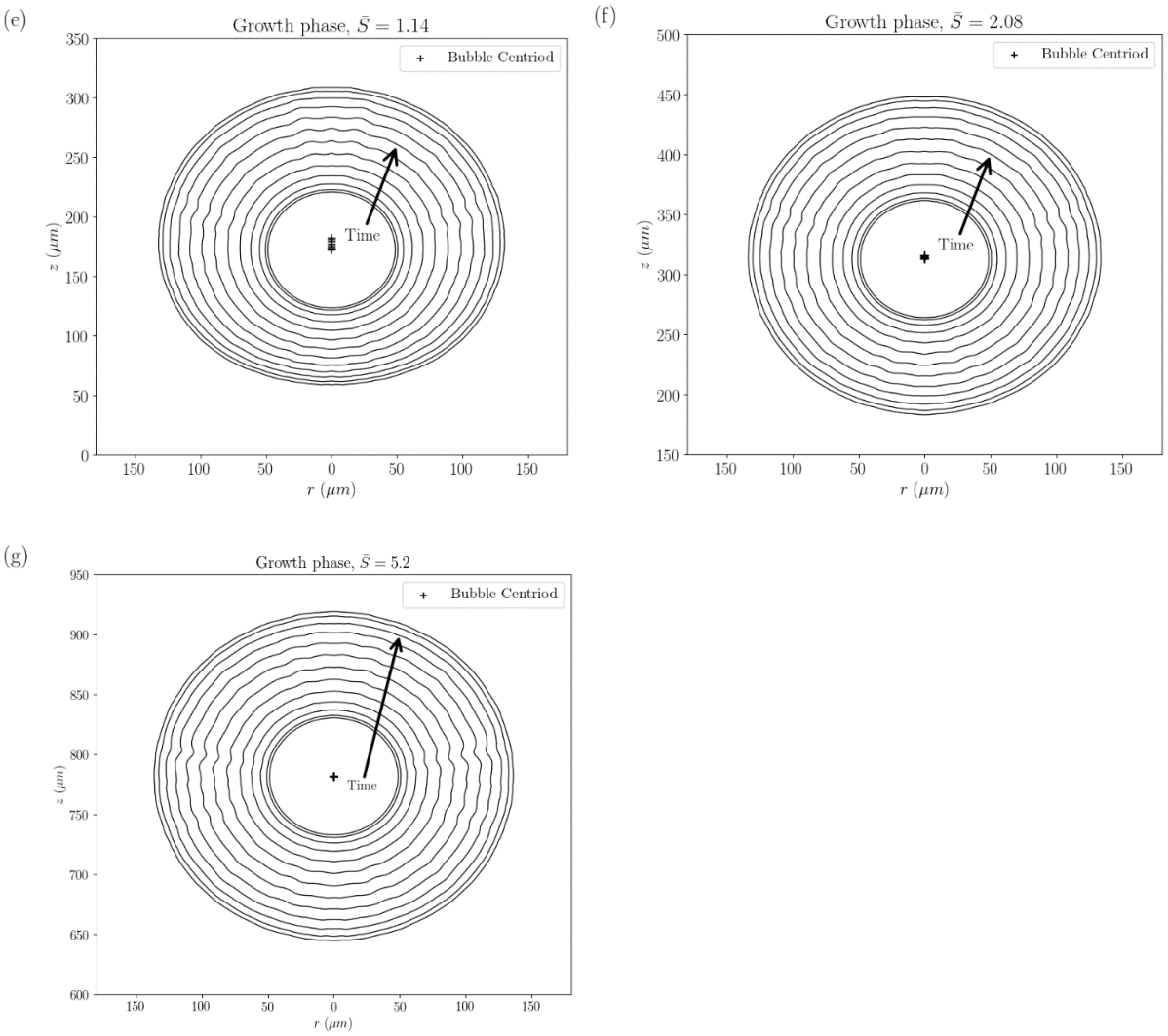

Figure 6.6. The bubble interface contour lines $(\alpha_1 = 0.95)$ for the growth of a bubble near a wall at various standoff distances: (a) $\bar{S} = 0.37$, (b) $\bar{S} = 0.52$, (c) $\bar{S} = 0.78$, (d) $\bar{S} = 0.94$, (e) $\bar{S} = 1.14$, (f) $\bar{S} = 2.08$, and (g) $\bar{S} = 5.2$. The markers (+) show the centroid of the bubble are each time increment.

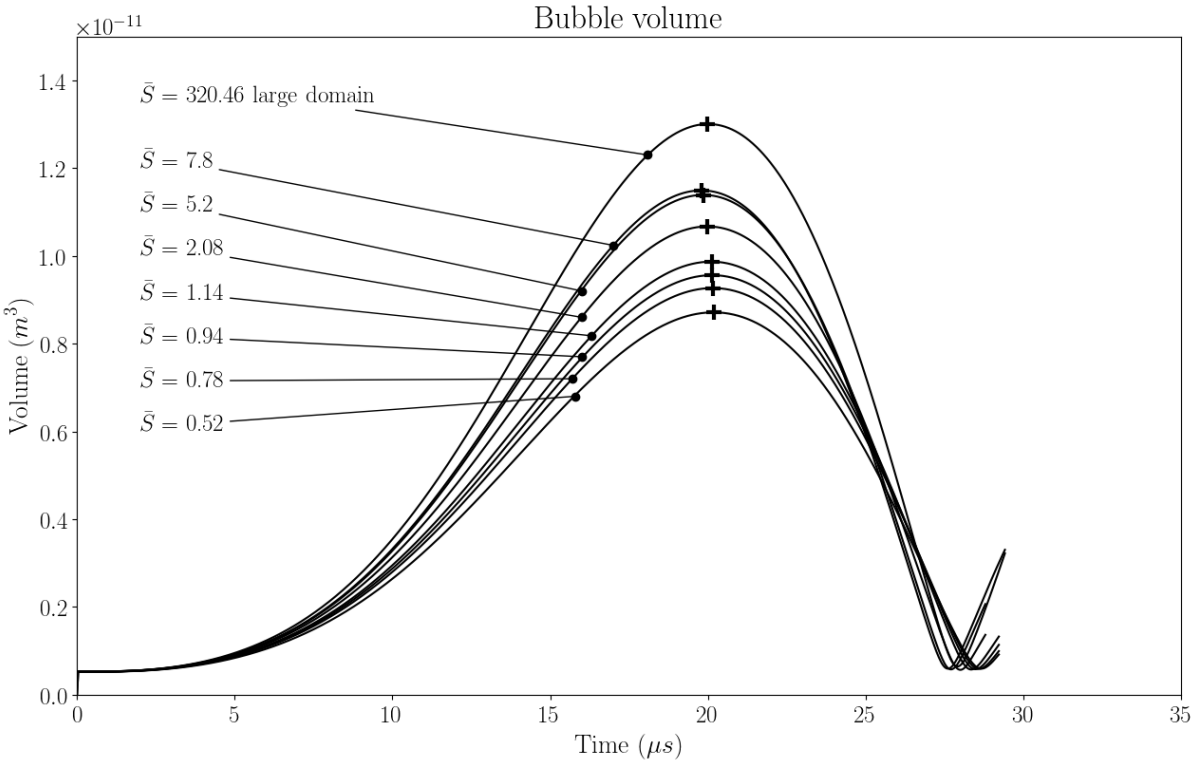

Figure 6.7. The bubble volume over the duration of the simulated bubble growth and collapse at five standoff distances of interest: $\bar{S} = 0.52$, $\bar{S} = 0.78$, $\bar{S} = 0.94$, $\bar{S} = 1.14$, $\bar{S} = 2.08$, $\bar{S} = 5.2$, **and** $\bar{S} = 7.8$ **. The + marker indicates the point of maximum bubble volume – the instant when the bubble growth ends and the bubble collapse begins (pre-collapse bubble).**

6.10.2 Influence of the Acoustic Standing Wave

Recall the results of the standing pressure wave in the very large domain that is depicted in Figure 6.3. There it is shown that the pressure amplitude of the standing wave is at a maximum near the wall and that this pressure amplitude decreases with distance from the wall until the node at $z \approx 1\ \text{cm}$ (Figure 6.3). In this section, we investigate the influence that the variations in the local pressure of the standing wave have on the growth of the bubble.

The domain that is used in these studies has a radius of 1 cm and a depth of 1 cm (Table 6.1). The acoustic-field is developed in 1D between the immersed moving boundary (the transducer face) and the wall (see section 6.3.2). The subsequent fully developed acoustic field results in a standing pressure wave between the immersed moving boundary (transducer face ~ $z \approx 1\ \text{cm}$) and the wall $(z = 0)$, as shown in Figure 6.8. The transducer face that oscillates at 30 kHz (ultrasound frequency) with a

displacement amplitude of $a = 0.6956$ results in a standing wave with the depth being approximately one-quarter of the ultrasound wavelength, see Figure 6.8.

The subsequent standing wave between the wall and the transducer face has a pressure antinode at the wall $(z = 0)$ (Figure 6.8). The shape of the wave is approximately sinusoidal; however, the pressure wave deviates from the sinusoidal shape near the transducer face $(z \approx 1\ \text{cm})$. Because the standing wave is approximately one-quarter of the ultrasound wavelength, the pressure amplitude experienced by the bubble $\left(p_A(z) = \left(p_{\max}(z) - p_{\min}(z)\right)/2\right)$ decreases monotonically with the increase in standoff distance (S), see Figure 6.8. A decreased acoustic pressure amplitude results in a lower driving force experience by the bubble in both the growth and collapse phases. Thus, the reduction in acoustic pressure amplitude with increased standoff distance is expected to result in less bubble growth.

At the wall, the pressure amplitude is approximately 200 kPa $\left(p_A(z = 0) = 200\ \text{kPa}\right)$, see Figure 6.8. For a standoff distance of $\bar{S} = 2.08$, the pressure amplitude reduces to 197.8 kPa - a 1.1 % reduction (Figure 6.8). Further out, where $\bar{S} = 7.8$, the pressure amplitude reduces to 195.6 kPa – still only a 2.2 % reduction (Figure 6.8). However, at $\bar{S} = 34.41$, the reduction in pressure amplitude is large; 154.4 kPa which is a 23 % reduction on the pressure amplitude (Figure 6.8). Thus, for the cases presented in the previous section (section 6.10.1 and Figure 6.7) where $\bar{S} \leq 7.8$, the reduction in the pressure amplitude is anticipated to have negligible influence on the bubble growth, with the influence of the wall on the bubble growth being the primary influence.

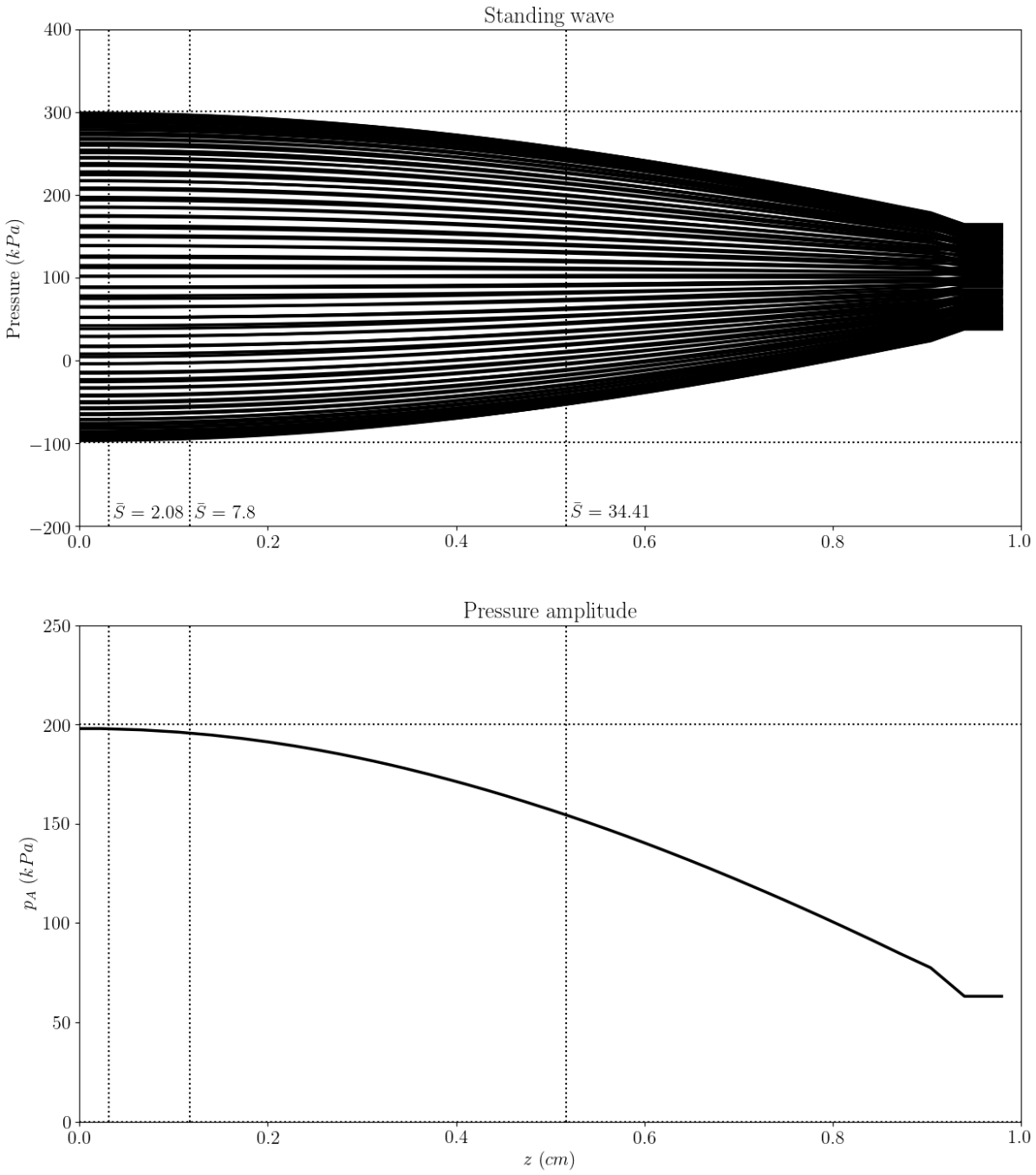

Figure 6.8. The ultrasound standing pressure wave (quarter wave) between the transducer face (immersed moving boundary condition) $\left(z \approx 1 \text{ cm}\right)$ **and the wall** $\left(z \approx 0 \text{ cm}\right)$ **(see section 6.3.2). The standing pressure wave is presented by showing the acoustic pressure wave at multiple different instances during the acoustic wave cycle after the acoustic field has been fully developed. The local pressure amplitude varies in the** z **direction:** $p_A(z) = \left(p_{\max}(z) - p_{\min}(z)\right)/2$.

Up until now, all the evidence seems to show that the maximum volume will monotonically increase with standoff distance (see section 6.10.1 and Figure 6.7). This is not the case for bubbles that are further from the wall. We wish to consider the cases that are further from the wall in which standoff distance exceeds $\bar{S} = 7.8$: a position in the domain (z) where the pressure amplitude (p_A) has a much smaller value than at the wall (Figure 6.7).

The influence of the reduction in pressure amplitude on the bubble growth is shown in Figure 6.9, where the bubble volume is depicted for the standoff distances $\bar{S} = 7.8$ and $\bar{S} = 34.41$. The comparison between the $\bar{S} = 7.8$ case to the $\bar{S} = 34.41$ case highlights the reduced growth of the bubble for the larger standoff distance case $\left(\bar{S} = 34.41\right)$. The $\bar{S} = 34.41$ results in a maximum bubble volume that is 40% less than in the $\bar{S} = 7.8$ case, see Figure 6.8. This is because the bubble growth is driven by the difference in the bubble pressure and the acoustic pressure. A reduction in the pressure amplitude experienced by the bubble results in a smaller pressure difference driving the bubble growth.

In the previous section (section 6.10.1), near the wall $\left(\bar{S} \leq 7.8\right)$, the maximum bubble volume after the growth increases with the distance from the wall is attributed to the fluid dynamics – the wall hinders the flow, restricting the bubble growth. In the case presented in this section, it is found that as the bubble moves further away from the pressure antinode at the wall (increasing standoff distance $\left(\bar{S}\right)$ – see Figure 6.8), the local pressure amplitude of the standing wave (p_A) decreases monotonically. Subsequently, we find that the maximum bubble volume after the growth then also decreases with standoff distance $\left(\bar{S}\right)$ because the bubble experiences a lower pressure amplitude (p_A) further away from the wall.

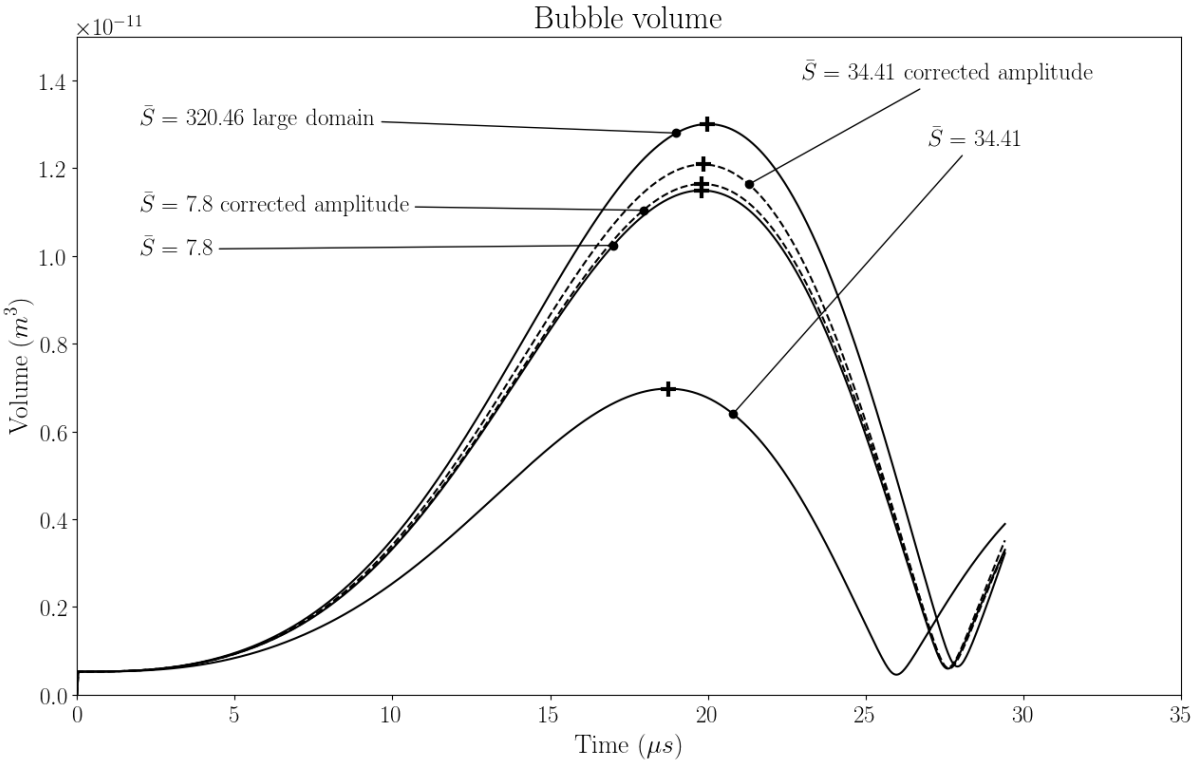

Figure 6.9. The bubble volume over the duration of the simulated bubble growth and collapse at two standoff distances of interest, $\bar{S} = 7.8$ and $\bar{S} = 34.41$. The dashed lines indicated a correction in the pressure amplitude to achieve the same far-field pressure at the outer boundary at the standoff distance from the wall as the bubble. The + marker indicates the point of maximum bubble volume – the instant when the bubble growth ends and the bubble collapse begins (pre-collapse bubble).

The influence of the acoustic standing wave is of interest because of the implications on ultrasound applications. Stable bubble behaviour may also occur if the pressure amplitude is *not* sufficient to grow the bubble to more than twice its initial size: this is the growth threshold required to produce a transient collapse [15]. In cases like the big domain case, Figure 6.3, stable bubble behaviour will occur in regions of the standing pressure wave where the pressure amplitude is too low to cause transient cavitation $\left(p_A < 1 \text{ atm}\right)$.

6.10.3 Bubble Shape: Growth Sphericity

In most previous studies of bubble collapse [18, 19, 38-40], the bubble collapse begins with a spherical bubble; this implicitly assumes the spherical growth of the bubble. In the RPGI model developed in Chapter 3, the bubble is assumed to grow spherically, where the growth is described by the RP equation.

However, the bubble shape deviates from a sphere as the bubble grows due to the influence of the near-wall (section 6.10.1). And the closer the bubble is to the wall (decrease in standoff distance) the more the bubble deviates from the spherical shape, as seen previously in Figure 6.6. In this section, we investigate the bubble sphericity at different standoff distances from the wall. The bubble sphericity is quantified by

$$\phi = \frac{2A}{R^* P} \tag{6.13}$$

which is similar to the notation used in [38], where A is the area of the bubble in cylindrical coordinates, P is the perimeter of the interface contour in cylindrical coordinates, and R^* is the effective radius of the contour line. A ϕ value of 1 implies a perfectly spherical bubble. The smaller the value of ϕ implies a more non-spherical bubble shape. The effective radius $\left(R^*\right)$ is determined using the area within the contour line $\left(A\right)$

$$R^* = \sqrt{\frac{A}{\pi}} \ . \tag{6.14}$$

A parametric study of the sphericity of the bubble after the growth phase (taken at the maximum bubble volume) for varying standoff distances is depicted in Figure 6.10 (the values are presented in Table 6.4). It is interesting to note that the bubble is approximately spherical $\left(\phi > 0.995\right)$ for standoff distances greater than $\bar{S} = 1$. This shows that the wall only significantly influences bubble sphericity when the standoff distance is less than the effective maximum radius of the bubble $\left(S < R_{\max}\right)$.

Caution must be taken with the outcome that the bubble growth is approximately spherical for small standoff distances $\left(\bar{S} = 1\right)$. The growth may be spherical, but this does not mean the RP equation is a good approximation of the bubble size. In the previous section on the wall influence (section 6.10.1), it was shown that bubble growth is significantly restricted by the nearby wall. The RP equation assumes the bubble is in an infinite body of fluid, with no nearby boundaries.

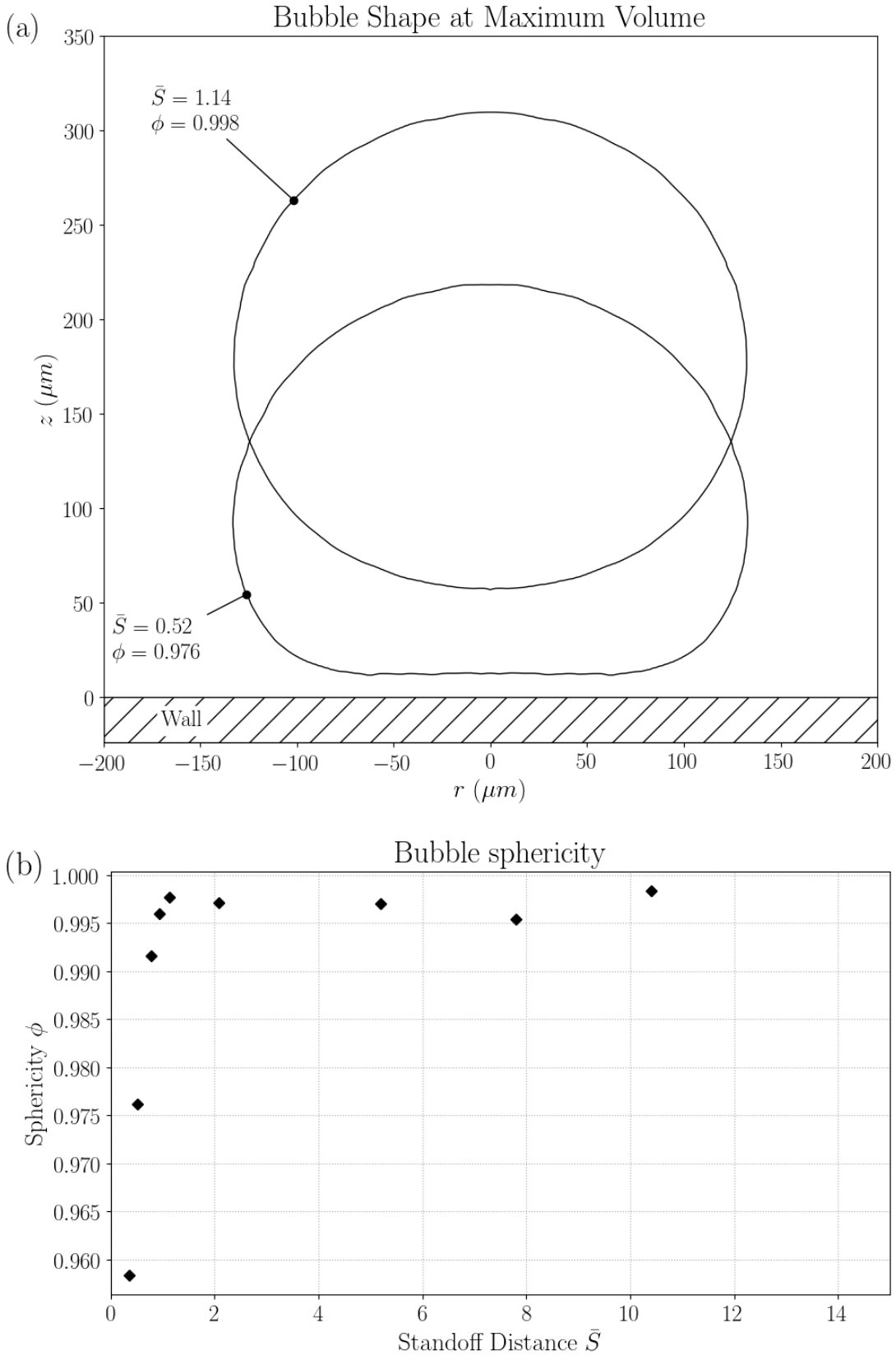

Figure 6.10. (a) Two cases, $\bar{S} = 0.52$ and $\bar{S} = 1.14$, showing the sphericity of the bubble at the maximum volume (ϕ) and (b) the sphericity (ϕ) of the bubble at its maximum size for various standoff distances.

Table 6.4. The sphericity of the bubble shape at the end of the growth phase where the bubble is at its maximum radius for various standoff distances.

$\bar{S}$	0.366	0.52	0.78	0.94	1.14	2.08	5.2	7.8	10.4	34.41
ϕ	0.9584	0.9761	0.9916	0.9959	0.9977	0.9971	0.9970	0.9954	0.9984	0.9965

6.10.4 Bubble Displacement

As the near-wall bubble grows, the centroid moves away from the wall; the centroid of the bubble moves towards the wall as the bubble collapses (Figure 6.5). To quantify the influence the wall has on the bubble displacement during the growth, we show the total centroid displacement (d) over the growth duration for various standoff distances in Figure 6.11 (the values are presented in Table 6.5).

For low standoff distances $(\bar{S} < 5)$, the displacement of the centroid over the growth phase decreases exponentially with increasing standoff distance. For the case when the bubble is the closest to the wall, $\bar{S} = 0.366$, the displacement of the centroid over the duration of the growth reaches a maximum: $d/R_{\max} = 0.7335$ (Table 6.5). This is due to the wall restricting the flow, hindering the growth of the bubble on the wall side. This results in the majority of the bubble growth occurring on the side far from the wall. Subsequently, the centroid moves away from the wall as the bubble grows. The effect is magnified as the standoff distance of the bubble is decreased (Figure 6.6)

For the larger standoff distances $(\bar{S} > 5)$, the magnitude of the bubble centroid displacement is negligible $(< 0.052 R_{\max})$, see Table 6.5. It is interesting to note that the bubble centroid displacement becomes less than zero for $\bar{S} \geq 7.8$ (Table 6.5), indicating a displacement of the bubble towards the wall during the growth phase. Far from the wall $(\bar{S} \geq 7.8)$, the bubbles move towards the wall because of the primary Bjerknes force. The primary Bjerknes force is the net force on a bubble over the acoustic wave cycle, where the force (F) on a bubble in a sound wave is

$$F = -V\nabla p \tag{6.15}$$

where V is the volume of the bubble and ∇p is the gradient of the pressure wave (see Figure 6.8 for the depiction of the standing pressure wave). If the bubble volume was unchanged over the cycle of the pressure wave the net force would be zero; however, the bubble volume does change, and the net force causes small bubbles (less than the resonant size) to migrate to the pressure antinode (the wall in our case – see Figure 6.8). Over the duration of the growth phase, the force on the bubble, from Eq. (6.15), is towards the wall because of the positive pressure gradient (∇p). For the $\bar{S} = 34.41$ case (the case where the bubble is the furthest from the wall) the bubble moves $d/R_{\max} = -0.0468$, which is approximately 7 µm towards the wall.

Table 6.5. The total displacement of the bubble centroid over the duration of the growth phase (from the initial bubble to bubble at its maximum volume) for various standoff distances.

$\bar{S}$	0.366	0.52	0.78	0.94	1.14	2.08	5.2	7.8	10.4	34.41
$d/R_{\max}$	0.7335	0.5831	0.3797	0.2889	0.2071	0.0629	0.0051	-0.0025	-0.0098	-0.0468

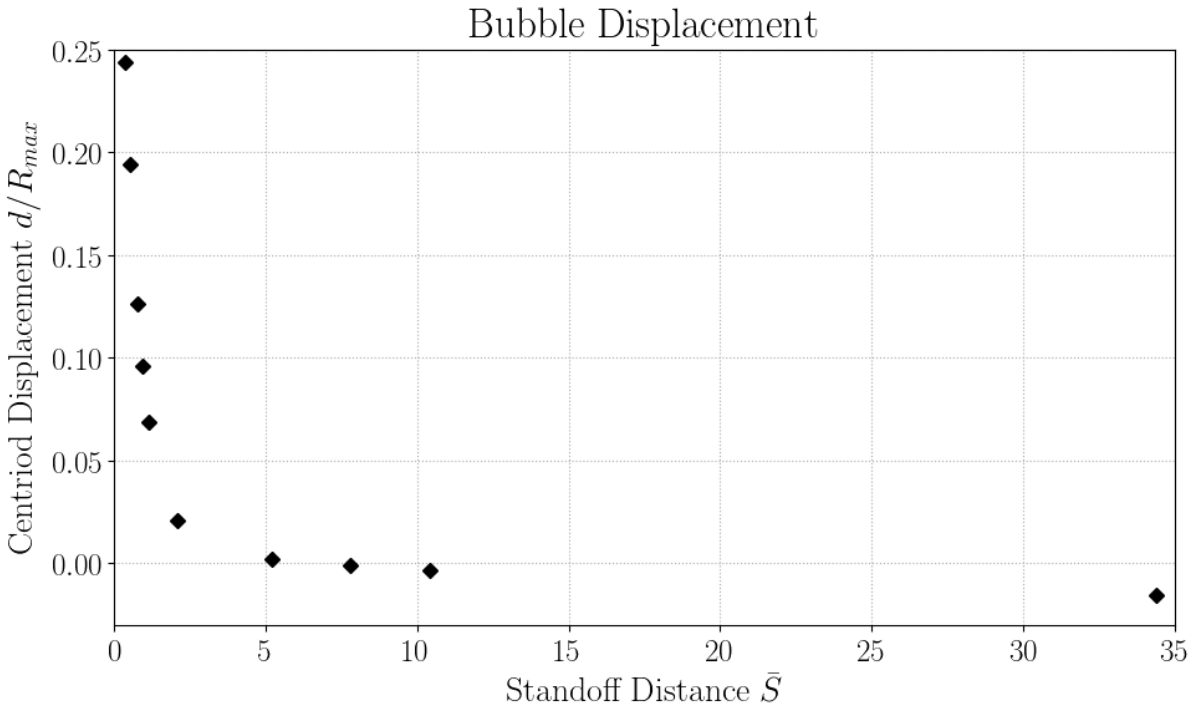

Figure 6.11. The total displacement of the bubble centroid over the duration of the growth phase (from initial bubble to bubble at its maximum volume) for various standoff distances.

6.11 Bubble Collapse

The acoustically-driven bubble collapse, after the bubble growth, is investigated in this section. The pressure experienced by the near-wall is an important consideration for a near-wall bubble collapse as it has practical implications in applications like ultrasound surface cleaning. The influence of standoff distance on the jetting and the maximum pressure experienced by the near-wall is considered.

6.11.1 Bubble Shape: Jetting during Collapse

Jetting occurs if the acoustically-driven bubble is close to a wall (solid boundary). It is important to show how the degree of jetting changes with standoff distance. The bubble interface contour lines $(\alpha_1 = 0.95)$ for the growth and collapse of a bubble near a wall at various standoff distances (a) $\bar{S} = 0.37$, (b) $\bar{S} = 0.52$, (c) $\bar{S} = 0.78$, (d) $\bar{S} = 0.94$, (e) $\bar{S} = 1.14$, (f) $\bar{S} = 2.08$, and (g) $\bar{S} = 5.2$ is depicted in Figure 6.12. Jetting is observed at the later stages for the collapse when a jet penetrates the bubble towards the near-wall $(z = 0)$, see Figure 6.12a-f ($\bar{S} = 0.37$ to $\bar{S} = 2.08$). The contour showing the formation of the jet is annotated in red in Figure 6.12c. However, for the case when the bubble is the further away from the wall, at $\bar{S} = 5.2$, no significant jetting is observed with the bubble collapsing approximately spherically, see Figure 6.12g. These findings are consistent with the numerical and experimental findings in [102], which considers the degree of jetting with standoff distance from a rigid wall for a laser-induced cavitation bubble collapse: in [102] they also find that the strength of the jet decreases with an increase in standoff distance.

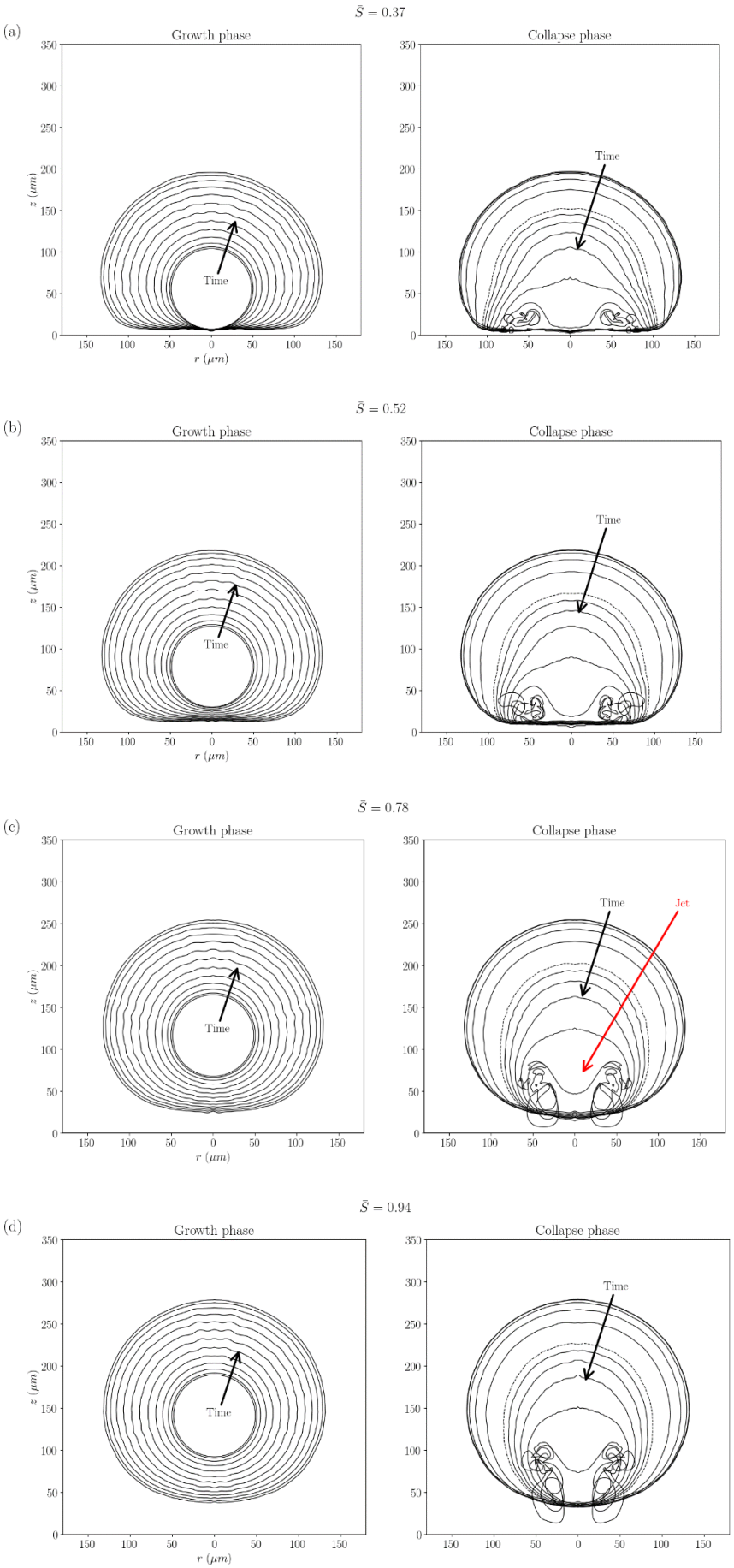
$\bar{S} = 0.37$
(a)
Growth phase
Collapse phase
Time
Time
$z\ (\mu m)$
$r\ (\mu m)$
$\bar{S} = 0.52$
(b)
Growth phase
Collapse phase
Time
Time
$z\ (\mu m)$
$r\ (\mu m)$
$\bar{S} = 0.78$
(c)
Growth phase
Collapse phase
Time
Jet
Time
$z\ (\mu m)$
$r\ (\mu m)$
$\bar{S} = 0.94$
(d)
Growth phase
Collapse phase
Time
Time
$z\ (\mu m)$
$r\ (\mu m)$

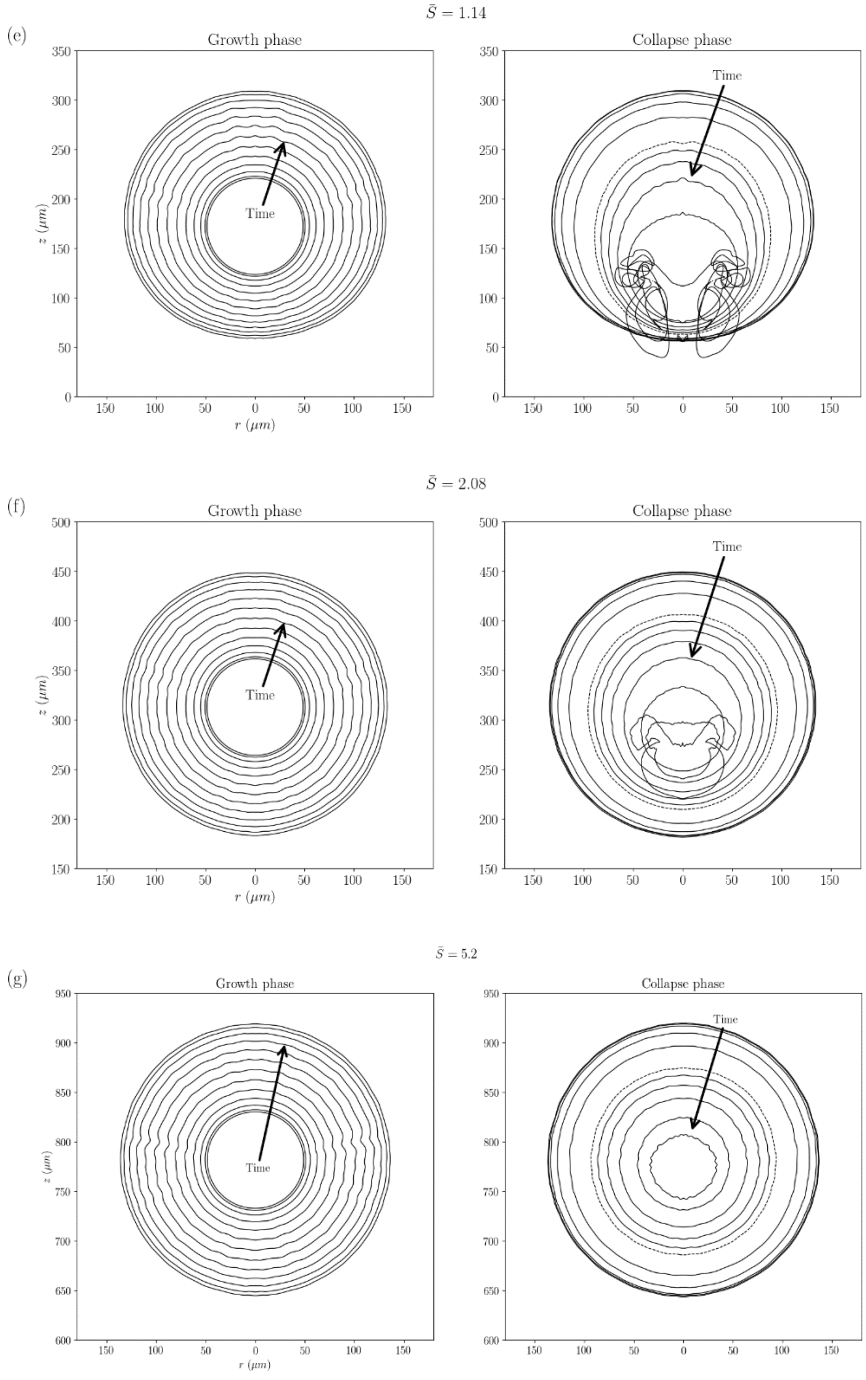

Figure 6.12. The bubble interface contour lines $(\alpha_1 = 0.95)$ for the growth and collapse of a bubble near a wall at various standoff distances: (a) $\bar{S} = 0.37$, (b) $\bar{S} = 0.52$, (c) $\bar{S} = 0.78$, (d) $\bar{S} = 0.94$, (e) $\bar{S} = 1.14$, (f) $\bar{S} = 2.08$, and (g) $\bar{S} = 5.2$.

6.11.2 Jet Velocity

To provide quantifiable comparisons of the jet characteristics for the different standoff distances, we introduce here a characteristic jet velocity. The jet velocity $\left(u_{jet}\right)$ is defined as the first order derivative of the interface contour location on the side of the bubble furthest from the wall at the *z*-axis $\left(z_{jet}{}^{n}\right)$ [77]

$$u_{jet} = \frac{z_{jet}{}^{n} - z_{jet}{}^{n-1}}{\Delta t} \tag{6.16}$$

where Δt is the time step between the time levels n and $n-1$.

The evolution of the jet velocity at the end of the collapse is presented in Figure 6.13 for various standoff distances: $\bar{S} = 0.37$, $\bar{S} = 0.52$, $\bar{S} = 0.78$, $\bar{S} = 0.94$, $\bar{S} = 1.14$, and $\bar{S} = 2.08$. The maximum jet velocity for these cases is depicted in Figure 6.14 (the values are provided in Table 6.6). For the further away cases $\left(\bar{S} \geq 5.2\right)$ jetting does not occur so we do not show the jet velocity of these cases; however, it is of interest to compare the jet velocities to the maximum radial velocity of the large domain case $\left(\bar{S} = 320.46\right)$ that approximates the bubble dynamics far from any boundaries. The maximum radial velocity for the spherical collapse case $\left(\bar{S} = 320.46\right)$ is 68.8 m/s, see Figure 6.14.

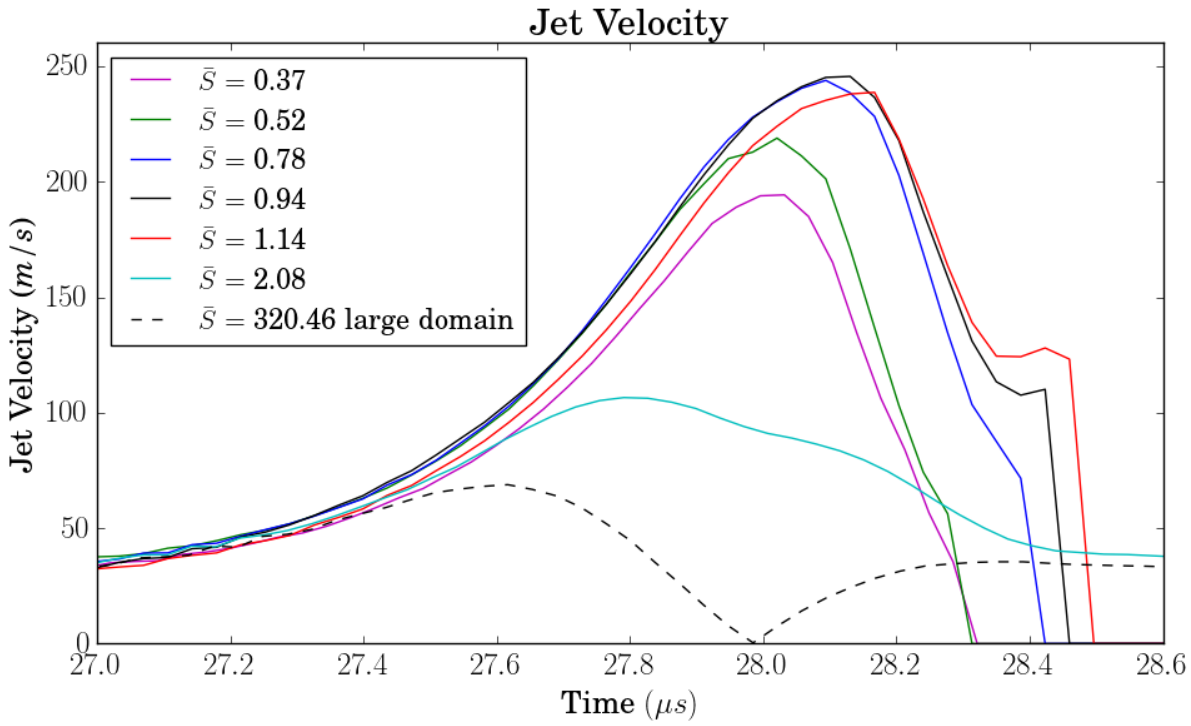

Figure 6.13. The velocity of the jet at the end of the collapse for various standoff distances. The dashed line depicts the interface velocity of the spherical collapse given by the large domain case where $\bar{S} = 320.46$.

Table 6.6. The maximum jet velocity over the duration of the collapse phase for various standoff distances.

$\bar{S}$	0.366	0.52	0.78	0.94	1.14	2.08
Maximum jet velocity (m/s)	194.27	218.86	243.85	245.57	238.66	106.54

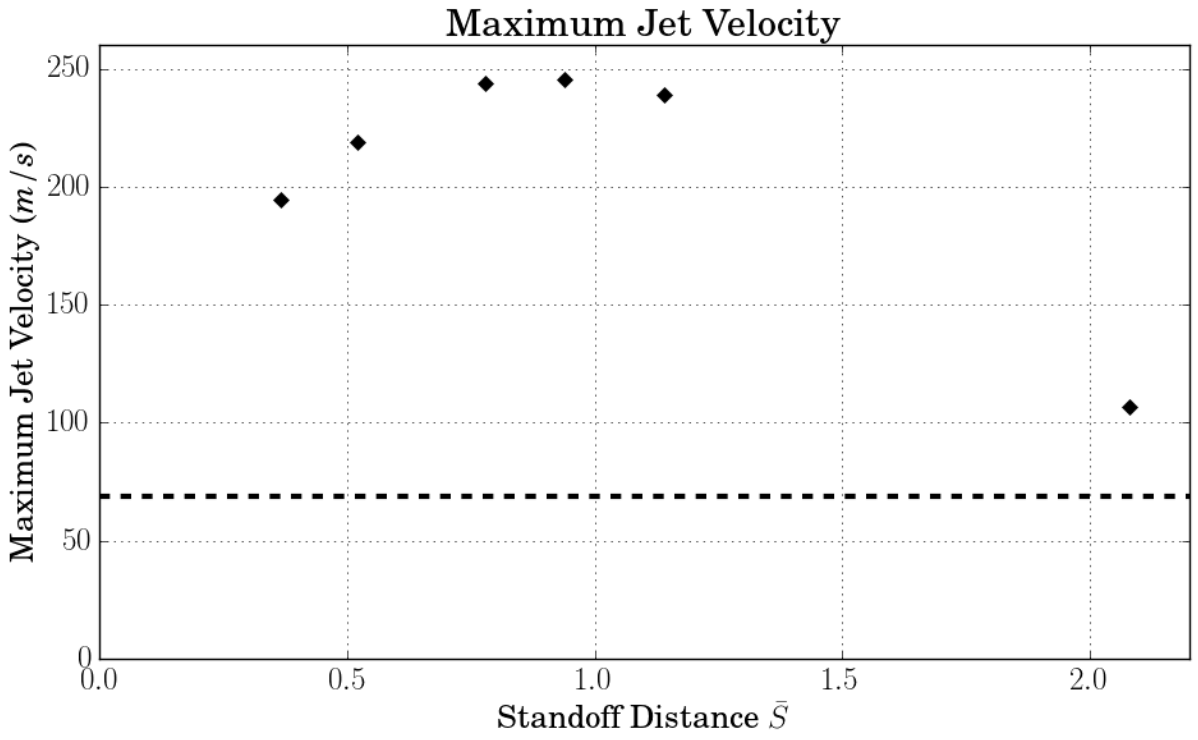

Figure 6.14. The maximum jet velocity over the duration of the collapse phase for various standoff distances. The maximum radial velocity for the spherical collapse case $\left(\bar{S}=320.46\right)$ is 68.8 m/s depicted by the dashed line.

The maximum jet velocity of 245.6 m/s occurs in the $\bar{S}=0.94$ case, which is more than three times the maximum radial velocity of the spherical collapse case $\left(\bar{S}=320.46\right)$, see Figure 6.14. For the cases where $\bar{S}<0.94$, the maximum jet velocity is less due to the non-sphericity of the pre-collapse bubble shape (the pre-collapse bubble shape is the first interface contour of the collapse phase in Figure 6.12). The comparison between the bubble shape before the collapse for the cases $\bar{S}=0.37$ (Figure 6.12a) and $\bar{S}=0.94$ (Figure 6.12d) show that the closer the bubble is to the wall, the shorter that the distance is from the top of the bubble to the bottom of the bubble. The shorter distance means the jet has less distance to develop momentum. This is also apparent in Figure 6.13 when comparing the jet velocity for the cases $\bar{S}=0.52$ and $\bar{S}=0.94$. The $\bar{S}=0.52$ case follows the same velocity profile as $\bar{S}=0.94$ until approximately 27.85 μs where the acceleration becomes less reaching its maximum velocity at approximately 28.0 μs compared to the $\bar{S}=0.94$ case where the maximum velocity is achieved at approximately 28.2 μs.

Jetting occurs in the near-wall collapse of a bubble because the wall boundary retards the fluid flow. The retardation of the fluid near the wall leads to a pressure difference in the liquid above and below the bubble [91, 103]. As the bubble collapses, the pressure difference becomes apparent with a low-pressure region developing below the bubble and a high-pressure region developing above the bubble, as shown in Figure 6.15. The change in pressure (pressure gradient) from above to below the bubble causes a jet to form, penetrating the bubble towards the wall along the *z*-axis (Figure 6.15).

For the cases where the $\bar{S} > 0.94$, the maximum jet velocity reduces. This is because the further the bubble is from the wall the less the wall retards the fluid flow of the lower region of the bubble. Less retardation of the flow results in a reduction in the pressure difference in the liquid from above the bubble to below the bubble. Thus, the pressure difference that drives the jetting reducing with standoff distance. Therefore, less jetting occurs the further the bubble is away from the wall and eventually the bubble collapses spherically (no jetting).

The drop in jet driving pressure for cases with increased standoff distance is seen in the comparison between Figure 6.15 $\left(\bar{S} = 0.94\right)$ and Figure 6.16 $\left(\bar{S} = 2.08\right)$. At 27.0 µs, the high-pressure contour (0.3MPa) above the bubble is more localised in the $\bar{S} = 0.94$ case (Figure 6.15a), compared to the $\bar{S} = 2.08$ case (Figure 6.16a). At 27.0 µs, the low-pressure contour (0.06MPa) of the bubble extends to the wall in the $\bar{S} = 0.94$ case (Figure 6.15a); whereas, the low-pressure contour is approximately spherical for the $\bar{S} = 2.08$ case (Figure 6.16a).

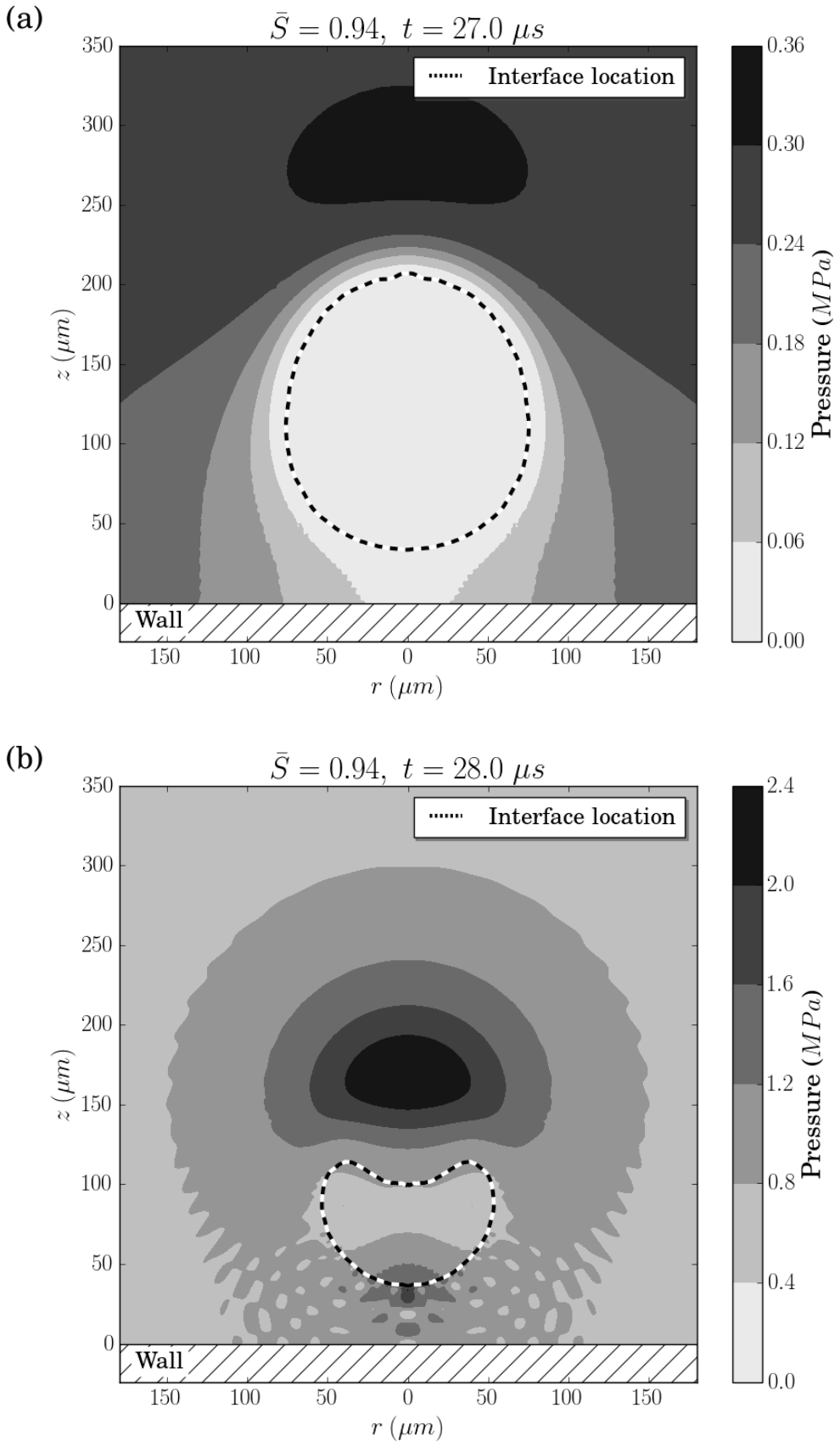

Figure 6.15. A depiction of the pressure distribution at two stages near the end of the collapse: (a) 27.0 µs and (b) 28.0 µs for the case where $\bar{S} = 0.94$.

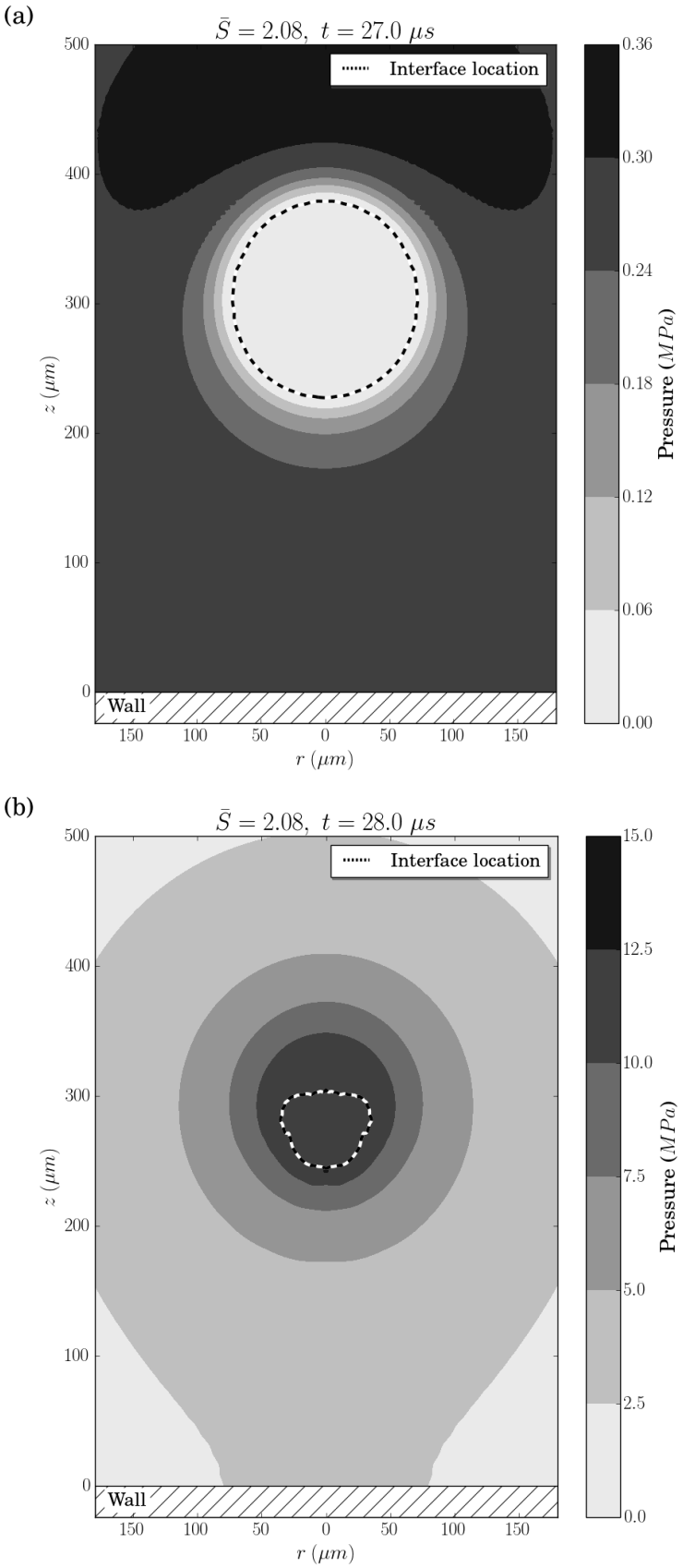

Figure 6.16. A depiction of the pressure distribution at two stages near the end of the collapse: (a) 27.0 µs and (b) 28.0 µs for the case where $\bar{S} = 2.08$.

6.11.3 Pressure Experienced by the Near-wall

The pressure experienced by the nearby wall during the collapse is of interest as the high pressure is used in many applications, like ultrasonic surface cleaning [4]. The high pressure experienced by the wall is due to the violent collapse of the nearby bubble and the water hammer pressure produced by the jetting through the bubble towards the wall. The wall pressure is compared for various standoff distances: $\bar{S} = 0.37$, $\bar{S} = 0.52$, $\bar{S} = 0.78$, $\bar{S} = 0.94$, $\bar{S} = 1.14$, $\bar{S} = 2.08$, and $\bar{S} = 5.2$, see Figure 6.17. The maximum wall pressure for these cases is shown in Figure 6.18, and the values are provided in Table 6.7.

The highest wall pressure occurs in the $\bar{S} = 0.78$ case (Figure 6.17c), with a maximum peak pressure of 13.8 MPa. The peak pressure is found to be lower, 12.2 MPa, for the closest case ($\bar{S} = 0.37$ - Figure 6.17a), which is due to the increased restriction on the growth and collapse of the bubble caused by the near-wall, and because of the restriction on the development in momentum of the jet (discussed in section 6.11.2). For a bubble that is too close to the wall, both the growth and the collapse are restricted by the wall and, therefore, the bubble does not collapse as violently and the pressure experienced by the wall is less.

The peak wall pressure also decreased to approximately 10.4 MPa as the standoff distance increased to $\bar{S} = 0.94$ (Figure 6.17d). In the same manner, the peak wall pressure continues to decrease with further increases in the standoff distance, see Figure 6.17d. The reduction in pressure for further away cases (Figure 6.17d) is due to transmission loss [37]. The maximum pressure occurs in the bubble at the end of the collapse (or on the edge of the bubble near the wall when jetting occurs) and as the pressure is transmitted through the liquid to the near-wall the spreading of the pressure results in a lower pressure experienced by the wall (spherical spreading loss). We show the spherical spreading of the pressure in the transmission to the wall for two cases: $\bar{S} = 2.08$ (Figure 6.19) and $\bar{S} = 5.2$ (Figure 6.20). The end of the bubble collapse occurs when the maximum pressure in the bubble is achieved, shown in Figure 6.19a $\left(\bar{S} = 2.08\right)$ and Figure 6.20a $\left(\bar{S} = 5.2\right)$. After the bubble has collapsed, the pressure propagates spherically from the localised maximum pressure in the bubble. The maximum pressure experienced

by the wall occurs sometime after the collapse when the peak of the emitted pressure wave impacts the wall, see Figure 6.19b and Figure 6.20b. The pressure experienced by the wall for the two cases, $\bar{S} = 2.08$ and $\bar{S} = 5.2$, are compared in Figure 6.21. In the closer case ($\bar{S} = 2.08$ - Figure 6.21a), the wall experiences a more localised pressure profile compared to the further away case ($\bar{S} = 5.2$ - Figure 6.21b). This is due to the increased spreading of the pressure because of the longer transmission from the bubble to the wall for the further away case. Note that transmission loss of pressure is relevant for both the spherical collapse ($\bar{S} = 5.2$ - Figure 6.20) and the collapse with jetting ($\bar{S} = 2.08$ - Figure 6.19) cases.

An optimum initial bubble standoff distance from the wall is expected to exist near $\bar{S} = 0.78$ where the bubble collapse will result in a maximum pressure experienced by the near-wall. As the bubble standoff distance is increased, its growth is less restricted so it will grow larger and collapse more violently. However, as the collapse occurs further away from the wall, the maximum pressure experienced by the wall is less due to the transmission loss as the pressure travels to the wall. Thus, the maximum wall pressure occurs at a standoff distance where the bubble is not too close to restrict the momentum developed in the collapse, and not too far away from the wall where the collapse pressure is lost in the transmission to the wall.

It is also important to note that the acoustic field does *not* affect the pressure experienced by the wall because $\bar{S} = 5.2$ is still close enough to the wall for the reduction in the driving pressure to be insignificant (section 6.10.2).

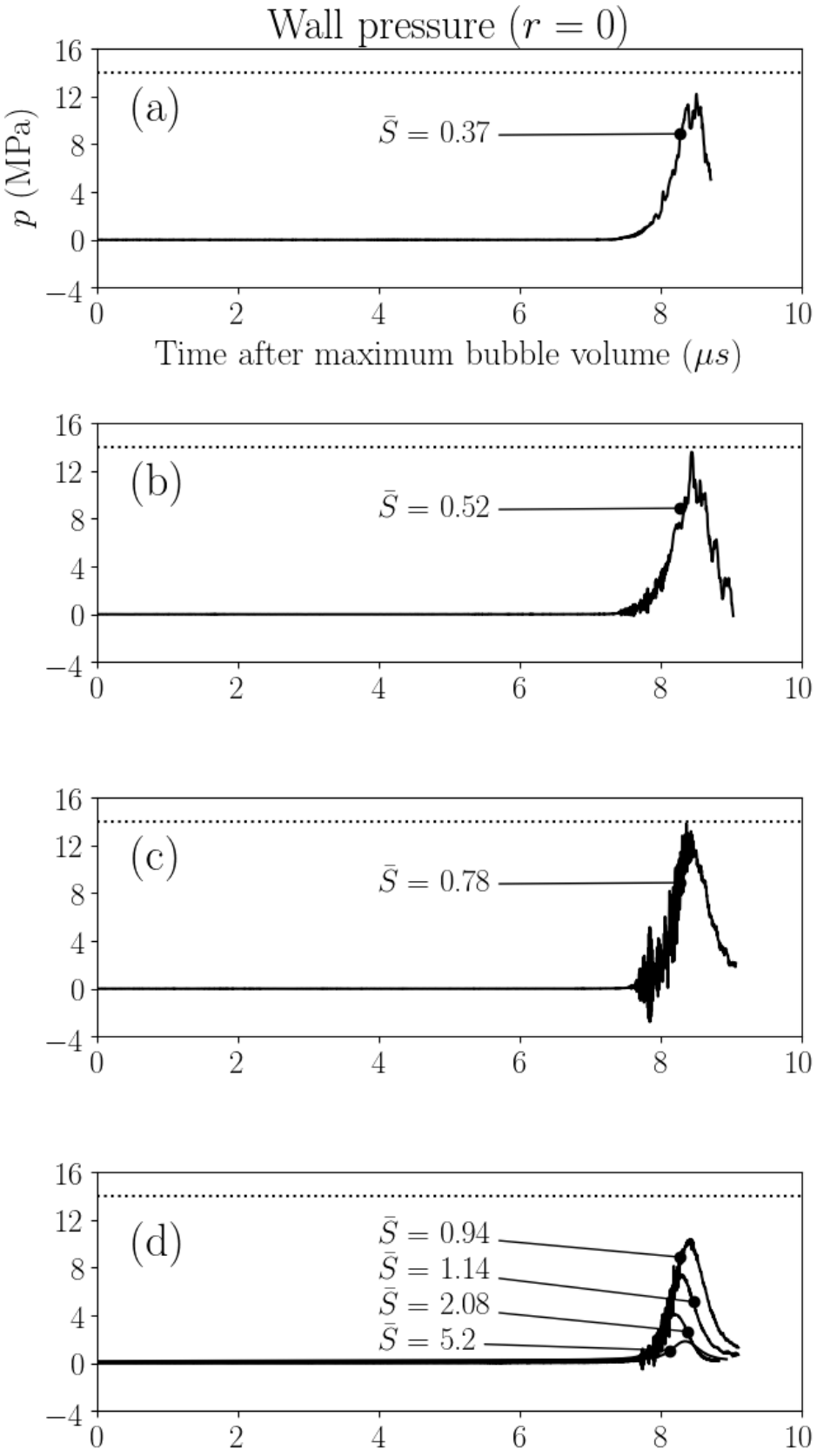

Figure 6.17. The pressure at the wall $(r = 0)$ over the duration of the collapse for various standoff distances: (a) $\bar{S} = 0.37$, (b) $\bar{S} = 0.52$, (c) $\bar{S} = 0.78$, (d) $\bar{S} = 0.94$, $\bar{S} = 1.14$, $\bar{S} = 2.08$, and $\bar{S} = 5.2$.

Table 6.7. The maximum pressure experienced by the wall over the duration of the collapse for various standoff distances.

$\bar{S}$	0.366	0.52	0.78	0.94	1.14	2.08	5.2
Maximum wall pressure (MPa)	12.21	13.60	13.82	10.39	7.57	4.10	1.83

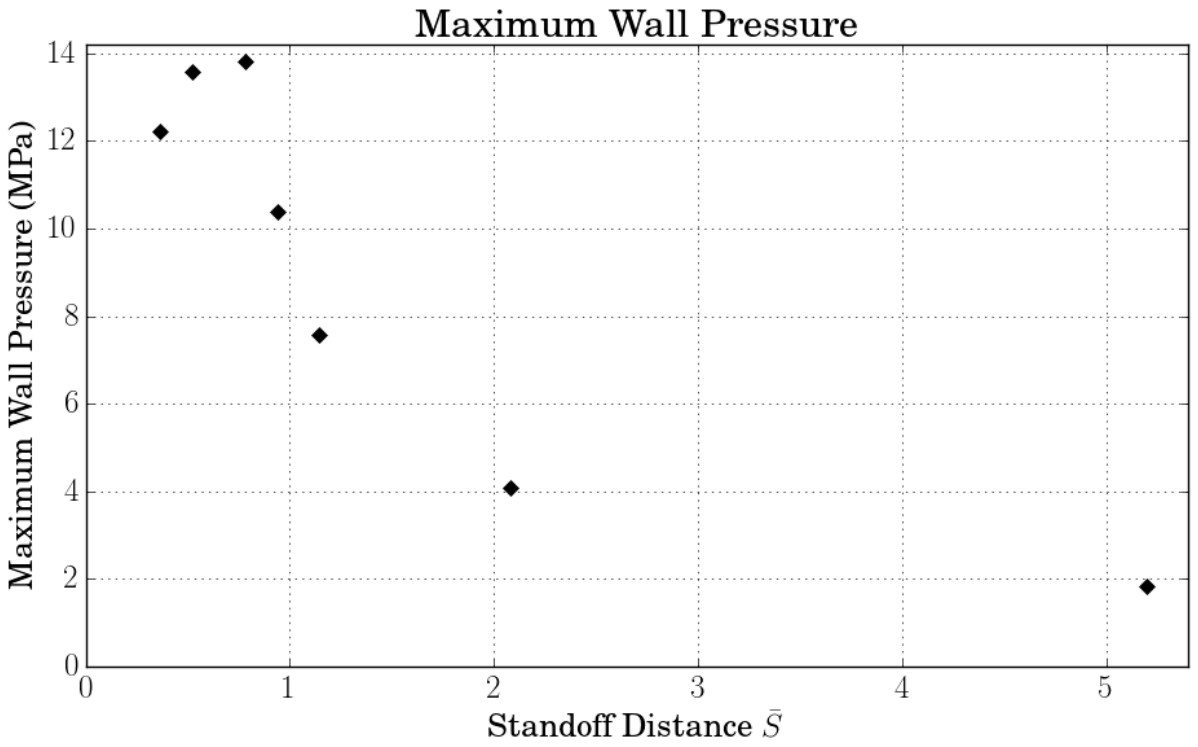

Figure 6.18. The maximum pressure experienced by the wall over the duration of the collapse for various standoff distances.

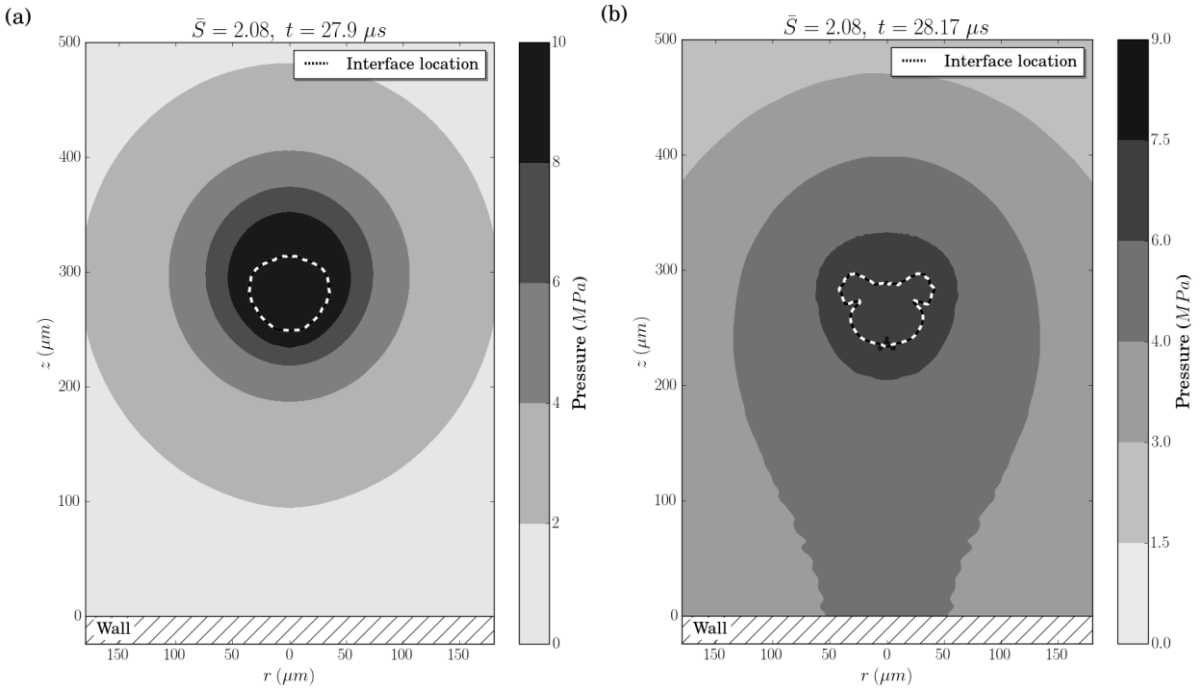

Figure 6.19. Depictions of the pressure distributions after collapse at (a) 27.9 µs (b) 28.17 µs, where the bubble reaches its minimum volume at approximately 27.8 µs (end of collapse) and the maximum pressure experienced by the wall occurs at 28.17 µs. $\bar{S} = 2.08$ **for the case shown.**

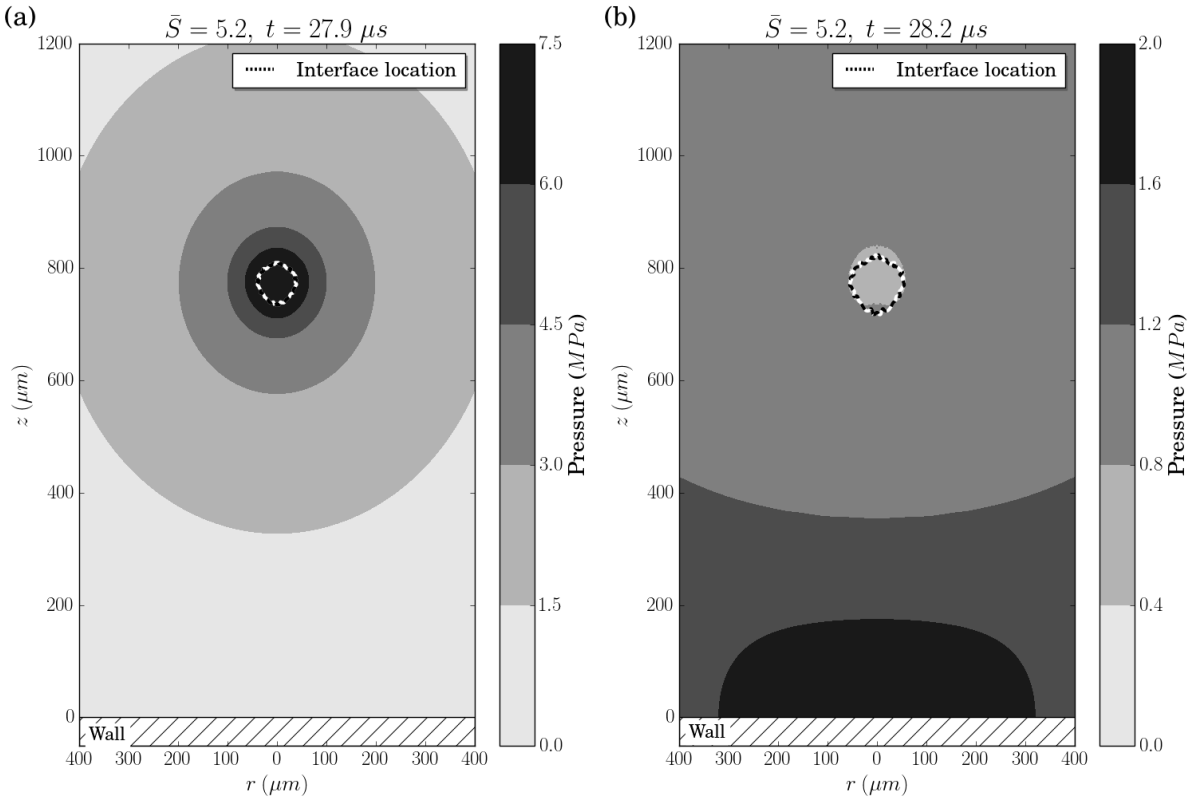

Figure 6.20. Depictions of the pressure distributions after collapse at (a) 27.9 µs and (d) 28.2 µs, where the bubble reaches its minimum volume at approximately 27.8 µs (end of collapse) and the maximum pressure experienced by the wall occurs at 28.2 µs. $\bar{S} = 5.2$ **for the case shown.**

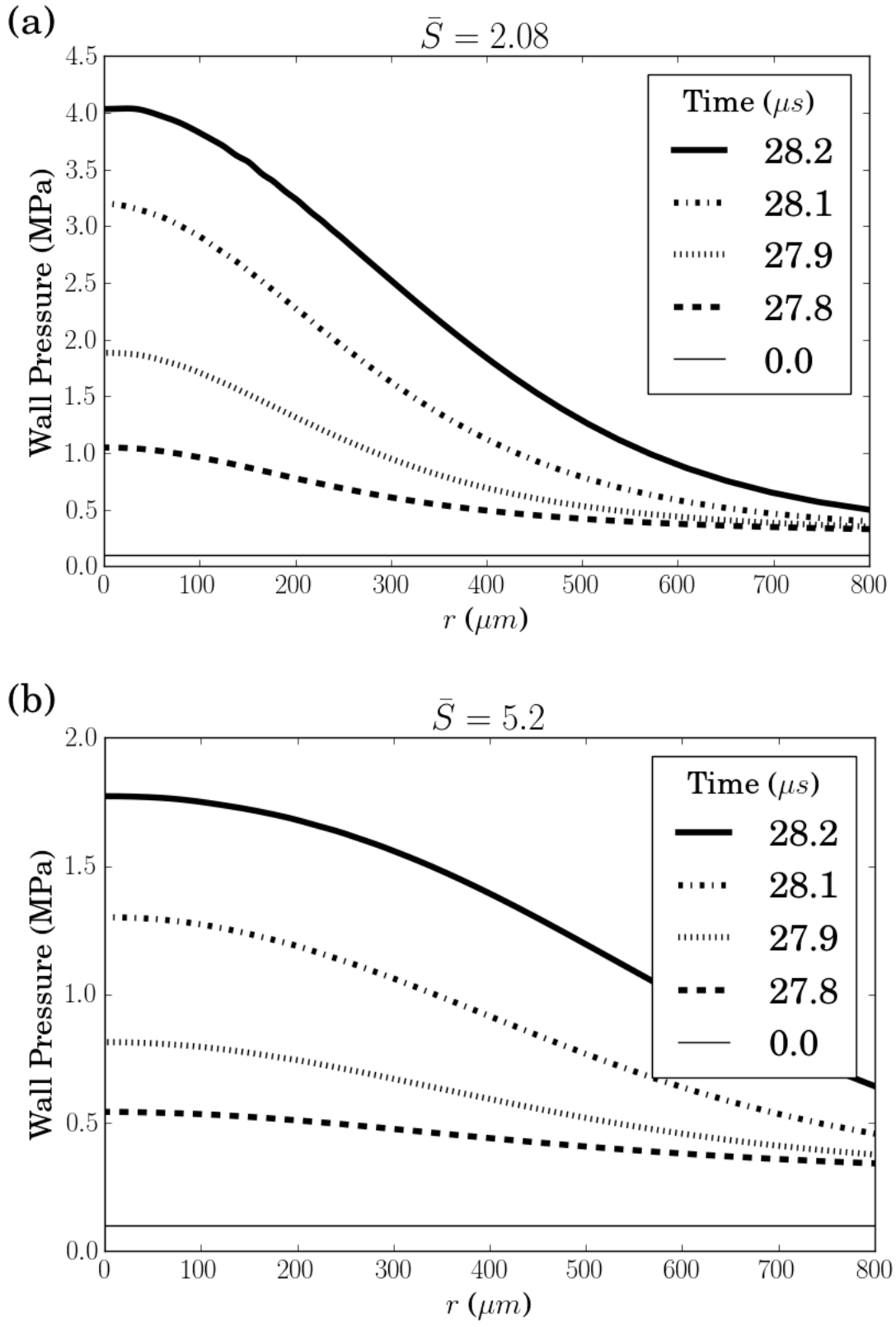

Figure 6.21. The wall pressure $(z = 0)$ in the radial direction (r) at various times for two cases: (a) $\bar{S} = 2.08$ and (b) $\bar{S} = 5.2$

6.11.4 Comparison of the ADGC model to Previous Models

The previously developed fully compressible models that capture the growth and collapse of a near-wall bubble are (1) the Rayleigh growth and collapse (RGC) model [4, 37] and (2) the RP growth initialised collapse (RPGI) model (Chapter 4). Here we compare the acoustically-driven growth and collapse (ADGC) model that is developed in this Chapter to the RGC model (section 6.11.4.1) and the RPGI model (section 6.11.4.2).

6.11.4.1 Comparison of the ADGC model to Rayleigh growth and collapse (RGC)

In this section, we compare the acoustically-driven growth and collapse (ADGC) to a previously developed model of bubble growth and collapse, which we refer to as the Rayleigh growth and collapse (RGC). The RGC is different from the Rayleigh collapse (RC) described in section 4.4.6. The Rayleigh collapse (RC) is where a bubble is collapsed from an initial condition where the bubble is at a low pressure and the surrounding fluid is at a uniform high pressure [4, 26-38]. The RGC is given by the opposite case, where initially the bubble is at a high pressure and the surrounding fluid is at a uniform low pressure, resulting in the growth and collapse of the bubble [4, 37].

We first compare the bubble behaviour in the free-field (no nearby boundaries) using the RP equation to model the two cases: (1) the acoustically-driven bubble growth and collapse of a bubble in the free field (ADGC-RP) and (2) the Rayleigh growth and collapse of a bubble in the free field (RGC-RP) (section 6.11.4.1.1). Note that the acronyms, ADGC-RP and RGC-RP, for the free-field cases contain RP because they are solved using the RP equation. This is done to determine the initial bubble pressure $\left(p_{0,B}\right)$ for the RGC-RP case that will give the same maximum bubble volume $\left(V_{\max,B}\right)$ after the growth phase as the ADGC-RP case. Then, we compare the near-wall bubble collapse of both cases: ADGC and RGC (section 6.11.4.1.2) to show how the model we developed is superior in capturing the important physics involved in the acoustically-driven growth and collapse of a near-wall bubble.

6.11.4.1.1 Free-field (RP) comparison

Before we compare the ADGC to the RGC cases near a wall, we consider both cases (ADGC and RGC) in an infinite body of liquid (far away from any boundaries), referred to as the free field, described by

the RP equation (ADGC-RP and RGC-RP). For the ADGC-RP case, the acoustic pressure amplitude (p_A) is 200 kPa, and the initial bubble is at atmospheric pressure (1 atm) with an initial size $R_0 = 50\ \mu\text{m}$.

The pressure of the far-field pressure (p_∞) in the RGC-RP case is 1 atm; however, it is unclear what pressure the bubble $(p_{0,B})$ should be initialised at to produce the same magnitude in bubble growth $(R_{\max}/R_0)$ as the ADGC case. To determine the initial pressure the bubble $(p_{0,B})$ for the RGC case, we iteratively changed the initial bubble pressure until the maximum bubble volume $R_{\max}$ was the same as ADGC-RP. This allows the ADGC and RGC case to be compared when they have the same growth magnitude. The initial bubble pressure $(p_{0,B})$ of the RGC-RP case was found to be 14.3366 atm. The bubble volume over the duration of the simulation for ADGC-RP and RGC-RP are compared in Figure 6.22 as well as the bubble pressure (p_B) and the far-field pressure (p_∞). Note that the maximum volume for the two cases is the same in Figure 6.22a.

For the RGC-RP cases, the bubble is found to grow more rapidly, reaching the maximum bubble size earlier, but collapses at a slower rate, reaching its minimum volume later than the ADGC-RP case (Figure 6.22a). This indicates that the RGC cases result in a significantly less violent collapse compare to the ADGC cases. This is further supported by the maximum bubble pressure reaching a very large peak pressure in the ADGC-RP case compared to the RGC-RP case which reaches a maximum pressure during the collapse that is approximately equivalent to its initial pressure (Figure 6.22b). Note that in Figure 6.22b the maximum bubble pressure is not shown because the value is insignificant due to some of the assumptions made by the RP equation (e.g. incompressible surrounding fluid) becoming invalid at the later stages of the violent collapse [14].

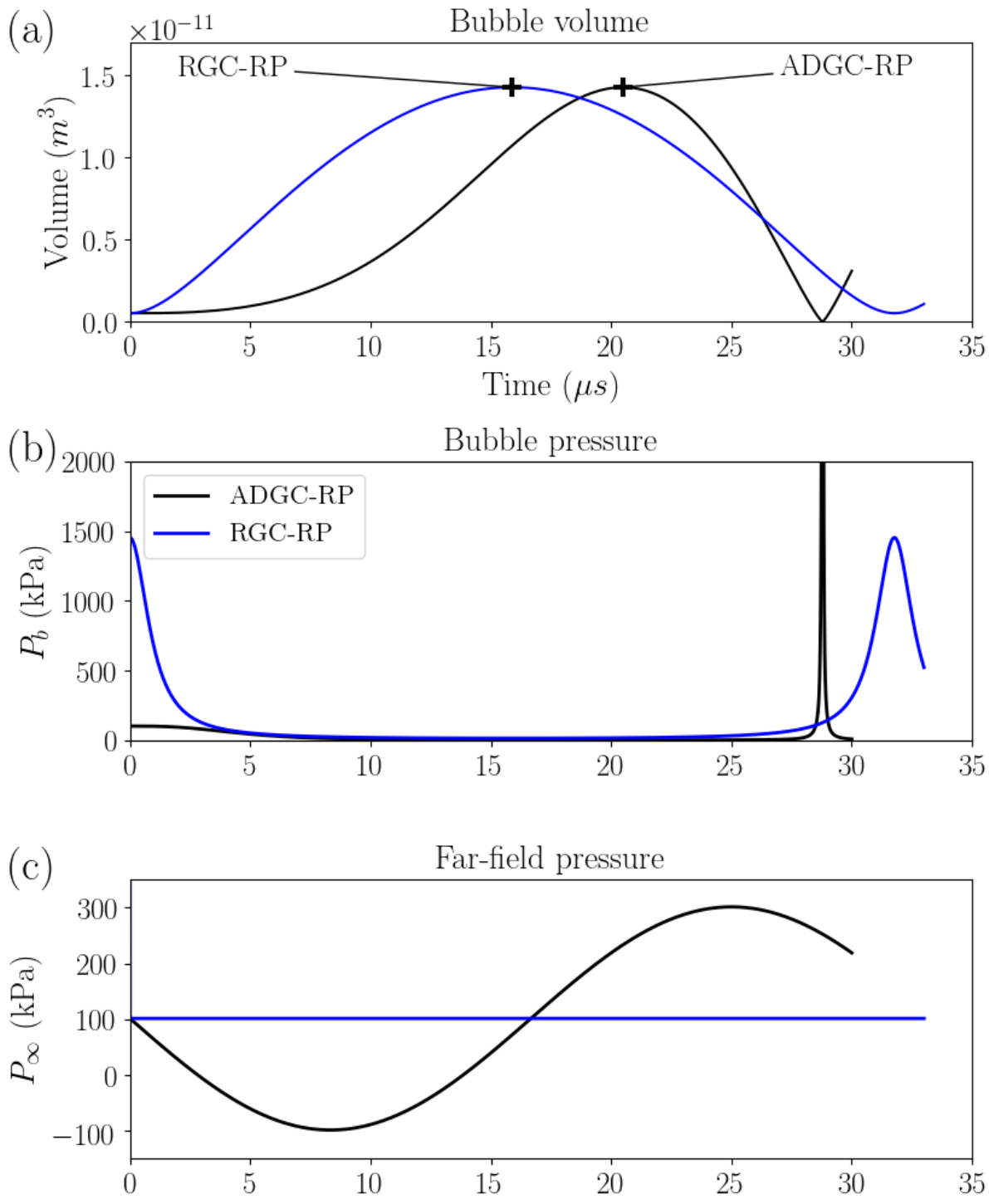

Figure 6.22. Comparison of the bubble volume for the Rayleigh growth-collapse (RGC) and the acoustically-driven growth and collapse (ADGC) given by the RP equation: RGC-RP and ADGC-RP. The RGC case results from a uniform initial condition with $p_B = 14.3366$ atm and $p_\infty = 1$ atm.

6.11.4.1.2 Near-wall comparison

The cases, ADGC and RGC, are simulated using the numerical model of a near-wall bubble with $\bar{S} = 0.78$. The ADGC near-wall collapse is the same case as presented in section 6.9 and shown in Figure 6.5a-b using the model parameters and properties provided in Table 6.1 and the domain-specific parameters in Table 6.3. The RGC is simulated using the same numerical solver as the ADGC model. The only difference between the RGC and ADGC models are that the RGC model (1) has a different boundary condition at the upper boundary of the domain, (2) has a domain that has dimensions that are approximately 10 times larger, and (3) the initial conditions are different. The upper boundary of the domain, which is a moving boundary condition in the ADGC case (see Figure 3.1), is a reflective boundary for the RGC model. The domain size is increased to ensure that there is no interaction between the bubble and the outer boundaries: $H_d = 10$ cm and $d_d = 10$ cm (see Figure 3.1). The initial condition for the RGC case the pressure in the water (p_L) is initially uniform at 1 atm (101.325 kPa) and the initial bubble pressure is at 14.3366 atm. The pressure difference between the fluid in the initial condition of the RGC case is what drives the bubble growth and the subsequent bubble collapse. The initial state of the air is given by the ideal gas law at 20 ºC (specific gas constant of air is 287 J/(kg·K))

$$\begin{bmatrix} \rho_B \\ p_B \\ \mathbf{u} \end{bmatrix} = \begin{bmatrix} 17.2625 \text{ kg/m}^3 \\ 1.4527 \text{ MPa} \\ \mathbf{0} \end{bmatrix} \tag{6.17}$$

The initial state of the surrounding water is

$$\begin{bmatrix} \rho_L \\ p_L \\ \mathbf{u} \end{bmatrix} = \begin{bmatrix} 1000.0 \text{ kg/m}^3 \\ 101.325 \text{ kPa} \\ \mathbf{0} \end{bmatrix} \tag{6.18}$$

Thus, the initial condition of the RGC numerical model is

$$\rho_1(r,z,t_0) = \rho_B,\ p(r,z,t_0) = p_B,\ \mathbf{u}(r,z,t_0) = \mathbf{0} \quad \text{for} \quad \sqrt{r^2 + (z-S)^2} < R_0 \tag{6.19}$$

within the bubble and

$$\rho_2(r,z,t_0)=\rho_L,\ p(r,z,t_0)=p_L,\ \mathbf{u}(r,z,t_0)=\mathbf{0} \quad \text{for} \quad \sqrt{r^2+(z-S)^2}>R_0 \tag{6.20}$$

outside of the bubble, where R_0 is the radius of the initial bubble and S is the standoff distance.

The evolution of the bubble volume for the RGC and ADGC cases are similar to the cases in the free-field (ADGC-RP and RGC-RP) presented in the previous section (section 6.11.4.1.1). Like the RGC-RP and ADGC-RP cases (Figure 6.22), the RGC case, the bubble is found to grow more rapidly, reaching the maximum bubble size earlier, but collapses at a slower rate, reaching its minimum volume later (Figure 6.23a). This indicates that the RGC cases result in a significantly less violent collapse compare to the ADGC cases. This is further confirmed by the peak pressure experienced by the wall being about 10 times higher in the ADGC case than the RGC case (Figure 6.23b). Also, both RGC-$\bar{S}=0.78$ and ADGC-$\bar{S}=0.78$ show a similar restriction on the growth (reduced maximum bubble volume – Figure 6.23a) due to the influence of the nearby wall when compared to the ADGC-RP and RGC-RP cases (Figure 6.22a). The maximum volume for the RGC case is approximately 30% less the RGC-RP case, and the maximum volume for the ADGC case is approximately 35% less the ADGC-RP case.

The difference in the growth rate (Figure 6.23) is primarily due to the difference in the initial condition pressure between the two cases and the difference between the evolution of the pressure in the surrounding fluid. The ADGC case has no initial pressure difference between the bubble and the surrounding fluid, and the RGC has its maximum pressure difference between the bubble and the surrounding fluid and, therefore, the acceleration of the bubble growth is initially zero for the ADGC case and the acceleration is initially at its maximum for the RGC case. The ADGC case has a transient pressure in the surrounding fluid, and the RGC has a constant far-field pressure; thus, the driving pressure and the growth rate evolves differently for the two cases.

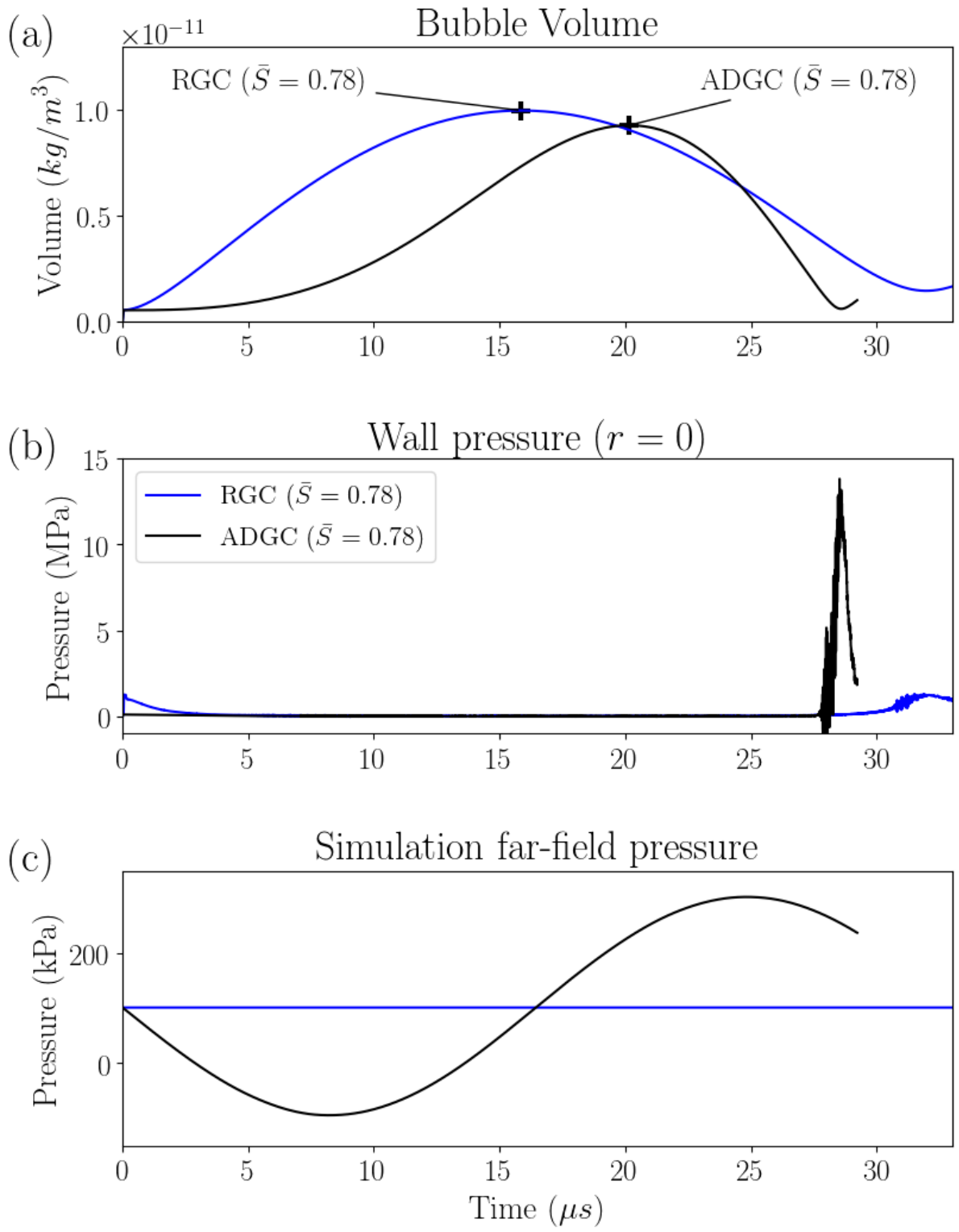

Figure 6.23. Comparison of the bubble volume, wall pressure $(z = r = 0)$, and the far field pressure for the Rayleigh growth-collapse (RGC) and the acoustically-driven growth and collapse, where $\bar{S} = 0.78$. The ADGC case is simulated using the model developed in this Chapter. The RGC case is simulated using a uniform initial condition with $p_B = 14.3366$ atm and $p_\infty = 1$ atm

The shape of the bubble during the growth and collapse are compared and contrasted for the two cases, RGC and ADGC. The interface location over the duration of the simulation for the RGC-$\bar{S}=0.78$ and ADGC-$\bar{S}=0.78$ cases are depicted in Figure 6.24 and Figure 6.25, respectively. The data used to describe Figure 6.25 is the same as is in used Figure 6.5a-b, but has been reproduced here for ease of comparison.

Despite the two cases (RGC-$\bar{S}=0.78$ and ADGC-$\bar{S}=0.78$) having different growth rates (Figure 6.23), they do result in very similar bubble shapes at the end of the growth phase (pre-collapse bubble shape). This is because for both cases the difference in pressure between the surrounding fluid and the bubble drives the growth, and the direction of the pressure forces driving the growth are very similar.

The main difference in bubble shape between the two cases occurs at the later stages of the collapse: the RGC-$\bar{S}=0.78$ case forms a larger, more stable (fewer interface instabilities) toroidal bubble at the end of the collapse than the ADGC-$\bar{S}=0.78$ case. This is primarily due to the initial state of the RGC bubble having a pressure that is approximately 14 times larger: 14.3366 atm compared to the ADGC case where the pressure bubble is initially at 1 atm (Table 6.1). At the later stages of the collapse, when the bubble volume is near its initial volume $\left(\approx V_0\right)$, the RGC bubble pressure will be about 14 times larger than the ADGC bubble, cushioning the collapse. This is because a polytropic bubble returns to its initial pressure $\left(p_{0,B}\right)$ when the bubble collapses back to its initial volume $\left(V_0\right)$

$$p_B = p_{0,B}\left(\frac{V_0}{V}\right)^{\eta}. \tag{6.21}$$

The cushioning of the collapse results in the lower rate of collapse (Figure 6.23) and the larger more stable bubble shape at the end of the collapse (compare Figure 6.24 to Figure 6.25).

It is important to note that the RGC case is developed to represent a case where the bubble and surrounding fluid are at a very high pressure (e.g. 14.3366 atm) and, suddenly, the pressure of the surrounding fluid drops (e.g. to 1 atm). This case is designed to mimic bubble hydrodynamic flow applications where the flow abruptly changes from a high pressure to a low pressure, and, subsequently,

the stable bubble at a high pressure then grows and collapses because of the drop in the pressure of the surrounding liquid [4]. An alternative application which the RGC model may model well is the laser or spark induced bubble growth and collapse. In the laser or spark induced cavitation, the laser or spark is focused on a location in the liquid near a wall [26, 33, 35]. The focused energy results in a high localised temperature and the formation of a cavitation bubble. This bubble is then at a very high temperature and pressure. The bubble, which is at a higher pressure than the surrounding fluid, grows large and then collapses violently.

The only difference between the state of the bubbles in the two cases, hydrodynamic and laser/spark induced, is that the high-pressure hydrodynamic bubble is very dense (ρ); whereas, the high-pressure laser/spark induced bubble is at a large temperature (T). The RGC case the initial state of the bubble air is $(\rho_B, p_B, T_B) = (17.2625 \text{ kg/m}^3,\ 14.3366 \text{ atm},\ 20\ ^\circ C)$ to simulate the very dense high-pressure bubble. If we were to model the high-temperature bubble case where the initial density of bubble air is the density of air at atmospheric pressure (1.204 kg/m^3), and the bubble is at the same high pressure as the RGC case (14.3366 atm), the initial high temperature of the bubble would be 4766.2 ºC, (determined using the ideal gas law). However, the polytropic bubble pressure is independent of temperature and density, so, given the same initial pressure $(p_{0,B})$, the bubble pressure will behave the same over the duration of the growth and collapse (see Eq. (6.21). In other words, the RGC cases (hydrodynamic high-density case and laser/spark high-temperature bubble) result in the same bubble dynamics as long as they have the same initial bubble pressure $(p_{0,B})$.

It is also important to note that the previous discussion on the RGC bubble case compares a high-pressure and high-temperature bubble composed fully of air, finding that the results are fully dependent on the initial bubble pressure and independent of the bubble temperature and density. However, consideration of the temperature of the bubble may be more important if the presence of vapour is considered in the bubble. The partial pressure of water vapour is dependent on the temperature and may result in differences in the two RGC cases.

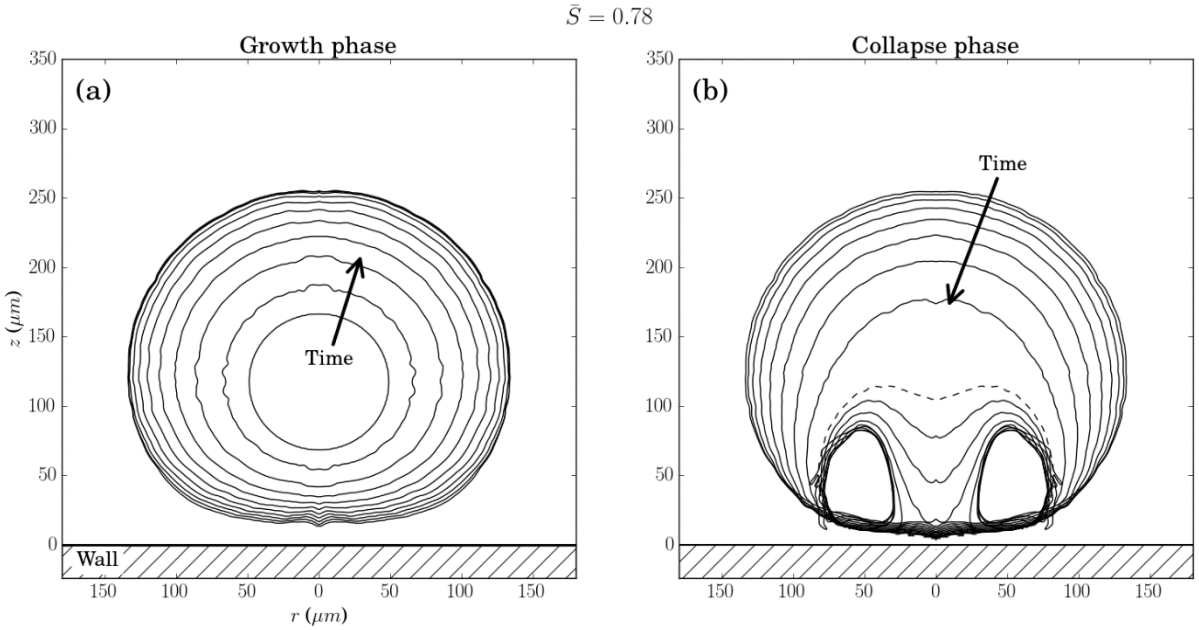

Figure 6.24. The Rayleigh (a) growth and (b) collapse of a bubble near a wall $\left(\bar{S} = 0.78\right)$. The bubble interface contour lines $\left(\alpha_1 = 0.95\right)$ are stepped in time in increments of 1.65 μs until the dashed contour line where the interface is stepped in time in increments of 0.41 μs

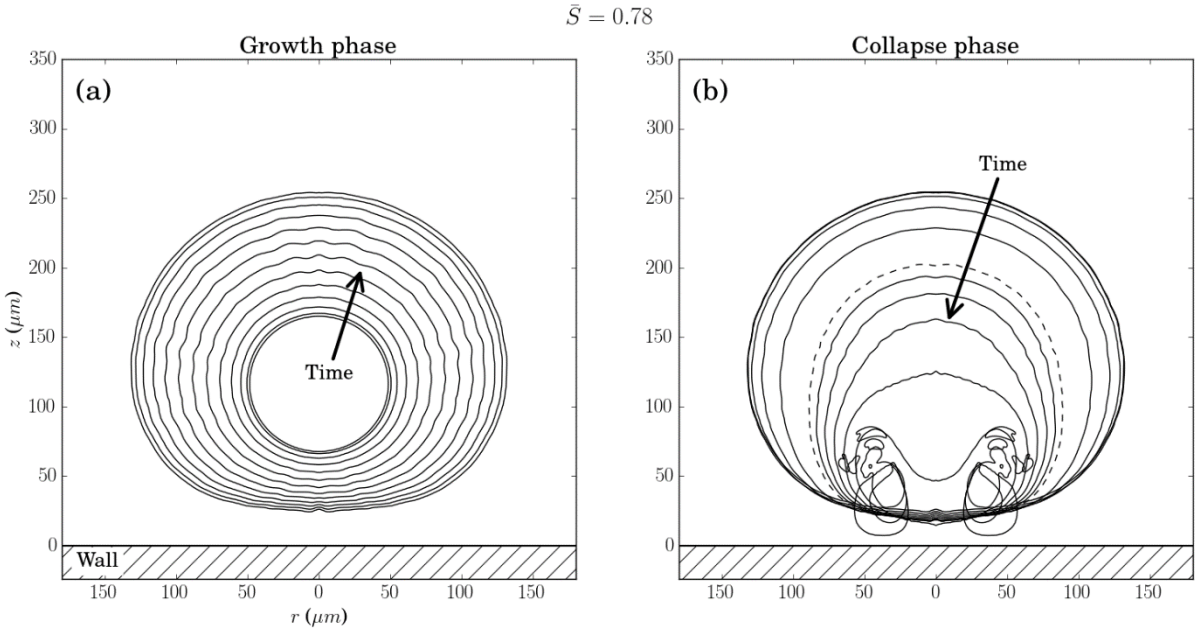

Figure 6.25. The acoustically-driven (a) growth and (b) collapse of a bubble near a wall $\left(\bar{S} = 0.78\right)$ - similar to Figure 6.5a-b. The bubble interface contour lines $\left(\alpha_1 = 0.95\right)$ are stepped in time in increments of 1.65 μs until the dashed contour line where the interface is stepped in time in increments of 0.41 μs.

The subsequent pressure on the near-wall for the RGC- $\bar{S} = 0.78$ and ADGC- $\bar{S} = 0.78$ cases is presented in Figure 6.23, as well as the bubble volume and the far-field pressure. It is apparent from Figure 6.23b that the pressure experienced by the wall in the ADGC- $\bar{S} = 0.78$ case is much larger: 14 MPa compared to 1 MPa of the RGC- $\bar{S} = 0.78$ case. The RGC bubble pressure that cushions the collapse, discussed previously, is the reason for the less violent collapse (Figure 6.23),

It becomes apparent for an ultrasound-induced collapse that the ADGC model does a better job of representing the acoustically-driven bubble in a physically correct manner. The RGC case does not attempt to consider a physically correct state of a bubble that is acoustically-driven. The Rayleigh growth-collapse (RGC) is unable to approximate the near-wall pressure for an acoustically-driven growth and collapse of a bubble. Thus, the ADGC model we developed is essential to capture the physics of the acoustically-driven growth and collapse of a near-wall bubble.

6.11.4.2 Comparison of the ADGC model to the RPGI model

Here we compare the growth and collapse simulation of the acoustic bubble to the previously developed RPGI model that uses the RP equation to initialise the collapse simulation (see Chapter 4). The benefits of the RP equation to model growth include, less numerical diffusion (sharper interface), reduced computational time, easy to change between adiabatic and isentropic growth, and simple to include the effects of surface tension and viscosity into the growth phase. The key limitations for the RPGI model are that it assumes that the bubble growth is uninfluenced by the near-wall and the spatial variations in the acoustic pressure field. To investigate the limitations introduced by the RP growth assumption (RPGI model), we compare the results of the two cases using the RPGI model with the simulated growth and collapse (ADGC) of the two cases: case 1 - $\bar{S} = 0.78$ and case 2 - $\bar{S} = 1.14$. In this section, both models (RPGI and ADGC) use the model parameters and properties provided in Table 6.1 and the domain-specific parameters in Table 6.3. From the RPGI model, the bubble collapse shape evolution for case 1 - $\bar{S} = 0.78$ and case 2 - $\bar{S} = 1.14$ is depicted in Figure 6.26. The bubble shape over the duration of the collapse from the ADGC model is depicted for the two cases, $\bar{S} = 0.78$ and $\bar{S} = 1.14$, in Figure 6.27, where the figure is reproduced from Figure 6.5b Figure 6.5d for ease of comparison.

When the normalised standoff distance is less than unity $\left(\bar{S}<1\right)$, as in Case 1 - $\bar{S}=0.78$, the assumption of spherical growth (RP growth) results in the attachment of the bubble to the wall, see Figure 6.26a. In practice, as a bubble that is initially unattached to a wall grows, it is always separated from the wall by a layer of liquid [4, 91], see Figure 6.27a. The limitation of the RPGI model is that it cannot capture this important physical condition. Also, the RP growth overestimates the size as it does not capture the influence of the near-wall, which restricts the bubble growth, see section 6.10.1 for details about the near-wall restricting the bubble growth. The difference in the final bubble size for the $\bar{S}=0.78$ case is shown in the comparison between Figure 6.26a and Figure 6.27a.

In Case 2 where the standoff distance is $\bar{S}=1.14$, the RP growth assumption of the RPGI model results in a bubble that does not connect to the wall (Figure 6.26b). From the simulated growth (ADGC model) depicted in Figure 6.27b, the bubble shape at the maximum size is approximately spherical which is captured correctly using the RP initialisation (RPGI model - Figure 6.26b), but, again, the RP growth approximation overestimates the size of the bubble after the growth phase.

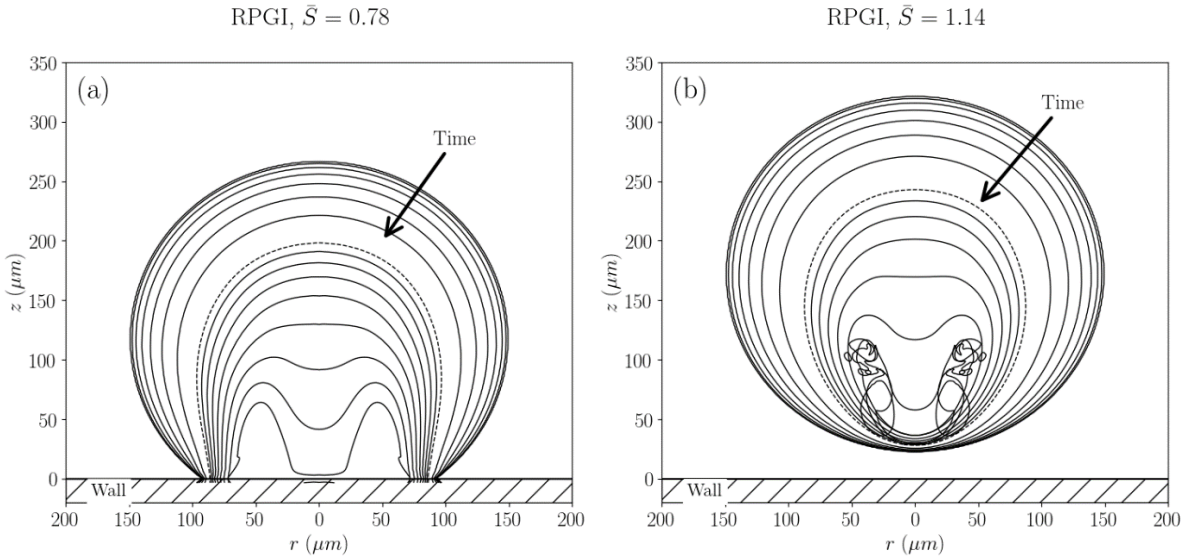

Figure 6.26. The collapse of a bubble using the RPGI model, where the standoff distance is (a) $\bar{S} = 0.78$ and (b) $\bar{S} = 1.14$.

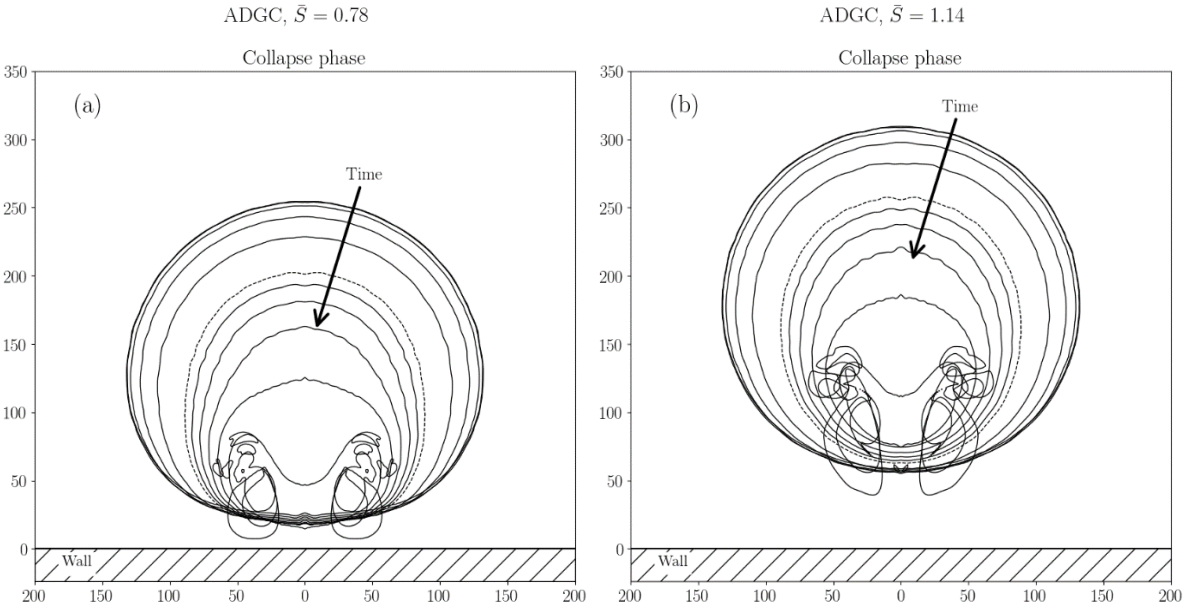

Figure 6.27. Collapse of a bubble using the ADGC model, where the standoff distance is (a) $\bar{S} = 0.78$ and (b) $\bar{S} = 1.14$. (a) and (b) are reproduced from Figure 6.5b Figure 6.5d, respectively, for ease of comparison to the collapse shape from the RPGI model (Figure 6.26).

During the simulated growth (ADGC model), the bubble moves away from the near-wall, increasing the standoff distance, as seen in section 6.10.4. However, the RP initialisation (RPGI model) does not capture the displacement of the bubble during the growth phase. This means that for the RPGI model

the initial standoff distance (at the start of the collapse when $R = R_{\max}$) will be less than the standoff distance of the bubble after the ADGC simulated growth. For example, Case 2 has a $\bar{S} = 0.78$ at the beginning of the collapse phase for the RPGI model, but for the ADGC simulated growth case, where initially $\bar{S} = 0.78$, the standoff distance increases to $\bar{S} = 0.90$ over the duration of the growth phase. Thus, $\bar{S} = 0.78$ for the RPGI model and $\bar{S} = 0.90$ for the ADGC model when the bubble is at its maximum volume.

As stated previously, the RP growth assumption results in an over-approximation of the bubble size before the collapse and does *not* capture the non-sphericity or the bubble displacement of the near-wall bubble growth. Next, we investigate the influence of the RP growth assumption on the subsequent collapse by comparing the results of the two models: the RPGI model and the ADGC model. To show the influence of the RP growth assumption on the subsequent collapse, we present the pressure experienced by the wall for near-wall bubbles at various standoff distances: $\bar{S} = 0.52$, $\bar{S} = 0.78$, $\bar{S} = 0.94$, $\bar{S} = 1.14$, $\bar{S} = 2.08$, and $\bar{S} = 5.2$, see Figure 6.28. The maximum pressure experienced by the wall during for all of these cases is presented in Figure 6.29 (values are provided in Table 6.8).

The peak wall pressure is delayed for the RPGI collapse for all the standoff distances presented, see Figure 6.28. This is a direct result of the reduced growth due to the nearby wall: the larger bubble at the beginning of the collapse phase for the RPGI case results in a longer collapse duration.

The larger bubble that is given by the RPGI model also results in a more violent collapse case, and the peak pressure is slightly larger in the closer cases, $\bar{S} = 0.52$, $\bar{S} = 0.78$, $\bar{S} = 0.94$, $\bar{S} = 1.14$, $\bar{S} = 2.08$ (Figure 6.28a-d). The further away cases, $\bar{S} = 2.08$, and $\bar{S} = 5.2$, the RPGI model results in a good approximation of the pressure experienced by the wall, see Figure 6.28e-f and Figure 6.29. Thus, the RP growth assumption of the RPGI model becomes more valid as the bubble standoff distance increases, as anticipated.

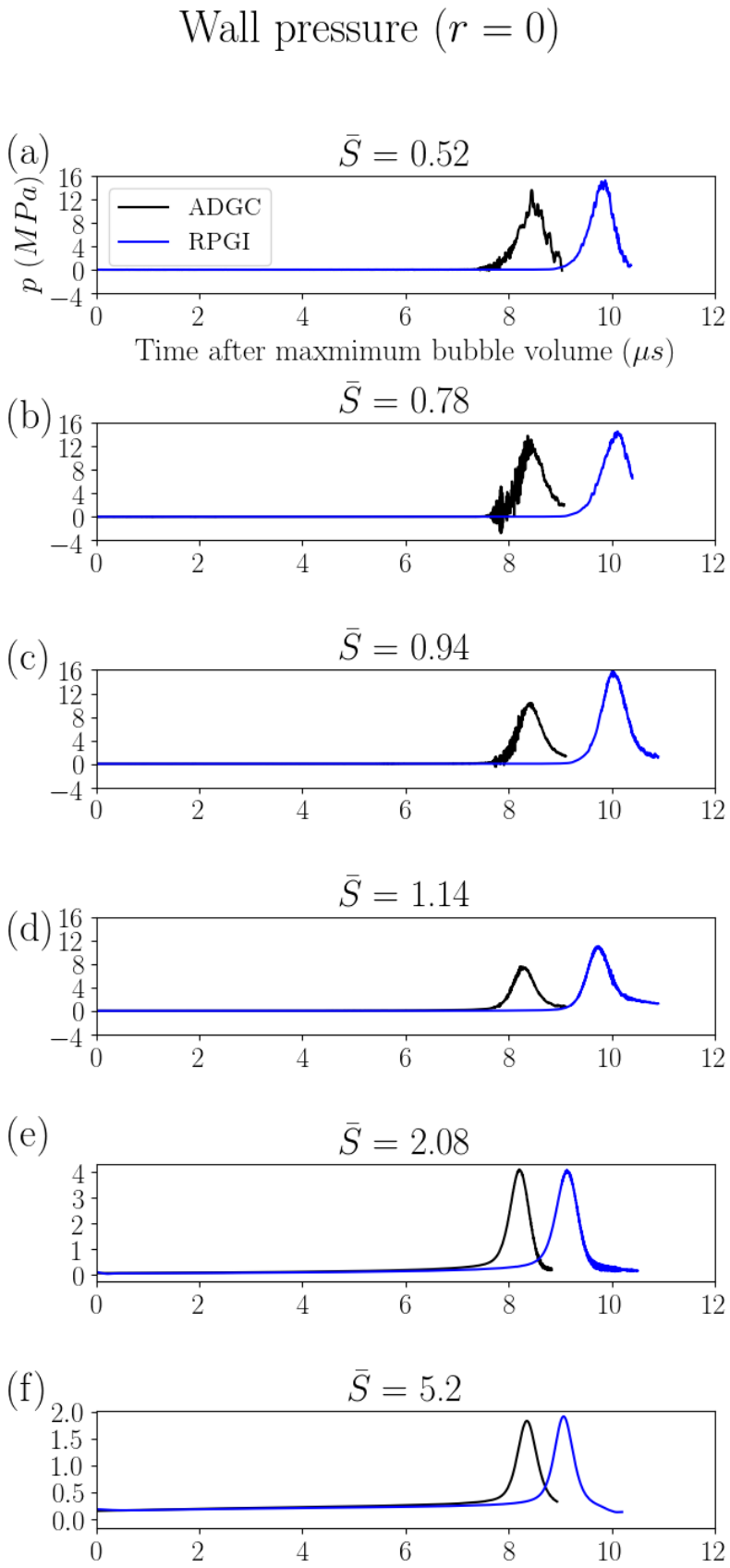

Figure 6.28. Comparison of the wall pressure for the ADGC cases to the RPGI cases for various standoff distances: $\bar{S} = 0.52$, $\bar{S} = 0.78$, $\bar{S} = 0.94$, $\bar{S} = 1.14$, $\bar{S} = 2.08$, **and** $\bar{S} = 5.2$.

Table 6.8. Comparison of the maximum pressure experienced by the wall over the duration of the collapse between the ADGC model and the RPGI model for various standoff distances: $\bar{S}=0.366$, $\bar{S}=0.52$, $\bar{S}=0.78$, $\bar{S}=0.94$, $\bar{S}=1.14$, $\bar{S}=2.08$, and $\bar{S}=5.2$.

$\bar{S}$		0.366	0.52	0.78	0.94	1.14	2.08	5.2
Maximum wall pressure (MPa)	ADGC	12.21	13.60	13.82	10.39	7.57	4.10	1.83
	RPGI	15.90	15.23	14.55	15.83	11.03	4.07	1.91

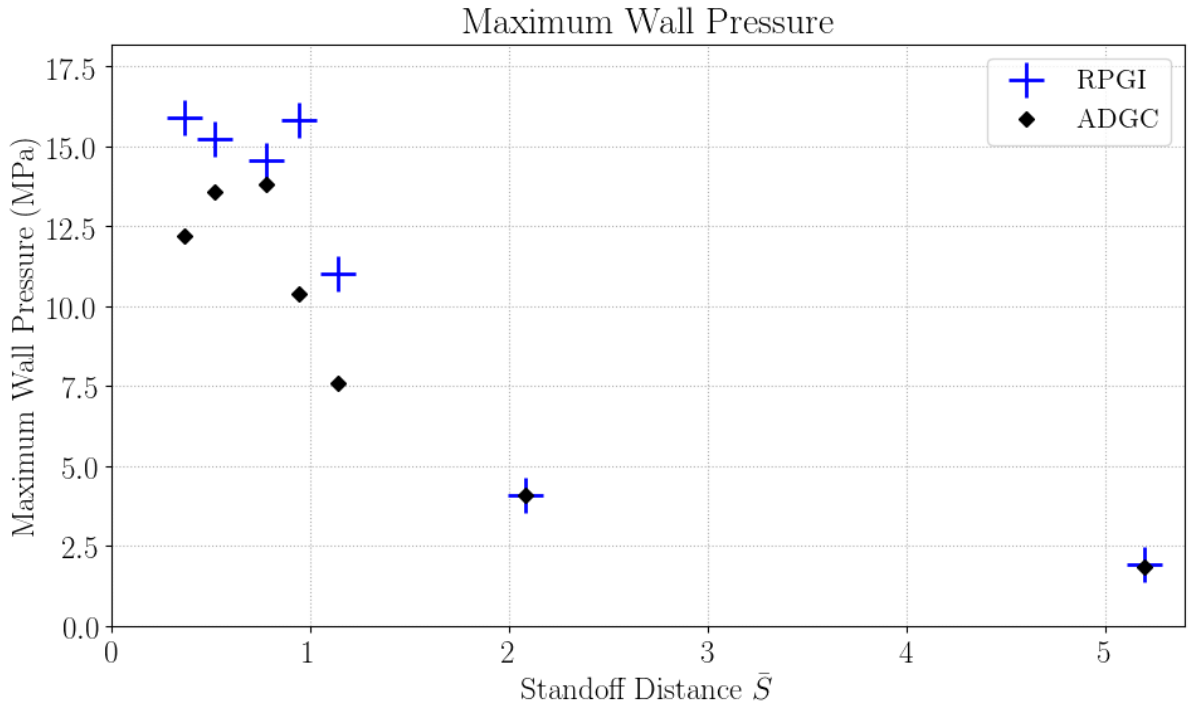

Figure 6.29. The maximum pressure experienced by the wall over the duration of the collapse for various standoff distances: $\bar{S}=0.366$, $\bar{S}=0.52$, $\bar{S}=0.78$, $\bar{S}=0.94$, $\bar{S}=1.14$, $\bar{S}=2.08$, and $\bar{S}=5.2$.

6.12 The influence of the Interface Sharpness

In the present ADGC model, the numerical handling of the multiphase system (Chapter 3) is anticipated to result in the numerical diffusion of the bubble interface (air-water interface). To reduce the numerical diffusion of the interface the model uses high order WENO reconstruction (WENO5) (section 3.3); however, numerical diffusion of the fluid volume fraction (α_1 - Eq. (2.5)) at the bubble interface still occurs. The ADGC model results in a longer simulation time compared to RPGI simulation because it directly simulates both the growth and collapse phases, not just the collapse phase. For example, in the comparison of the ADGC and RPGI models in section 6.11.4.2, the duration of the RPGI simulation was about 10 μs, and the duration of the ADGC simulation was about 29 μs. Therefore, more numerical diffusion is anticipated to occur in the ADGC simulation compared to the RPGI.

Here we investigate the extent of the numerical diffusion by analysing the sharpness of the bubble interface. To quantify the sharpness of the interface, we take the average distance between the contour lines $\alpha_1 = 0.01$ and $\alpha_1 = 0.99$. When the bubble is at its maximum size, we assume the bubble is approximately spherical and, thus, in cylindrical coordinates the contour lines $\alpha_1 = 0.01$ and $\alpha_1 = 0.99$ are approximately circular. Thus, the average distance between the contour lines, $\alpha = 0.01$ and $\alpha = 0.99$, is the change in radius of the circular contour lines. The change in the radius between the contour lines (Δr_C) is approximated as using the area within the contour lines (A_C)

$$\Delta r_C = \sqrt{\left(\frac{A_C\left(\alpha_1 = 0.01\right)}{\pi}\right)} - \sqrt{\left(\frac{A_C\left(\alpha_1 = 0.99\right)}{\pi}\right)} \tag{6.22}$$

As presented in section 4.3.3, the volume fraction is initialised with a smoothing of the initial material interface over a few grid cells to increase the numerical stability. The smoothing of the interface is implemented in the initialisation of the volume fraction of the bubble (α_1) using

$$\alpha_1(r,z,t_0)=\left(\frac{|z|}{|z|+|r|}\right)\left(\frac{1-\tanh\left(\frac{\beta}{\Delta z_{\min}}\left(\sqrt{r^2+(z-S)^2}-R_{\max}\right)\right)}{2}\right)+\left(\frac{|r|}{|z|+|r|}\right)\left(\frac{1-\tanh\left(\frac{\beta}{\Delta r_{\min}}\left(\sqrt{r^2+(z-S)^2}-R_{\max}\right)\right)}{2}\right)^2 \quad (6.23)$$

where $\Delta r_{\min}$ and $\Delta z_{\min}$ are the dimensions of the cells in the refined region of the domain (Table 6.1). β is a coefficient which governs the amount of interface smoothing [77]: the present study uses $\beta=2$.

Recall the ADGC and RPGI cases presented in the previous section (section 6.11.4.2) where $\bar{S}=1.14$ (Figure 6.26b and Figure 6.27b). At the conclusion of the simulated growth phase of the ADGC model, when the bubble reached its maximum volume (pre-collapse bubble), the interface thickness (Δr_C) was approximately 6 µm. In contrast, the RPGI model, where the interface smoothing parameter is $\beta=2$, produces an initial condition with an interface thickness (Δr_C) of approximately 2 µm. Thus, the RPGI model results in an interface prior to the collapse phase that is 3 times sharper than the interface of the pre-collapse bubble after the simulated growth phase of the ADGC model.

We attempt to quantify the significance of this additional numerical diffusion that is introduced in the ADGC model by simulating the growth phase., by quantifying the effect the interface sharpness has on the pressure experienced by the near-wall. As previously discussed, the simulated growth results in a less sharp interface, but the significance of the reduced interface sharpness is unclear. To investigate the influence of the interface sharpness on the pressure experienced by the wall, we compare two cases: the RPGI model with an interface smoothing parameter $\beta=2$ and a smoother interface case where $\beta=2/3$ which results in an interface thickness 6 µm: equivalent to the interface thickness after the ADGC simulated growth. The parameters used for the RPGI are the same as in the previous section (section 6.11.4.2) where $\bar{S}=1.14$; the model parameters and properties provided in Table 6.1 and the domain-specific parameters in Table 6.3. The pressure experienced by the near-wall for the two collapse

cases, smooth and sharp interface, are depicted in Figure 6.30. The subsequent peak pressure experienced by the wall is 11 MPa for the sharp interface and 9.7 MPa for the smooth interface. Thus, the sharpening of the interface (approximately three times sharper) resulted in a peak pressure that increased by approximately 14 %. The reason the smooth interface results in a less violent collapse is because more numerical diffusion of the air-water interface results in cushioning of the collapse.

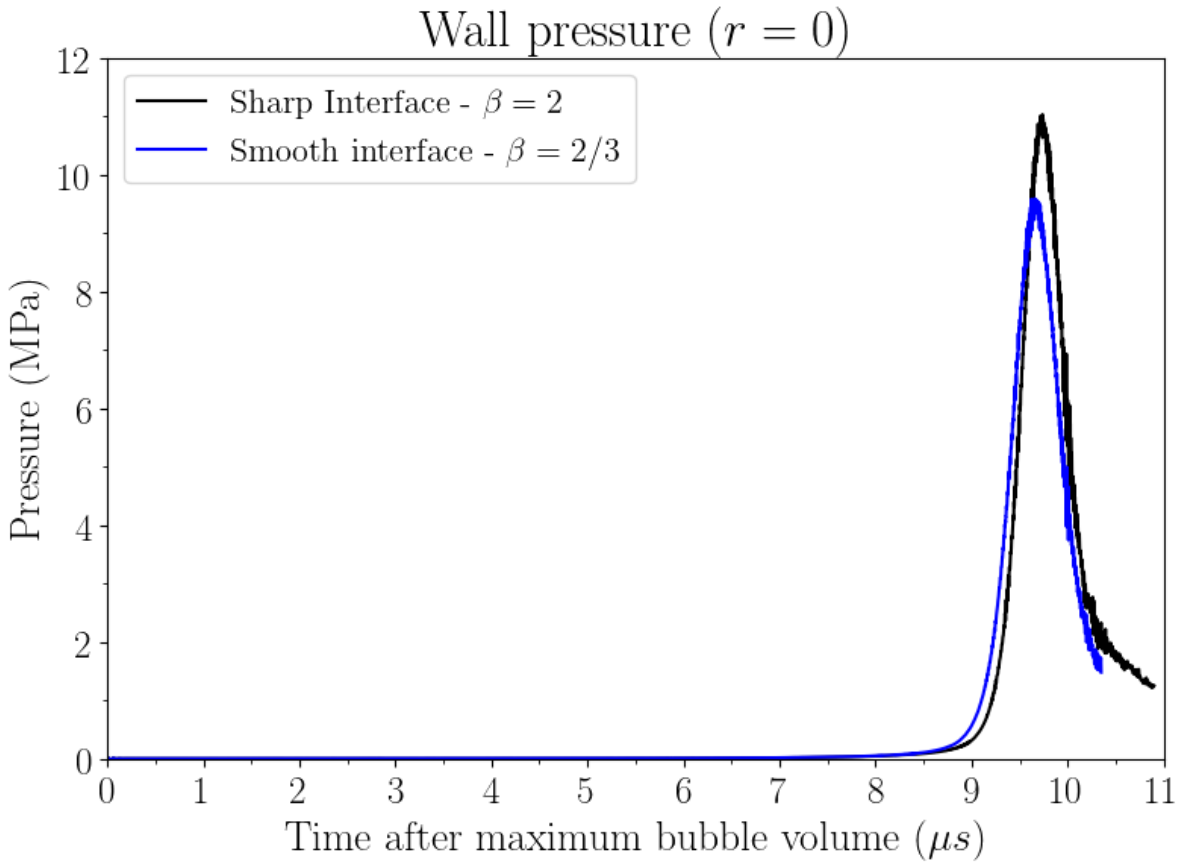

Figure 6.30. A comparison of the pressure experienced by the wall during the RPGI collapse of a bubble with a sharp interface $(\beta = 2)$ vs the smooth interface $(\beta = 2/3)$. Results are for case $\bar{S} = 1.14$.

6.13 Summary

In this Chapter, we developed a fully compressible model that is able to capture the growth and collapse of a near-wall bubble in an acoustic field. The growth of the bubble is investigated by considering the evolution of the bubble volume at various standoff distances of the bubble from the wall. The near-wall is found to significantly restrict the growth rate of the bubble and the maximum bubble volume achieved

after the growth phase. As expected, the wall is more restrictive on the growth the closer the initial bubble is to the wall. A less anticipated finding was that the bubble growth rate was still significantly restricted by the wall relatively far away from the wall $\left(\overline{S} = 34.41\right)$. The wall also significantly changed the sphericity of the bubble but only for bubbles that were very close to the wall $\overline{S} < 1$. The displacement of the bubble centroid over the duration of the growth phase was significant out to about $\overline{S} = 5$.

Another significant influence on the growth of the bubble that is investigated is the position of the bubble in the acoustic field. For the case presented, a standing wave between the transducer face and the wall occurs, with a pressure antinode at the wall. The pressure amplitude experienced by the bubble reduces as the standoff distance of the bubble increases. The standing wave is dependent on the domain depth and the frequency of the ultrasound. The reduction in the pressure amplitude slightly reduced the bubble growth at approximately $\overline{S} = 7.8$. Further from the wall, at $\overline{S} = 34.41$, the large reduction in the pressure amplitude ($\approx 23\%$) dramatically reduced the growth of the bubble.

The maximum peak wall pressure is considered for various standoff distances. The maximum peak wall pressure of 13.8 MPa occurred for an initial standoff distance of $\overline{S} = 0.78$. The larger pressure occurs at this standoff distance because if it were closer to the wall, the growth and collapse would be restricted by the near-wall, reducing the momentum developed during the collapse. If the bubble is further away from the wall the pressure experienced by the wall is less due to the transmission loss of the bubble jet pressure.

The comparison of the acoustically-driven growth and collapse (ADGC) model to the previously developed Rayleigh growth and collapse (RGC) model highlighted the limitations of the RGC model. The ADGC model is superior to the RGC model for simulations of the bubble dynamics in acoustic applications because it captures the state of the bubble correctly: the ADGC bubble is initially in pressure equilibrium with the surrounding liquid; whereas, the RGC bubble is initially at a far higher pressure than the surrounding liquid. Also, the ADGC model captures the transient far-field pressure of the acoustic field; the RGC model has a constant far-field pressure and, therefore, does not consider the

acoustic input. The RGC model is more suited for other applications like hydrodynamic flow cavitation and spark or laser-induced cavitation applications.

Also, the comparison of the acoustically-driven growth and collapse (ADGC) model to the Rayleigh-Plesset growth initialised collapse (RPGI) model, which was developed in Chapter 4, highlighted the limitations of the RPGI model. The influence of the wall on the bubble growth is considered in the ADGC model but is neglected in the RPGI model. The use of the ADGC model is more critical for a bubble that is close to the wall, especially when the normalised standoff distance was less the unity $\left(\bar{S}<1\right)$. For ADGC model when $\bar{S}<1$, the influence of the wall changed the pre-collapse bubble shape so that it did *not* connect to the wall; however, the RPGI predicts that the bubble to attach to the wall if $\bar{S}<1$. Close to the wall $\bar{S}\leq 2$, the RPGI overpredict the pressure experienced by the wall, but far from the wall $\bar{S}>2$ the RPGI model provides a good approximation of the pressure experienced by the near-wall. The ADGC model is, therefore, an important advance in modelling the dynamics of a bubble close to the wall.

Chapter 7

Bubble Growth and Collapse in a Bubble Cloud

7.1 Introduction

In acoustic cavitation applications, multiple cavitation bubbles are typically present in the coupling fluid. A cluster of cavitation bubbles is referred to as a bubble cloud. Our previous studies have focused on a single bubble to investigate the dynamics of growth and collapse. However, the influence of nearby bubbles is an important consideration.

Numerical studies of bubble cloud dynamics have been conducted previously [47-53]. The model of bubble clouds either model a bubble mixture [48-51, 104] or a multiphase system [47, 53], explicitly considering the different phases (e.g. air and water), in a similar manner to the multiphase model developed in Chapter 2 and Chapter 3. The bubble mixture method typically assumes the bubbles are always spherical [48-51, 104] and, therefore, is unable to capture the non-spherical collapse of the near-wall bubbles. Modelling the bubble cloud using the multiphase system becomes computationally expensive because the model developed in Chapter 2 and Chapter 3 needs to be extended to a 3D model to capture multiple bubbles.

The recently developed numerical model of a bubble cloud subjected to an acoustic source captures the bubble-mixture using volume-averaged equations of motion, and the gas phase is modelled using a Lagrangian point-bubble approach considering the bubbles in the cloud as spherical [50]. Thus, the numerical model is very different from the multiphase model we use, see Chapter 2 and Chapter 3. Figure 7.1a provides a representative depiction of the case that is described in [50]. In Figure 7.1a, the bubble cloud, which is small relative to the size of the domain, is positioned in the centre of the domain and the domain is sufficiently large to mimic bubble cloud in free space. The model is used to capture the dynamics of the bubble cloud when it interacts with the incident acoustic wave (Figure 7.1a).

The cloud behaviour we wish to model in this Chapter concerns the case in which the cloud occupies a larger portion of the domain and is near a wall, see Figure 7.1b. This is the case in applications like sonoporation experiments where the ultrasound transducer occupies a large portion of the domain [105]. Figure 7.1 provides a depiction that highlights the fundamental differences between the current study and the models of previous works [50]. The key difference is that the previous models the cluster of bubbles in free space and in the case we intend on modelling (Figure 7.1b) the bubbles are near a wall and occupies a large portion of the domain. In other words, the existing models do not consider a near-wall bubble cloud that occupies a large portion of the domain. The cloud occupying a large portion is an important consideration because the far field pressure is expected to be significantly influenced by the cloud size because of the presence of bubbles changing the bulk fluid properties (the presence of multiple bubbles in water changes the compressibility of the bulk fluid). Whereas, in the previously investigated case [50] (Figure 7.1b), the bubble cluster only composes a small portion of the domain so it does *not* influence the far-field pressure or the magnitude of the incident acoustic pressure.

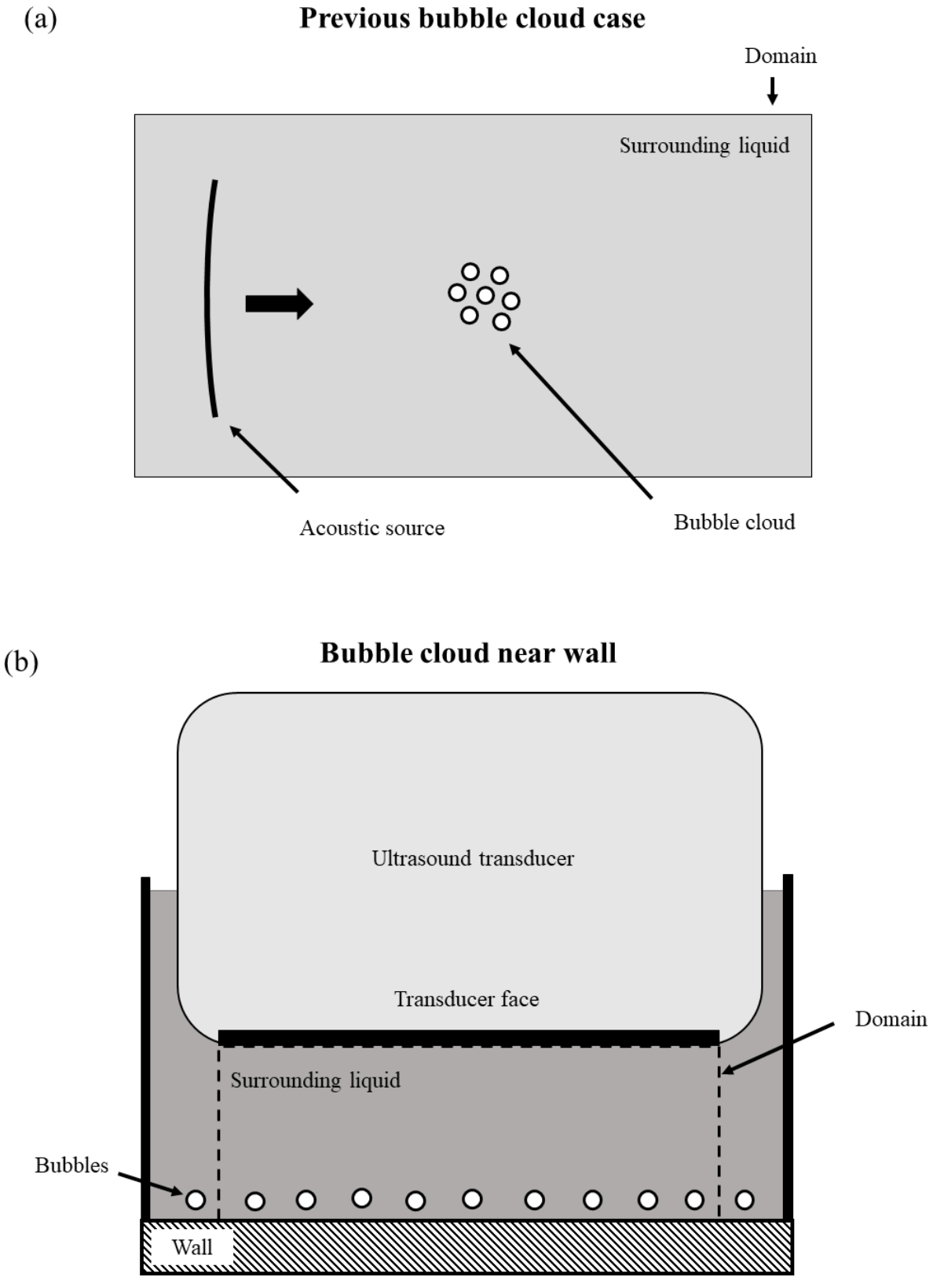

Figure 7.1. Comparison of (a) the bubble cloud near a wall that intends to model to (b) the system that is model in [50] designed to mimic a bubble cloud in free space subjected to an ultrasound field.

In this brief Chapter, we investigate the influence of nearby bubbles on the growth and collapse behaviour of a single bubble. Directly modelling all of the bubbles in a cloud of bubbles using the numerical method presented (Chapter 3) is not feasible due to the computational cost. Therefore, we make some assumptions and simplifications to capture the influence of near bubbles on the acoustically-driven bubble using the model in axisymmetric cylindrical coordinates.

7.2 Methodology

We consider an idealised bubble cloud is an infinite array of equally spaced bubbles, where all of the bubbles are the same size and are arranged in a single layer at the same standoff distance, see Figure 7.2. The idealised bubble cloud means that only one bubble needs to be modelled if the symmetry boundaries are applied around the bubble (Figure 7.2). However, the symmetry boundaries around one bubble make a rectangular cuboid; therefore, a fully three-dimensional (3D) model is required. The extension of the numerical method of the 2D axisymmetric cylindrical model developed in Chapter 3 to 3D is trivial [39]; however, the computational expense is large. The 3D model is not feasible as the 2D axisymmetric cylindrical model already requires a large amount of computational time and resources.

A simplification is required to apply the symmetry boundary condition to the model in axisymmetric cylindrical coordinates. We use a symmetric boundary in the radial direction, as depicted in Figure 7.3, to capture the influence of the nearby bubble. This simplification is not entirely correct as symmetry in the radial direction implies the presence of a toroidal bubble surrounding the simulated bubble. However, the boundary condition does give an approximation to the presence of near bubbles which will be used to make qualitative findings on the collapse behaviour.

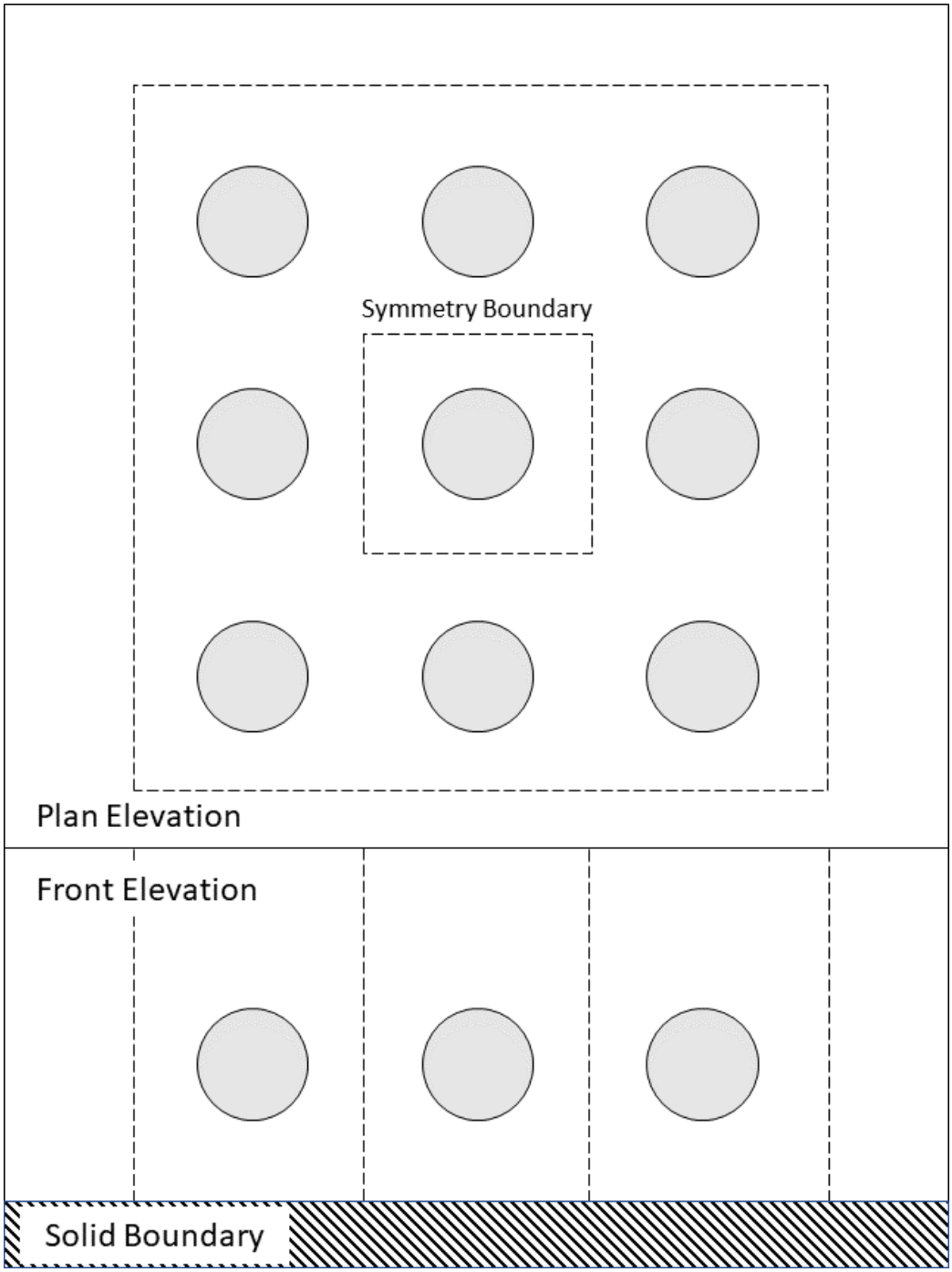

Figure 7.2. An array of bubbles making up an idealised bubble cloud, where all of the bubbles are the same size, equally spaced with the same standoff distances, and the number of bubbles in the array is infinite.

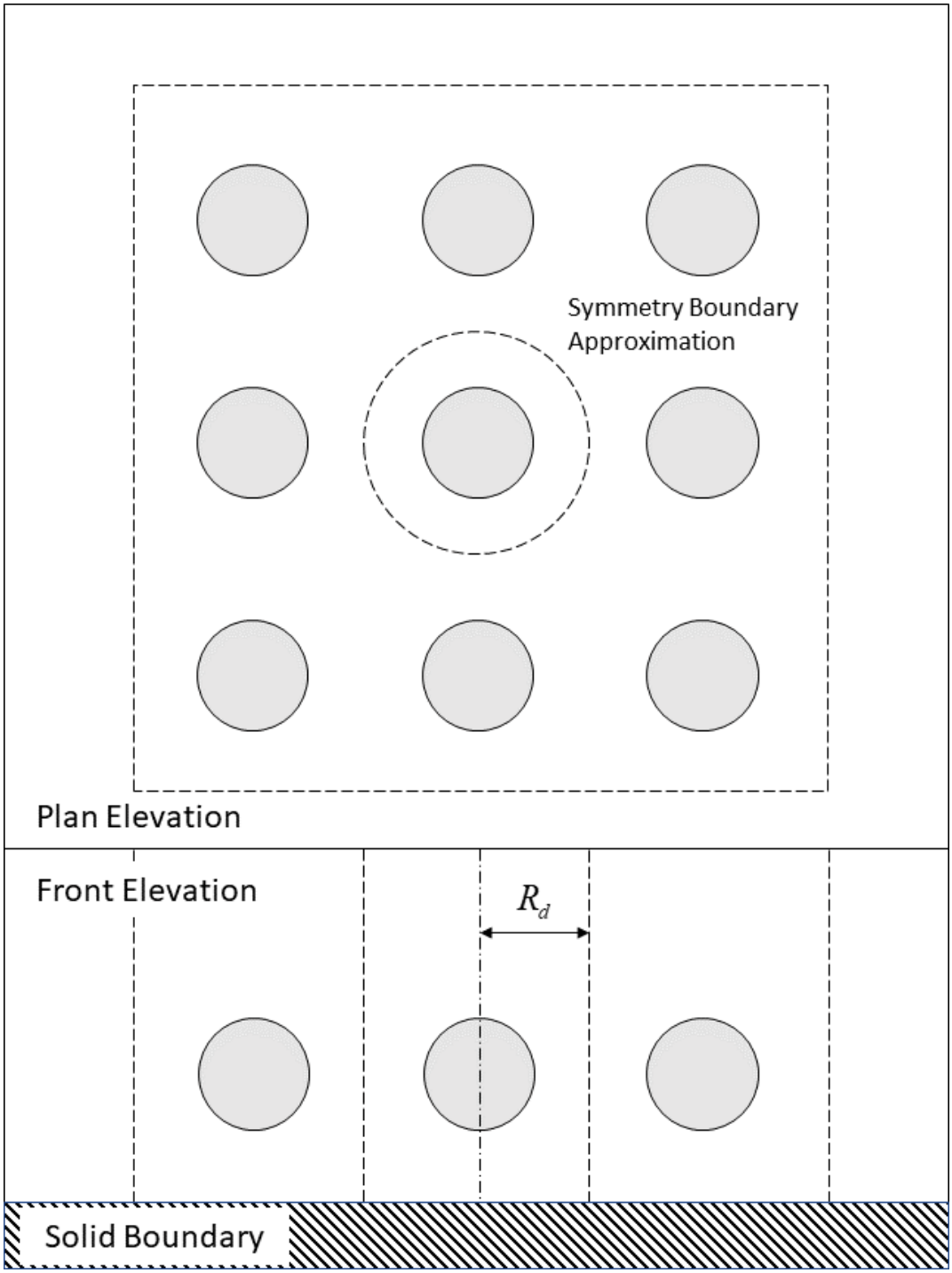

Figure 7.3. Approximate symmetry boundary for use in the axisymmetric cylindrical coordinates.

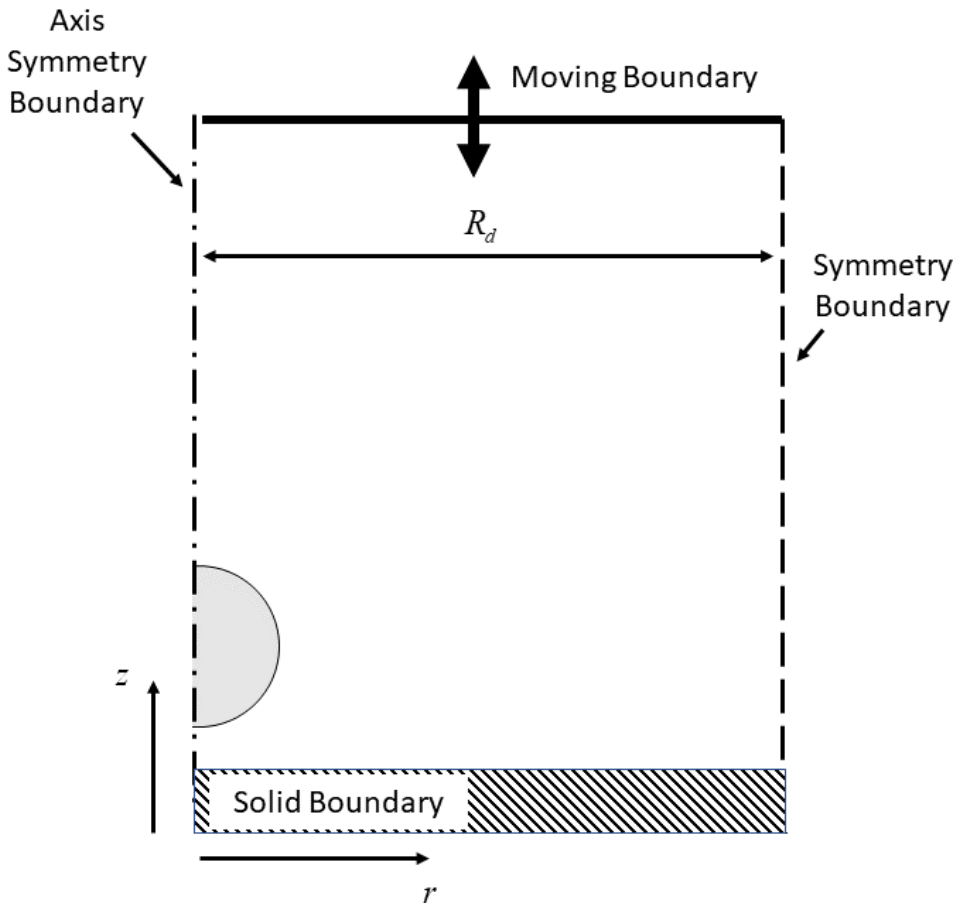

Figure 7.4. Symmetry boundary at a distance of R_d from the axis symmetry boundary; thus, R_d is the radius of the domain.

The symmetry boundary is at a radial distance of R_d from the z axis. The domain radius (R_d) represents half the spacing between bubbles, see Figure 7.3 and Figure 7.4. Here we non-dimensionalized the domain radius in the same manner as described in section 6.8. It is of interest to present the domain radius (R_d) in terms of a dimension of the bubble when it is at its maximum size as it gives insight into how close the fully-grown bubble is to the outer symmetry boundary before it collapses. However, the bubble growth depends on the dimensions of the domain and the standoff distance of the bubble from the near-wall. To nondimensionalize the domain radius with a consistent dimension, we use the maximum radius after the spherical growth of the bubble in the absence of the nearby boundaries, which is computed using the RP equation to give $R_{\max}$. As seen in section 6.7.1, the growth is represented as adiabatic and, therefore, $R_{\max} = 150.32$ μm for all of the cases presented in this Chapter. The nondimensionalized domain radius is

$$\bar{R}_d = \frac{R_d}{R_{\max}} \ . \tag{7.1}$$

It may also be of interest to note that the bubble in axisymmetric cylindrical coordinates near an outer symmetry boundary (Figure 7.4) could also be considered to represent a bubble in a rigid tube. This is because a symmetry boundary is effectively the same as a rigid or reflective boundary (section 3.8.1).

7.3 Results

Using the bubble collapse model with the symmetry boundary at a radial distance of R_d from the *z*-axis, we simulate the acoustically-driven growth and collapse of the bubble (ADGC) described in Chapter 6 (section 6.9) with $\bar{S} = 1.14$. The model uses the model parameters and properties provided in Table 6.1 and the domain-specific parameters in Table 6.3; the only difference is that the domain radius, R_d, is varied in this section. The distance from the *z*-axis to the symmetry boundary $\left(R_d\right)$ is varied to investigate the influence of nearby bubbles on the growth and collapse of a single bubble. The cases, $\bar{R}_d = 1.33$, $\bar{R}_d = 2.66$, $\bar{R}_d = 5.32$, $\bar{R}_d = 10.64$, $\bar{R}_d = 21.29$, $\bar{R}_d = 42.58$, and $\bar{R}_d = 85.15$, are presented in Figure 7.5 showing the bubble volume, wall pressure at $r = 0$, and the far-field pressure which is taken at $\left[r = R_d, z = 0\right]$. The maximum pressure for each of the cases is compared in Figure 7.6 (values are provided in Table 7.1). Note that $\bar{R}_d = 85.15$ results in $R_d = 12800\ \mu\text{m} \approx 1.28\ \text{cm}$, which is close to the case presented in section 6.9 where $R_d = 1\ \text{cm}$. The value $R_d = 1\ \text{cm}$ was chosen in section 6.9 to be sufficiently large so that the dynamics of the single bubble do not change with further increases in the domain radius $\left(R_d\right)$.

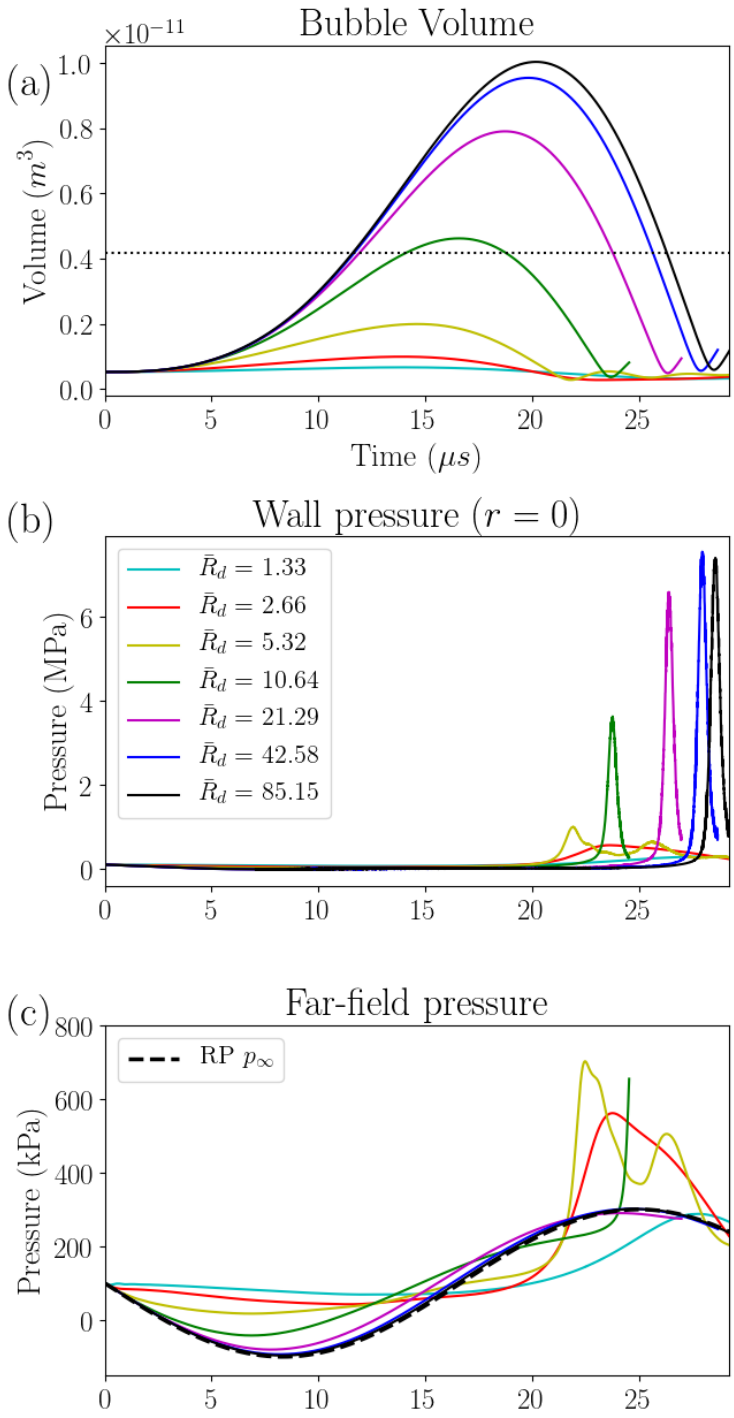

Figure 7.5. (a) The bubble volume, (b) wall pressure $(r = z = 0)$, and (c) the far field pressure for various domain radii: $\bar{R}_d = 1.33$, $\bar{R}_d = 2.66$, $\bar{R}_d = 5.32$, $\bar{R}_d = 10.64$, $\bar{R}_d = 21.29$, $\bar{R}_d = 42.58$, and $\bar{R}_d = 85.15$. The dotted line in (a) shows the bubble volume for the onset of transient cavitation for a spherical growth and collapse, where the bubble radius is twice the initial radius ($R_{\max} = 2R_0$). In (c) the dashed line depicts a sinusoidal pressure wave that represents the RP far-field pressure (p_∞) for an acoustic wave (Eq. (7.2))

Table 7.1. The maximum pressure experienced by the wall over the duration of the collapse for various domain radius's $\left(\bar{R}_d\right)$.

$\bar{R}_d$	1.33	2.66	5.32	10.64	21.29	42.58	85.15
R_d (μm)	200	400	800	1600	3200	6400	12800
Maximum wall pressure (MPa)	12.21	13.60	13.82	10.39	7.57	4.10	1.83

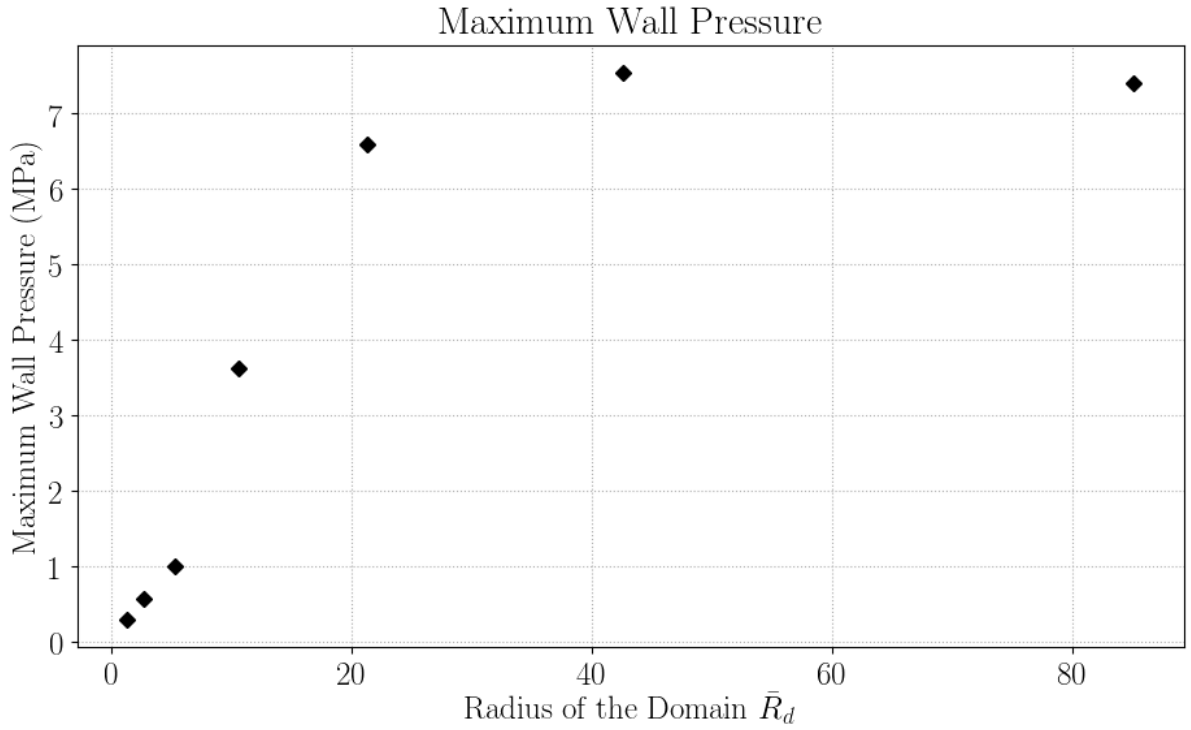

Figure 7.6. The maximum pressure experienced by the wall over the duration of the collapse for various domain radii.

In Figure 7.5, it is apparent that the increase in bubble volume (growth) increases with increasing domain radius $\left(R_d\right)$. This is due to the reduction in the driving pressure; the far-field pressure is very different for each case (Figure 7.5c). The transducer displacement remains constant for all of the cases $\left(a = 0.6956\ \mu\text{m}\right)$; however, with a small domain radius $\left(R_d\right)$ the bubble takes up a larger portion of the domain increasing the overall compressibility of the multiphase system. An increase in compressibility results in a lower amplitude of the far-field pressure. Because the bubble is closer to the

outer boundary for a smaller domain radius $\left(R_d\right)$, the far-field pressure is influenced more by the bubble pressure; hence, the large increase in far-field pressure for the collapse of the bubble in the cases: $\bar{R}_d = 2.66$, $\bar{R}_d = 5.32$, and $\bar{R}_d = 10.64$.

As previously stated, the influence of the bubble on the far-field pressure decreases as the domain radius $\left(R_d\right)$ increases. As a result, the far-field pressure at the wall approaches the approximate far-field pressure used in the RP analysis of a bubble in infinite body of incompressible liquid (section 1.1.1), see Figure 7.7c. Note that the far-field pressure for an acoustic input in the RP analysis $\left(p_\infty\right)$ is

$$p_\infty = p_0 - p_A \sin\left(2\pi ft\right) \tag{7.2}$$

where p_A is the pressure amplitude of the acoustic field, f is the frequency of the acoustic wave, and p_0 is the steady pressure in the absence of the sound field, which is equal to the atmospheric pressure in this study: $p_0 = p_{atm}$.

The $\bar{R}_d = 10.64$ case is the smallest domain radius to result in the transient collapse of a bubble; the bubble volume increases to more than the volume of a bubble with twice its initial radius ($R_{\max} = 2R_0$ - dotted line in Figure 7.5a) which is the approximate threshold for transient cavitation for a spherical bubble [15]. Further increases in the domain radius result in further increases in the peak pressure experienced by the wall.

It is also interesting to note from Figure 7.5 and Figure 7.6 that from $\bar{R}_d = 42.58$ to $\bar{R}_d = 85.15$ the peak pressure experienced by the wall decreases slightly. For ease of analysis, we reproduce the results from these two cases, $\bar{R}_d = 42.58$ and $\bar{R}_d = 85.15$, in Figure 7.7. The maximum bubble volume continues to increase with the increase in domain radius from $\bar{R}_d = 42.58$ to $\bar{R}_d = 85.15$ (Figure 7.7a) because the far-field pressure approaches the RP infinite far-field pressure $\left(p_\infty\right)$, which is given by Eq. (7.2), see Figure 7.7c. With the increase in bubble volume, we would expect the collapse to be more violent because of the lower bubble pressure (a lower bubble pressure means a larger driving pressure) and a

longer collapse duration (more time for momentum to develop). However, for the $\bar{R}_d = 42.58$ case, the collapse occurs slightly earlier than the $\bar{R}_d = 85.15$ case where the far-field pressure is higher. The increase in the far-field pressure for the smaller domain radius case, $\bar{R}_d = 42.58$, produces a slightly more violent collapse and a higher peak pressure experienced by the wall. Although the change is only slight, it is an interesting example of the collapse coinciding with a far-field pressure that is lower because the growth and collapse duration has exceeded three-quarters of the ultrasound wave period $\left(\frac{3}{4}T_U\right)$, when the far-field pressure begins to drop again (see Figure 7.7)

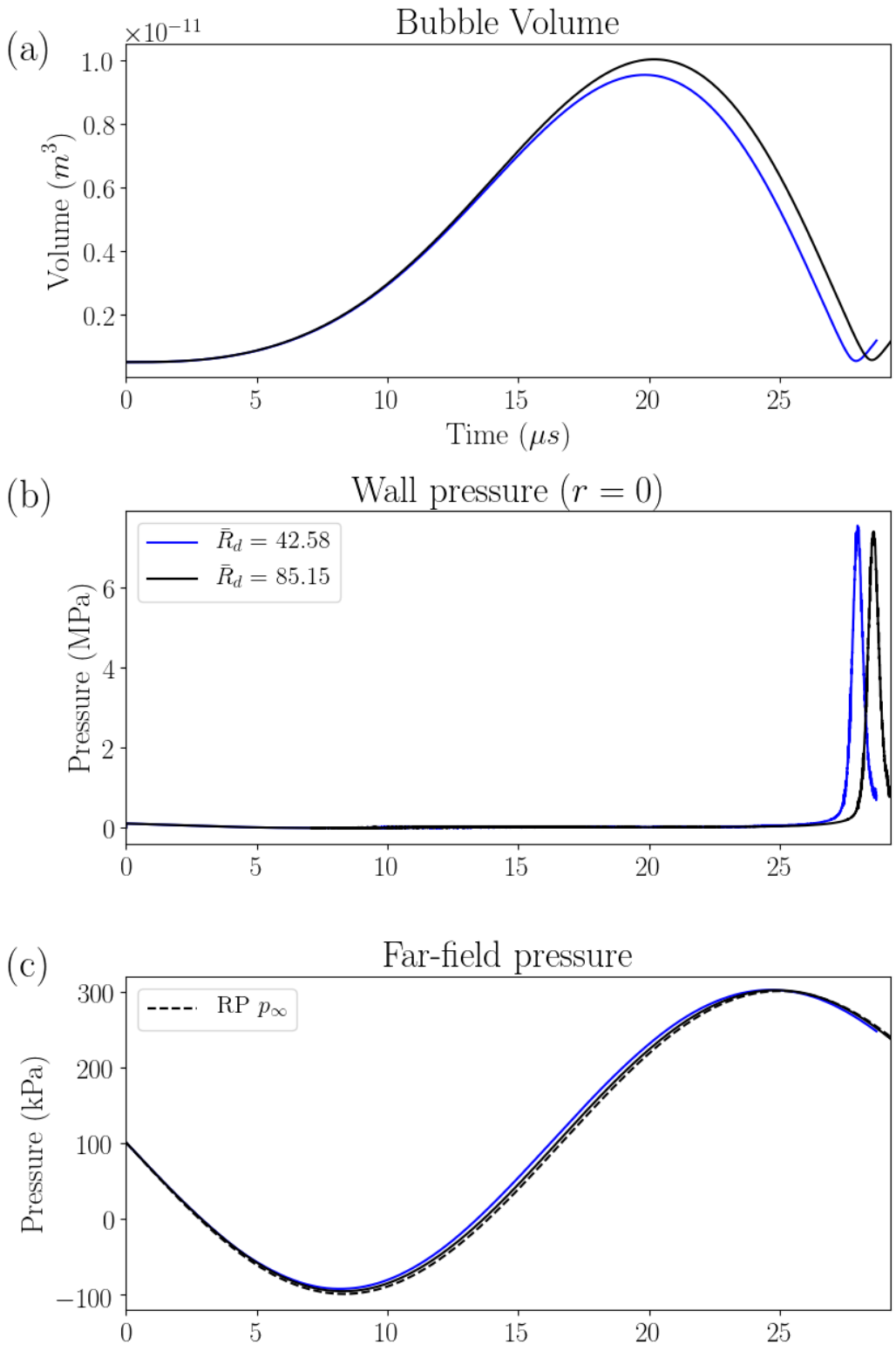

Figure 7.7. (a) The bubble volume, (b) wall pressure $(r = z = 0)$, and (c) the far field pressure for two cases which vary in domain radius: $\bar{R}_d = 42.58$ and $\bar{R}_d = 85.15$. In (c) the dashed line depicts a sinusoidal pressure wave that represents the RP far-field pressure (p_∞) for an acoustic wave (Eq. (7.2))

7.4 Conclusions

In acoustic cavitation applications (e.g. sonoporation), there is a threshold ultrasound intensity (or transducer amplitude) below which cavitation does not occur [106]. So, above this threshold cavitation occurs and with further increase in the ultrasound intensity, we would expect more cavitation activity and more violent collapses. However, as seen in this Chapter, the increased cavitation activity (more cavitation bubbles) may result in a less violent collapse of the bubbles. A similar phenomenon occurs when the presence of many bubbles near the transducer face reduces the magnitude of the violent cavitation behaviour: this phenomenon is observed in acoustic cavitation applications and is termed acoustic decoupling [106, 107]. Acoustic decoupling occurs above a certain threshold in ultrasound intensity, where the formation of a large number of cavities near the transducer face reduces the amount of energy delivered to the system [107].

What is shown in this Chapter is that the formation of a large number of cavities anywhere in the system will result in less violent collapse behaviour of the bubbles: not just for the case where the formation of a large number of cavities is near the transducer. This is because the transducer face is unable to produce a large enough pressure wave in the fluid due to the increase in the global compressibility of the coupling fluid caused by the presence of the bubbles. This has major implications on the single bubble studies in the previous Chapters (Chapter 4, Chapter 5, and Chapter 6), with the key implication being that the acoustic pressure amplitude that drives the growth and collapse is going to be less for the same transducer displacement if more bubbles are present throughout the solution.

In this Chapter, we investigated the influence of the bubble spacing using a fixed transducer displacement. These findings lead to further questions like what influence does the bubble spacing have on the bubble dynamics if the transducer power input or intensity is kept constant (as opposed to keeping the transducer amplitude constant)?

The increase in the spacing of the bubbles results in the reduction in compressibility of the multiphase fluid system. With a fixed transducer input amplitude, the pressure amplitude produced by the transducer increases with the reduction in compressibility of the fluid system. Thus, the pressure amplitude of the far-field pressure increases with increased bubble spacing. The growth of the bubble also increases with the increase in the far-field pressure amplitude. Thus, for a fixed transducer input amplitude, the growth of the bubble is found to increase with increased bubble spacing. Generally, the increased bubble growth will result in a more violent collapse. Therefore, to increase the pressure experienced by the wall in bubble cloud application, it is of interest to consider the bubble spacing and distribution.

Chapter 8 Collapse near Tissue (Future Work)

8.1 Motivation

In this Chapter, we describe the extension of the acoustically-driven bubble (ADGC) model to capture the dynamics of a bubble near a deformable boundary. The main application that motivates this model is sonoporation where the bubble is near biological tissue. The most developed model of the ultrasound-induced growth and collapse of a bubble near tissue is in [58]; however, it does not capture the compressibility of the surrounding fluid and the tissue which is important when the bubble collapses violently. This model is yet to be completed (future work) but we hope that it will provide insight into the mechanism in applications like sonoporation. Here we review the literature on the mechanisms involved in sonoporation.

8.1.1 Sonoporation

Sonoporation is a general term referring to the increase in permeability of biological tissue, due to the application of sound energy, typically ultrasound [22]. The observed permeability increase is due to the introduction of porous pathways. Sonoporation is observed to increase the permeability of the Stratum Corneum (SC) [12, 22, 23, 54-57], which is the outer layer of skin tissue, as well as the cell membrane [25], endothelium, and other biological membranes (e.g. blood-brain barrier [54]). Applications of sonoporation include transdermal drug delivery, delivery of cancer treatment solutes [108], and the transport of Alzheimer's antibody across the blood-brain barrier [108, 109].

Transdermal drug delivery (TDD) is limited by the Stratum Corneum (SC) due to it being highly resistant to mass transport. Sonoporation can increase the permeability of the skin, providing a significant drug transport enhancement. The application of low-frequency sonoporation (LFS), 20 to 100 kHz, provides significantly larger increases in skin permeability compared to high-frequency sonoporation (HFS), 1 to 3 MHz [57]. Thus, LFS is typically used in for TDD.

It is generally accepted that the primary increase in skin permeability after LFS is a result of transient bubble collapse events near the surface of the skin. The resulting jet impacts the surface, producing a high impact pressure. These jets have *not* been observed to penetrate the skin, but the impact does result in porous pathways in the SC [12]. When LFS is applied to the skin, macroscopic regions of increased permeability are formed, termed local transport regions (LTR's), where more transient cavitation events occur [22].

TDD using ultrasound is categorized into two methods: (1) simultaneous sonication and drug application and (2) pre-treatment sonication of the skin followed by the application of the drug. The idea behind simultaneous sonication and drug application is that the acoustic field provides a driving force for the drug as well as permeabilising the skin. The acoustic driving of the applied drug is termed sonophoresis. Sonophoresis is found to provide negligible benefit to the process [110], and the simultaneous method is less practical [22]. Therefore, the study will focus on the LFS pre-treatment of the skin.

Models of skin sonoporation exist, providing insight into the mechanisms of LFS permeability enhancement. A modified porous model for the permeability caused by LFS for hydrophilic solutes provides valuable insight into the mechanism of sonoporation of the SC [57]. This model is also modified to incorporate lipophilic pathways for moderate hydrophilic and hydrophobic solutes of low molecular weight (MW< 400 Da) [111]. The model presents and hypothesises that LFS disrupts the SC structure, increasing the number and connectivity of defects. These defects are considered as pores, providing diffusive paths. The model assumes that the LFS results in more pathways similar to the already present pore but does not create new types of pathways or increase the size of current pathways. With LFS the increased number of defects results in increase tortuosity and porosity of the SC. Since the model was proposed, it has been directly experimentally verified using the quantum dots study provided in Ref. [23]. An important experimental consideration for measuring the permeability increase of the skin is that it is directly related to the conductivity of the skin for LFS [112]. However, the electrical conductivity (an indicator of skin permeability) does differ significantly with frequency at a

constant energy density. The relationship between frequency and permeability has not been analysed but is known to be related to the dynamics of the transient cavitation at the skin surface [22].

Sonoporation permeability enhancement of skin is very heterogeneous on the macro, micro, and nano scales, all showing relative local transport regions [23]. Quantum dot tracers were used to experimentally verify the modified porous pathway model [23], showing perpetration depths of up to 60 micrometres. The porous pathway consists of lacunar imperfections in the SC, increasing in number and size with LFS. This increase in porosity due to imperfections is expected to form a network of pores for the transport of macromolecules [23]. It is not surprising that these lacunar imperfections cause the increase in permeability of the skin when other studies have shown that photomechanical waves (laser light) increase permeability through lacunar dilation and SLS, a chemical permeability enhancer, is known to cause lipid bilayer serration and lacunar continuities [23, 113].

The impact of the jet on the SC has also been considered in [12] by approximating the applied pressure. The applied pressure and the subsequent skin stress are expected to be the cause of the increased number of SC defects. This is supported by the molecular dynamics simulations which have shown that applied tension stress to a cell membrane or lipid bilayer membranes (BLM), a building block of the SC, can lead to the formation of a metastable pore due to the reduction in free energy [114, 115].

As transient cavitation is accepted as the mechanism for sonoporation of the skin, a model of the bubble collapse would be valuable. As discussed before, the impact pressure is easily approximated given the jet speed [12] but lacks many aspects that influence the collapse event. Additionally, the approximation gives an impact pressure capable of rupturing the skin, which is inconsistent with experimental observations with no micro-scale disruption of the skin after LFS [23]. Multiple numerical studies have been conducted on the collapse behaviour of a single bubble near a boundary [38, 116-119]. These studies applied in a sonoporation scenario to focus on the subsequent stress on the skin would provide valuable insight into the mechanisms of sonoporation and defect formation.

The most developed model of the ultrasound-induced growth and collapse of a bubble near tissue is in [58]. In [58], they find a new peeling mechanism which occurs in the rebounding stage, where the tissue

is peeling by the re-expansion of the toroidal bubble. The key limitation of this previously developed model [58] is that it does not capture the compressibility of the surrounding fluid and the compressibility of the tissue which is important when the bubble collapses violently.

The previous models described are lacking insight into the relationship between the behaviour of the cavitation bubble and the permeability increase of the skin. We propose the development of a model to capture a bubble in a liquid near a deformable solid. The deformable elastic solid is used to represent the skin tissue. The liquid and skin tissue will be treated as compressible because the effects of compressibility become important at the later stages of a violent bubble collapse. The model we propose will be using investigate the interaction of the transient cavitation bubble and the skin tissue, providing insight into the mechanisms involved in skin sonoporation.

8.2 Physical model

The model uses the same physical model as described in Chapter 2. The main difference being the addition of a deformable solid to represent the skin and tissue, see Figure 8.1. It is difficult to model a compressible solid model using the diffuse interface method on an Eulerian mesh like the multifluid model presented in Chapter 3 [120-123]; thus, we use a Lagrangian model to capture the compressible solid component.

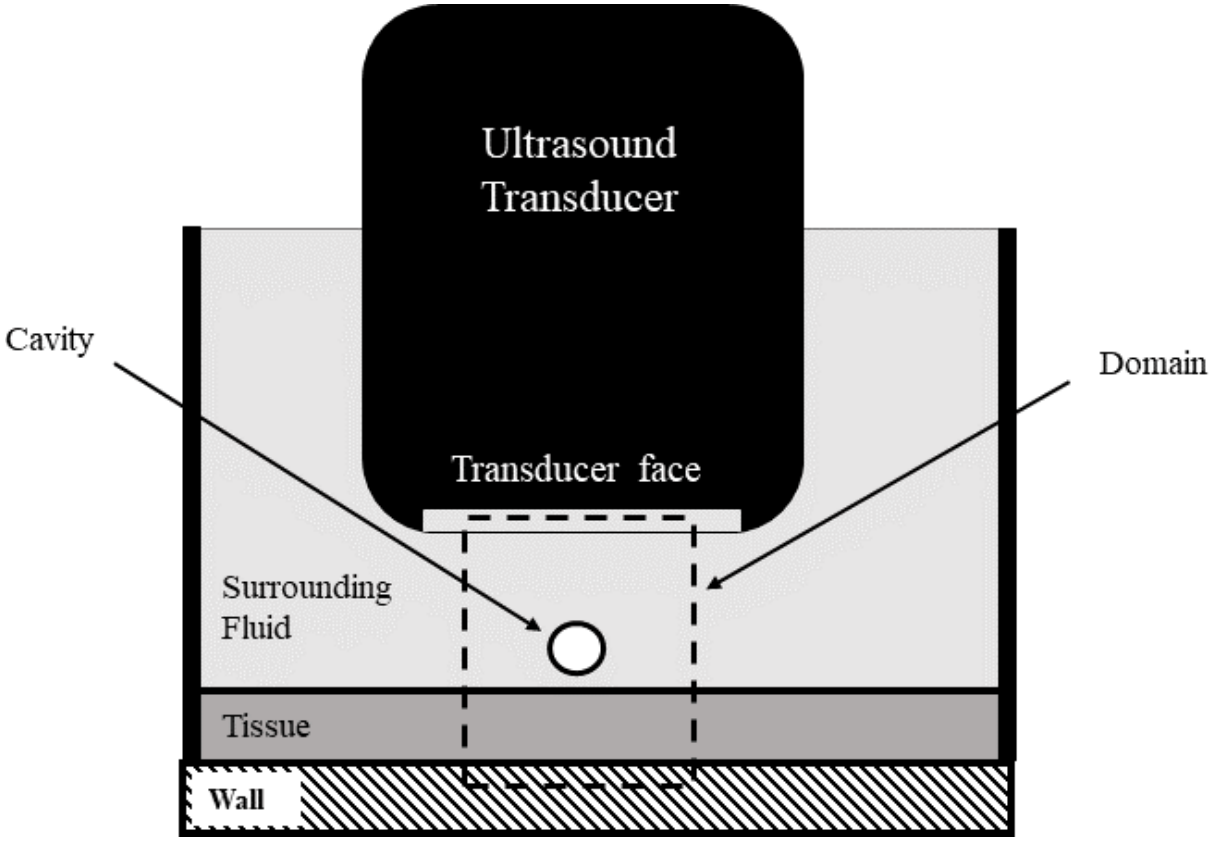

Figure 8.1. A representative depiction of an ultrasound transducer setup for Sonoporation of skin tissue where the bubble collapses near the skin (not drawn to scale).

8.3 Numerical Model

We seek a numerical method that is able to capture the collapse of a bubble near a deformable solid. To capture the solid component, we use a compressible Lagrangian solid model. The Lagrangian model is coupled with the Eulerian fluid model at the fluid/solid interface using the Ghost Fluid Method (GFM). The Eulerian multifluid model is described in Chapter 2 and Chapter 3, so here we focus on showing the Lagrangian model and the GFM used.

8.3.1 Lagrangian Model

The Lagrangian model considers a discrete volume element, V_i, where the mass of the volume element is constant M_i (no mass flows through the boundary of the volume elements). The density of the element is then $\rho(t) = \frac{M_i}{V_i(t)}$. The continuity for the element can be expressed as [124]

$$\frac{1}{V_i}\frac{dV_i}{dt} = (\nabla \cdot \mathbf{u})_i . \tag{8.1}$$

Because mass is conserved for each discrete volume element, the total mass of the domain is conserved. The conservation of momentum and energy is considered using the equation of motion and the evolution of specific internal energy [124]

$$\rho\frac{d\mathbf{u}}{dt} = -\nabla p \tag{8.2}$$

$$\rho\frac{de}{dt} = -p\nabla \cdot \mathbf{u} \tag{8.3}$$

given in the Lagrangian form.

The discussed model applies to fluids; however, it is able to be extended to model solids. The equations describing the Lagrangian model for a compressible solid are presented in [125, 126]. The equations are very similar; the key difference is that solids deal with stress whereas fluids deal with pressure.

$$\rho\frac{d\mathbf{u}}{dt} = -\nabla \sigma^{pk1} \tag{8.4}$$

$$\rho\frac{de}{dt} = -\nabla \mathbf{u}^T \sigma^{pk1} \tag{8.5}$$

where σ^{pk1} is the first Piola-Kirchoff stress tensor given by

$$\sigma^{pk1} = \det(\mathbf{F})\sigma^T \mathbf{F}^{-1} \tag{8.6}$$

where σ is the Cauchy stress tensor and $\mathbf{F}$ is the deformation gradient tensor. With mass conservation $\det(\mathbf{F}) = \frac{\rho_0}{\rho}$.

It is shown in [125] for the Lagrangian solid model presented that considering the properties of a fluid simplifies the equation of state (EOS) and recovers the Euler equations. The equations are more complex for the solid model than for the fluid case because stress depends on the deformation of the element and varies with the direction; whereas, fluid pressure is simply determined using the stiffened EOS.

The solid requires two equations of state (EOS): the thermodynamic EOS and a mechanical EOS [125]. For the linear elasticity case from [125], the thermodynamic EOS is described as the Saint Venant-Kirchoff material

$$\rho_0 e = \mu(I_1 - 3) + \frac{\lambda + 2\mu}{8}(I_1 - 3)^2 - \frac{\mu}{2}(I_2 - 3) \tag{8.7}$$

where λ and μ are the Lamé parameters I_1 and I_2 are two of the three tensorial invariants of $\mathbf{B} = \mathbf{F}\mathbf{F}^T$ (the left Cauchy-Green strain tensor)

$$I_1 = tr(\mathbf{B}) \tag{8.8}$$

$$I_2 = \frac{1}{2}\left(tr(\mathbf{B})^2 - tr(\mathbf{B}^2)\right) \tag{8.9}$$

The mechanical EOS is given by Hooke's law (small deformation hypothesis)

$$\hat{\sigma} = 2\mu\varepsilon + \lambda tr(\varepsilon)\mathbf{I} \tag{8.10}$$

where ε is the strain tensor:

$$\varepsilon = \frac{1}{2}\left(\mathbf{F}^T + \mathbf{F}\right) - \mathbf{I}\ . \tag{8.11}$$

8.3.1.1 Numerical method

The numerical method following the work of [124], using a staggered spatial grid formulation of a quadrilateral zone defined by points, referred to as nodes. Each quadrilateral zone is a discrete volume element is composed for four corner zones called a subzone. The zone mass $\left(M_z\right)$ is equal to the sum of the four subzone masses m^z that make up that zone

$$M_z = \sum m^z \tag{8.12}$$

The nodes (points that make up the quadrilateral zone) are considered to have a nodal mass $\left(M_p\right)$ which is given by the sum of the four subzone masses m^z that are connected to the node, making the node element.

The momentum equation is considered for the node elements to determine the velocity of the nodes

$$M_p \frac{d\mathbf{u}}{dt} = \sum \mathbf{f}^p \tag{8.13}$$

where $\mathbf{f}^p$ are the corner forces acting on the node. Thus, the displacement of the node is given by the velocity

$$\frac{d\mathbf{x}}{dt} = \mathbf{u} \tag{8.14}$$

where $\mathbf{x} = \begin{bmatrix} r \\ z \end{bmatrix}$ and $\mathbf{u} = \begin{bmatrix} u_r \\ u_z \end{bmatrix}$ in axisymmetric cylindrical coordinates.

The energy equation is considered for the zone through the evolution of the internal energy $\left(\mathbf{e}\right)$

$$M_z \frac{d\mathbf{e}}{dt} = \sum \mathbf{f}^z \cdot \mathbf{u}_p \tag{8.15}$$

where $\mathbf{f}^z$ are the corner forces acting on the zone and $\mathbf{u}_p$ is the velocity vector at the corresponding corner node. The forces are determined from the Piola-Kirchoff stress tensor of the subzone of interest and the area of the element it is applied too.

The Lagrangian numerical method uses artificial viscosity to smear out shocks [127], making the method stable. We use the artificial viscosity method developed in [128]. The artificial viscosity is applied as an additional force component in $\mathbf{f}^{p}$ Eq. (8.13) and $\mathbf{f}^{z}$ (Eq. (8.15)).

8.3.2 Ghost fluid method (Eulerian and Lagrangian coupling)

The coupling of the Eulerian and Lagrangian uses the method described in [127]. To couple the Eulerian and Lagrangian grids, boundary conditions are imposed on both Eulerian and Lagrangian grids at the intersection. The intersection between the two grids is by the outer Lagrangian nodes. The boundary conditions on the Eulerian and Lagrangian models are given by the ghost fluid method.

From the Eulerian point of view, the Eulerian overlaps the Lagrangian mesh. The overlap of Eulerian grid over the Lagrangian boundary are the Eulerian ghost cells. To impose the boundary condition for the Eulerian grid the Ghost fluid method is used to define the conserved variable for the ghost cells. The boundary condition applied to the Lagrangian grid is given by the pressure for the Eulerian cells: the pressure on the Lagrangian node is determined by interpolation between the near Eulerian cells (including the ghost cells) [127].

The Ghost fluid method for the defining the conserved variable for the ghost cells uses the normal velocity of the interface (Eulerian and Lagrangian boundary). The normal velocity is taken as the velocity of the outer Lagrangian nodes. The Eulerian ghost nodes are defined by extrapolating the pressure across the interface; the same extrapolation is done for entropy and tangential velocity.

The extrapolation procedure used a signed distance ϕ, typically referred to as a let-set function, where $\phi \leq 0$ for real cells and $\phi > 0$ for ghost cells. The signed distance is defined as the shortest distance to the linear spline that is fitted to the outer Lagrangian nodes that define the internal boundary between the Lagrangian and Eulerian meshes. The signed distance of the Eulerian cells neighbouring the internal boundary nodes are calculated first; the signed distances for the rest of the Eulerian cells are computed using the Fast Marching Method [129] to speed the process up. The extrapolation of entropy, pressure, and velocity to the ghost cells can be determined in parallel to the signed distance construction

procedure. The velocity at the Eulerian ghost nodes is determined using the extrapolated velocity $(\mathbf{u}_{ext})$ and the closest interface velocity $(\mathbf{u}_I)$ using the basis free projection method [81]

$$\mathbf{u} = (\mathbf{u}_I \cdot \mathbf{n})\mathbf{n} + \mathbf{u}_{ext} - (\mathbf{u}_{ext} \cdot \mathbf{n})\mathbf{n} \tag{8.16}$$

where the closest interface velocity $(\mathbf{u}_I)$ is given by the interpolation of the velocity at the Lagrangian nodes making the linear spline that defined the interface location. The unit normal vector is given by the signed distance at the centre of the ghost cell

$$\mathbf{n} = \frac{\nabla \phi}{|\nabla \phi|} \tag{8.17}$$

The conserved variables for the ghost cells are reassembled using the entropy (S_{ext}), pressure (p_{ext}), and velocity $(\mathbf{u})$. The conserved variables for the ghost cells are reassembled using the entropy (S_{ext}), pressure (p_{ext}), and velocity $(\mathbf{u})$. However, the entropy is not required to reassemble the conserved variable, but density is required. Because the pressure and entropy are extrapolated in a consistent manner, density is also able to be extrapolated using the same method because the adiabatic stiffened EOS is only dependant on pressure [94] (set constant pressure and constant entropy mean constant density). The adiabatic stiffened EOS is

$$\rho_{ext} = \rho_0 \left(\frac{\gamma p_{ext} + \pi_\infty}{\gamma p_0 + \pi_\infty} \right)^{\frac{1}{\gamma}} \tag{8.18}$$

where ρ_0 and p_0 are the reference density and pressure, respectively.

8.4 Verification

8.4.1 1D gas-liquid Riemann test case

We use the gas-liquid Riemann test case taken from [60, 66] to numerically verify the model in one dimension as we did in section 3.10.1 for the Eulerian model. Initially, a stationary diaphragm between

two fluids is located at $x = 0.5$, with a liquid on the left and a gas on the right. The initial properties of the liquid are

$$\left(\rho,\, u,\, P,\, \gamma,\, \pi_\infty,\, \alpha_1\right)_L = \left(0.991,\, 0,\, 3.059\times10^{-4},\, 5.5,\, 1.505,\, 0\right). \tag{8.19}$$

The initial properties of the gas are

$$\left(\rho,\, u,\, P,\, \gamma,\, \pi_\infty,\, \alpha_1\right)_R = \left(1.241,\, 0,\, 2.753,\, 1.4,\, 0,\, 1\right) \tag{8.20}$$

where α_1 is the volume fraction of the gas.

8.4.1.1 Lagrangian Model

First, we verify that the Lagrangian model is working correctly. Because the Lagrangian model volume elements conserve mass $\left(m_z\right)$, modelling multicomponent systems is relatively simple. There is no advection of species between elements, and the material interface is always located between the same neighbouring elements. As discussed previously, the Lagrangian model for solids can be simplified to consider fluids [125]. Here we verify the Lagrangian numerical method for the 1D two-fluid system. The results of the gas-liquid Riemann test case using the Lagrangian model is presented in Figure 8.2. The subsequent volume fraction, density, pressure, velocity, and internal energy after 0.01 seconds are compared to the exact solution to the Riemann problem [71] (Figure 8.2). The result of the Lagrangian model shows good agreement with the exact solution, capturing all of the flow features (e.g. the shock wave).

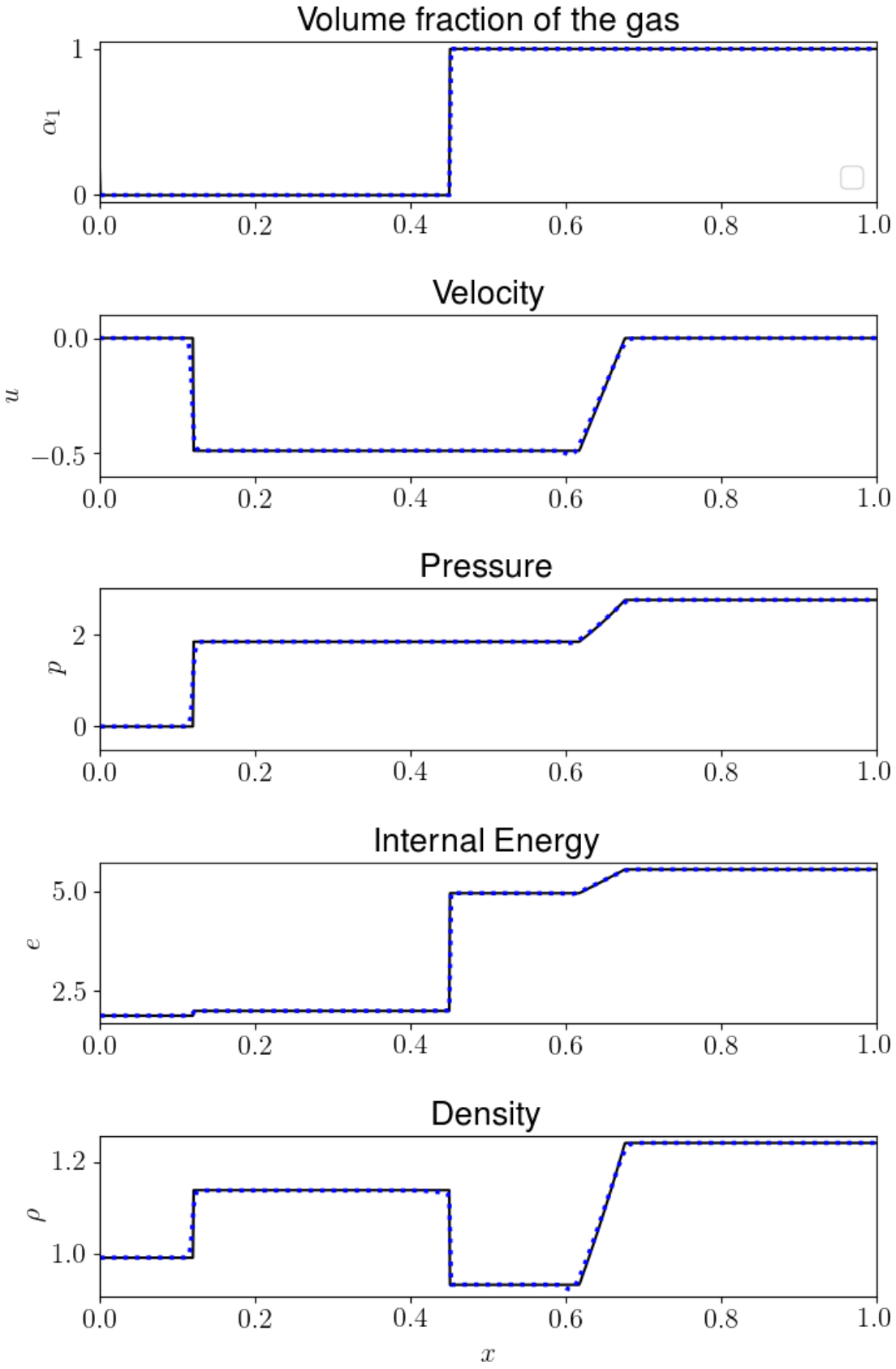

Figure 8.2. The results of the 1D gas-liquid Riemann problem at time t=0.01 using the 1D Lagrangian model (simplified for the multifluid system). The solid line is the exact solution and the points are the solution from the presented numerical scheme for a mesh of 500 cells and a CFL = 0.5.

8.4.1.2 Eulerian-Lagrangian Model using the GFM

The same test case is used to verify the Eulerian-Lagrangian model that is coupled using the GFM. The liquid on the left (Eq. (8.20) is captured using the Eulerian model and the gas on the right (Eq. (8.19)) is captured using the Lagrangian model. The subsequent volume fraction, density, pressure, velocity, and internal energy after 0.01 seconds are compared to the exact solution to the Riemann problem in Figure 8.3. Note that in Figure 8.3 the extrapolated conserved variable for the Eulerian ghost cells from the GFM are shown, however, the solution at these points is given by the Lagrangian cells. The results from the model show good agreement with the exact solution, verifying the numerical procedure of the coupled Eulerian-Lagrangian model in 1D.

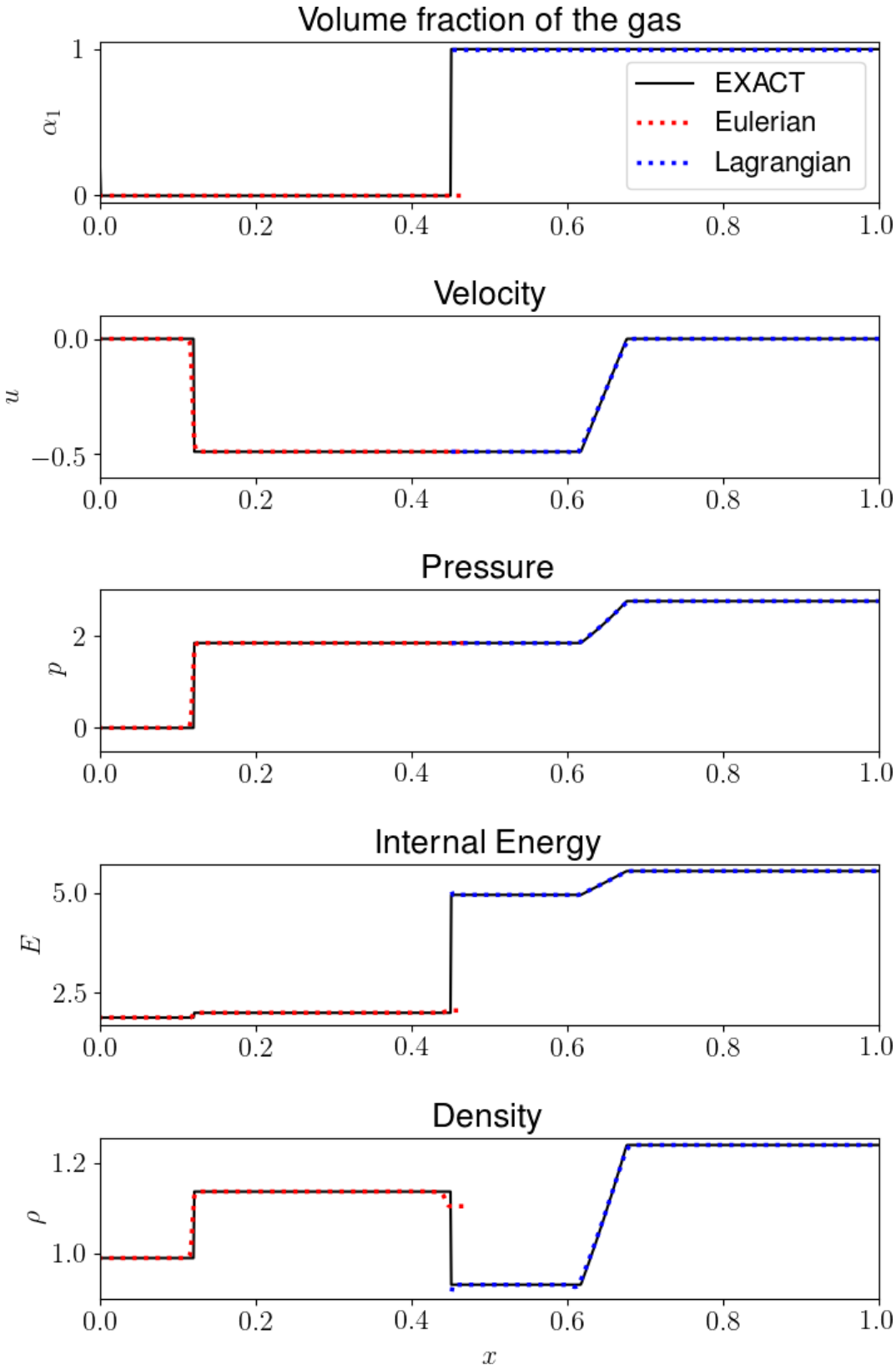

Figure 8.3. The results of the 1D gas-liquid Riemann problem at time t=0.01 for the 1D Eulerian-Lagrangian model using the GFM at the material interface. The solid black line is the exact solution, and the points are the solution from the presented numerical scheme for a mesh of 1000 cells (500 Eulerian cells and 500 Lagrangian cells) and CFL = 0.1.

8.4.2 Bubble growth and collapse near fluid case

The Eulerian numerical model presented in Chapter 3 is able to capture multiple fluids. Previously, we considered a two fluids system, but the extension to a three-fluid system is straightforward. The extension to a three-fluid system requires an additional conservation equation for the extra fluid species and an additional advection equation. The additional advection equation is chosen for the implementation of the maximum-principle-satisfying and positivity-preserving limiter. The complication arises when we consider the volume fraction of the three fluids: α_1, α_2, and α_3. We wish to ensure that

$$0 \le \alpha_i \le 1 \quad \text{for } i = 1,2,3. \tag{8.21}$$

However, if we use the two advection equations

$$\frac{\partial \alpha_1}{\partial t} + \mathbf{u} \cdot \nabla \alpha_1 = 0 \tag{8.22}$$

$$\frac{\partial \alpha_2}{\partial t} + \mathbf{u} \cdot \nabla \alpha_2 = 0 \tag{8.23}$$

with the limits: $0 \le \alpha_1 \le 1$ and $0 \le \alpha_2 \le 1$, and the third volume fraction is given by the mixture rule $\alpha_3 = 1 - (\alpha_1 + \alpha_2)$ then there is no insurance that $0 \le \alpha_3 \le 1$. Thus, to resolve this issue, we consider the advection of α_1 and $\alpha_1 + \alpha_2$

$$\frac{\partial \alpha_1}{\partial t} + \mathbf{u} \cdot \nabla \alpha_1 = 0 \tag{8.24}$$

$$\frac{\partial (\alpha_1 + \alpha_2)}{\partial t} + \mathbf{u} \cdot \nabla (\alpha_1 + \alpha_2) = 0 \tag{8.25}$$

with the limits $0 \le \alpha_1 \le 1$ and $0 \le (\alpha_1 + \alpha_2) \le 1$. These two equations and two limits ensure $0 \le \alpha_i \le 1$ for $i = 1,2,3$ (Eq. (8.21)). Thus, the governing equations for the three-fluid system are

$$\frac{\partial(\alpha_1\rho_1)}{\partial t}+\nabla\cdot(\alpha_1\rho_1\mathbf{u})=0 \tag{8.26}$$

$$\frac{\partial(\alpha_2\rho_2)}{\partial t}+\nabla\cdot(\alpha_2\rho_2\mathbf{u})=0 \tag{8.27}$$

$$\frac{\partial(\alpha_3\rho_3)}{\partial t}+\nabla\cdot(\alpha_3\rho_3\mathbf{u})=0 \tag{8.28}$$

$$\frac{\partial(\rho\mathbf{u})}{\partial t}+\nabla\cdot(\rho\mathbf{u}\otimes\mathbf{u}+p\mathbf{I})=\mathbf{0} \tag{8.29}$$

$$\frac{\partial E}{\partial t}+\nabla\cdot(\mathbf{u}(E+p))=0 \tag{8.30}$$

$$\frac{\partial\alpha_1}{\partial t}+\mathbf{u}\cdot\nabla\alpha_1=0 \tag{8.31}$$

$$\frac{\partial(\alpha_1+\alpha_2)}{\partial t}+\mathbf{u}\cdot\nabla(\alpha_1+\alpha_2)=0\ . \tag{8.32}$$

The mixture rules for the three-fluid system are

$$\alpha_1+\alpha_2+\alpha_3=1 \tag{8.33}$$

$$\rho=\alpha_1\rho_1+\alpha_2\rho_2+\alpha_3\rho_3 \tag{8.34}$$

$$E=\alpha_1E_1+\alpha_2E_2+\alpha_3E_3 \tag{8.35}$$

$$\Gamma=\alpha_1\Gamma_1+\alpha_2\Gamma_2+\alpha_3\Gamma_3 \tag{8.36}$$

$$\Pi=\alpha_1\Pi_1+\alpha_2\Pi_2+\alpha_3\Pi_3\,. \tag{8.37}$$

The maximum-principle-satisfying and positivity-preserving limits are

$$0\le\alpha_1\le1 \tag{8.38}$$

$$0\le(\alpha_1+\alpha_2)\le1 \tag{8.39}$$

$$0<\alpha_1\rho_1 \tag{8.40}$$

$$0 < \alpha_2 \rho_2 \tag{8.41}$$

$$0 < \alpha_3 \rho_3 \tag{8.42}$$

$$0 \le \left(p + \pi_\infty \right) \tag{8.43}$$

We use the Eulerian three-fluid model to verify the Eulerian-Lagrangian model. To do this, we compare the growth and collapse of an air bubble in the water near another liquid, see Figure 8.4. The additional fluid layer is introduced (Fluid 3) between the bubble and the near-wall (Figure 8.4). The Eulerian-Lagrangian model uses the Eulerian mesh to capture the bubble and water, and the Lagrangian mesh captures Fluid 3.

We use Fluid 3 to simulate soft tissue which has previously been modelled by a solution composed of water and Gelatin, where the Gelatin is 10 % of the solution [18]. The density of the 10% Gelation is $1030\ \text{kg/m}^3$, and the stiffened EOS properties are $\gamma = 6.72$ and $\pi_\infty = 3.70 \times 10^8$ Pa .

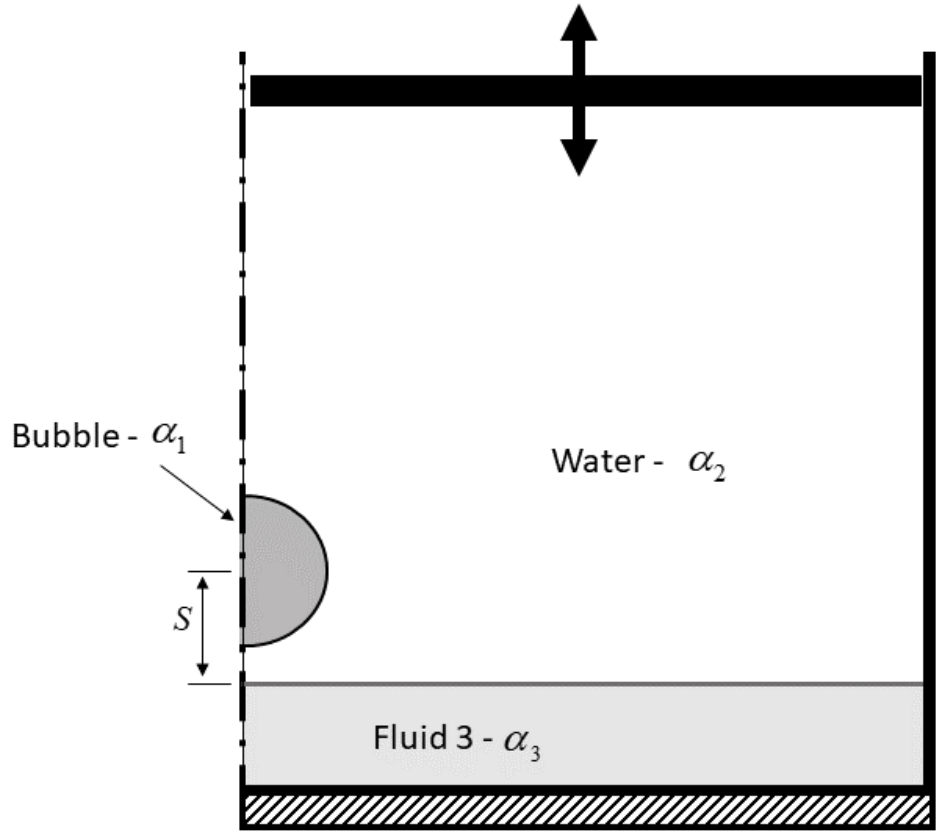

Figure 8.4. The initial state for the acoustically-driven bubble near another fluid (fluid 3). The case is the same as depicted in Figure 3.1, initialised in the same manner as in section 6.3. The only difference is the introduction of Fluid 3 between the wall and the bubble.

At this stage, this concludes the progress of the model development to capture the acoustically-driven bubble near a deformable boundary. We are attempting to verify the Eulerian-Lagrangian model by comparing it to the known case where the Eulerian model is used to simulate the growth and collapse of a bubble near another fluid.

8.5 Next steps

Once the numerical model is verified, we will verify that the Lagrangian mesh captures the dynamics of a compressible solid correctly (at this point we have only used the Lagrangian model to model fluids). The model will then be able to simulate the acoustically-driven bubble near a deformable solid (e.g. skin tissue). By simulating the acoustically-driven bubble near a deformable solid, we will be able to investigate the bubble dynamics and provide insight into applications like sonoporation.

Chapter 9 Concluding Remarks

In the present work, we developed a numerical model able to capture an acoustically-driven bubble. The numerical model consists of a fully-compressible high-order multiphase model to capture a gas bubble surrounded by a liquid. The acoustic input is directly simulated using an immersed moving reflective boundary condition, simulating the dynamics of the active face of an ultrasound transducer. The model developed was first used to simulate the acoustically-driven bubble collapse: a method was developed for initialising the collapse simulation using the RP equation to approximate the bubble growth. The model was then further developed to simulate the growth phase directly and the subsequent collapse, capturing the influence of the near-wall on the growth phase.

The RP growth initialised collapse (RPGI) model provided a valuable tool to investigate the acoustically-driven collapse of a bubble near a wall. Approximating the growth using the RP equation allowed the effects during growth like surface tension, the presence of vapour, viscous effects, surrounding fluid compressibility, and heat transfer (adiabatic vs isothermal growth) to be considered, investigating their significance on the growth and the subsequent collapse of the bubble. For the case considered, the influence of surface tension, vapour, and heat transfer during the growth phase were found to affect the growth and subsequent collapse significantly. However, the influence of viscous effects and the compressibility effects in the surrounding fluid had an insignificant effect on the growth and the subsequent collapse.

We then developed the model to directly simulate the bubble growth, prior to the collapse, of the near-wall bubble, as opposed to approximating the pre-collapse bubble using the RP growth in the RPGI model. The simulation of the near-wall bubble growth captured the influence of the wall on the growth, which is neglected in the RP growth. The model was then able to capture the acoustically-driven collapse, after the simulated growth, referred to as the ADGC model. The ADGC model was used to investigate the influence of varying the initial standoff distance from the wall on the bubble growth and the subsequent collapse. It was found that the near-wall significantly restricts the bubble growth, and during the growth, changed the sphericity of the bubble shape, and increase the displacement of the

bubble centroid from the wall. The influences of the near-wall on the bubble growth were found to increase the closer the initial bubble was to the wall (smaller standoff distances). The ADGC model was found to be superior in capturing the physics of an acoustically-driven bubble compared to the previously develop Rayleigh growth and collapse (RGC) case. The ADGC model was able to capture the physically correct bubble state and the transient far-field pressure produced by the acoustic input of the immersed moving boundary.

The ADGC model was then modified to capture the influence of nearby bubbles on the bubble behaviour. By making assumptions about the distribution of the bubble cloud, the model is able to approximate the influence on the nearby bubble. In the case considered, the bubbles are near a wall and compose a large portion of the domain. It is found that with more bubbles present (a smaller bubble spacing) results in less bubble growth and, subsequently, a less abrupt collapse. This is because the more bubbles that are present in the solution, the more compressible the multifluid system becomes. The reduction in the bulk compressibility of the system means the subsequent pressure amplitude produced by the immerse moving boundary with a fixed displacement amplitude is significantly less. And the pressure amplitude is what drives the growth and collapse. This finding agrees with the phenomenon called acoustic decoupling that occurs in acoustic cavitation applications where the acoustic input is decoupled from the liquid because of the overpopulation of cavitation bubbles. However, acoustic decoupling typically refers to the presence of bubbles near the transducer, but we show that the same effect will occur if the bubbles are near the wall (far from the transducer face).

In the final Chapter (Chapter 8), we present the current development of a model to capture the acoustically-driven growth and collapse of a bubble near a deformable solid (instead of a rigid wall). The model consists of the same Eulerian compressible multiphase model to capture the air bubble in the liquid. The difference is the Eulerian model is coupled to a Lagrangian compressible solid model to capture the deformable solid using the Ghost fluid method (GFM). The model is still in the verification and validation stages, but in future work, we hope to use the model to provide insight into the mechanisms involved in applications like sonoporation.

Appendix A Cylindrical Discretisation of the Governing Equations

The Euler equations in axisymmetric cylindrical coordinates are [130]

$$\frac{\partial}{\partial t}\begin{bmatrix}\rho\\ \rho u_r\\ \rho u_z\\ \rho E\end{bmatrix}+\begin{bmatrix}\frac{1}{r}\frac{\partial\left(r\rho u_r\right)}{\partial r}+\frac{\partial \rho u_z}{\partial z}\\ \frac{1}{r}\frac{\partial\left(r\rho u_r^2\right)}{\partial r}+\frac{\partial\left(\rho u_r u_z\right)}{\partial z}+\frac{\partial p}{\partial r}\\ \frac{1}{r}\frac{\partial\left(r\rho u_r u_z\right)}{\partial r}+\frac{\partial\left(\rho u_z^2\right)}{\partial z}+\frac{\partial p}{\partial z}\\ \frac{1}{r}\frac{\partial\left(ru_r\left(E+p\right)\right)}{\partial r}+\frac{\partial\left(u_z\left(E+p\right)\right)}{\partial z}\end{bmatrix}=\mathbf{0} \tag{A.1}$$

The extension to the governing equation for the multiphase system is

$$\frac{\partial}{\partial t}\begin{bmatrix}\alpha_1\rho_1\\ \alpha_2\rho_2\\ \rho u_r\\ \rho u_z\\ \rho E\\ \alpha_1\end{bmatrix}+\begin{bmatrix}\frac{1}{r}\frac{\partial\left(r\alpha_1\rho_1 u_r\right)}{\partial r}+\frac{\partial \alpha_1\rho_1 u_z}{\partial z}\\ \frac{1}{r}\frac{\partial\left(r\alpha_2\rho_2 u_r\right)}{\partial r}+\frac{\partial \alpha_2\rho_2 u_z}{\partial z}\\ \frac{1}{r}\frac{\partial\left(r\rho u_r^2\right)}{\partial r}+\frac{\partial\left(\rho u_r u_z\right)}{\partial z}+\frac{\partial p}{\partial r}\\ \frac{1}{r}\frac{\partial\left(r\rho u_r u_z\right)}{\partial r}+\frac{\partial\left(\rho u_z^2\right)}{\partial z}+\frac{\partial p}{\partial z}\\ \frac{1}{r}\frac{\partial\left(ru_r\left(E+p\right)\right)}{\partial r}+\frac{\partial\left(u_z\left(E+p\right)\right)}{\partial z}\\ \frac{1}{r}\frac{\partial r\alpha_1 u}{\partial r}-\alpha_1\frac{1}{r}\frac{\partial ru}{\partial r}+\frac{\partial \alpha_1 u_z}{\partial z}-\alpha_1\frac{\partial u_z}{\partial z}\end{bmatrix}=\mathbf{0} \tag{A.2}$$

The partial differential system of equations for the governing equations in cylindrical coordinates is

$$\frac{\partial\left(r\mathbf{U}\right)}{\partial t}+\frac{\partial\left(r\mathbf{F}\right)}{\partial r}+\frac{\left(r\mathbf{G}\right)}{\partial z}=\mathbf{S}, \tag{A.3}$$

where

$$\mathbf{U}=\begin{bmatrix}\alpha_1\rho_1\\ \alpha_2\rho_2\\ \rho u_r\\ \rho u_z\\ E\\ \alpha_1\end{bmatrix},\ \mathbf{F}=\begin{bmatrix}\alpha_1\rho_1 u_r\\ \alpha_2\rho_2 u_r\\ \rho u_r^{\,2}+p\\ \rho u_r u_z\\ u_r\left(E+p\right)\\ \alpha_1 u_r\end{bmatrix},\ \mathbf{G}=\begin{bmatrix}\alpha_1\rho_1 u_z\\ \alpha_2\rho_2 u_z\\ \rho u_r u_z\\ \rho u_z^{\,2}+p\\ u_z\left(E+p\right)\\ \alpha_1 u_z\end{bmatrix}\ \mathrm{S}=\begin{bmatrix}0\\ 0\\ p\\ 0\\ 0\\ \alpha_1\nabla\cdot\mathbf{u}\end{bmatrix}. \tag{A.4}$$

A.1 Cartesian Coordinates (*z*-direction)

The governing equations, Eqs. (2.1)-(2.5), are discretised in the *z*-direction $\left(I_i=\left[z_{j-1/2},z_{j+1/2}\right]\right)$ to give the semi-discrete equations for mass, momentum, energy, and volume fraction.

A.1.1 Mass

The finite volume discretisation of the mass conservation for fluid 1 $\left(\alpha_1\rho_1\right)$

$$\frac{\partial\alpha_1\rho_1}{\partial t}=-\frac{\partial\alpha_1\rho_1 u_z}{\partial z} \tag{A.5}$$

$$\int\frac{\partial\alpha_1\rho_1}{\partial t}dV=-\int\left(\nabla\cdot\alpha_1\rho_1 u_z\right)dV \tag{A.6}$$

divergence theorem
$$\int_V\nabla\cdot\mathbf{f}dV=\oint_S\mathbf{f}\cdot\mathbf{n}dA \tag{A.7}$$

$dA=rdrd\theta$ (in the *z*-direction) (A.8)

$$dV=rdrdzd\theta \tag{A.9}$$

$$\int\frac{\partial\alpha_1\rho_1}{\partial t}dV=-\int\left(\nabla\cdot\alpha_1\rho_1 u_z\right)dV \tag{A.10}$$

$$\int\frac{\partial\alpha_1\rho_1}{\partial t}dV=\int\left(\frac{\partial\alpha_1\rho_1 u_z}{\partial z}\right)dV \tag{A.11}$$

$$\int_0^{2\pi}\int_0^1\int_{z_{j-1/2}}^{z_{j+1/2}}\left(\frac{\partial\alpha_1\rho_1}{\partial t}\right)dzrdrd\theta=-\left[\int_0^{2\pi}\int_0^1\left(\mathbf{n}\cdot\alpha_1\rho_1 u_z\right)rdrd\theta-\int_0^{2\pi}\int_0^1\left(\mathbf{n}\cdot\alpha_1\rho_1 u_z\right)rdrd\theta\right] \tag{A.12}$$

$$\left(\frac{\partial\overline{\alpha_1\rho_1}}{\partial t}\right)\int_0^{2\pi}\int_0^1\int_{z_{j-1/2}}^{z_{j+1/2}} dzrdrd\theta = -\left[\int_0^{2\pi}\int_0^1\left(\mathbf{n}\cdot\alpha_1\rho_1u_z\right)rdrd\theta - \int_0^{2\pi}\int_0^1\left(\mathbf{n}\cdot\alpha_1\rho_1u_z\right)rdrd\theta\right] \tag{A.13}$$

where $\overline{\alpha_1\rho_1}$ is the cell average of $\alpha_1\rho_1$

$$\left(\frac{\partial\overline{\alpha_1\rho_1}}{\partial t}\right)\int_0^{2\pi}\int_0^1\left[z\right]_{z_{j-1/2}}^{z_{j+1/2}} rdrd\theta = -\left[\int_0^{2\pi}\int_0^1\left(\mathbf{n}\cdot\alpha_1\rho_1u_z\right)rdrd\theta - \int_0^{2\pi}\int_0^1\left(\mathbf{n}\cdot\alpha_1\rho_1u_z\right)rdrd\theta\right] \tag{A.14}$$

$$\left(z_{j+1/2}-z_{j-1/2}\right)\left(\frac{\partial\overline{\alpha_1\rho_1}}{\partial t}\right)\left(\int_0^{2\pi}\int_0^1 1rdrd\theta\right) = -\left[\left(\alpha_1\rho_1u_z\right)_{j+1/2} - \left(\alpha_1\rho_1u_z\right)_{j-1/2}\right]\left(\int_0^{2\pi}\int_0^1 1rdrd\theta\right) \tag{A.15}$$

$$\Delta z = \left(z_{j+1/2}-z_{j-1/2}\right) \tag{A.16}$$

$$\Delta z\left(\frac{\partial\overline{\alpha_1\rho_1}}{\partial t}\right) = -\left[\left(\alpha_1\rho_1u_z\right)_{j+1/2} - \left(\alpha_1\rho_1u_z\right)_{j-1/2}\right] \tag{A.17}$$

$$\left(\frac{\partial\overline{\alpha_1\rho_1}}{\partial t}\right) = -\frac{\left[\left(\alpha_1\rho_1u_z\right)_{j+1/2} - \left(\alpha_1\rho_1u_z\right)_{j-1/2}\right]}{\Delta z} \tag{A.18}$$

The same applied for the conservation of mass of the second fluid $\left(\alpha_2\rho_2\right)$

$$\left(\frac{\partial\overline{\alpha_2\rho_2}}{\partial t}\right) = -\frac{\left[\left(\alpha_2\rho_2u_z\right)_{j+1/2} - \left(\alpha_2\rho_2u_z\right)_{j-1/2}\right]}{\Delta z} \tag{A.19}$$

A.1.2 **Momentum (r)**

The finite volume discretisation of the momentum in the *r*-direction $\left(\rho u_r\right)$

$$\frac{\partial\rho u_r}{\partial t} = -\frac{\partial\rho u_ru_z}{\partial z} \tag{A.20}$$

$$\int\frac{\partial\rho u_r}{\partial t}dV = -\int\left(\nabla\cdot\rho u_ru_z\right)dV \tag{A.21}$$

divergence theorem

$$\int_V \nabla \cdot \mathbf{f} dV = \oint_S \mathbf{f} \cdot \mathbf{n} dA \tag{A.22}$$

$dA = rdrd\theta$ (in the *z*-direction) (A.23)

$$dV = rdrdzd\theta \tag{A.24}$$

$$\int \frac{\partial \rho u_r}{\partial t} dV = -\int (\nabla \cdot \rho u_r u_z) dV \tag{A.25}$$

$$\int \frac{\partial \rho u_r}{\partial t} dV = \int \left(\frac{\partial \rho u_r u_z}{\partial z} \right) dV \tag{A.26}$$

$$\int_0^{2\pi} \int_0^1 \int_{z_{j-1/2}}^{z_{j+1/2}} \left(\frac{\partial \rho u_r}{\partial t} \right) dz r dr d\theta = -\left[\int_0^{2\pi} \int_0^1 (\mathbf{n} \cdot \rho u_r u_z) r dr d\theta - \int_0^{2\pi} \int_0^1 (\mathbf{n} \cdot \rho u_r u_z) r dr d\theta \right] \tag{A.27}$$

$$\left(\frac{\partial \rho u_r}{\partial t} \right) \int_0^{2\pi} \int_0^1 \int_{z_{j-1/2}}^{z_{j+1/2}} dz r dr d\theta = -\left[\int_0^{2\pi} \int_0^1 (\mathbf{n} \cdot \rho u_r u_z) r dr d\theta - \int_0^{2\pi} \int_0^1 (\mathbf{n} \cdot \rho u_r u_z) r dr d\theta \right] \tag{A.28}$$

where $\overline{\rho u_r}$ is the cell average of ρu_r

$$\left(\frac{\partial \overline{\rho u_r}}{\partial t} \right) \int_0^{2\pi} \int_0^1 [z]_{z_{j-1/2}}^{z_{j+1/2}} r dr d\theta = -\left[\int_0^{2\pi} \int_0^1 (\mathbf{n} \cdot \rho u_r u_z) r dr d\theta - \int_0^{2\pi} \int_0^1 (\mathbf{n} \cdot \rho u_r u_z) r dr d\theta \right] \tag{A.29}$$

$$\left(z_{j+1/2} - z_{j-1/2} \right) \left(\frac{\partial \overline{\rho u_r}}{\partial t} \right) \left(\int_0^{2\pi} \int_0^1 1 r dr d\theta \right) = -\left[\left(\rho u_r u_z \right)_{j+1/2} - \left(\rho u_r u_z \right)_{j-1/2} \right] \left(\int_0^{2\pi} \int_0^1 1 r dr d\theta \right) \tag{A.30}$$

$$\Delta z = \left(z_{j+1/2} - z_{j-1/2} \right) \tag{A.31}$$

$$\Delta z \left(\frac{\partial \overline{\rho u_r}}{\partial t} \right) = -\left[\left(\rho u_r u_z \right)_{j+1/2} - \left(\rho u_r u_z \right)_{j-1/2} \right] \tag{A.32}$$

$$\left(\frac{\partial \overline{\rho u_r}}{\partial t} \right) = -\frac{\left[\left(\rho u_r u_z \right)_{j+1/2} - \left(\rho u_r u_z \right)_{j-1/2} \right]}{\Delta z} \tag{A.33}$$

A.1.3 **Momentum (z)**

The finite volume discretisation of the momentum in the *z*-direction $\left(\rho u_z\right)$

$$\frac{\partial \rho u_z}{\partial t} = \frac{\partial\left(\rho u_z^2\right)}{\partial z} + \frac{\partial p}{\partial z} \tag{A.34}$$

$$\frac{\partial \rho u_z}{\partial t} = \frac{\partial\left(\rho u_z^2 + p\right)}{\partial z} \tag{A.35}$$

$$\int \frac{\partial \rho u_z}{\partial t} dV = -\int \left(\nabla \cdot \left(\rho u_z^2 + p\right)\right) dV \tag{A.36}$$

divergence theorem

$$\int_V \nabla \cdot \mathbf{f} dV = \oint_S \mathbf{f} \cdot \mathbf{n} dA \tag{A.37}$$

$dA = r dr d\theta$ (in the *z*-direction) (A.38)

$$dV = r dr dz d\theta \tag{A.39}$$

$$\int \frac{\partial \rho u_z}{\partial t} dV = -\int \left(\nabla \cdot \left(\rho u_z^2 + p\right)\right) dV \tag{A.40}$$

$$\int \frac{\partial \rho u_z}{\partial t} dV = \int \left(\frac{\partial\left(\rho u_z^2 + p\right)}{\partial z} \right) dV \tag{A.41}$$

$$\int_0^{2\pi} \int_0^1 \int_{z_{j-1/2}}^{z_{j+1/2}} \left(\frac{\partial \rho u_z}{\partial t} \right) dz r dr d\theta = -\left[\int_0^{2\pi} \int_0^1 \left(\mathbf{n} \cdot \left(\rho u_z^2 + p\right)\right) r dr d\theta - \int_0^{2\pi} \int_0^1 \left(\mathbf{n} \cdot \left(\rho u_z^2 + p\right)\right) r dr d\theta \right] \tag{A.42}$$

$$\left(\frac{\partial \overline{\rho u_z}}{\partial t} \right) \int_0^{2\pi} \int_0^1 \int_{z_{j-1/2}}^{z_{j+1/2}} dz r dr d\theta = -\left[\int_0^{2\pi} \int_0^1 \left(\mathbf{n} \cdot \left(\rho u_z^2 + p\right)\right) r dr d\theta - \int_0^{2\pi} \int_0^1 \left(\mathbf{n} \cdot \left(\rho u_z^2 + p\right)\right) r dr d\theta \right] \tag{A.43}$$

where $\overline{\rho u_z}$ is the cell average of ρu_z

$$\left(\frac{\partial\overline{\rho u_z}}{\partial t}\right)\int_0^{2\pi}\int_0^1\left[z\right]_{z_{j-1/2}}^{z_{j+1/2}}rdrd\theta=-\left[\int_0^{2\pi}\int_0^1\left(\mathbf{n}\cdot\left(\rho u_z^2+p\right)\right)rdrd\theta-\int_0^{2\pi}\int_0^1\left(\mathbf{n}\cdot\left(\rho u_z^2+p\right)\right)rdrd\theta\right]$$

(A.44)

$$\left(z_{j+1/2}-z_{j-1/2}\right)\left(\frac{\partial\overline{\rho u_z}}{\partial t}\right)\left(\int_0^{2\pi}\int_0^1 1rdrd\theta\right)=-\left[\left(\rho u_z^2+p\right)_{j+1/2}-\left(\rho u_z^2+p\right)_{j-1/2}\right]\left(\int_0^{2\pi}\int_0^1 1rdrd\theta\right)$$

(A.45)

$$\Delta z=\left(z_{j+1/2}-z_{j-1/2}\right) \tag{A.46}$$

$$\Delta z\left(\frac{\partial\overline{\rho u_z}}{\partial t}\right)=-\left[\left(\rho u_z^2+p\right)_{j+1/2}-\left(\rho u_z^2+p\right)_{j-1/2}\right] \tag{A.47}$$

$$\left(\frac{\partial\overline{\rho u_z}}{\partial t}\right)=-\frac{\left[\left(\rho u_z^2+p\right)_{j+1/2}-\left(\rho u_z^2+p\right)_{j-1/2}\right]}{\Delta z} \tag{A.48}$$

A.1.4 Energy

The finite volume discretisation of the energy conservation (E)

$$\frac{\partial E}{\partial t}=-\frac{\partial\left(E+p\right)u_z}{\partial z} \tag{A.49}$$

$$\int\frac{\partial E}{\partial t}dV=-\int\left(\nabla\cdot\left(E+p\right)u_z\right)dV \tag{A.50}$$

divergence theorem

$$\int_V\nabla\cdot\mathbf{f}dV=\oint_S\mathbf{f}\cdot\mathbf{n}dA \tag{A.51}$$

$dA=rdrd\theta$ (in the *z*-direction) (A.52)

$$dV=rdrdzd\theta \tag{A.53}$$

$$\int\frac{\partial E}{\partial t}dV=-\int\left(\nabla\cdot\left(E+p\right)u_z\right)dV \tag{A.54}$$

$$\int \frac{\partial E}{\partial t} dV = \int \left(\frac{\partial (E+p) u_z}{\partial z} \right) dV \tag{A.55}$$

$$\int_0^{2\pi} \int_0^1 \int_{z_{j-1/2}}^{z_{j+1/2}} \left(\frac{\partial E}{\partial t} \right) dz r dr d\theta = -\left[\int_0^{2\pi} \int_0^1 \left(\mathbf{n} \cdot (E+p) u_z \right) r dr d\theta - \int_0^{2\pi} \int_0^1 \left(\mathbf{n} \cdot (E+p) u_z \right) r dr d\theta \right]$$

(A.56)

$$\left(\frac{\partial \overline{E}}{\partial t} \right) \int_0^{2\pi} \int_0^1 \int_{z_{j-1/2}}^{z_{j+1/2}} dz r dr d\theta = -\left[\int_0^{2\pi} \int_0^1 \left(\mathbf{n} \cdot (E+p) u_z \right) r dr d\theta - \int_0^{2\pi} \int_0^1 \left(\mathbf{n} \cdot (E+p) u_z \right) r dr d\theta \right]$$

(A.57)

where $\overline{E}$ is the cell average of E

$$\left(\frac{\partial \overline{E}}{\partial t} \right) \int_0^{2\pi} \int_0^1 \left[z \right]_{z_{j-1/2}}^{z_{j+1/2}} r dr d\theta = -\left[\int_0^{2\pi} \int_0^1 \left(\mathbf{n} \cdot (E+p) u_z \right) r dr d\theta - \int_0^{2\pi} \int_0^1 \left(\mathbf{n} \cdot (E+p) u_z \right) r dr d\theta \right]$$

(A.58)

$$\left(z_{j+1/2} - z_{j-1/2} \right) \left(\frac{\partial \overline{E}}{\partial t} \right) \left(\int_0^{2\pi} \int_0^1 1 r dr d\theta \right) = -\left[\left((E+p) u_z \right)_{j+1/2} - \left((E+p) u_z \right)_{j-1/2} \right] \left(\int_0^{2\pi} \int_0^1 1 r dr d\theta \right)$$

(A.59)

$$\Delta z = \left(z_{j+1/2} - z_{j-1/2} \right) \tag{A.60}$$

$$\Delta z \left(\frac{\partial \overline{E}}{\partial t} \right) = -\left[\left((E+p) u_z \right)_{j+1/2} - \left((E+p) u_z \right)_{j-1/2} \right] \tag{A.61}$$

$$\left(\frac{\partial \overline{E}}{\partial t} \right) = -\frac{\left[\left((E+p) u_z \right)_{j+1/2} - \left((E+p) u_z \right)_{j-1/2} \right]}{\Delta z} \tag{A.62}$$

A.1.5 Volume fraction

The finite volume discretisation of the volume fraction (α_1) advection equation

$$\frac{\partial \alpha_1}{\partial t} = -u \cdot \nabla \alpha_1 \tag{A.63}$$

product rule

$$\nabla\left(u\cdot\alpha_1\right)=u\cdot\nabla\alpha_1+\alpha_1\cdot\nabla u \tag{A.64}$$

$$u\cdot\nabla\alpha_1=\nabla\left(u\cdot\alpha_1\right)-\alpha_1\cdot\nabla u$$

$$\frac{\partial\alpha_1}{\partial t}=-\nabla\left(\alpha_1 u\right)+\alpha_1\cdot\nabla u \tag{A.65}$$

$$\frac{\partial\alpha_1}{\partial t}=-\frac{\partial\alpha_1 u_z}{\partial z}+\alpha_1\frac{\partial u_z}{\partial z} \tag{A.66}$$

$$\int\frac{\partial\alpha_1}{\partial t}dV=-\int\left(\frac{\partial\alpha_1 u_z}{\partial z}+\alpha_1\frac{\partial u_z}{\partial z}\right)dV \tag{A.67}$$

$$\int\frac{\partial\alpha_1}{\partial t}dV=-\int\left(\frac{\partial\alpha_1 u_z}{\partial z}\right)dV+\int\left(\alpha_1\frac{\partial u_z}{\partial z}\right)dV \tag{A.68}$$

$$\int\frac{\partial\alpha_1}{\partial t}dV=-\int\left(\frac{\partial\alpha_1 u_z}{\partial z}\right)dV+\bar{\alpha}_1\int\left(\frac{\partial u_z}{\partial z}\right)dV \tag{A.69}$$

divergence in cylindrical coordinates

$$\nabla\cdot\mathbf{f}=\frac{1}{r}\left(\frac{\partial\left(rf_r\right)}{\partial r}\right)+\frac{1}{r}\frac{\partial\left(f_\theta\right)}{\partial\theta}+\frac{\partial\left(f_z\right)}{\partial z}$$

divergence theorem (A.70)

$$\int_V\nabla\cdot\mathbf{f}dV=\oint_S\mathbf{f}\cdot\mathbf{n}dA$$

$$\int\left(\frac{1}{r}\frac{\partial f_r}{\partial r}\right)dV=\oint_S f_r dA\rightarrow\int\left(\frac{1}{r}\frac{\partial f_r}{\partial r}\right)dV=\oint_S f_r dA$$

$dA=rdrd\theta$ (in the *z*-direction) (A.71)

$$dV=rdrdzd\theta \tag{A.72}$$

$dA=rdrd\theta$ (in the *z*-direction) (A.73)

$$dV=rdrdzd\theta \tag{A.74}$$

$$\int\frac{\partial\alpha_1}{\partial t}dV=-\int\left(\frac{\partial\alpha_1 u_z}{\partial z}\right)dV+\bar{\alpha}_1\int\left(\frac{\partial u_z}{\partial z}\right)dV \tag{A.75}$$

$$\int_0^{2\pi}\int_0^1\int_{z_{j-1/2}}^{z_{j+1/2}}\left(\frac{\partial\alpha_1}{\partial t}\right)dzrdrd\theta=-\left[\int_0^{2\pi}\int_0^1(\mathbf{n}\cdot\alpha_1u_z)rdrd\theta-\int_0^{2\pi}\int_0^1(\mathbf{n}\cdot\alpha_1u_z)rdrd\theta\right]+\bar{\alpha}_1\left[\int_0^{2\pi}\int_0^1(\mathbf{n}\cdot u_z)rdrd\theta-\int_0^{2\pi}\int_0^1(\mathbf{n}\cdot u_z)rdrd\theta\right] \tag{A.76}$$

$$\left(\frac{\partial\overline{\alpha_1}}{\partial t}\right)\int_0^{2\pi}\int_0^1\int_{z_{j-1/2}}^{z_{j+1/2}}dzrdrd\theta=-\left[\int_0^{2\pi}\int_0^1(\mathbf{n}\cdot\alpha_1u_z)rdrd\theta-\int_0^{2\pi}\int_0^1(\mathbf{n}\cdot\alpha_1u_z)rdrd\theta\right]+\bar{\alpha}_1\left[\int_0^{2\pi}\int_0^1(\mathbf{n}\cdot u_z)rdrd\theta-\int_0^{2\pi}\int_0^1(\mathbf{n}\cdot u_z)rdrd\theta\right] \tag{A.77}$$

where $\overline{\alpha_1}$ is the cell average of α_1

$$\left(\frac{\partial\overline{\alpha_1}}{\partial t}\right)\int_0^{2\pi}\int_0^1[z]_{z_{j-1/2}}^{z_{j+1/2}}rdrd\theta=-\left[\int_0^{2\pi}\int_0^1(\mathbf{n}\cdot\alpha_1u_z)rdrd\theta-\int_0^{2\pi}\int_0^1(\mathbf{n}\cdot\alpha_1u_z)rdrd\theta\right]+\bar{\alpha}_1\left[\int_0^{2\pi}\int_0^1(\mathbf{n}\cdot u_z)rdrd\theta-\int_0^{2\pi}\int_0^1(\mathbf{n}\cdot u_z)rdrd\theta\right] \tag{A.78}$$

$$\left(z_{j+1/2}-z_{j-1/2}\right)\left(\frac{\partial\overline{\alpha_1}}{\partial t}\right)\left(\int_0^{2\pi}\int_0^1 1rdrd\theta\right)=-\left[\left(\alpha_1u_z\right)_{j+1/2}-\left(\alpha_1u_z\right)_{j-1/2}\right]\left(\int_0^{2\pi}\int_0^1 1rdrd\theta\right)+\bar{\alpha}_1\left[\left(u_z\right)_{j+1/2}-\left(u_z\right)_{j-1/2}\right]\left(\int_0^{2\pi}\int_0^1 1rdrd\theta\right) \tag{A.79}$$

$$\Delta z=\left(z_{j+1/2}-z_{j-1/2}\right) \tag{A.80}$$

$$\Delta z\left(\frac{\partial\overline{\alpha_1}}{\partial t}\right)=-\left[\left(\alpha_1u_z\right)_{j+1/2}-\left(\alpha_1u_z\right)_{j-1/2}\right]+\bar{\alpha}_1\left[\left(u_z\right)_{j+1/2}-\left(u_z\right)_{j-1/2}\right] \tag{A.81}$$

$$\left(\frac{\partial\overline{\alpha_1}}{\partial t}\right)=-\frac{\left[\left(\alpha_1u_z\right)_{j+1/2}-\left(\alpha_1u_z\right)_{j-1/2}\right]}{\Delta z}+\frac{\bar{\alpha}_1\left[\left(u_z\right)_{j+1/2}-\left(u_z\right)_{j-1/2}\right]}{\Delta z} \tag{A.82}$$

A.2 Radial Coordinates (*r*-direction)

The governing equations, Eqs. (2.1)-(2.5), are discretised in the *r*-direction in Appendix A.2 to give the semi-discrete equations for mass, momentum, energy, and volume fraction. The discretisation procedure differs for a finite volume element at the axis of symmetry (*z*-axis), thus, we discrete for a typical element (no boundary - section 3.4.2.1) and an element on the axis of symmetry (section 3.4.2.2).

A.2.1 **No boundary**

The semi-discrete equations in the *r*-direction for the interval $I_i = \left[r_{i-1/2}, r_{i+1/2} \right]$ are

A.2.1.1 Mass

The finite volume discretisation of the mass conservation for fluid 1 $(\alpha_1 \rho_1)$

$$\frac{\partial \alpha_1 \rho_1}{\partial t} = -\frac{1}{r} \frac{\partial r \alpha_1 \rho_1 u_r}{\partial r} \tag{A.83}$$

$$\int \frac{\partial \alpha_1 \rho_1}{\partial t} dV = -\int \left(\frac{1}{r} \frac{\partial r \alpha_1 \rho_1 u_r}{\partial r} \right) dV \tag{A.84}$$

divergence in cylindrical coordinates

$$\nabla \cdot \mathbf{f} = \frac{1}{r} \left(\frac{\partial (r f_r)}{\partial r} \right) + \frac{1}{r} \frac{\partial (f_\theta)}{\partial \theta} + \frac{\partial (f_z)}{\partial z} \tag{A.85}$$

divergence theorem

$$\int_V \nabla \cdot \mathbf{f} dV = \oint_S \mathbf{f} \cdot \mathbf{n} dA \tag{A.86}$$

$$\int \left(\frac{1}{r} \frac{\partial f_r}{\partial r} \right) dV = \oint_S f_r dA \rightarrow \int \left(\frac{1}{r} \frac{\partial f_r}{\partial r} \right) dV = \oint_S f_r dA$$

$dA = r dz d\theta$ (in the *r*-direction) (A.87)

$dV = r dr dz d\theta$ (A.88)

$$\int_0^{2\pi} \int_0^1 \int_{r_{i-1/2}}^{r_{i+1/2}} \left(\frac{\partial \alpha_1 \rho_1}{\partial t} \right) r dr dz d\theta = -\left[\int_0^{2\pi} \int_0^1 (\mathbf{n} \cdot \alpha_1 \rho_1 u_r) r_{i+1/2} dz d\theta - \int_0^{2\pi} \int_0^1 (\mathbf{n} \cdot \alpha_1 \rho_1 u_r) r_{i-1/2} dz d\theta \right] \tag{A.89}$$

$$\left(\frac{\partial \overline{\alpha_1 \rho_1}}{\partial t} \right) \int_0^{2\pi} \int_0^1 \int_{r_{i-1/2}}^{r_{i+1/2}} r dr dz d\theta = -\left[\int_0^{2\pi} \int_0^1 (\mathbf{n} \cdot \alpha_1 \rho_1 u_r) r_{i+1/2} dz d\theta - \int_0^{2\pi} \int_0^1 (\mathbf{n} \cdot \alpha_1 \rho_1 u_r) r_{i-1/2} dz d\theta \right] \tag{A.90}$$

where $\overline{\alpha_1 \rho_1}$ is the cell average of $\alpha_1 \rho_1$

$$\left(\frac{\partial \overline{\alpha_1 \rho_1}}{\partial t} \right) \int_0^{2\pi} \int_0^1 \left[\frac{r^2}{2} \right]_{r_{i-1/2}}^{r_{i+1/2}} dz d\theta = -\left[\int_0^{2\pi} \int_0^1 (\mathbf{n} \cdot \alpha_1 \rho_1 u_r) r_{i+1/2} dz d\theta - \int_0^{2\pi} \int_0^1 (\mathbf{n} \cdot \alpha_1 \rho_1 u_r) r_{i-1/2} dz d\theta \right] \tag{A.91}$$

$$\left(\frac{{r_{i+1/2}}^2-{r_{i-1/2}}^2}{2}\right)\left(\frac{\partial\overline{\alpha_1\rho_1}}{\partial t}\right)\left(\int_0^{2\pi}\int_0^1 1dzd\theta\right)=-\left[\left(\alpha_1\rho_1u_r r\right)_{i+1/2}-\left(\alpha_1\rho_1u_r r\right)_{i-1/2}\right]\left(\int_0^{2\pi}\int_0^1 1dzd\theta\right) \tag{A.92}$$

$$\left(\frac{{r_{i+1/2}}^2-{r_{i-1/2}}^2}{2}\right)=r_i\Delta r \tag{A.93}$$

$$r_i\Delta r\left(\frac{\partial\overline{\alpha_1\rho_1}}{\partial t}\right)=-\left[\left(\alpha_1\rho_1u_r r\right)_{i+1/2}-\left(\alpha_1\rho_1u_r r\right)_{i-1/2}\right] \tag{A.94}$$

$$\left(\frac{\partial\overline{\alpha_1\rho_1}}{\partial t}\right)=-\frac{1}{r_i\Delta r}\left[\left(\alpha_1\rho_1u_r r\right)_{i+1/2}-\left(\alpha_1\rho_1u_r r\right)_{i-1/2}\right] \tag{A.95}$$

$$\left(\frac{\partial\overline{\alpha_1\rho_1}}{\partial t}\right)=\frac{\left(\left(\alpha_1\rho_1u_r\right)_{i-1/2}\left(r_i-\frac{\Delta r}{2}\right)\right)-\left(\left(\alpha_1\rho_1u_r\right)_{i+1/2}\left(r_i+\frac{\Delta r}{2}\right)\right)}{r_i\Delta r} \tag{A.96}$$

$$\left(\frac{\partial\overline{\alpha_1\rho_1}}{\partial t}\right)=\frac{r_i\left(\alpha_1\rho_1u_r\right)_{i-1/2}-\frac{\Delta r}{2}\left(\alpha_1\rho_1u_r\right)_{i-1/2}-r_i\left(\alpha_1\rho_1u_r\right)_{i+1/2}-\frac{\Delta r}{2}\left(\alpha_1\rho_1u_r\right)_{i+1/2}}{r_i\Delta r} \tag{A.97}$$

$$\left(\frac{\partial\overline{\alpha_1\rho_1}}{\partial t}\right)=\frac{r_i\left(\alpha_1\rho_1u_r\right)_{i-1/2}-r_i\left(\alpha_1\rho_1u_r\right)_{i+1/2}-\frac{\Delta r}{2}\left(\alpha_1\rho_1u_r\right)_{i-1/2}-\frac{\Delta r}{2}\left(\alpha_1\rho_1u_r\right)_{i+1/2}}{r_i\Delta r} \tag{A.98}$$

$$\left(\frac{\partial\overline{\alpha_1\rho_1}}{\partial t}\right)=\frac{r_i\left(\alpha_1\rho_1u_r\right)_{i-1/2}-r_i\left(\alpha_1\rho_1u_r\right)_{i+1/2}}{r_i\Delta r}+\frac{-\frac{\Delta r}{2}\left(\alpha_1\rho_1u_r\right)_{i-1/2}-\frac{\Delta r}{2}\left(\alpha_1\rho_1u_r\right)_{i+1/2}}{r_i\Delta r} \tag{A.99}$$

$$\left(\frac{\partial\overline{\alpha_1\rho_1}}{\partial t}\right)=-\frac{\left(\alpha_1\rho_1u_r\right)_{i+1/2}-\left(\alpha_1\rho_1u_r\right)_{i-1/2}}{\Delta r}-\frac{\left(\alpha_1\rho_1u_r\right)_{i+1/2}+\left(\alpha_1\rho_1u_r\right)_{i-1/2}}{2r_i} \tag{A.100}$$

The same applied for the conservation of mass of the second fluid $\left(\alpha_2\rho_2\right)$

$$\left(\frac{\partial\overline{\alpha_2\rho_2}}{\partial t}\right)=-\frac{\left(\alpha_2\rho_2u_r\right)_{i+1/2}-\left(\alpha_2\rho_2u_r\right)_{i-1/2}}{\Delta r}-\frac{\left(\alpha_2\rho_2u_r\right)_{i+1/2}+\left(\alpha_2\rho_2u_r\right)_{i-1/2}}{2r_i} \tag{A.101}$$

A.2.1.2 Momentum (r)

The finite volume discretisation of the momentum in the *r*-direction $\left(\rho u_r\right)$

$$\frac{\partial \rho u_r}{\partial t} = -\frac{1}{r}\frac{\partial r \rho u_r^2}{\partial r} - \frac{\partial p}{\partial r} \tag{A.102}$$

chain rule

$$r\frac{\partial p}{\partial r} + p\frac{\partial r}{\partial r} = \frac{\partial rp}{\partial r} \tag{A.103}$$

$$\rightarrow \frac{\partial p}{\partial r} = \frac{1}{r}\frac{\partial rp}{\partial r} - \frac{p}{r}$$

$$\frac{\partial \rho u_r}{\partial t} = -\frac{1}{r}\frac{\partial r \rho u_r^2}{\partial r} - \frac{1}{r}\frac{\partial rp}{\partial r} + \frac{p}{r} \tag{A.104}$$

$$\frac{\partial \rho u_r}{\partial t} = -\frac{1}{r}\frac{\partial r\left(\rho u_r^2 + p\right)}{\partial r} + \frac{p}{r} \tag{A.105}$$

$$\int \frac{\partial \rho u_r}{\partial t} dV = -\int\left(\frac{1}{r}\frac{\partial\left(r\rho u_r^2 + p\right)}{\partial r}\right)dV + \int\left(\frac{p}{r}\right)dV \tag{A.106}$$

divergence in cylindrical coordinates

$$\nabla \cdot \mathbf{f} = \frac{1}{r}\left(\frac{\partial\left(rf_r\right)}{\partial r}\right) + \frac{1}{r}\frac{\partial\left(f_\theta\right)}{\partial \theta} + \frac{\partial\left(f_z\right)}{\partial z} \tag{A.107}$$

divergence theorem

$$\int_V \nabla \cdot \mathbf{f} dV = \oint_S \mathbf{f} \cdot \mathbf{n} dA \tag{A.108}$$

$$\int\left(\frac{1}{r}\frac{\partial f_r}{\partial r}\right)dV = \oint_S f_r dA \rightarrow \int\left(\frac{1}{r}\frac{\partial f_r}{\partial r}\right)dV = \oint_S f_r dA$$

$dA = rdzd\theta$ (in the *r*-direction) (A.109)

$dV = rdrdzd\theta$ (A.110)

$$\int \frac{\partial \rho u_r}{\partial t} dV = -\int\left(\frac{1}{r}\frac{\partial\left(r\rho u_r^2 + p\right)}{\partial r}\right)dV + \int\left(\frac{\overline{p}}{r}\right)dV \tag{A.111}$$

where $\overline{p}$ is the cell average of p

$$\int \frac{\partial \rho u_r}{\partial t} dV = -\int \left(\mathbf{n} \cdot \left(\rho u_r^2 + p \right) \right) dA + \int \left(\frac{\overline{p}}{r} \right) dV \tag{A.112}$$

$$\int_0^{2\pi} \int_0^1 \int_{r_{i-1/2}}^{r_{i+1/2}} \left(\frac{\partial \rho u_r}{\partial t} \right) r dr dz d\theta =$$
$$-\left[\int_0^{2\pi} \int_0^1 \left(\mathbf{n} \cdot \left(\rho u_r^2 + p \right) \right) r_{i+1/2} dz d\theta - \int_0^{2\pi} \int_0^1 \left(\mathbf{n} \cdot \left(\rho u_r^2 + p \right) \right) r_{i-1/2} dz d\theta \right] + \int \left(\frac{\overline{p}}{r} \right) r dr d\theta dz \tag{A.113}$$

$$\left(\frac{\partial \overline{\rho u_r}}{\partial t} \right) \int_0^{2\pi} \int_0^1 \int_{r_{i-1/2}}^{r_{i+1/2}} r dr dz d\theta = -\left[\int_0^{2\pi} \int_0^1 \left(\mathbf{n} \cdot \left(\rho u_r^2 + p \right) \right) r_{i+1/2} dz d\theta - \int_0^{2\pi} \int_0^1 \left(\mathbf{n} \cdot \left(\rho u_r^2 + p \right) \right) r_{i-1/2} dz d\theta \right]$$
$$+ \overline{p} \int_0^{2\pi} \int_0^1 \int_{r_{i-1/2}}^{r_{i+1/2}} 1 dr d\theta dz \tag{A.114}$$

where $\overline{\rho u_r}$ is the cell average of ρu_r

$$\left(\frac{\partial \overline{\rho u_r}}{\partial t} \right) \int_0^{2\pi} \int_0^1 \left[\frac{r^2}{2} \right]_{r_{i-1/2}}^{r_{i+1/2}} dz d\theta = -\left[\int_0^{2\pi} \int_0^1 \left(\mathbf{n} \cdot \left(\rho u_r^2 + p \right) \right) r_{i+1/2} dz d\theta - \int_0^{2\pi} \int_0^1 \left(\mathbf{n} \cdot \left(\rho u_r^2 + p \right) \right) r_{i-1/2} dz d\theta \right]$$
$$+ \overline{p} \int_0^{2\pi} \int_0^1 \left[(r)_{i+1/2} - (r)_{i-1/2} \right] d\theta dz \tag{A.115}$$

$$\left(\frac{r_{i+1/2}{}^2 - r_{i-1/2}{}^2}{2} \right) \left(\frac{\partial \overline{\rho u_r}}{\partial t} \right) \left(\int_0^{2\pi} \int_0^1 1 dz d\theta \right) = -\left[\left(\rho u_r^2 r \right)_{i+1/2} - \left(\rho u_r^2 r \right)_{i-1/2} \right] \left(\int_0^{2\pi} \int_0^1 1 dz d\theta \right)$$
$$+ \overline{p} \left[(r)_{i+1/2} - (r)_{i-1/2} \right] \left(\int_0^{2\pi} \int_0^1 1 dz d\theta \right) \tag{A.116}$$

$$r_i \Delta r \left(\frac{\partial \overline{\rho u_r}}{\partial t} \right) = -\left[\left(\left(\rho u_r^2 + p \right) r \right)_{i+1/2} - \left(\left(\rho u_r^2 + p \right) r \right)_{i-1/2} \right] + \Delta r \overline{p} \tag{A.117}$$

$$\left(\frac{\partial \overline{\rho u_r}}{\partial t} \right) = -\frac{\left[\left(\left(\rho u_r^2 + p \right) r \right)_{i+1/2} - \left(\left(\rho u_r^2 + p \right) r \right)_{i-1/2} \right]}{r_i \Delta r} + \frac{\Delta r \overline{p}}{r_i \Delta r} \tag{A.118}$$

$$\left(\frac{\partial\overline{\rho u_r}}{\partial t}\right)=-\frac{\left[\left(\rho u_r^2+p\right)_{i+1/2}\left(r_i+\frac{\Delta r}{2}\right)-\left(\rho u_r^2+p\right)_{i-1/2}\left(r_i-\frac{\Delta r}{2}\right)\right]}{r_i\Delta r}+\frac{\Delta r\overline{p}}{r_i\Delta r} \tag{A.119}$$

$$\left(\frac{\partial\overline{\rho u_r}}{\partial t}\right)=-\frac{\left[\left(\rho u_r^2+p\right)_{i+1/2}\left(r_i+\frac{\Delta r}{2}\right)-\left(\rho u_r^2+p\right)_{i-1/2}\left(r_i-\frac{\Delta r}{2}\right)\right]}{r_i\Delta r}+\frac{\Delta r\overline{p}}{r_i\Delta r} \tag{A.120}$$

$$\Delta r\overline{p}=\Delta r\frac{p_{i+1/2}+p_{i-1/2}}{2}=p_{i+1/2}\frac{\Delta r}{2}+p_{i-1/2}\frac{\Delta r}{2} \tag{A.121}$$

$$\left(\frac{\partial\overline{\rho u_r}}{\partial t}\right)=\frac{\left[-\left(\rho u_r^2+p\right)_{i+1/2}\left(r_i+\frac{\Delta r}{2}\right)+\left(\rho u_r^2+p\right)_{i-1/2}\left(r_i-\frac{\Delta r}{2}\right)+p_{i+1/2}\frac{\Delta r}{2}+p_{i-1/2}\frac{\Delta r}{2}\right]}{r_i\Delta r} \tag{A.122}$$

$$\left(\frac{\partial\overline{\rho u_r}}{\partial t}\right)=\frac{\left[-\left(\rho u_r^2+p\right)_{i+1/2}r_i-\left(\rho u_r^2+p\right)_{i+1/2}\frac{\Delta r}{2}+\left(\rho u_r^2+p\right)_{i-1/2}r_i-\left(\rho u_r^2+p\right)_{i-1/2}\frac{\Delta r}{2}+p_{i+1/2}\frac{\Delta r}{2}+p_{i-1/2}\frac{\Delta r}{2}\right]}{r_i\Delta r} \tag{A.123}$$

$$\left(\frac{\partial\overline{\rho u_r}}{\partial t}\right)=\frac{\left[-\left(\rho u_r^2+p\right)_{i+1/2}r_i+\left(\rho u_r^2+p\right)_{i-1/2}r_i\right]}{r_i\Delta r}+\frac{\left[-\left(\rho u_r^2+p\right)_{i+1/2}\frac{\Delta r}{2}_i-\left(\rho u_r^2+p\right)_{i-1/2}\frac{\Delta r}{2}_i+(p)_{i+1/2}\frac{\Delta r}{2}+(p)_{i-1/2}\frac{\Delta r}{2}\right]}{r_i\Delta r} \tag{A.124}$$

$$\left(\frac{\partial\overline{\rho u_r}}{\partial t}\right)=-\frac{\left[\left(\rho u_r^2+p\right)_{i+1/2}-\left(\rho u_r^2+p\right)_{i-1/2}\right]}{\Delta r}-\frac{\left[\left(\rho u_r^2\right)_{i+1/2}+\left(\rho u_r^2\right)_{i-1/2}\right]}{2r_i} \tag{A.125}$$

A.2.1.3 Momentum (z)

The finite volume discretisation of the momentum in the *z*-direction $\left(\rho u_z\right)$

$$\frac{\partial\rho u_z}{\partial t}=-\frac{1}{r}\frac{\partial r\rho u_r u_z}{\partial r} \tag{A.126}$$

$$\int\frac{\partial\rho u_z}{\partial t}dV=-\int\left(\frac{1}{r}\frac{\partial r\rho u_r u_z}{\partial r}\right)dV \tag{A.127}$$

divergence in cylindrical coordinates

$$\nabla \cdot \mathbf{f} = \frac{1}{r}\left(\frac{\partial (r f_r)}{\partial r}\right) + \frac{1}{r}\frac{\partial (f_\theta)}{\partial \theta} + \frac{\partial (f_z)}{\partial z} \tag{A.128}$$

divergence theorem

$$\int_V \nabla \cdot \mathbf{f} dV = \oint_S \mathbf{f} \cdot \mathbf{n} dA \tag{A.129}$$

$$\int\left(\frac{1}{r}\frac{\partial f_r}{\partial r}\right)dV = \oint_S f_r dA \rightarrow \int\left(\frac{1}{r}\frac{\partial f_r}{\partial r}\right)dV = \oint_S f_r dA$$

$dA = r dz d\theta$ (in the *r*-direction) (A.130)

$dV = r dr dz d\theta$ (A.131)

$$\int_0^{2\pi}\int_0^1\int_{r_{i-1/2}}^{r_{i+1/2}}\left(\frac{\partial \rho u_z}{\partial t}\right) r dr dz d\theta = -\left[\int_0^{2\pi}\int_0^1 (\mathbf{n}\cdot\rho u_r u_z) r_{i+1/2} dz d\theta - \int_0^{2\pi}\int_0^1 (\mathbf{n}\cdot\rho u_r u_z) r_{i-1/2} dz d\theta\right] \tag{A.132}$$

$$\left(\frac{\partial \overline{\rho u_z}}{\partial t}\right)\int_0^{2\pi}\int_0^1\int_{r_{i-1/2}}^{r_{i+1/2}} r dr dz d\theta = -\left[\int_0^{2\pi}\int_0^1 (\mathbf{n}\cdot\rho u_r u_z) r_{i+1/2} dz d\theta - \int_0^{2\pi}\int_0^1 (\mathbf{n}\cdot\rho u_r u_z) r_{i-1/2} dz d\theta\right] \tag{A.133}$$

where $\overline{\rho u_z}$ is the cell average of ρu_z

$$\left(\frac{\partial \overline{\rho u_z}}{\partial t}\right)\int_0^{2\pi}\int_0^1\left[\frac{r^2}{2}\right]_{r_{i-1/2}}^{r_{i+1/2}} dz d\theta = -\left[\int_0^{2\pi}\int_0^1 (\mathbf{n}\cdot\rho u_r u_z) r_{i+1/2} dz d\theta - \int_0^{2\pi}\int_0^1 (\mathbf{n}\cdot\rho u_r u_z) r_{i-1/2} dz d\theta\right] \tag{A.134}$$

$$\left(\frac{r_{i+1/2}^{\ 2} - r_{i-1/2}^{\ 2}}{2}\right)\left(\frac{\partial \overline{\rho u_z}}{\partial t}\right)\left(\int_0^{2\pi}\int_0^1 1 dz d\theta\right) = -\left[(\rho u_r u_z r)_{i+1/2} - (\rho u_r u_z r)_{i-1/2}\right]\left(\int_0^{2\pi}\int_0^1 1 dz d\theta\right) \tag{A.135}$$

$$\left(\frac{r_{i+1/2}^{\ 2} - r_{i-1/2}^{\ 2}}{2}\right) = r_i \Delta r \tag{A.136}$$

$$r_i \Delta r\left(\frac{\partial \overline{\rho u_z}}{\partial t}\right) = -\left[(\rho u_r u_z r)_{i+1/2} - (\rho u_r u_z r)_{i-1/2}\right] \tag{A.137}$$

$$\left(\frac{\partial \overline{\rho u_z}}{\partial t}\right) = -\frac{1}{r_i \Delta r}\left[(\rho u_r u_z r)_{i+1/2} - (\rho u_r u_z r)_{i-1/2}\right] \tag{A.138}$$

$$\left(\frac{\partial\overline{\rho u_z}}{\partial t}\right)=\frac{\left(\left(\rho u_r u_z\right)_{i-1/2}\left(r_i-\frac{\Delta r}{2}\right)\right)-\left(\left(\rho u_r u_z\right)_{i+1/2}\left(r_i+\frac{\Delta r}{2}\right)\right)}{r_i\Delta r} \tag{A.139}$$

$$\left(\frac{\partial\overline{\rho u_z}}{\partial t}\right)=\frac{r_i\left(\rho u_r u_z\right)_{i-1/2}-\frac{\Delta r}{2}\left(\rho u_r u_z\right)_{i-1/2}-r_i\left(\rho u_r u_z\right)_{i+1/2}-\frac{\Delta r}{2}\left(\rho u_r u_z\right)_{i+1/2}}{r_i\Delta r} \tag{A.140}$$

$$\left(\frac{\partial\overline{\rho u_z}}{\partial t}\right)=\frac{r_i\left(\rho u_r u_z\right)_{i-1/2}-r_i\left(\rho u_r u_z\right)_{i+1/2}-\frac{\Delta r}{2}\left(\rho u_r u_z\right)_{i-1/2}-\frac{\Delta r}{2}\left(\rho u_r u_z\right)_{i+1/2}}{r_i\Delta r} \tag{A.141}$$

$$\left(\frac{\partial\overline{\rho u_z}}{\partial t}\right)=\frac{r_i\left(\rho u_r u_z\right)_{i-1/2}-r_i\left(\rho u_r u_z\right)_{i+1/2}}{r_i\Delta r}+\frac{-\frac{\Delta r}{2}\left(\rho u_r u_z\right)_{i-1/2}-\frac{\Delta r}{2}\left(\rho u_r u_z\right)_{i+1/2}}{r_i\Delta r} \tag{A.142}$$

$$\left(\frac{\partial\overline{\rho u_z}}{\partial t}\right)=-\frac{\left(\rho u_r u_z\right)_{i+1/2}-\left(\rho u_r u_z\right)_{i-1/2}}{\Delta r}-\frac{\left(\rho u_r u_z\right)_{i+1/2}+\left(\rho u_r u_z\right)_{i-1/2}}{2r_i} \tag{A.143}$$

A.2.1.4 Energy

The finite volume discretisation of the energy conservation $\left(E\right)$

$$\frac{\partial E}{\partial t}=-\frac{1}{r}\frac{\partial r\left(E+p\right)u_r}{\partial r} \tag{A.144}$$

$$\int\frac{\partial E}{\partial t}dV=-\int\left(\frac{1}{r}\frac{\partial r\left(E+p\right)u_r}{\partial r}\right)dV \tag{A.145}$$

divergence in cylindrical coordinates

$$\nabla\cdot\mathbf{f}=\frac{1}{r}\left(\frac{\partial\left(rf_r\right)}{\partial r}\right)+\frac{1}{r}\frac{\partial\left(f_\theta\right)}{\partial\theta}+\frac{\partial\left(f_z\right)}{\partial z}$$

divergence theorem (A.146)

$$\int_V\nabla\cdot\mathbf{f}dV=\oint_S\mathbf{f}\cdot\mathbf{n}dA$$

$$\int\left(\frac{1}{r}\frac{\partial f_r}{\partial r}\right)dV=\oint_S f_r dA\rightarrow\int\left(\frac{1}{r}\frac{\partial f_r}{\partial r}\right)dV=\oint_S f_r dA$$

$dA=rdzd\theta$ (in the *r*-direction) (A.147)

$dV=rdrdzd\theta$ (A.148)

$$\int_0^{2\pi}\int_0^1\int_{r_{i-1/2}}^{r_{i+1/2}}\left(\frac{\partial E}{\partial t}\right)rdrdzd\theta=-\left[\int_0^{2\pi}\int_0^1\left(\mathbf{n}\cdot\left(E+p\right)u_r\right)r_{i+1/2}dzd\theta-\int_0^{2\pi}\int_0^1\left(\mathbf{n}\cdot\left(E+p\right)u_r\right)r_{i-1/2}dzd\theta\right] \tag{A.149}$$

$$\left(\frac{\partial\overline{E}}{\partial t}\right)\int_0^{2\pi}\int_0^1\int_{r_{i-1/2}}^{r_{i+1/2}}rdrdzd\theta=-\left[\int_0^{2\pi}\int_0^1\left(\mathbf{n}\cdot\left(E+p\right)u_r\right)r_{i+1/2}dzd\theta-\int_0^{2\pi}\int_0^1\left(\mathbf{n}\cdot\left(E+p\right)u_r\right)r_{i-1/2}dzd\theta\right] \tag{A.150}$$

where $\overline{E}$ is the cell average of E

$$\left(\frac{\partial\overline{E}}{\partial t}\right)\int_0^{2\pi}\int_0^1\left[\frac{r^2}{2}\right]_{r_{i-1/2}}^{r_{i+1/2}}dzd\theta=-\left[\int_0^{2\pi}\int_0^1\left(\mathbf{n}\cdot\left(E+p\right)u_r\right)r_{i+1/2}dzd\theta-\int_0^{2\pi}\int_0^1\left(\mathbf{n}\cdot\left(E+p\right)u_r\right)r_{i-1/2}dzd\theta\right] \tag{A.151}$$

$$\left(\frac{{r_{i+1/2}}^2-{r_{i-1/2}}^2}{2}\right)\left(\frac{\partial\overline{E}}{\partial t}\right)\left(\int_0^{2\pi}\int_0^1 1dzd\theta\right)=-\left[\left(u_r\left(E+p\right)r\right)_{i+1/2}-\left(u_r\left(E+p\right)r\right)_{i-1/2}\right]\left(\int_0^{2\pi}\int_0^1 1dzd\theta\right) \tag{A.152}$$

$$\left(\frac{{r_{i+1/2}}^2-{r_{i-1/2}}^2}{2}\right)=r_i\Delta r \tag{A.153}$$

$$r_i\Delta r\left(\frac{\partial\overline{E}}{\partial t}\right)=-\left[\left(u_r\left(E+p\right)r\right)_{i+1/2}-\left(u_r\left(E+p\right)r\right)_{i-1/2}\right] \tag{A.154}$$

$$\left(\frac{\partial\overline{E}}{\partial t}\right)=-\frac{1}{r_i\Delta r}\left[\left(u_r\left(E+p\right)r\right)_{i+1/2}-\left(u_r\left(E+p\right)r\right)_{i-1/2}\right] \tag{A.155}$$

$$\left(\frac{\partial\overline{E}}{\partial t}\right)=\frac{\left(\left((E+p)u_r\right)_{i-1/2}\left(r_i-\frac{\Delta r}{2}\right)\right)-\left(\left((E+p)u_r\right)_{i+1/2}\left(r_i+\frac{\Delta r}{2}\right)\right)}{r_i\Delta r} \tag{A.156}$$

$$\left(\frac{\partial\overline{E}}{\partial t}\right)=\frac{r_i\left((E+p)u_r\right)_{i-1/2}-\frac{\Delta r}{2}\left((E+p)u_r\right)_{i-1/2}-r_i\left((E+p)u_r\right)_{i+1/2}-\frac{\Delta r}{2}\left((E+p)u_r\right)_{i+1/2}}{r_i\Delta r} \tag{A.157}$$

$$\left(\frac{\partial \overline{E}}{\partial t}\right)=\frac{r_i\left((E+p)u_r\right)_{i-1/2}-r_i\left((E+p)u_r\right)_{i+1/2}-\frac{\Delta r}{2}\left((E+p)u_r\right)_{i-1/2}-\frac{\Delta r}{2}\left((E+p)u_r\right)_{i+1/2}}{r_i\Delta r} \tag{A.158}$$

$$\left(\frac{\partial \overline{E}}{\partial t}\right)=\frac{r_i\left((E+p)u_r\right)_{i-1/2}-r_i\left((E+p)u_r\right)_{i+1/2}}{r_i\Delta r}+\frac{-\frac{\Delta r}{2}\left((E+p)u_r\right)_{i-1/2}-\frac{\Delta r}{2}\left((E+p)u_r\right)_{i+1/2}}{r_i\Delta r} \tag{A.159}$$

$$\left(\frac{\partial \overline{E}}{\partial t}\right)=-\frac{\left((E+p)u_r\right)_{i+1/2}-\left((E+p)u_r\right)_{i-1/2}}{\Delta r}-\frac{\left((E+p)u_r\right)_{i+1/2}+\left((E+p)u_r\right)_{i-1/2}}{2r_i} \tag{A.160}$$

A.2.1.5 Volume fraction

The finite volume discretisation of the volume fraction (α_1) advection equation

$$\frac{\partial \alpha_1}{\partial t}=-u_r\cdot\nabla\alpha_1 \tag{A.161}$$

product rule

$$\begin{aligned}&\nabla\left(u_r\cdot\alpha_1\right)=u_r\cdot\nabla\alpha_1+\alpha_1\cdot\nabla u_r\\&u_r\cdot\nabla\alpha_1=\nabla\left(u_r\cdot\alpha_1\right)-\alpha_1\cdot\nabla u_r\end{aligned} \tag{A.162}$$

$$\frac{\partial \alpha_1}{\partial t}=-\nabla\left(\alpha_1 u_r\right)+\alpha_1\cdot\nabla u_r \tag{A.163}$$

$$\frac{\partial \alpha_1}{\partial t}=-\frac{1}{r}\frac{\partial r\alpha_1 u_r}{\partial r}+\alpha_1\frac{1}{r}\frac{\partial r u_r}{\partial r} \tag{A.164}$$

$$\int\frac{\partial \alpha_1}{\partial t}dV=-\int\left(\frac{1}{r}\frac{\partial r\alpha_1 u_r}{\partial r}+\alpha_1\frac{1}{r}\frac{\partial r u_r}{\partial r}\right)dV \tag{A.165}$$

$$\int\frac{\partial \alpha_1}{\partial t}dV=-\int\left(\frac{1}{r}\frac{\partial r\alpha_1 u_r}{\partial r}\right)dV+\int\left(\alpha_1\frac{1}{r}\frac{\partial r u_r}{\partial r}\right)dV \tag{A.166}$$

$$\int\frac{\partial \alpha_1}{\partial t}dV=-\int\left(\frac{1}{r}\frac{\partial r\alpha_1 u_r}{\partial r}\right)dV+\overline{\alpha}_1\int\left(\frac{1}{r}\frac{\partial r u_r}{\partial r}\right)dV \tag{A.167}$$

divergence in cylindrical coordinates

$$\nabla \cdot \mathbf{f} = \frac{1}{r}\left(\frac{\partial(rf_r)}{\partial r}\right) + \frac{1}{r}\frac{\partial(f_\theta)}{\partial \theta} + \frac{\partial(f_z)}{\partial z}$$

divergence theorem (A.168)

$$\int_V \nabla \cdot \mathbf{f} dV = \oint_S \mathbf{f} \cdot \mathbf{n} dA$$

$$\int\left(\frac{1}{r}\frac{\partial f_r}{\partial r}\right)dV = \oint_S f_r dA \rightarrow \int\left(\frac{1}{r}\frac{\partial f_r}{\partial r}\right)dV = \oint_S f_r dA$$

$dA = rdzd\theta$ (in the *r*-direction) (A.169)

$dV = rdrdzd\theta$ (A.170)

$$\int_0^{2\pi}\int_0^1\int_{r_{i-1/2}}^{r_{i+1/2}}\left(\frac{\partial \alpha_1}{\partial t}\right)rdrdzd\theta = -\left[\int_0^{2\pi}\int_0^1(\mathbf{n}\cdot\alpha_1 u_r)r_{i+1/2}dzd\theta - \int_0^{2\pi}\int_0^1(\mathbf{n}\cdot\alpha_1 u_r)r_{i-1/2}dzd\theta\right] + \bar{\alpha}_1\left[\int_0^{2\pi}\int_0^1(\mathbf{n}\cdot u_r)r_{i+1/2}dzd\theta - \int_0^{2\pi}\int_0^1(\mathbf{n}\cdot u_r)r_{i-1/2}dzd\theta\right]$$

(A.171)

$$\left(\frac{\partial \overline{\alpha_1}}{\partial t}\right)\int_0^{2\pi}\int_0^1\int_{r_{i-1/2}}^{r_{i+1/2}} rdrdzd\theta = -\left[\int_0^{2\pi}\int_0^1(\mathbf{n}\cdot\alpha_1 u_r)r_{i+1/2}dzd\theta - \int_0^{2\pi}\int_0^1(\mathbf{n}\cdot\alpha_1 u_r)r_{i-1/2}dzd\theta\right] + \bar{\alpha}_1\left[\int_0^{2\pi}\int_0^1(\mathbf{n}\cdot u_r)r_{i+1/2}dzd\theta - \int_0^{2\pi}\int_0^1(\mathbf{n}\cdot u_r)r_{i-1/2}dzd\theta\right]$$

(A.172)

where $\overline{\alpha_1}$ is the cell average of α_1

$$\left(\frac{\partial \overline{\alpha_1}}{\partial t}\right)\int_0^{2\pi}\int_0^1\left[\frac{r^2}{2}\right]_{r_{i-1/2}}^{r_{i+1/2}}dzd\theta = -\left[\int_0^{2\pi}\int_0^1(\mathbf{n}\cdot\alpha_1 u_r)r_{i+1/2}dzd\theta - \int_0^{2\pi}\int_0^1(\mathbf{n}\cdot\alpha_1 u_r)r_{i-1/2}dzd\theta\right] + \bar{\alpha}_1\left[\int_0^{2\pi}\int_0^1(\mathbf{n}\cdot u_r)r_{i+1/2}dzd\theta - \int_0^{2\pi}\int_0^1(\mathbf{n}\cdot u_r)r_{i-1/2}dzd\theta\right]$$

(A.173)

$$\left(\frac{{r_{i+1/2}}^2 - {r_{i-1/2}}^2}{2}\right)\left(\frac{\partial \overline{\alpha_1}}{\partial t}\right)\left(\int_0^{2\pi}\int_0^1 1dzd\theta\right) = -\left[(\alpha_1 u_r r)_{i+1/2} - (\alpha_1 u_r r)_{i-1/2}\right]\left(\int_0^{2\pi}\int_0^1 1dzd\theta\right) + \bar{\alpha}_1\left[(u_r r)_{i+1/2} - (u_r r)_{i-1/2}\right]\left(\int_0^{2\pi}\int_0^1 1dzd\theta\right)$$

(A.174)

$$\left(\frac{r_{i+1/2}{}^2 - r_{i-1/2}{}^2}{2}\right) = r_i \Delta r \tag{A.175}$$

$$r_i \Delta r \left(\frac{\partial \overline{\alpha_1}}{\partial t}\right) = -\left[\left(\alpha_1 u_r r\right)_{i+1/2} - \left(\alpha_1 u_r r\right)_{i-1/2}\right] + \bar{\alpha}_1 \left[\left(u_r r\right)_{i+1/2} - \left(u_r r\right)_{i-1/2}\right] \tag{A.176}$$

$$\left(\frac{\partial \overline{\alpha_1}}{\partial t}\right) = -\frac{1}{r_i \Delta r}\left[\left(u_r r\right)_{i+1/2} - \left(\alpha_1 u_r r\right)_{i-1/2}\right] + \bar{\alpha}_1 \frac{1}{r_i \Delta r}\left[\left(u_r r\right)_{i+1/2} - \left(u_r r\right)_{i-1/2}\right] \tag{A.177}$$

$$\left(\frac{\partial \overline{\alpha_1}}{\partial t}\right) = \frac{\left(\left(\alpha_1 u_r\right)_{i-1/2}\left(r_i - \frac{\Delta r}{2}\right)\right) - \left(\left(\alpha_1 u_r\right)_{i+1/2}\left(r_i + \frac{\Delta r}{2}\right)\right)}{r_i \Delta r} - \frac{\bar{\alpha}_1\left(\left(u_r\right)_{i-1/2}\left(r_i - \frac{\Delta r}{2}\right)\right) - \left(\left(u_r\right)_{i+1/2}\left(r_i + \frac{\Delta r}{2}\right)\right)}{r_i \Delta r} \tag{A.178}$$

$$\left(\frac{\partial \overline{\alpha_1}}{\partial t}\right) = \frac{r_i\left(\alpha_1 u_r\right)_{i-1/2} - \frac{\Delta r}{2}\left(\alpha_1 u_r\right)_{i-1/2} - r_i\left(\alpha_1 u_r\right)_{i+1/2} - \frac{\Delta r}{2}\left(\alpha_1 u_r\right)_{i+1/2}}{r_i \Delta r} - \bar{\alpha}_1 \frac{r_i\left(u_r\right)_{i-1/2} - \frac{\Delta r}{2}\left(u_r\right)_{i-1/2} - r_i\left(u_r\right)_{i+1/2} - \frac{\Delta r}{2}\left(u_r\right)_{i+1/2}}{r_i \Delta r} \tag{A.179}$$

$$\left(\frac{\partial \overline{\alpha_1}}{\partial t}\right) = \frac{r_i\left(\alpha_1 u_r\right)_{i-1/2} - r_i\left(\alpha_1 u_r\right)_{i+1/2} - \frac{\Delta r}{2}\left(\alpha_1 u_r\right)_{i-1/2} - \frac{\Delta r}{2}\left(\alpha_1 u_r\right)_{i+1/2}}{r_i \Delta r} - \bar{\alpha}_1 \frac{r_i\left(u_r\right)_{i-1/2} - r_i\left(u_r\right)_{i+1/2} - \frac{\Delta r}{2}\left(u_r\right)_{i-1/2} - \frac{\Delta r}{2}\left(u_r\right)_{i+1/2}}{r_i \Delta r} \tag{A.180}$$

$$\left(\frac{\partial \overline{\alpha_1}}{\partial t}\right) = \frac{\left(\alpha_1 u_r\right)_{i-1/2} - \left(\alpha_1 u_r\right)_{i+1/2}}{\Delta r} - \frac{\left(\alpha_1 u_r\right)_{i-1/2} + \left(\alpha_1 u_r\right)_{i+1/2}}{2 r_i} - \bar{\alpha}_1 \frac{\left(u_r\right)_{i-1/2} - \left(u_r\right)_{i+1/2}}{\Delta r} + \bar{\alpha}_1 \frac{\left(u_r\right)_{i-1/2} + \left(u_r\right)_{i+1/2}}{2 r_i} \tag{A.181}$$

$$\left(\frac{\partial \overline{\alpha_1}}{\partial t}\right) = -\frac{\left(\alpha_1 u_r\right)_{i+1/2} - \left(\alpha_1 u_r\right)_{i-1/2}}{\Delta r} - \frac{\left(\alpha_1 u_r\right)_{i+1/2} + \left(\alpha_1 u_r\right)_{i-1/2}}{2 r_i} + \bar{\alpha}_1 \frac{\left(u_r\right)_{i+1/2} - \left(u_r\right)_{i-1/2}}{\Delta r} + \bar{\alpha}_1 \frac{\left(u_r\right)_{i+1/2} + \left(u_r\right)_{i-1/2}}{2 r_i} \tag{A.182}$$

$$\left(\frac{\partial\overline{\alpha_1}}{\partial t}\right)=-\frac{(\alpha_1 u_r)_{i+1/2}-(\alpha_1 u_r)_{i-1/2}}{\Delta r}+\frac{\bar{\alpha}_1(u_r)_{i+1/2}-\bar{\alpha}_1(u_r)_{i-1/2}}{\Delta r}$$
$$-\frac{(\alpha_1 u_r)_{i+1/2}+(\alpha_1 u_r)_{i-1/2}}{2r_i}+\frac{\bar{\alpha}_1(u_r)_{i+1/2}+\bar{\alpha}_1(u_r)_{i-1/2}}{2r_i} \tag{A.183}$$

$$\left(\frac{\partial\overline{\alpha_1}}{\partial t}\right)=-\frac{(\alpha_1 u_r)_{i+1/2}-(\alpha_1 u_r)_{i-1/2}}{\Delta r}-\frac{-\bar{\alpha}_1(u_r)_{i+1/2}+\bar{\alpha}_1(u_r)_{i-1/2}}{\Delta r}$$
$$-\frac{(\alpha_1 u_r)_{i+1/2}+(\alpha_1 u_r)_{i-1/2}}{2r_i}-\frac{-\bar{\alpha}_1(u_r)_{i+1/2}-\bar{\alpha}_1(u_r)_{i-1/2}}{2r_i} \tag{A.184}$$

$$\left(\frac{\partial\overline{\alpha_1}}{\partial t}\right)=-\frac{(\alpha_1 u_r)_{i+1/2}-(\alpha_1 u_r)_{i-1/2}-\bar{\alpha}_1(u_r)_{i+1/2}+\bar{\alpha}_1(u_r)_{i-1/2}}{\Delta r}$$
$$-\frac{(\alpha_1 u_r)_{i+1/2}+(\alpha_1 u_r)_{i-1/2}-\bar{\alpha}_1(u_r)_{i+1/2}-\bar{\alpha}_1(u_r)_{i-1/2}}{2r_i} \tag{A.185}$$

$$\left(\frac{\partial\overline{\alpha_1}}{\partial t}\right)=-\frac{\left((\alpha_1 u_r)_{i+1/2}-\bar{\alpha}_1(u_r)_{i+1/2}\right)-\left((\alpha_1 u_r)_{i-1/2}-\bar{\alpha}_1(u_r)_{i-1/2}\right)}{\Delta r}$$
$$-\frac{\left((\alpha_1 u_r)_{i+1/2}-\bar{\alpha}_1(u_r)_{i+1/2}\right)+\left((\alpha_1 u_r)_{i-1/2}-\bar{\alpha}_1(u_r)_{i-1/2}\right)}{2r_i} \tag{A.186}$$

A.2.2 At the axis of symmetry

To discretise the governing equations at the axis of symmetry in the radial direction (r) we integrate from $r=0$ to $r=r_{i+1/2}$ $\left(I_i=\left[0,r_{i+1/2}\right]\right)$

A.2.2.1 Mass

The finite volume discretisation of the mass conservation for fluid 1 $(\alpha_1\rho_1)$

$$\frac{\partial\alpha_1\rho_1}{\partial t}=-\frac{1}{r}\frac{\partial r\alpha_1\rho_1 u_r}{\partial r} \tag{A.187}$$

$$\int\frac{\partial\alpha_1\rho_1}{\partial t}dV=-\int\left(\frac{1}{r}\frac{\partial r\alpha_1\rho_1 u_r}{\partial r}\right)dV \tag{A.188}$$

divergence in cylindrical coordinates

$$\nabla \cdot \mathbf{f} = \frac{1}{r}\left(\frac{\partial(rf_r)}{\partial r}\right) + \frac{1}{r}\frac{\partial(f_\theta)}{\partial \theta} + \frac{\partial(f_z)}{\partial z}$$

divergence theorem (A.189)

$$\int_V \nabla \cdot \mathbf{f} dV = \oint_S \mathbf{f} \cdot \mathbf{n} dA$$

$$\int\left(\frac{1}{r}\frac{\partial rf_r}{\partial r}\right)dV = \oint_S f_r dA \rightarrow \int\left(\frac{1}{r}\frac{\partial rf_r}{\partial r}\right)dV = \oint_S f_r dA$$

$dA = rdzd\theta$ (in the *r*-direction) (A.190)

$$dV = rdrdzd\theta \tag{A.191}$$

$$\int \frac{\partial \alpha_1 \rho_1}{\partial t} dV = -\int (\mathbf{n} \cdot r\alpha_1 \rho_1 u_r) dA \tag{A.192}$$

$$\int_0^{2\pi}\int_0^1\int_0^{r_{i+1/2}}\left(\frac{\partial \alpha_1 \rho_1}{\partial t}\right) r dr dz d\theta = -\left[\int_0^{2\pi}\int_0^1 (\mathbf{n} \cdot \alpha_1 \rho_1 u_r) r_{i+1/2} dz d\theta - \int_0^{2\pi}\int_0^1 (\mathbf{n} \cdot \alpha_1 \rho_1 u_r) \overset{\rightarrow 0}{r_{i-1/2}} dz d\theta\right] \tag{A.193}$$

$$\left(\frac{\partial \overline{\alpha_1 \rho_1}}{\partial t}\right)\int_0^{2\pi}\int_0^1\int_0^{r_{i+1/2}} r dr dz d\theta = -\left[\int_0^{2\pi}\int_0^1 (\mathbf{n} \cdot \alpha_1 \rho_1 u_r) r_{i+1/2} dz d\theta\right] \tag{A.194}$$

$$\left(\frac{\partial \overline{\alpha_1 \rho_1}}{\partial t}\right)\int_0^{2\pi}\int_0^1\left[\frac{r^2}{2}\right]_0^{r_{i+1/2}} dz d\theta = -\left[\int_0^{2\pi}\int_0^1 (\mathbf{n} \cdot \alpha_1 \rho_1 u_r) r_{i+1/2} dz d\theta\right] \tag{A.195}$$

$$\left(\frac{r_{i+1/2}{}^2}{2}\right)\left(\frac{\partial \overline{\alpha_1 \rho_1}}{\partial t}\right)\left(\int_0^{2\pi}\int_0^1 1 dz d\theta\right) = -\left[(\alpha_1 \rho_1 u_r r)_{i+1/2} - (\alpha_1 \rho_1 u_r r)_{i-1/2}\right]\left(\int_0^{2\pi}\int_0^1 1 dz d\theta\right) \tag{A.196}$$

$$\left(\frac{r_{i+1/2}{}^2}{2}\right) = \frac{(2r_i + \Delta r)^2}{8} = \frac{\Delta r^2}{8} \tag{A.197}$$

$$\frac{\Delta r^2}{8}\left(\frac{\partial \overline{\alpha_1 \rho_1}}{\partial t}\right) = -\left[(\alpha_1 \rho_1 u_r r)_{i+1/2}\right] \tag{A.198}$$

$$\left(\frac{\partial \overline{\alpha_1 \rho_1}}{\partial t}\right) = -\frac{8}{\Delta r^2}\left[(\alpha_1 \rho_1 u_r r)_{i+1/2}\right] \tag{A.199}$$

$$\left(\frac{\partial\overline{\alpha_1\rho_1}}{\partial t}\right)=\frac{-\left(\left(\alpha_1\rho_1u_r\right)_{i+1/2}\left(r_i+\frac{\Delta r}{2}\right)\right)}{\frac{\Delta r^2}{8}} \tag{A.200}$$

$$r_i=0 \tag{A.201}$$

$$\left(\frac{\partial\overline{\alpha_1\rho_1}}{\partial t}\right)=\frac{-\left(\left(\alpha_1\rho_1u_r\right)_{i+1/2}\left(\frac{\Delta r}{2}\right)\right)}{\frac{\Delta r^2}{8}} \tag{A.202}$$

$$\left(\frac{\partial\overline{\alpha_1\rho_1}}{\partial t}\right)=-\frac{8}{\Delta r^2}\frac{\Delta r}{2}\left(\alpha_1\rho_1u_r\right)_{i+1/2} \tag{A.203}$$

$$\left(\frac{\partial\overline{\alpha_1\rho_1}}{\partial t}\right)=-\frac{4\left(\alpha_1\rho_1u_r\right)_{i+1/2}}{\Delta r} \tag{A.204}$$

The same applied for the conservation of mass of the second fluid $\left(\alpha_2\rho_2\right)$

$$\left(\frac{\partial\overline{\alpha_2\rho_2}}{\partial t}\right)=-\frac{4\left(\alpha_2\rho_2u_r\right)_{i+1/2}}{\Delta r} \tag{A.205}$$

A.2.2.2 Momentum (r)

The finite volume discretisation of the momentum in the *r*-direction $\left(\rho u_r\right)$

$$\int\frac{\partial\rho u_r}{\partial t}dV=-\int\left(\frac{1}{r}\frac{\partial\left(r\rho u_r^2+p\right)}{\partial r}\right)dV+\int\left(\frac{\overline{p}}{r}\right)dV \tag{A.206}$$

divergence in cylindrical coordinates

$$\nabla\cdot\mathbf{f}=\frac{1}{r}\left(\frac{\partial\left(rf_r\right)}{\partial r}\right)+\frac{1}{r}\frac{\partial\left(f_\theta\right)}{\partial\theta}+\frac{\partial\left(f_z\right)}{\partial z}$$

divergence theorem (A.207)

$$\int_V\nabla\cdot\mathbf{f}dV=\oint_S\mathbf{f}\cdot\mathbf{n}dA$$

$$\int\left(\frac{1}{r}\frac{\partial rf_r}{\partial r}\right)dV=\oint_S f_r dA\rightarrow\int\left(\frac{1}{r}\frac{\partial rf_r}{\partial r}\right)dV=\oint_S f_r dA$$

$dA = rdzd\theta$ (in the r-direction) (A.208)

$$dV = rdrdzd\theta \tag{A.209}$$

$$\int \frac{\partial \rho u_r}{\partial t} dV = -\int \left(\mathbf{n} \cdot \left(\rho u_r^2 + p \right) \right) dA + \int \left(\frac{\bar{p}}{r} \right) dV \tag{A.210}$$

$$\int_0^{2\pi} \int_0^1 \int_0^{r_{i+1/2}} \left(\frac{\partial \rho u_r}{\partial t} \right) rdrdzd\theta = -\left[\int_0^{2\pi} \int_0^1 \left(\mathbf{n} \cdot \left(\rho u_r^2 + p \right) \right) r_{i+1/2} dzd\theta - \int_0^{2\pi} \int_0^1 \left(\mathbf{n} \cdot \left(\rho u_r^2 + p \right) \right) r_{i-1/2} dzd\theta \right] + \int \left(\frac{\bar{p}}{r} \right) rdrd\theta dz \tag{A.211}$$

$$\left(\frac{\partial \overline{\rho u_r}}{\partial t} \right) \int_0^{2\pi} \int_0^1 \int_0^{r_{i+1/2}} rdrdzd\theta = -\left[\int_0^{2\pi} \int_0^1 \left(\mathbf{n} \cdot \left(\rho u_r^2 + p \right) \right) r_{i+1/2} dzd\theta \right] + \bar{p} \int_0^{2\pi} \int_0^1 \int_0^{r_{i+1/2}} 1 drd\theta dz \tag{A.212}$$

$$\left(\frac{\partial \overline{\rho u_r}}{\partial t} \right) \int_0^{2\pi} \int_0^1 \left[\frac{r^2}{2} \right]_0^{r_{i+1/2}} dzd\theta = -\left[\int_0^{2\pi} \int_0^1 \left(\mathbf{n} \cdot \left(\rho u_r^2 + p \right) \right) r_{i+1/2} dzd\theta \right] + \bar{p} \int_0^{2\pi} \int_0^1 \left[(r)_{i+1/2} \right] d\theta dz \tag{A.213}$$

$$\left(\frac{r_{i+1/2}^{\ 2}}{2} \right) \left(\frac{\partial \overline{\rho u_r}}{\partial t} \right) \left(\int_0^{2\pi} \int_0^1 1 dzd\theta \right) = -\left[\left(\rho u_r^2 + p \right) r_{i+1/2} \right] \left(\int_0^{2\pi} \int_0^1 1 dzd\theta \right) + \bar{p} \left[(r)_{i+1/2} \right] \left(\int_0^{2\pi} \int_0^1 1 dzd\theta \right) \tag{A.214}$$

$$\left(\frac{r_{i+1/2}^{\ 2}}{2} \right) \left(\frac{\partial \overline{\rho u_r}}{\partial t} \right) = -\left[\left(\rho u_r^2 + p \right) r_{i+1/2} \right] + \bar{p} \left[(r)_{i+1/2} \right] \tag{A.215}$$

$$\left(\frac{r_{i+1/2}^{\ 2}}{2} \right) = \frac{\Delta r^2}{8} \tag{A.216}$$

$$\frac{\Delta r^2}{8} \left(\frac{\partial \overline{\rho u_r}}{\partial t} \right) = -\left[\left(\rho u_r^2 + p \right) r_{i+1/2} \right] + \bar{p} \left[(r)_{i+1/2} \right] \tag{A.217}$$

$$\left(\frac{\partial \overline{\rho u_r}}{\partial t} \right) = -\frac{8}{\Delta r^2} \left[\left(\rho u_r^2 + p \right)_{i+1/2} \left(r_i + \frac{\Delta r}{2} \right) - \bar{p} \left(r_i + \frac{\Delta r}{2} \right) \right] \tag{A.218}$$

$$\left(\frac{\partial \overline{\rho u_r}}{\partial t} \right) = -\frac{8}{\Delta r^2} \left(\frac{\Delta r}{2} \left(\rho u_r^2 + p \right)_{i+1/2} - \frac{\Delta r}{2} \bar{p} \right) \tag{A.219}$$

$$\left(\frac{\partial\overline{\rho u_r}}{\partial t}\right)=-\frac{4\left(\left(\rho u_r^2+p\right)_{i+1/2}-\bar{p}\right)}{\Delta r} \tag{A.220}$$

A.2.2.3 Momentum (z)

The finite volume discretisation of the momentum in the *z*-direction $\left(\rho u_z\right)$

$$\frac{\partial\rho u_z}{\partial t}=-\frac{1}{r}\frac{\partial r\rho u_r u_z}{\partial r} \tag{A.221}$$

$$\int\frac{\partial\rho u_z}{\partial t}dV=-\int\left(\frac{1}{r}\frac{\partial r\rho u_r u_z}{\partial r}\right)dV \tag{A.222}$$

divergence in cylindrical coordinates

$$\nabla\cdot\mathbf{f}=\frac{1}{r}\left(\frac{\partial\left(rf_r\right)}{\partial r}\right)+\frac{1}{r}\frac{\partial\left(f_\theta\right)}{\partial\theta}+\frac{\partial\left(f_z\right)}{\partial z}$$

divergence theorem (A.223)

$$\int_V\nabla\cdot\mathbf{f}dV=\oint_S\mathbf{f}\cdot\mathbf{n}dA$$

$$\int\left(\frac{1}{r}\frac{\partial rf_r}{\partial r}\right)dV=\oint_S f_r dA\rightarrow\int\left(\frac{1}{r}\frac{\partial rf_r}{\partial r}\right)dV=\oint_S f_r dA$$

$dA=rdzd\theta$ (in the *r*-direction) (A.224)

$$dV=rdrdzd\theta \tag{A.225}$$

$$\int\frac{\partial\rho u_z}{\partial t}dV=-\int\left(\mathbf{n}\cdot r\rho u_r u_z\right)dA \tag{A.226}$$

$$\int_0^{2\pi}\int_0^1\int_0^{r_{i+1/2}}\left(\frac{\partial\rho u_z}{\partial t}\right)rdrdzd\theta=-\left[\int_0^{2\pi}\int_0^1\left(\mathbf{n}\cdot\rho u_r u_z\right)r_{i+1/2}dzd\theta-\int_0^{2\pi}\int_0^1\left(\mathbf{n}\cdot\rho u_r u_z\right)\overset{\rightarrow 0}{r_{i-1/2}}dzd\theta\right] \tag{A.227}$$

$$\left(\frac{\partial\overline{\rho u_z}}{\partial t}\right)\int_0^{2\pi}\int_0^1\int_0^{r_{i+1/2}}rdrdzd\theta=-\left[\int_0^{2\pi}\int_0^1\left(\mathbf{n}\cdot\rho u_r u_z\right)r_{i+1/2}dzd\theta\right] \tag{A.228}$$

$$\left(\frac{\partial\overline{\rho u_z}}{\partial t}\right)\int_0^{2\pi}\int_0^1\left[\frac{r^2}{2}\right]_0^{r_{i+1/2}}dzd\theta=-\left[\int_0^{2\pi}\int_0^1\left(\mathbf{n}\cdot\rho u_r u_z\right)r_{i+1/2}dzd\theta\right] \tag{A.229}$$

$$\left(\frac{r_{i+1/2}{}^2}{2}\right)\left(\frac{\partial\overline{\rho u_z}}{\partial t}\right)\left(\int_0^{2\pi}\int_0^1 1dzd\theta\right)=-\left[\left(\rho u_r u_z r\right)_{i+1/2}-\left(\rho u_r u_z r\right)_{i-1/2}\right]\left(\int_0^{2\pi}\int_0^1 1dzd\theta\right) \tag{A.230}$$

$$\left(\frac{r_{i+1/2}{}^2}{2}\right)=\frac{\left(2r_i+\Delta r\right)^2}{8}=\frac{\Delta r^2}{8} \tag{A.231}$$

$$\frac{\Delta r^2}{8}\left(\frac{\partial\overline{\rho u_z}}{\partial t}\right)=-\left[\left(\rho u_r u_z r\right)_{i+1/2}\right] \tag{A.232}$$

$$\left(\frac{\partial\overline{\rho u_z}}{\partial t}\right)=-\frac{8}{\Delta r^2}\left[\left(\rho u_r u_z r\right)_{i+1/2}\right] \tag{A.233}$$

$$\left(\frac{\partial\overline{\rho u_z}}{\partial t}\right)=\frac{-\left(\left(\rho u_r u_z\right)_{i+1/2}\left(r_i+\frac{\Delta r}{2}\right)\right)}{\frac{\Delta r^2}{8}} \tag{A.234}$$

$$r_i=0 \tag{A.235}$$

$$\left(\frac{\partial\overline{\rho u_z}}{\partial t}\right)=\frac{-\left(\left(\rho u_r u_z\right)_{i+1/2}\left(\frac{\Delta r}{2}\right)\right)}{\frac{\Delta r^2}{8}} \tag{A.236}$$

$$\left(\frac{\partial\overline{\rho u_z}}{\partial t}\right)=-\frac{8}{\Delta r^2}\frac{\Delta r}{2}\left(\rho u_r u_z\right)_{i+1/2} \tag{A.237}$$

$$\left(\frac{\partial\overline{\rho u_z}}{\partial t}\right)=-\frac{4\left(\rho u_r u_z\right)_{i+1/2}}{\Delta r} \tag{A.238}$$

A.2.2.4 Energy

The finite volume discretisation of the energy conservation $\left(E\right)$

$$\frac{\partial E}{\partial t}=-\frac{1}{r}\frac{\partial r\left(E+p\right)u_r}{\partial r} \tag{A.239}$$

$$\int \frac{\partial E}{\partial t} dV = -\int \left(\frac{1}{r} \frac{\partial r(E+p)u_r}{\partial r} \right) dV \tag{A.240}$$

divergence in cylindrical coordinates

$$\nabla \cdot \mathbf{f} = \frac{1}{r}\left(\frac{\partial (r f_r)}{\partial r} \right) + \frac{1}{r}\frac{\partial (f_\theta)}{\partial \theta} + \frac{\partial (f_z)}{\partial z}$$

divergence theorem (A.241)

$$\int_V \nabla \cdot \mathbf{f} dV = \oint_S \mathbf{f} \cdot \mathbf{n} dA$$

$$\int \left(\frac{1}{r} \frac{\partial r f_r}{\partial r} \right) dV = \oint_S f_r dA \rightarrow \int \left(\frac{1}{r} \frac{\partial r f_r}{\partial r} \right) dV = \oint_S f_r dA$$

$dA = r dz d\theta$ (in the *r*-direction) (A.242)

$$dV = r dr dz d\theta \tag{A.243}$$

$$\int \frac{\partial E}{\partial t} dV = -\int \left(\mathbf{n} \cdot r(E+p)u_r \right) dA \tag{A.244}$$

$$\int_0^{2\pi} \int_0^1 \int_0^{r_{i+1/2}} \left(\frac{\partial E}{\partial t} \right) r dr dz d\theta = -\left[\int_0^{2\pi} \int_0^1 \left(\mathbf{n} \cdot (E+p)u_r \right) r_{i+1/2} dz d\theta \right] \tag{A.245}$$

$$\left(\frac{\partial \overline{E}}{\partial t} \right) \int_0^{2\pi} \int_0^1 \int_0^{r_{i+1/2}} r dr dz d\theta = -\left[\int_0^{2\pi} \int_0^1 \left(\mathbf{n} \cdot (E+p)u_r \right) r_{i+1/2} dz d\theta \right] \tag{A.246}$$

$$\left(\frac{\partial \overline{E}}{\partial t} \right) \int_0^{2\pi} \int_0^1 \left[\frac{r^2}{2} \right]_0^{r_{i+1/2}} dz d\theta = -\left[\int_0^{2\pi} \int_0^1 \left(\mathbf{n} \cdot (E+p)u_r \right) r_{i+1/2} dz d\theta \right] \tag{A.247}$$

$$\left(\frac{{r_{i+1/2}}^2}{2} \right) \left(\frac{\partial \overline{E}}{\partial t} \right) \left(\int_0^{2\pi} \int_0^1 1 dz d\theta \right) = -\left[\left(u_r (E+p) r \right)_{i+1/2} \right] \left(\int_0^{2\pi} \int_0^1 1 dz d\theta \right) \tag{A.248}$$

$$\left(\frac{{r_{i+1/2}}^2}{2} \right) = \frac{\Delta r^2}{8} \tag{A.249}$$

$$\frac{\Delta r^2}{8} \left(\frac{\partial \overline{E}}{\partial t} \right) = -\left[\left(u_r (E+p) r \right)_{i+1/2} \right] \tag{A.250}$$

$$\left(\frac{\partial \overline{E}}{\partial t} \right) = -\frac{8}{\Delta r^2} \left(\left((E+p)u_r \right)_{i+1/2} \left(r_i + \frac{\Delta r}{2} \right) \right) \tag{A.251}$$

$$r_i = 0 \tag{A.252}$$

$$\left(\frac{\partial \overline{E}}{\partial t}\right) = -\frac{8}{\Delta r^2}\frac{\Delta r}{2}\left(\left((E+p)u_r\right)_{i+1/2}\right) \tag{A.253}$$

$$\left(\frac{\partial \overline{E}}{\partial t}\right) = -\frac{4\left((E+p)u_r\right)_{i+1/2}}{\Delta r} \tag{A.254}$$

A.2.2.5 Volume fraction

The finite volume discretisation of the volume fraction (α_1) advection equation

$$\frac{\partial \alpha_1}{\partial t} = -u_r \cdot \nabla \alpha_1 \tag{A.255}$$

product rule

$$\nabla\left(u_r \cdot \alpha_1\right) = u_r \cdot \nabla \alpha_1 + \alpha_1 \cdot \nabla u_r \tag{A.256}$$

$$u_r \cdot \nabla \alpha_1 = \nabla\left(u_r \cdot \alpha_1\right) - \alpha_1 \cdot \nabla u_r$$

$$\frac{\partial \alpha_1}{\partial t} = -\nabla\left(\alpha_1 u_r\right) + \alpha_1 \cdot \nabla u_r \tag{A.257}$$

$$\frac{\partial \alpha_1}{\partial t} = -\frac{1}{r}\frac{\partial r\alpha_1 u_r}{\partial r} + \alpha_1 \frac{1}{r}\frac{\partial r u_r}{\partial r} \tag{A.258}$$

$$\int \frac{\partial \alpha_1}{\partial t} dV = -\int\left(\frac{1}{r}\frac{\partial r\alpha_1 u_r}{\partial r} + \alpha_1 \frac{1}{r}\frac{\partial r u_r}{\partial r}\right) dV \tag{A.259}$$

$$\int \frac{\partial \alpha_1}{\partial t} dV = -\int\left(\frac{1}{r}\frac{\partial r\alpha_1 u_r}{\partial r}\right) dV + \int\left(\alpha_1 \frac{1}{r}\frac{\partial r u_r}{\partial r}\right) dV \tag{A.260}$$

$$\int \frac{\partial \alpha_1}{\partial t} dV = -\int\left(\frac{1}{r}\frac{\partial r\alpha_1 u_r}{\partial r}\right) dV + \bar{\alpha}_1 \int\left(\frac{1}{r}\frac{\partial r u_r}{\partial r}\right) dV \tag{A.261}$$

divergence in cylindrical coordinates

$$\nabla \cdot \mathbf{f} = \frac{1}{r}\left(\frac{\partial(rf_r)}{\partial r}\right) + \frac{1}{r}\frac{\partial(f_\theta)}{\partial \theta} + \frac{\partial(f_z)}{\partial z}$$

divergence theorem (A.262)

$$\int_V \nabla \cdot \mathbf{f} dV = \oint_S \mathbf{f} \cdot \mathbf{n} dA$$

$$\int\left(\frac{1}{r}\frac{\partial f_r}{\partial r}\right)dV = \oint_S f_r dA \rightarrow \int\left(\frac{1}{r}\frac{\partial f_r}{\partial r}\right)dV = \oint_S f_r dA$$

$dA = rdzd\theta$ (in the *r*-direction) (A.263)

$$dV = rdrdzd\theta \tag{A.264}$$

$$\begin{aligned}\int_0^{2\pi}\int_0^1\int_0^{r_{i+1/2}}\left(\frac{\partial \alpha_1}{\partial t}\right)rdrdzd\theta = &-\left[\int_0^{2\pi}\int_0^1(\mathbf{n}\cdot\alpha_1 u_r)r_{i+1/2}dzd\theta - \int_0^{2\pi}\int_0^1(\mathbf{n}\cdot\alpha_1 u_r)\overset{\rightarrow 0}{r_{i-1/2}}dzd\theta\right] \\ &+\bar{\alpha}_1\left[\int_0^{2\pi}\int_0^1(\mathbf{n}\cdot u_r)r_{i+1/2}dzd\theta - \int_0^{2\pi}\int_0^1(\mathbf{n}\cdot u_r)\overset{\rightarrow 0}{r_{i-1/2}}dzd\theta\right]\end{aligned} \tag{A.265}$$

$$\left(\frac{\partial\overline{\alpha_1}}{\partial t}\right)\int_0^{2\pi}\int_0^1\int_0^{r_{i+1/2}} rdrdzd\theta = -\left[\int_0^{2\pi}\int_0^1(\mathbf{n}\cdot\alpha_1 u_r)r_{i+1/2}dzd\theta\right] + \bar{\alpha}_1\left[\int_0^{2\pi}\int_0^1(\mathbf{n}\cdot u_r)r_{i+1/2}dzd\theta\right] \tag{A.266}$$

$$\left(\frac{\partial\overline{\alpha_1}}{\partial t}\right)\int_0^{2\pi}\int_0^1\left[\frac{r^2}{2}\right]_0^{r_{i+1/2}} dzd\theta = -\left[\int_0^{2\pi}\int_0^1(\mathbf{n}\cdot\alpha_1 u_r)r_{i+1/2}dzd\theta\right] + \bar{\alpha}_1\left[\int_0^{2\pi}\int_0^1(\mathbf{n}\cdot u_r)r_{i+1/2}dzd\theta\right] \tag{A.267}$$

$$\left(\frac{{r_{i+1/2}}^2}{2}\right)\left(\frac{\partial\overline{\alpha_1}}{\partial t}\right)\left(\int_0^{2\pi}\int_0^1 1dzd\theta\right) = -\left[(\alpha_1 u_r r)_{i+1/2}\right]\left(\int_0^{2\pi}\int_0^1 1dzd\theta\right) + \bar{\alpha}_1\left[(u_r r)_{i+1/2}\right]\left(\int_0^{2\pi}\int_0^1 1dzd\theta\right)$$

(A.268)

$$\left(\frac{{r_{i+1/2}}^2}{2}\right) = \frac{(2r_i + \Delta r)^2}{8} = \frac{\Delta r^2}{8} \tag{A.269}$$

$$\frac{\Delta r^2}{8}\left(\frac{\partial\overline{\alpha_1}}{\partial t}\right) = -\left[(\alpha_1 u_r r)_{i+1/2}\right] + \bar{\alpha}_1\left[(u_r r)_{i+1/2}\right] \tag{A.270}$$

$$\left(\frac{\partial\overline{\alpha_1}}{\partial t}\right) = -\frac{8r_{i+1/2}}{\Delta r^2}\left[(\alpha_1 u_r)_{i+1/2} - \bar{\alpha}_1(u_r)_{i+1/2}\right] \tag{A.271}$$

$$\left(\frac{\partial\overline{\alpha_1}}{\partial t}\right)=-\frac{8\left(r_i+\frac{\Delta r}{2}\right)}{\Delta r^2}\left[\left(\alpha_1 u_r\right)_{i+1/2}-\bar{\alpha}_1\left(u_r\right)_{i+1/2}\right] \tag{A.272}$$

$$r_i=0 \tag{A.273}$$

$$\left(\frac{\partial\overline{\alpha_1}}{\partial t}\right)=-\frac{8\left(\frac{\Delta r}{2}\right)}{\Delta r^2}\left[\left(\alpha_1 u_r\right)_{i+1/2}-\bar{\alpha}_1\left(u_r\right)_{i+1/2}\right] \tag{A.274}$$

$$\left(\frac{\partial\overline{\alpha_1}}{\partial t}\right)=-\frac{4\left(\left(\alpha_1 u_r\right)_{i+1/2}-\bar{\alpha}_1\left(u_r\right)_{i+1/2}\right)}{\Delta r} \tag{A.275}$$

Appendix B Immersed Moving Boundary Discretisation

The immersed moving boundary in the fixed Eulerian grid results in a change in momentum and energy. It also results in a change in the volume, thus, the density in the conservation of mass equation changes. The moving boundary, however, does not change the volume fraction (α_1). Therefore, we consider the discretisation of the set of conversation equations, excluding the advection equation, at the moving boundary in the *z*-direction

$$\frac{\partial \mathbf{U}(r,z,t)}{\partial t} + \frac{\partial \mathbf{F}\left(\mathbf{U}(r,z,t)\right)}{\partial r} + \frac{\partial \mathbf{G}\left(\mathbf{U}(r,z,t)\right)}{\partial z} = 0 \tag{B.1}$$

where

$$\mathbf{U} = \left[\alpha_1\rho_1,\ \alpha_2\rho_2,\ \rho u_r\ \rho u_z,\ E\right]^T \tag{B.2}$$

$$\mathbf{F} = \left[\alpha_1\rho_1 u_x,\ \alpha_2\rho_2 u_r,\ \rho u_r u_r + p,\ \rho u_r u_z,\ u_r\left(E+p\right)\right]^T \tag{B.3}$$

$$\mathbf{G} = \left[\alpha_1\rho_1 u_y,\ \alpha_2\rho_2 u_y,\ \rho u_x u_y,\ \rho u_y u_y + p,\ u_y\left(E+p\right)\right]^T \tag{B.4}$$

$$\mathbf{S} = \left[0,\ 0,\ 0,\ 0,\ 0,\ \alpha_1\nabla\cdot\mathbf{u}\right]^T \tag{B.5}$$

$$\int \frac{\partial \alpha_C \mathbf{U}}{\partial t} dV = -\int \left(\nabla\cdot\alpha_c \mathbf{G}\left(\mathbf{U}\right)\right) dV \tag{B.6}$$

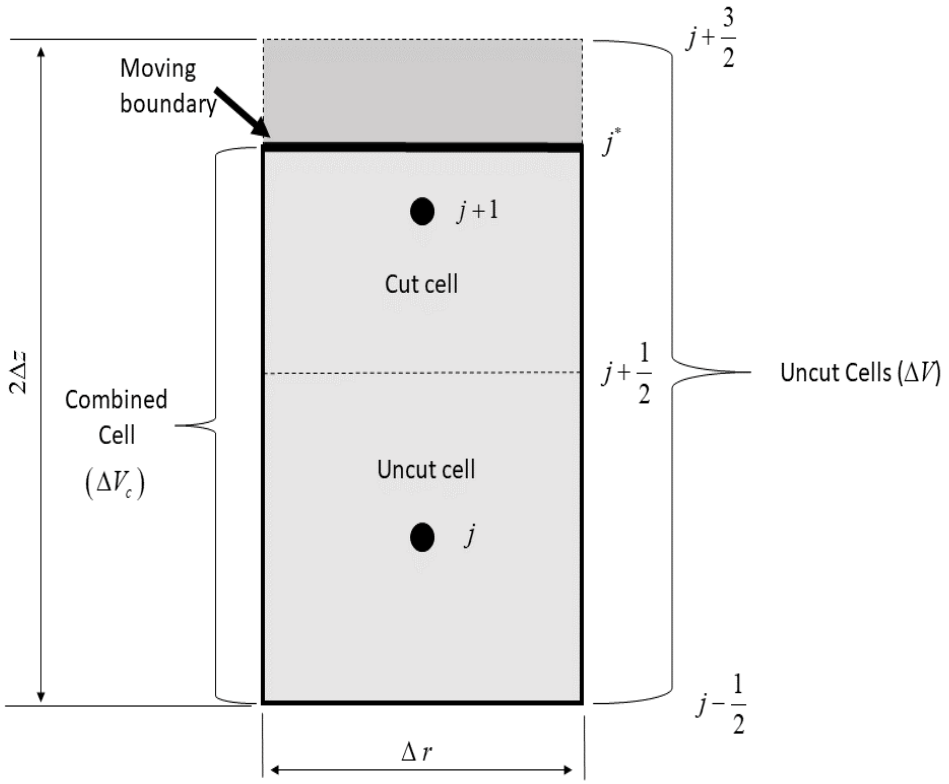

Figure 9.1. The depiction of the moving boundary forming a cut cell. The cut cell is combined with its neighbouring uncut cell to make the combined cell.

$$\alpha_c^n = \frac{\Delta V_c}{\Delta V} \tag{B.7}$$

It is Important to note that the volume of when solving for the combined cell uses the volume of the two cells: $\Delta V = \Delta r\left(2\Delta z\right)$.

divergence theorem

$$\int_V \nabla \cdot \mathbf{f} dV = \oint_S \mathbf{f} \cdot \mathbf{n} dA \tag{B.8}$$

divergence in cylindrical coordinates

$$\nabla \cdot \mathbf{f} = \frac{1}{r}\left(\frac{\partial (rf_r)}{\partial r}\right) + \frac{1}{r}\frac{\partial (f_\theta)}{\partial \theta} + \frac{\partial (f_z)}{\partial z}$$

divergence theorem (B.9)

$$\int_V \nabla \cdot \mathbf{f} dV = \oint_S \mathbf{f} \cdot \mathbf{n} dA$$

$$\int\left(\frac{1}{r}\frac{\partial rf_r}{\partial r}\right)dV = \oint_S f_r dA \rightarrow \int\left(\frac{1}{r}\frac{\partial rf_r}{\partial r}\right)dV = \oint_S f_r dA$$

$dA = rdrd\theta$ (in the *z*-direction) (B.10)

$dV = rdrdzd\theta$ (B.11)

$$\int \frac{\partial \alpha_C \mathbf{U}}{\partial t} dV = -\int \left(\nabla \cdot \mathbf{G}(\mathbf{U})\right) dV \tag{B.12}$$

$$\int \frac{\partial \alpha_C \mathbf{U}}{\partial t} dV = \int\left(\frac{\partial \mathbf{G}(\mathbf{U})}{\partial z}\right) dV \tag{B.13}$$

Note that for a combined cell, the conserved variables are integrated from $z_{j-\frac{1}{2}}$ to $z_{j+\frac{3}{2}}$ giving $2\Delta z$

$$\int_0^{2\pi}\int_0^1\int_{z_{j-1/2}}^{z_{j+3/2}}\left(\frac{\partial \alpha_c \mathbf{U}}{\partial t}\right) dz r dr d\theta = -\left[\int_0^{2\pi}\int_0^1 \left(\mathbf{n}\cdot\mathbf{G}(\mathbf{U})\right) r dr d\theta - \int_0^{2\pi}\int_0^1 \left(\mathbf{n}\cdot\mathbf{G}(\mathbf{U})\right) r dr d\theta\right] \tag{B.14}$$

$$\left(\frac{\partial \overline{\alpha_c \mathbf{U}}}{\partial t}\right)\int_0^{2\pi}\int_0^1\int_{z_{j-1/2}}^{z_{j+3/2}} dz r dr d\theta = -\left[\int_0^{2\pi}\int_0^1 \left(\mathbf{n}\cdot\mathbf{G}(\mathbf{U})\right) r dr d\theta - \int_0^{2\pi}\int_0^1 \left(\mathbf{n}\cdot\mathbf{G}(\mathbf{U})\right) r dr d\theta\right] \tag{B.15}$$

$$\left(\frac{\partial \overline{\alpha_c \mathbf{U}}}{\partial t}\right)\int_0^{2\pi}\int_0^1 [z]_{z_{j-1/2}}^{z_{j+3/2}} r dr d\theta = -\left[\int_0^{2\pi}\int_0^1 \left(\mathbf{n}\cdot\mathbf{G}(\mathbf{U})\right) r dr d\theta - \int_0^{2\pi}\int_0^1 \left(\mathbf{n}\cdot\mathbf{G}(\mathbf{U})\right) r dr d\theta\right] \tag{B.16}$$

$$\left(z_{j+3/2} - z_{j-1/2}\right)\left(\frac{\partial \overline{\alpha_c \mathbf{U}}}{\partial t}\right)\left(\int_0^{2\pi}\int_0^1 1 r dr d\theta\right) = -\left[\left(\mathbf{G}(\mathbf{U})\right)_{j^*} - \left(\mathbf{G}(\mathbf{U})\right)_{j-1/2}\right]\left(\int_0^{2\pi}\int_0^1 1 r dr d\theta\right) \tag{B.17}$$

Note that $\left(\mathbf{G}(\mathbf{U})\right)_{j^*}$ is the flux at the immersed moving boundary, which is given by the one-sided Riemann problem.

$$2\Delta z = \left(z_{j+3/2} - z_{j-1/2}\right) \tag{B.18}$$

$$2\Delta z\left(\frac{\partial\overline{\alpha_c\mathbf{U}}}{\partial t}\right)=-\left[\left(\mathbf{G}(\mathbf{U})\right)_{j^*}-\left(\mathbf{G}(\mathbf{U})\right)_{j-1/2}\right] \tag{B.19}$$

$$\left(\frac{\partial\overline{\alpha_c\mathbf{U}}}{\partial t}\right)=-\frac{\left[\left(\mathbf{G}(\mathbf{U})\right)_{j^*}-\left(\mathbf{G}(\mathbf{U})\right)_{j-1/2}\right]}{2\Delta z} \tag{B.20}$$

This is the semi-discrete form for the 1D case in the *z*-direction.

Now we integrate in time using the explicit first-order Euler time integration (flux taken at the previous time step (n)). Note that the adaption to use the RK3TVD scheme instead is trivial.

$$\int_n^{n+1}\left(\frac{\partial\overline{\alpha_c\mathbf{U}}}{\partial t}\right)dt=\int_n^{n+1}\left(-\frac{\left[\mathbf{G}(\mathbf{U})_{j^*}-\mathbf{G}(\mathbf{U})_{j-1/2}\right]}{2\Delta z}\right)dt \tag{B.21}$$

$$\left(\overline{\alpha_c{}^{n+1}\mathbf{U}^{n+1}}-\overline{\alpha_c{}^{n}\mathbf{U}^{n}}\right)\Delta t=-\frac{\left[\mathbf{G}(\mathbf{U})_{j^*}-\mathbf{G}(\mathbf{U})_{j-1/2}\right]}{2\Delta z} \tag{B.22}$$

$$\overline{\alpha_c{}^{n+1}\mathbf{U}^{n+1}}=\overline{\alpha_c{}^{n}\mathbf{U}^{n}}+\frac{1}{\Delta t}\left(-\frac{\left[\mathbf{G}(\mathbf{U})_{j^*}-\mathbf{G}(\mathbf{U})_{j-1/2}\right]}{2\Delta z}\right) \tag{B.23}$$

$$\overline{\alpha_c{}^{n+1}\mathbf{U}^{n+1}}=\frac{\overline{\alpha_c{}^{n}\mathbf{U}^{n}}+\frac{1}{\Delta t}\left(-\frac{\left[\mathbf{G}(\mathbf{U})_{j^*}-\mathbf{G}(\mathbf{U})_{j-1/2}\right]}{\Delta z}\right)}{\alpha_c{}^{n+1}} \tag{B.24}$$

The subsequent semi-discrete equations for the combined cell are

$$\left(\frac{\partial\overline{\alpha_c\alpha_1\rho_1}}{\partial t}\right)=-\frac{\left(\alpha_1\rho_1u_z\right)_{j^*}-\left(\alpha_1\rho_1u_z\right)_{j-1/2}}{2\Delta z} \tag{B.25}$$

$$\left(\frac{\partial\overline{\alpha_c\alpha_2\rho_2}}{\partial t}\right)=-\frac{\left(\alpha_2\rho_2u_z\right)_{j^*}-\left(\alpha_2\rho_2u_z\right)_{j-1/2}}{2\Delta z} \tag{B.26}$$

$$\left(\frac{\partial\overline{\alpha_c\rho u}}{\partial t}\right)=-\frac{\left[\left(\rho u_z^2+p\right)_{j^*}-\left(\rho u_z^2+p\right)_{j-1/2}\right]}{2\Delta z} \tag{B.27}$$

$$\left(\frac{\partial\overline{\alpha_c E}}{\partial t}\right)=-\frac{\left((E+p)u_z\right)_{j^*}-\left((E+p)u_z\right)_{j-1/2}}{2\Delta z} \tag{B.28}$$

$$\left(\frac{\partial\overline{\alpha_1}}{\partial t}\right)=-\frac{\left(\left(\alpha_1 u_z\right)_{j^*}-\bar{\alpha}_1\left(u_z\right)_{j^*}\right)-\left(\left(\alpha_1 u_z\right)_{j-1/2}-\bar{\alpha}_1\left(u_z\right)_{j-1/2}\right)}{2\Delta z} \tag{B.29}$$

Thus, the key changes to the semi-discrete equations for a combined cell are (1) the inclusion of the volume fraction of the combined cell $\left(\alpha_c=\frac{\Delta V_c}{\Delta V}\right)$ and (2) the combined cell is the combination of two finite volume cells, $I=\left[r_{i-1/2},r_{i+1/2}\right]\times\left[z_{j-1/2},z_{j+3/2}\right]$, so it is integrated over two cells, (i,j) and $(i,j+1)$, resulting in the $2\Delta z$ term. Note that the volume fraction Eq. (B.29) is not influenced by the volume fraction of the combined cell.

The one-sided Riemann problem at the moving boundary results in no mass and volume fraction flux because the immersed boundary implied a no-through-flow boundary condition; thus, those equations simplify to

$$\left(\frac{\partial\overline{\alpha_c\alpha_1\rho_1}}{\partial t}\right)=\frac{\left(\alpha_1\rho_1 u_z\right)_{j-1/2}}{2\Delta z} \tag{B.30}$$

$$\left(\frac{\partial\overline{\alpha_c\alpha_2\rho_2}}{\partial t}\right)=-\frac{\left(\alpha_2\rho_2 u_z\right)_{j-1/2}}{2\Delta z} \tag{B.31}$$

$$\left(\frac{\partial\overline{\alpha_1}}{\partial t}\right)=\frac{\left(\left(\alpha_1 u_z\right)_{j-1/2}-\bar{\alpha}_1\left(u_z\right)_{j-1/2}\right)}{2\Delta z} \tag{B.32}$$

The inclusion of the radial flux terms requires the radial flux from the two cells, (i,j) and $(i,j+1)$, that compose the combined cell. The 2D discrete equations for the combined cells (not at the axis of symmetry) are

$$\left(\frac{\partial\overline{\alpha_c\alpha_1\rho_1}}{\partial t}\right)=\frac{\left(\alpha_1\rho_1u_z\right)_{j-1/2}}{2\Delta z}+\sum_{n=0}^{1}\left(-\frac{\left(\alpha_1\rho_1u_r\right)_{i+1/2,\,j+n}-\left(\alpha_1\rho_1u_r\right)_{i-1/2,\,j+n}}{\Delta r}-\frac{\left(\alpha_1\rho_1u_r\right)_{i+1/2,\,j+n}+\left(\alpha_1\rho_1u_r\right)_{i-1/2,\,j+n}}{2r_i}\right) \tag{B.33}$$

$$\left(\frac{\partial\overline{\alpha_c\alpha_2\rho_2}}{\partial t}\right)=-\frac{\left(\alpha_2\rho_2u_z\right)_{j-1/2}}{2\Delta z}+\sum_{n=0}^{1}\left(-\frac{\left(\alpha_2\rho_2u_r\right)_{i+1/2,\,j+n}-\left(\alpha_2\rho_2u_r\right)_{i-1/2,\,j+n}}{\Delta r}-\frac{\left(\alpha_2\rho_2u_r\right)_{i+1/2,\,j+n}+\left(\alpha_2\rho_2u_r\right)_{i-1/2,\,j+n}}{2r_i}\right) \tag{B.34}$$

$$\left(\frac{\partial\overline{\alpha_c\rho u_r}}{\partial t}\right)=-\frac{\left[\left(\rho u_ru_z\right)_{j^*}-\left(\rho u_ru_z\right)_{j-1/2}\right]}{2\Delta z}+\sum_{n=0}^{1}\left(-\frac{\left[\left(\rho u_r^2+p\right)_{i+1/2,\,j+n}-\left(\rho u_r^2+p\right)_{i-1/2,\,j+n}\right]}{\Delta r}-r\frac{\left[\left(\rho u_r^2\right)_{i+1/2,\,j+n}+\left(\rho u_r^2\right)_{i-1/2,\,j+n}\right]}{2r_i}\right) \tag{B.35}$$

$$\left(\frac{\partial\overline{\alpha_c\rho u_z}}{\partial t}\right)=-\frac{\left[\left(\rho u_z^2+p\right)_{j^*}-\left(\rho u_z^2+p\right)_{j-1/2}\right]}{2\Delta z}+\sum_{n=0}^{1}\left(-\frac{\left[\left(\rho u_ru_z\right)_{i+1/2,\,j+n}-\left(\rho u_ru_z\right)_{i-1/2,\,j+n}\right]}{\Delta r}-\frac{\left[\left(\rho u_ru_z\right)_{i+1/2,\,j+n}+\left(\rho u_ru_z\right)_{i-1/2,\,j+n}\right]}{2r_i}\right) \tag{B.36}$$

$$\left(\frac{\partial\overline{\alpha_cE}}{\partial t}\right)=-\frac{\left(\left(E+p\right)u_z\right)_{j^*}-\left(\left(E+p\right)u_z\right)_{j-1/2}}{2\Delta z}+\sum_{n=0}^{1}\left(-\frac{\left(\left(E+p\right)u_r\right)_{i+1/2,\,j+n}-\left(\left(E+p\right)u_r\right)_{i-1/2,\,j+n}}{\Delta r}-\frac{\left(\left(E+p\right)u_r\right)_{i+1/2,\,j+n}+\left(\left(E+p\right)u_r\right)_{i-1/2,\,j+n}}{2r_i}\right) \tag{B.37}$$

$$\left(\frac{\partial \alpha_1}{\partial t}\right) = \frac{\left((\alpha_1 u_z)_{j-1/2} - \bar{\alpha}_1 (u_z)_{j-1/2}\right)}{2\Delta z} + \sum_{n=0}^{1} \left(\begin{array}{c} -\dfrac{\left((\alpha_1 u_r)_{i+1/2,\, j+n} - \bar{\alpha}_1 (u_r)_{i+1/2,\, j+n}\right) - \left((\alpha_1 u_r)_{i-1/2,\, j+n} - \bar{\alpha}_1 (u_r)_{i-1/2,\, j+n}\right)}{\Delta r} \\ -\dfrac{\left((\alpha_1 u_r)_{i+1/2,\, j+n} - \bar{\alpha}_1 (u_r)_{i+1/2,\, j+n}\right) + \left((\alpha_1 u_r)_{i-1/2,\, j+n} - \bar{\alpha}_1 (u_r)_{i-1/2,\, j+n}\right)}{2 r_i} \end{array} \right) \quad \text{(B.38)}$$

B.1 Moving boundary check

A check was conducted to ensure that the displacement amplitude of the moving boundary (a) gives the correct acoustic pressure amplitude (p_A). This is done by approximating the maximum pressure emitted by a moving boundary and comparing this pressure to the maximum pressure produced by the moving reflective boundary in the numerical model.

To approximate the pressure emitted from a moving reflective boundary, we consider a case where the boundary is moving at a velocity of v as depicted in Figure B.1.1. The maximum velocity of the boundary is $v_{\max} = 2\pi fa$ for a moving boundary oscillating in a sinusoidal manner, where f is the frequency of the moving boundary. The largest pressure occurs when the boundary reaches its maximum velocity.

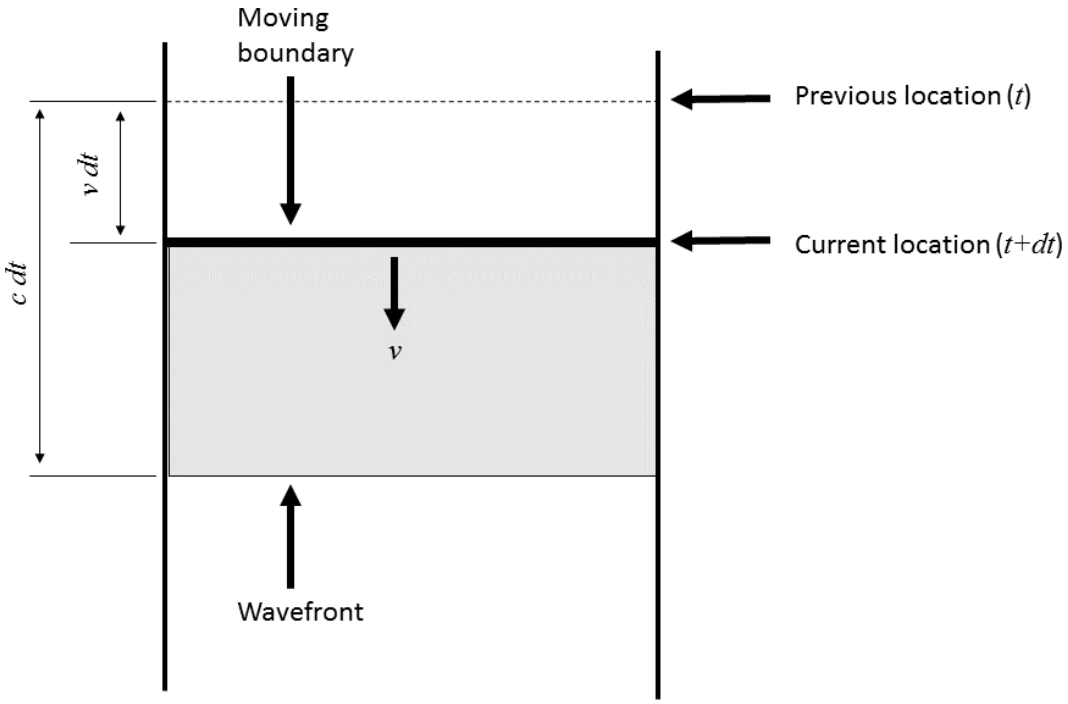

Figure B.1.1. Depiction of the moving boundary input into the system.

The change in pressure of a fluid (Δp) for a volume (V) depends on the change in volume (ΔV):

$$\Delta p = -B\frac{\Delta V}{V} \tag{B.39}$$

where the adiabatic bulk modulus of water which is $B = 2.15e9$ Pa. The volume we consider is between the wavefront that is travelling at the speed of sound (c) and the initial position (t) of the moving boundary (see Figure B.1.1)

$$V = A \cdot c \cdot dt\,. \tag{B.40}$$

The maximum change in volume as the boundary moves from its initial position (t) to its final position $(t + dt)$ (see Figure B.1.1) is

$$\Delta V = -A \cdot v_{\max} \cdot dt \tag{B.41}$$

Thus, we approximate the pressure amplitude of the resulting acoustic wave by $p_A \approx \Delta p$. Substitution of Eq. (B.40) and Eq. (B.41) into Eq. (B.39) gives

$$p_A = -B\frac{-A \cdot v_{\max} \cdot dt}{A \cdot c \cdot dt} \tag{B.42}$$

$$p_A = B\frac{v_{\max}}{c} \tag{B.43}$$

$$p_A = B\frac{2\pi fa}{c} \tag{B.44}$$

$$\begin{aligned} a &= \frac{v_{\max} p_A}{2\pi fB} \\ &= \frac{1484\ [\text{m/s}]\ \times\ 1.2\text{e}5\ [\text{Pa}]}{2\pi\left(30e3\ [1/s]\right)\ \times\ 2.15e9\ [\text{Pa}]} \\ &= 4.4e-7\ [m] \\ &= 0.44\ [\mu m] \end{aligned} \tag{B.45}$$

From the model, a pressure amplitude $\left(p_A\right)$ of 1.2 Bar was given by a displacement amplitude $\left(a\right)$ of 0.41 µm. Thus, the moving boundary solver correctly captures the ultrasound transducer face input as it agrees well with the theoretical approximation of the relationship between pressure amplitude to displacement amplitude.

Appendix C Local characteristic decomposition

Here we show the local characteristic decomposition of the primitive variables. Note that the process used for the WENO reconstruction in two-dimensional Cartesian coordinates (x, y) is the same as for the axisymmetric cylindrical coordinates (r, z). The governing system of Eqs. (2.1)-(2.5) expressed as a function of the primitive variables in the two-dimensional system is

$$\mathbf{V}_t + \mathbf{A}(\mathbf{V})\mathbf{V}_x + \mathbf{B}(\mathbf{V})\mathbf{V}_y = \mathbf{0} \ . \tag{B.46}$$

where

$$\mathbf{V} = \begin{bmatrix} \alpha_1\rho_1 \\ \alpha_2\rho_2 \\ u \\ v \\ p \\ \alpha_1 \end{bmatrix}, \ \mathbf{A} = \begin{bmatrix} u & 0 & \alpha_1\rho_1 & 0 & 0 & 0 \\ 0 & u & \alpha_2\rho_2 & 0 & 0 & 0 \\ 0 & 0 & u & 0 & \frac{1}{\rho} & 0 \\ 0 & 0 & 0 & u & 0 & 0 \\ 0 & 0 & \rho c^2 & 0 & u & 0 \\ 0 & 0 & 0 & 0 & 0 & u \end{bmatrix}, \ \mathbf{B} = \begin{bmatrix} v & 0 & 0 & \alpha_1\rho_1 & 0 & 0 \\ 0 & v & 0 & \alpha_2\rho_2 & 0 & 0 \\ 0 & 0 & v & 0 & 0 & 0 \\ 0 & 0 & 0 & v & \frac{1}{\rho} & 0 \\ 0 & 0 & 0 & \rho c^2 & v & 0 \\ 0 & 0 & 0 & 0 & 0 & v \end{bmatrix} \tag{B.47}$$

When considering the reconstruction in the *x*-direction (i), we need the Jacobian matrix in the *x*-direction, $\mathbf{A}$, and the vector of primitive variables, $\mathbf{V}$. Firstly, we decompose $\mathbf{A}$:

$$\mathbf{A} = \mathbf{Q}_i \mathbf{\Lambda}_i \mathbf{Q}_i^{-1} \tag{B.48}$$

where $\mathbf{\Lambda}_i$ is a diagonal matrix of the eigenvalues:

$$\mathbf{\Lambda}_i = \begin{bmatrix} u & 0 & 0 & 0 & 0 & 0 \\ 0 & u & 0 & 0 & 0 & 0 \\ 0 & 0 & u & 0 & 0 & 0 \\ 0 & 0 & 0 & u & 0 & 0 \\ 0 & 0 & 0 & 0 & u+c & 0 \\ 0 & 0 & 0 & 0 & 0 & u-c \end{bmatrix} \tag{B.49}$$

and

$$\mathbf{Q}_i = \begin{bmatrix} 0 & 0 & 0 & 1 & \frac{\alpha_1\rho_1}{\rho c^2} & \frac{\alpha_1\rho_1}{\rho c^2} \\ 0 & 0 & 1 & 0 & \frac{\alpha_2\rho_2}{\rho c^2} & \frac{\alpha_2\rho_2}{\rho c^2} \\ 0 & 0 & 0 & 0 & \frac{1}{\rho c} & -\frac{1}{\rho c} \\ 0 & 1 & 0 & 0 & 0 & 0 \\ 0 & 0 & 0 & 0 & 1 & 1 \\ 1 & 0 & 0 & 0 & 0 & 0 \end{bmatrix} \tag{B.50}$$

$$\mathbf{Q}_i^{-1} = \begin{bmatrix} 0 & 0 & 0 & 0 & 0 & 1 \\ 0 & 0 & 0 & 1 & 0 & 0 \\ 0 & 1 & 0 & 0 & -\frac{\alpha_2\rho_2}{\rho c^2} & 0 \\ 1 & 0 & 0 & 0 & -\frac{\alpha_1\rho_1}{\rho c^2} & 0 \\ 0 & 0 & \frac{\rho c}{2} & 0 & \frac{1}{2} & 0 \\ 0 & 0 & -\frac{\rho c}{2} & 0 & \frac{1}{2} & 0 \end{bmatrix} \tag{B.51}$$

The characteristic variables, $\mathbf{W}$, are obtained using the projection of the primitive variable onto the characteristic fields in the *x*-direction:

$$\mathbf{W} = \mathbf{Q}_i^{-1}\mathbf{V} \tag{B.52}$$

Given the characteristic variables, the WENO construction is performed. After, the characteristic variables are projected back to physical space:

$$\mathbf{V} = \mathbf{Q}_i\mathbf{W} \tag{B.53}$$

The decomposition in the *y*-direction (j) follows the same process with the corresponding Jacobian matrix, $\mathbf{B}$, which is also decomposed:

$$\mathbf{B} = \mathbf{Q}_j\mathbf{\Lambda}_j\mathbf{Q}_j^{-1} \tag{B.54}$$

where

$$\mathbf{Q}_j = \begin{bmatrix} 0 & 0 & 0 & 1 & \frac{\alpha_1\rho_1}{\rho c^2} & \frac{\alpha_1\rho_1}{\rho c^2} \\ 0 & 0 & 1 & 0 & \frac{\alpha_2\rho_2}{\rho c^2} & \frac{\alpha_2\rho_2}{\rho c^2} \\ 0 & 1 & 0 & 0 & 0 & 0 \\ 0 & 0 & 0 & 0 & \frac{1}{\rho c} & -\frac{1}{\rho c} \\ 0 & 0 & 0 & 0 & 1 & 1 \\ 1 & 0 & 0 & 0 & 0 & 0 \end{bmatrix} \tag{B.55}$$

$$\mathbf{\Lambda}_j = \begin{bmatrix} v & 0 & 0 & 0 & 0 & 0 \\ 0 & v & 0 & 0 & 0 & 0 \\ 0 & 0 & v & 0 & 0 & 0 \\ 0 & 0 & 0 & v & 0 & 0 \\ 0 & 0 & 0 & 0 & v+c & 0 \\ 0 & 0 & 0 & 0 & 0 & v-c \end{bmatrix} \tag{B.56}$$

$$\mathbf{Q}_j^{-1} = \begin{bmatrix} 0 & 0 & 0 & 0 & 0 & 1 \\ 0 & 0 & 1 & 0 & 0 & 0 \\ 0 & 1 & 0 & 0 & -\frac{\alpha_2\rho_2}{\rho c^2} & 0 \\ 1 & 0 & 0 & 0 & -\frac{\alpha_1\rho_1}{\rho c^2} & 0 \\ 0 & 0 & 0 & \frac{\rho c}{2} & \frac{1}{2} & 0 \\ 0 & 0 & 0 & -\frac{\rho c}{2} & \frac{1}{2} & 0 \end{bmatrix} \tag{B.57}$$

The characteristic variables, $\mathbf{W}$, are obtained using the projection of the primitive variable onto the characteristic fields in the *y*-direction:

$$\mathbf{W} = \mathbf{Q}_j^{-1}\mathbf{V}. \tag{B.58}$$

Given the characteristic variables, the WENO construction is performed. After, the characteristic variables are projected back to physical space:

$$\mathbf{V} = \mathbf{Q}_j\mathbf{W}. \tag{B.59}$$

References

1. Boyd, B. and S. Becker, *Numerical modelling of an acoustically-driven bubble collapse near a solid boundary.* Fluid Dynamics Research, 2018. **50**(6): p. 065506.
2. Argus, F., B. Boyd, and S.M. Becker, *Electroporation of tissue and cells: A three-equation model of drug delivery.* Computers in biology and medicine, 2017. **84**: p. 226-234.
3. Boyd, B. and S. Becker, *Macroscopic Modeling of In Vivo Drug Transport in Electroporated Tissue.* Journal of Biomechanical Engineering, 2016. **138**(3): p. 031008-031008-11.
4. Chahine, G.L., et al., *Modeling of surface cleaning by cavitation bubble dynamics and collapse.* Ultrasonics Sonochemistry, 2016. **29**: p. 528-549.
5. Reuter, F., et al., *Membrane cleaning with ultrasonically driven bubbles.* Ultrasonics Sonochemistry, 2017. **37**: p. 542-560.
6. Chandrapala, J., et al., *Ultrasonics in food processing.* Ultrasonics Sonochemistry, 2012. **19**(5): p. 975-983.
7. Yoshizawa, S., et al., *High intensity focused ultrasound lithotripsy with cavitating microbubbles.* Med Biol Eng Comput, 2009. **47**(8): p. 851-60.
8. Wang, Y.U., et al., *Antitumor effect of microbubbles enhanced by low frequency ultrasound cavitation on prostate carcinoma xenografts in nude mice.* Experimental and Therapeutic Medicine, 2012. **3**(2): p. 187-191.
9. Feng, G., et al., *Hemostatic Effects of Microbubble-Enhanced Low-Intensity Ultrasound in a Liver Avulsion Injury Model.* PLoS ONE, 2014. **9**(5): p. e95589.
10. Topaz, M., et al., *Acoustic cavitation in phacoemulsification: chemical effects, modes of action and cavitation index.* Ultrasound in Medicine & Biology, 2002. **28**(6): p. 775-784.
11. Paliwal, S. and S. Mitragotri, *Ultrasound-induced cavitation: applications in drug and gene delivery.* Expert Opinion on Drug Delivery, 2006. **3**(6): p. 713-726.
12. Tezel, A. and S. Mitragotri, *Interactions of Inertial Cavitation Bubbles with Stratum Corneum Lipid Bilayers during Low-Frequency Sonophoresis.* Biophysical Journal, 2003. **85**(6): p. 3502-3512.
13. Unga, J. and M. Hashida, *Ultrasound induced cancer immunotherapy.* Advanced drug delivery reviews, 2014. **72**: p. 144-153.
14. Brennen, C.E., *Cavitation and bubble dynamics*. Vol. 44. 1995, New York: Oxford University Press.
15. Young, F.R., *Cavitation*. 1999: World Scientific.

16. Leong, T., M. Ashokkumar, and S. Kentish, *The Growth of Bubbles in an Acoustic Field by Rectified Diffusion*, in *Handbook of Ultrasonics and Sonochemistry*. 2016, Springer Singapore: Singapore. p. 69-98.
17. Tomita, Y. and A. Shima, *High-speed photographic observations of laser-induced cavitation bubbles in water.* Acta Acustica united with Acustica, 1990. **71**(3): p. 161-171.
18. Coralic, V. and T. Colonius, *Shock-induced collapse of a bubble inside a deformable vessel.* European Journal of Mechanics - B/Fluids, 2013. **40**: p. 64-74.
19. Johnsen, E. and T. Colonius, *Shock-induced collapse of a gas bubble in shockwave lithotripsy.* The Journal of the Acoustical Society of America, 2008. **124**(4): p. 2011-2020.
20. Chahine, G.L. and K.M. Kalumuck, *The influence of structural deformation on water jet impact loading.* Journal of Fluids and Structures, 1998. **12**(1): p. 103-121.
21. Liu, L.T., et al., *Numerical analysis of the jet stage of bubble near a solid wall using a front tracking method.* Physics of Fluids, 2017. **29**(1): p. 012105.
22. Polat, B.E., et al., *Ultrasound-mediated transdermal drug delivery: Mechanisms, scope, and emerging trends.* Journal of Controlled Release, 2011. **152**(3): p. 330-348.
23. Paliwal, S., G.K. Menon, and S. Mitragotri, *Low-Frequency Sonophoresis: Ultrastructural Basis for Stratum Corneum Permeability Assessed Using Quantum Dots.* Journal of Investigative Dermatology, 2006. **126**(5): p. 1095-1101.
24. Ohl, C.-D., et al., *Sonoporation from Jetting Cavitation Bubbles.* Biophysical Journal, 2006. **91**(11): p. 4285-4295.
25. Zhou, Y., et al., *Controlled permeation of cell membrane by single bubble acoustic cavitation.* Journal of Controlled Release, 2012. **157**(1): p. 103-111.
26. Jayaprakash, A., C.-T. Hsiao, and G. Chahine, *Numerical and Experimental Study of the Interaction of a Spark-Generated Bubble and a Vertical Wall.* Journal of Fluids Engineering, 2012. **134**(3): p. 031301.
27. Naudé, C.F. and A.T. Ellis, *On the Mechanism of Cavitation Damage by Nonhemispherical Cavities Collapsing in Contact With a Solid Boundary.* Journal of Basic Engineering, 1961. **83**(4): p. 648-656.
28. Plesset, M.S. and R.B. Chapman, *Collapse of an initially spherical vapour cavity in the neighbourhood of a solid boundary.* Journal of Fluid Mechanics, 1971. **47**(2): p. 283-290.
29. Zhang, S., J.H. Duncan, and G.L. Chahine, *The final stage of the collapse of a cavitation bubble near a rigid wall.* Journal of Fluid Mechanics, 1993. **257**: p. 147-181.
30. Yu, P.W., S.L. Ceccio, and G. Tryggvason, *The collapse of a cavitation bubble in shear flows—A numerical study.* Physics of Fluids, 1995. **7**(11): p. 2608-2616.

31. Popinet, S. and S. Zaleski, *Bubble collapse near a solid boundary: a numerical study of the influence of viscosity.* Journal of Fluid Mechanics, 2002. **464**: p. 137-163.
32. Sussman, M., *A second order coupled level set and volume-of-fluid method for computing growth and collapse of vapor bubbles.* Journal of Computational Physics, 2003. **187**(1): p. 110-136.
33. Brujan, E.A., et al., *The final stage of the collapse of a cavitation bubble close to a rigid boundary.* Physics of Fluids, 2002. **14**(1): p. 85-92.
34. Blake, J., B. Taib, and G. Doherty, *Transient cavities near boundaries. Part 1. Rigid boundary.* Journal of Fluid Mechanics, 1986. **170**: p. 479-497.
35. Chahine, G.L., *Experimental and asymptotic study of nonspherical bubble collapse.* Applied Scientific Research, 1982. **38**(1): p. 187-197.
36. Best, J., *The formation of toroidal bubbles upon the collapse of transient cavities.* Journal of Fluid Mechanics, 1993. **251**: p. 79-107.
37. Chahine, G.L., *Modeling of Cavitation Dynamics and Interaction with Material*, in *Advanced Experimental and Numerical Techniques for Cavitation Erosion Prediction*, K.-H. Kim, et al., Editors. 2014, Springer Netherlands: Dordrecht. p. 123-161.
38. Johnsen, E. and T.I.M. Colonius, *Numerical simulations of non-spherical bubble collapse.* Journal of Fluid Mechanics, 2009. **629**: p. 231-262.
39. Coralic, V., *Simulation of shock-induced bubble collapse with application to vascular injury in shockwave lithotripsy*. 2015, California Institute of Technology.
40. Quirk, J.J. and S. Karni, *On the dynamics of a shock-bubble interaction.* Journal of Fluid Mechanics, 1996. **318**(1): p. 129-163.
41. Wang, Q.X. and J.R. Blake, *Non-spherical bubble dynamics in a compressible liquid. Part 1. Travelling acoustic wave.* Journal of Fluid Mechanics, 2010. **659**: p. 191-224.
42. Wang, Q.X. and J.R. Blake, *Non-spherical bubble dynamics in a compressible liquid. Part 2. Acoustic standing wave.* Journal of Fluid Mechanics, 2011. **679**: p. 559-581.
43. Garen, W., et al., *Shock wave emission during the collapse of cavitation bubbles.* Shock Waves, 2016. **26**(4): p. 385-394.
44. Ochiai, N. and J. Ishimoto, *Computational study of the dynamics of two interacting bubbles in a megasonic field.* Ultrasonics - Sonochemistry, 2015. **26**: p. 351-360.
45. Ochiai, N. and J. Ishimoto, *Numerical investigation of multiple-bubble behaviour and induced pressure in a megasonic field.* Journal of Fluid Mechanics, 2017. **818**: p. 562-594.
46. Abgrall, R. and S. Karni, *Computations of Compressible Multifluids.* Journal of Computational Physics, 2001. **169**(2): p. 594-623.
47. Chahine, G.L. and R. Duraiswami, *Dynamical Interactions in a Multi-Bubble Cloud.* Journal of Fluids Engineering, 1992. **114**(4): p. 680-686.

48. d'Agostino, L. and C. Brennen, *On the acoustical dynamics of bubble clouds.* 1983.
49. Fuster, D. and T. Colonius, *Modelling bubble clusters in compressible liquids.* Journal of Fluid Mechanics, 2011. **688**: p. 352-389.
50. Maeda, K. and T. Colonius, *Bubble cloud dynamics in an ultrasound field.* 2018.
51. Maeda, K. and T. Colonius, *Eulerian–Lagrangian method for simulation of cloud cavitation.* Journal of Computational Physics, 2018. **371**: p. 994-1017.
52. Van Wijngaarden, L., *On the collective collapse of a large number of gas bubbles in water*, in *Applied Mechanics*. 1966, Springer. p. 854-861.
53. Tiwari, A., C. Pantano, and J.B. Freund, *Growth-and-collapse dynamics of small bubble clusters near a wall.* Journal of Fluid Mechanics, 2015. **775**: p. 1-23.
54. Polat, B.E., et al., *A physical mechanism to explain the delivery of chemical penetration enhancers into skin during transdermal sonophoresis — Insight into the observed synergism.* Journal of Controlled Release, 2012. **158**(2): p. 250-260.
55. Schoellhammer, C.M., D. Blankschtein, and R. Langer, *Skin permeabilization for transdermal drug delivery: recent advances and future prospects.* EXPERT OPINION ON DRUG DELIVERY, 2014. **11**(3): p. 393-407.
56. Ogura, M., S. Paliwal, and S. Mitragotri, *Low-frequency sonophoresis: Current status and future prospects.* Advanced Drug Delivery Reviews, 2008. **60**(10): p. 1218-1223.
57. Tezel, A., A. Sens, and S. Mitragotri, *Description of transdermal transport of hydrophilic solutes during low-frequency sonophoresis based on a modified porous pathway model.* Journal of Pharmaceutical Sciences, 2003. **92**(2): p. 381-393.
58. Curtiss, G.A., et al., *Ultrasonic cavitation near a tissue layer.* Journal of Fluid Mechanics, 2013. **730**: p. 245-272.
59. Plesset, M.S. and R.B. Chapman, *Collapse of an initially spherical vapor cavity in the neighborhood of a solid boundary.* 1970.
60. Johnsen, E. and T. Colonius, *Implementation of WENO schemes in compressible multicomponent flow problems.* Journal of Computational Physics, 2006. **219**(2): p. 715-732.
61. Beig, S.A., B. Aboulhasanzadeh, and E. Johnsen, *Temperatures produced by inertially collapsing bubbles near rigid surfaces.* Journal of Fluid Mechanics, 2018. **852**: p. 105-125.
62. Fujikawa, S. and T. Akamatsu, *Effects of the non-equilibrium condensation of vapour on the pressure wave produced by the collapse of a bubble in a liquid.* Journal of Fluid Mechanics, 1980. **97**(3): p. 481-512.
63. Maisonhaute, E., P.C. White, and R.G. Compton, *Surface Acoustic Cavitation Understood via Nanosecond Electrochemistry.* The Journal of Physical Chemistry B, 2001. **105**(48): p. 12087-12091.

64. Allaire, G., S. Clerc, and S. Kokh, *A Five-Equation Model for the Simulation of Interfaces between Compressible Fluids.* Journal of Computational Physics, 2002. **181**(2): p. 577-616.
65. Coralic, V. and T. Colonius, *Finite-volume WENO scheme for viscous compressible multicomponent flows.* Journal of Computational Physics, 2014. **274**: p. 95-121.
66. Shyue, K.-M., *An Efficient Shock-Capturing Algorithm for Compressible Multicomponent Problems.* Journal of Computational Physics, 1998. **142**(1): p. 208-242.
67. Saurel, R. and R. Abgrall, *A Multiphase Godunov Method for Compressible Multifluid and Multiphase Flows.* Journal of Computational Physics, 1999. **150**(2): p. 425-467.
68. Marsh, S.P., *LASL shock Hugoniot data*. Vol. 5. 1980: Univ of California Press.
69. Cocchi, J.P., R. Saurel, and J.C. Loraud, *Treatment of interface problems with Godunov-type schemes.* Shock Waves, 1996. **5**(6): p. 347-357.
70. Shu, C.-W., *Essentially non-oscillatory and weighted essentially non-oscillatory schemes for hyperbolic conservation laws*, in *Advanced numerical approximation of nonlinear hyperbolic equations*. 1998, Springer. p. 325-432.
71. Toro, E.F., *Riemann solvers and numerical methods for fluid dynamics: a practical introduction*. Vol. 3rd. 2013: Springer Science & Business Media.
72. Balsara, D.S. and C.-W. Shu, *Monotonicity Preserving Weighted Essentially Non-oscillatory Schemes with Increasingly High Order of Accuracy.* Journal of Computational Physics, 2000. **160**(2): p. 405-452.
73. Laney, C.B., *Computational gasdynamics*. 1998: Cambridge university press.
74. Zhang, X. and C.-W. Shu, *Maximum-principle-satisfying and positivity-preserving high-order schemes for conservation laws: survey and new developments.* Proceedings of the Royal Society A: Mathematical, Physical and Engineering Science, 2011. **467**(2134): p. 2752.
75. Guo, Y., T. Xiong, and Y. Shi, *A positivity-preserving high order finite volume compact-WENO scheme for compressible Euler equations.* Journal of Computational Physics, 2014. **274**: p. 505-523.
76. Chi-Shu, W., *Essentially Non-Oscillatory and Weighted Essentially Non-Oscillatory Schemes for Hyperbolic Conservation Laws*. 1997, Institute for Computer Applications in Science and Engineering (ICASE).
77. Johnsen, E., *Numerical simulations of non-spherical bubble collapse: With applications to shockwave lithotripsy*. 2008, California Institute of Technology.
78. Qiu, J. and C.-W. Shu, *On the Construction, Comparison, and Local Characteristic Decomposition for High-Order Central WENO Schemes.* Journal of Computational Physics, 2002. **183**(1): p. 187-209.

79. Strang, G., *Linear Algebra and Its Applications*. 2014: Elsevier Science.
80. Hu, X.Y., et al., *A conservative interface method for compressible flows.* Journal of Computational Physics, 2006. **219**(2): p. 553-578.
81. Fedkiw, R.P., et al., *A Non-oscillatory Eulerian Approach to Interfaces in Multimaterial Flows (the Ghost Fluid Method).* Journal of Computational Physics, 1999. **152**(2): p. 457-492.
82. Hejazialhosseini, B., et al., *High order finite volume methods on wavelet-adapted grids with local time-stepping on multicore architectures for the simulation of shock-bubble interactions.* Journal of Computational Physics, 2010. **229**(22): p. 8364-8383.
83. Hu, X.Y. and B.C. Khoo, *An interface interaction method for compressible multifluids.* Journal of Computational Physics, 2004. **198**(1): p. 35-64.
84. Liu, W., L. Yuan, and C.-W. Shu, *A Conservative Modification to the Ghost Fluid Method for Compressible Multiphase Flows.* Communications in Computational Physics, 2011. **10**(4): p. 785-806.
85. Marquina, A. and P. Mulet, *A flux-split algorithm applied to conservative models for multicomponent compressible flows.* Journal of Computational Physics, 2003. **185**(1): p. 120-138.
86. Shukla, R.K., C. Pantano, and J.B. Freund, *An interface capturing method for the simulation of multi-phase compressible flows.* Journal of Computational Physics, 2010. **229**(19): p. 7411-7439.
87. So, K.K., X.Y. Hu, and N.A. Adams, *Anti-diffusion interface sharpening technique for two-phase compressible flow simulations.* Journal of Computational Physics, 2012. **231**(11): p. 4304-4323.
88. Terashima, H. and G. Tryggvason, *A front-tracking/ghost-fluid method for fluid interfaces in compressible flows.* Journal of Computational Physics, 2009. **228**(11): p. 4012-4037.
89. Wang, L., et al., *An immersed boundary method for fluid–structure interaction with compressible multiphase flows.* Journal of Computational Physics, 2017. **346**: p. 131-151.
90. Haas, J.F. and B. Sturtevant, *Interaction of weak shock waves with cylindrical and spherical gas inhomogeneities.* Journal of Fluid Mechanics, 1987. **181**(1): p. 41-76.
91. Vogel, A., W. Lauterborn, and R. Timm, *Optical and acoustic investigations of the dynamics of laser-produced cavitation bubbles near a solid boundary.* Journal of Fluid Mechanics, 1989. **206**: p. 299-338.
92. Alehossein, H. and Z. Qin, *Numerical analysis of Rayleigh–Plesset equation for cavitating water jets.* International Journal for Numerical Methods in Engineering, 2007. **72**(7): p. 780-807.

93. Rayleigh, L., *VIII. On the pressure developed in a liquid during the collapse of a spherical cavity.* Philosophical Magazine Series 6, 1917. **34**(200): p. 94-98.
94. Cole, R.H. and R. Weller, *Underwater Explosions.* Physics Today, 1948. **1**: p. 35.
95. Georgi, H., *The physics of waves*. 1993: Prentice Hall Englewood Cliffs, NJ.
96. Hsiao, C.-T., et al., *Modelling of material pitting from cavitation bubble collapse.* Journal of Fluid Mechanics, 2014. **755**: p. 142-175.
97. Hammitt, F., *Cavitation and Multiphase Flow Phenomena,(1980).* McGrow Hill.
98. Lide, D.R., *CRC handbook of chemistry and physics*. 2012: CRC Boca Raton.
99. Vokurka, K., *Comparison of Rayleigh's, Herring's, and Gilmore's models of gas bubbles.* Acta Acustica united with Acustica, 1986. **59**(3): p. 214-219.
100. Hickling, R. and M.S. Plesset, *Collapse and Rebound of a Spherical Bubble in Water.* Physics of Fluids, 1964. **7**(1): p. 7-14.
101. Gilmore, F.R., *The growth or collapse of a spherical bubble in a viscous compressible liquid.* 1952.
102. Supponen, O., et al., *Scaling laws for jets of single cavitation bubbles.* Journal of Fluid Mechanics, 2016. **802**: p. 263-293.
103. Benjamin, T.B. and A.T. Ellis, *The Collapse of Cavitation Bubbles and the Pressures thereby Produced against Solid Boundaries.* Philosophical Transactions of the Royal Society of London. Series A, Mathematical and Physical Sciences, 1966. **260**(1110): p. 221-240.
104. van Wijngaarden, L. *On the collective collapse of a large number of gas bubbles in water*. 1966. Berlin, Heidelberg: Springer Berlin Heidelberg.
105. Robertson, J. and S. Becker, *Influence of Acoustic Reflection on the Inertial Cavitation Dose in a Franz Diffusion Cell.* Ultrasound in medicine & biology, 2018. **44**(5): p. 1100.
106. Terahara, T., et al., *Dependence of low-frequency sonophoresis on ultrasound parameters; distance of the horn and intensity.* International Journal of Pharmaceutics, 2002. **235**(1): p. 35-42.
107. Mitragotri, S., et al., *Determination of threshold energy dose for ultrasound-induced transdermal drug transport.* Journal of Controlled Release, 2000. **63**(1-2): p. 41-52.
108. Bazan-Peregrino, M., et al., *Ultrasound-induced cavitation enhances the delivery and therapeutic efficacy of an oncolytic virus in an in vitro model.* Journal of Controlled Release, 2012. **157**(2): p. 235-242.
109. Collis, J., et al., *Cavitation microstreaming and stress fields created by microbubbles.* Ultrasonics, 2010. **50**(2): p. 273-279.
110. Zorec, B., et al., *Ultrasound and electric pulses for transdermal drug delivery enhancement: Ex vivo assessment of methods with in vivo oriented experimental protocols.* International Journal of Pharmaceutics, 2015. **490**(1–2): p. 65-73.

111. Tezel, A., A. Sens, and S. Mitragotri, *Incorporation of lipophilic pathways into the porous pathway model for describing skin permeabilization during low-frequency sonophoresis.* Journal of Controlled Release, 2002. **83**(1): p. 183-188.
112. Tezel, A., A. Sens, and S. Mitragotri, *A theoretical analysis of low-frequency sonophoresis: Dependence of transdermal transport pathways on frequency and energy density.* Pharmaceutical Research, 2002. **19**(12): p. 1841-1846.
113. Menon, G.K., S.H. Lee, and M.S. Roberts, *Ultrastructural effects of some solvents and vehicles on the stratum corneum and other skin components: Evidence for an "extended mosaic-partitioning model of the skin barrier".* Dermal Absorption and Toxicity Assessment, 1998. **91**: p. 727-751.
114. Sens, P. and S.A. Safran, *Pore formation and area exchange in tense membranes.* EPL (Europhysics Letters), 1998. **43**(1): p. 95-100.
115. Bennett, W.F.D., N. Sapay, and D.P. Tieleman, *Atomistic Simulations of Pore Formation and Closure in Lipid Bilayers.* BIOPHYSICAL JOURNAL, 2014. **106**(1): p. 210-219.
116. Yu, P.-W., S.L. Ceccio, and G. Tryggvason, *The collapse of a cavitation bubble in shear flows-A numerical study.* Physics of Fluids, 1995. **7**(11): p. 2608-2616.
117. Osterman, A., M. Dular, and B. Sirok, *Numerical simulation of a near-wall bubble collapse in an ultrasonic field.* Journal of Fluid Science and Technology, 2009. **4**(1): p. 210-221.
118. Johnsen, E. and T. Colonius, *Shock-induced collapse of a gas bubble in shockwave lithotripsy.* Journal of the Acoustical Society of America, 2008. **124**(4): p. 2011-2020.
119. Perigaud, G. and R. Saurel, *A compressible flow model with capillary effects.* Journal of Computational Physics, 2005. **209**(1): p. 139-178.
120. Favrie, N. and S.L. Gavrilyuk, *Diffuse interface model for compressible fluid – Compressible elastic–plastic solid interaction.* Journal of Computational Physics, 2012. **231**(7): p. 2695-2723.
121. Favrie, N., S.L. Gavrilyuk, and R. Saurel, *Solid–fluid diffuse interface model in cases of extreme deformations.* Journal of Computational Physics, 2009. **228**(16): p. 6037-6077.
122. Hank, S., et al., *Impact simulation by an Eulerian model for interaction of multiple elastic-plastic solids and fluids.* International Journal of Impact Engineering, 2017. **109**: p. 104-111.
123. Ndanou, S., N. Favrie, and S. Gavrilyuk, *Multi-solid and multi-fluid diffuse interface model: Applications to dynamic fracture and fragmentation.* Journal of Computational Physics, 2015. **295**: p. 523-555.

124. Caramana, E.J., et al., *The Construction of Compatible Hydrodynamics Algorithms Utilizing Conservation of Total Energy.* Journal of Computational Physics, 1998. **146**(1): p. 227-262.
125. Kluth, G. and B. Després, *Perfect plasticity and hyperelastic models for isotropic materials.* Continuum Mechanics and Thermodynamics, 2008. **20**(3): p. 173-192.
126. Kluth, G. and B. Després, *Discretization of hyperelasticity on unstructured mesh with a cell-centered Lagrangian scheme.* Journal of Computational Physics, 2010. **229**(24): p. 9092-9118.
127. Fedkiw, R.P., *Coupling an Eulerian Fluid Calculation to a Lagrangian Solid Calculation with the Ghost Fluid Method.* Journal of Computational Physics, 2002. **175**(1): p. 200-224.
128. Caramana, E.J., M.J. Shashkov, and P.P. Whalen, *Formulations of Artificial Viscosity for Multi-dimensional Shock Wave Computations.* Journal of Computational Physics, 1998. **144**(1): p. 70-97.
129. Sethian, J.A., *Fast marching methods.* SIAM review, 1999. **41**(2): p. 199-235.
130. Masatsuka, K., *I do like CFD, VOL.1, Second Edition*. 2013: K. Masatsuka.